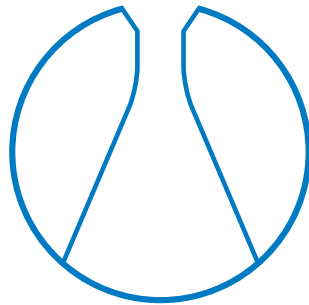


TECHNISCHE UNIVERSITÄT MÜNCHEN

Department Chemie
Lehrstuhl für Theoretische Chemie



Solid State QM/MM Embedding for a First-Principles
Description of Catalytic Processes

DISSERTATION

Daniel Berger



TECHNISCHE UNIVERSITÄT MÜNCHEN

Lehrstuhl für Theoretische Chemie

Solid State QM/MM Embedding for a First-Principles
Description of Catalytic Processes

Daniel Berger

Vollständiger Abdruck der von der Fakultät für Chemie der Technischen
Universität München zur Erlangung des akademischen Grades eines
Doktors der Naturwissenschaften (Dr. rer. nat.)
genehmigten Dissertation.

Vorsitzende : Univ.-Prof. Dr. Kathrin Lang

Prüfer der Dissertation:

1. Univ.-Prof. Dr. Karsten Reuter
2. Univ.-Prof. Dr. Ville Kaila

Die Dissertation wurde am 20.11.2014 bei der Technischen Universität
München eingereicht und durch die Fakultät für Chemie am 16.01.2015
angenommen.

Abstract

Catalysis and even more so photocatalysis are promising technologies to save and produce energy and fuels for a sustainable energy future. Existing photocatalytic devices are yet far from operating on a level of efficiency, which is economically feasible for large scale energy production. Also, although having been studied for more than a century, industrial catalysts still exhibit room for improvement. On top of that many novel material classes like zeolites or metal organic frameworks hold great potential which we have not even begun to exploit. In all these cases further fundamental research, especially focusing on the microscopic reaction details is highly necessary. Considering the complexity of experiments on the atomic scale, only highly accurate first principles computational studies can yield insights on the required level of detail.

When addressing catalyst functionalities through quantitative first-principles calculations, exploitation of the localized character of the chemical processes yields numerically most efficient approaches. To this end we augment the *FHI-aims* package with QM/MM solid state embedding capabilities, in which the expensive quantum mechanical (QM) description is reduced to the central chemically active region. Long range electrostatic interactions with the system remainder are accounted for on a classical level. Norm-conserving pseudopotentials and specifically optimized interatomic potentials allow for a smooth transition between both domains. With this approach, we allow for particularly efficient application of accurate high-level quantum mechanical methods beyond standard semi-local density functional theory. Where possible we validate our new implementation by benchmarking against the conventional periodic approach.

We use our implementation to study three very important materials in heterogeneous catalysis/photocatalysis, namely TiO_2 , MgO and the ZSM-5 zeolite. First, we studied the oxygen evolution reaction at the TiO_2 surface treating electronic exchange and correlation on accurate levels of theory up to so called double hybrids based on second order perturbation theory. Furthermore, we study oxygen vacancies at the TiO_2 surface which despite their abundance so far have mostly been neglected in studies of the catalytic activity of TiO_2 . Here, we address the fundamental question of thermodynamic stability of such vacancies, and found that the doubly charged defect is thermodynamically favored over a wide range of electrochemical potentials. We further study corner and step sites at the MgO -crystal, an important but not fully understood catalyst and support material for industrial catalysis. There, we compare the thermodynamic stability of O-vacancies and O/ O_2 -interstitials in different charge states. We surprisingly found the concentration of oxygen-interstitial with charge +1 at corner and steps sites is almost 100 % over a wide range of thermodynamical and doping conditions, even for electrochemical potentials which would favor defects at the plane surface. In a final application, we investigated the catalytic reduction of methanol to ethylene in the ZSM-5 zeolite along two recently proposed pathways and found the one involving decarboxylation to be energetically more favored. We suggest this as the dominant reaction route

In all these, chemically very different catalyst materials we found our new QM/MM solid state embedding approach to give us access to levels of theoretical accuracy not otherwise achievable. Furthermore, only through our embedding we were able to study defected and charged systems without computational artefacts inherent to standard periodic calculations.

Zusammenfassung

Katalyse und Photokatalyse sind vielversprechende Technologien zur künftigen umweltfreundlichen Energiegewinnung und -speicherung. Allerdings ist die Effizienz bisheriger Photokatalysatoren weit von einer ökonomisch rentablen Energiegewinnung entfernt. Selbst Katalysatoren, die bereits flächendeckend in der chemischen Industrie eingesetzt werden, haben trotz eines Jahrhunderts intensiver Forschung noch Optimierungsbedarf. Hierzu bieten neue funktionale Materialien, wie z.B. Zeolithe oder metall-organische Hybridstrukturen, zahlreiche noch weitestgehend ungenutzte Anwendungsmöglichkeiten. Um all diese Kapazitäten auf einer atomaren Skala verstehen und optimieren zu können, ist vor allem theoretische, computergestützte Grundlagenforschung von besonderer Notwendigkeit.

Nicht-elektrostatische Effekte in chemischen Prozessen an Oberflächen, die einer quantenmechanischen Beschreibung bedürfen, sind relativ lokal. Man kann hier die aufwendige quantenmechanische (QM) Beschreibung auf den chemisch aktiven Bereich reduzieren, während die langreichweitige elektrostatische Wechselwirkung mit der verbleibenden Oberfläche auf einem klassischen Kraftfeldniveau (MM) behandelt wird. Um dies zu ermöglichen wurden normerhaltende Pseudopotentiale in das Quantenchemieprogramm *FHI-aims* implementiert, die zusammen mit speziell optimierten Kraftfeldparametern für einen sanften Übergang zwischen beiden Domänen sorgen. Dieser Ansatz erlaubt sowohl eine Anwendung von Dichtefunktionaltheorie über die semi-lokale Formulierung hinaus als auch eine Behandlung von geladenen Zuständen, die beide für eine akkurate Beschreibung oberflächenchemischer Prozesse von besonderer Notwendigkeit sind. Die Implementation wurde dazu verwendet, drei besonders prominente (Photo-) Katalysatoren zu untersuchen: TiO_2 , MgO und das ZSM-5 Zeolith. An der TiO_2 -Oberfläche untersuchten wir die photokatalytische Wasserspaltung mit akkuraten quantenmechanischen Methoden bis hin zu sogenannten Doppelhybridfunktionalen. Desweiteren wurden die Sauerstoffstellen an der TiO_2 -Oberfläche untersucht, die trotz ihrer nachgewiesenen Häufigkeit bisher weitestgehend vernachlässigt wurden. Durch eine Analyse der thermodynamischen Stabilität solcher Fehlstellen fanden wir heraus, dass der zweifach geladene Ladungszustand über einen weiten Bereich von elektrochemischen Potentialen bevorzugt wird. Wir führten eine ähnliche Studie für die Ecken und Kanten an der MgO -Oberfläche durch. Dabei konnte überraschenderweise festgestellt werden, dass eine Sauerstoffanlagerung gleichzeitig an fast 100% der Ecken und Kanten einer Oberfläche thermodynamisch am stabilsten ist. Dies gilt für einen weiten Temperaturbereich, sogar für Dotierungskonzentrationen, welche auf der flachen Oberfläche Fehlstellen begünstigen würde. In einer letzten Anwendung untersuchten wir die katalytische Reduktion von Methanol zu Ethylen im ZSM-5 Zeolith entlang zweier kürzlich vorgeschlagener Reaktionspfade. Dabei erwies sich eine Reaktion mittels CO_2 -Abspaltung am energetisch günstigsten, weswegen wir diesen Weg als vorrangigen Reaktionsmechanismus vorschlagen. In all diesen chemisch sehr unterschiedlichen Katalysatoren erlaubte unser QM/MM Einbettungsansatz für Festkörper eine Anwendung jener höheren theoretischen Ansätze, die im konventionellen periodischen Ansatz nicht möglich gewesen wären. Desweiteren war es nur durch unseren Einbettungsansatz möglich, *geladene* Defekte inklusive der langreichweitigen Polarisation zu untersuchen, was in einem periodischen Ansatz nur schwer zu realisieren wäre.

Contents

Abstract	i
Zusammenfassung	iii
Contents	iv
1 Introduction	1
I Methods and Theoretical Background	5
2 Schroedinger Equation and Electronic Structure Theory	9
2.1 The Electronic Schroedinger Equation	10
2.2 Density Functional Theory	12
2.3 Basis sets and boundary conditions	18
2.4 Pseudopotentials	21
3 Solid-state Embedding	25
3.1 The QM/MM approach	26
3.2 <i>Seamless</i> coupling for solid-state embedding	28
3.3 Reproducing the long-range Electrostatic Potential	29
3.4 Solid-state embedding with ChemShell	31
3.5 Charged QM-region in the dilute limit	33
II Implementation	35
4 Implementation of Pseudopotentials	39
4.1 Energy Evaluation	40
4.2 Force Evaluation	42
4.3 Parallelization	43
4.4 Towards “full” pseudopotential functionality	43
5 Force Field Optimization with Evolutionary Algorithms	47
III Best-Practice and Benchmark	49
6 General Input Structure	53
6.1 <i>ChemShell</i> geometry input	53
6.2 FHI-aims input	54

6.3	GULP input	56
7	Benchmark against PBC: the $\text{TiO}_2(110)$ surface	57
7.1	Challenges with TiO_2	57
7.2	Best practice setup for high-dielectrics	60
7.3	Benchmark: the clean surface	67
7.4	Benchmark: Adsorption of small molecules	70
IV	Applications	77
8	Photocatalytic watersplitting at the pristine TiO_2 surface - Dependence on the xc-functional	81
8.1	Electronic contributions	82
8.2	Structural contributions	83
8.3	Conclusion	85
9	Surface oxygen vacancy at the TiO_2 rutile surface	87
9.1	Methodology	87
9.2	Results	93
9.3	Discussion	97
9.4	Summary/Conclusion	99
10	MgO - oxygen vacancies and interstitials at corner and step sites	101
10.1	Introduction	101
10.2	Defects at the MgO surface	102
10.3	Conclusion	107
11	Catalytic reactions in ZSM-5 zeolites	109
11.1	Embedding in covalent material	110
11.2	$\text{Fe}^{3+/2+}$ reduction potential of Fe doped ZSM-5	110
11.3	Catalytic reduction of methanol to ethylene	113
12	Conclusion & Outlook	121
	Appendices	125
A	Force Field generator	127
	List of Figures	131
	List of Tables	135
	Bibliography	137
	Acknowledgement	155

1 Introduction

The increasing world population and increased standards of living in developing countries are predicted to result in a massive increase of energy demand in the next decades. [1] To comply with this demand, while simultaneously accomplishing UN objectives to reduce man-made emission of CO₂ in order to decelerate global warming, is *the* major challenge for this and the coming generation. This urgently requires novel technologies to provide energy — in particular also fuels — but also an increased energy efficiency in every sector of consumption. This challenge, of course has to be tackled from all possible sides, as energy sources and consumers are highly diverse. Achieving this goal will likely only be possible through a mixture of tried and tested methods (e.g. wind and water power) combined with radically new ideas. Especially for the latter basic research, experimental as well as theoretical, has a lot to contribute in terms of materials discovery and optimization.

Of the available renewable sources of energy on the planet solar power is by far the most abundant and most equally distributed. Harvesting this energy through photovoltaic devices is a sustainable means of providing electricity, best suited to cover residential energy demand. Factories and chemical production sites, on the other hand, rely on a constant energy supply through the electric grid. As photovoltaic power stations are subject to weather conditions and time of day, they cannot provide a constant energy supply. In order to still pose a viable alternative to current technologies solar power conversion would need to also provide efficient energy storage solutions, which unfortunately it currently lacks. One of the best candidates for such a storage solution is photocatalysis, allowing to directly store solar energy in chemical bonds. A prominent example is given by the water-splitting reaction on TiO₂ to produce hydrogen, a possible alternative fuel, from sunlight [2]. Yet, existing photocatalytic devices are far from operating on a level of efficiency, which is economically feasible for large scale energy production. So far, the present understanding of the involved reaction mechanisms did not lead to a break-through increase in efficiency. To improve existing catalysts, extend their scope of applications or find new nanostructured compound catalysts, present photocatalytic models need to be revisited with fundamental research. For example the exact role of co-catalysts or surface defects is not fully understood on an atomistic scale including their influence on the electronic structure [3].

Computational approaches have been established as a powerful method to study such catalytic reactions from first-principles. Because of their favorable scaling with system size, the by far most widely used methods are such based on *density functional theory* (DFT) [4]. Due to subsequent progress in theory and numerical realization during the last 50 years these approaches have gained predictive power and are almost universally applicable from molecules to solid state materials [5]. Benefiting from widely available supercomputers with millions of CPUs, such methods became applicable for catalytic applications, which typically require considerable system sizes.

In addressing solid state systems through quantitative first-principles calculations, applying periodic boundary conditions (PBC) is the common approach. It elegantly exploits crystal periodicity and reduces the computational effort to the periodic supercell. Such a periodic setup

however becomes numerically inefficient when addressing non-periodicities in crystals, such as adsorbed nanoclusters, impurities or localized charges. In such cases, the unit cells hosting the non-periodicity have to be sufficiently large to avoid spurious interactions between periodic replica. Yet, depending on the necessary level of theory, such large supercells potentially lead to prohibitive demands on computer memory and on CPU time. This issue is further enhanced when addressing overall charged systems, due to long-range Coulomb interaction. An example for such non-periodic systems are nanostructured oxide surfaces which are promising candidates for a wide range of catalytic applications. For such materials, an alternative approach, efficiently exploiting the localized character of such non-periodicities and chemical processes, is given through the QM/MM embedded cluster approach. Here, the expensive quantum mechanical (QM) description is confined to a central region, while the system remainder is treated on a classical molecular mechanics level (MM).

In the present work, we present a novel QM/MM functionality connecting the all-electron quantum chemistry package *FHI-aims* with the general QM/MM environment *ChemShell*. Within this framework, the self-consistent polarization of the MM remainder is calculated through adequate (polarizable) interatomic potentials, interfacing *FHI-aims* with several molecular mechanics packages through the *ChemShell* environment. A major part of this work has been the implementation of norm-conserving pseudopotentials in *FHI-aims*. For QM/MM applications, these pseudopotentials are needed for accurate and consistent cluster termination, in order to prevent charge leakage into the MM region. *FHI-aims* allows especially efficient access to a wide range of beyond-DFT methods, yielding a very accurate resolution of the electronic structure within the QM region. With that we ultimately have a computational tool for calculations of catalytic processes with predictive qualitative, including full charge flexibility.

This work is divided into four parts. The first part outlines the theoretical background. Starting from an accurate analytic description of the many-electron problem, we discuss Hartree-Fock and density functional theory as approximate but numerically feasible methods to resolve the electronic structure. Along these lines, important technicalities for a numerical realization like the basis set, integration grids and boundary conditions as well as the concept of pseudopotentials will be introduced. Furthermore, the theoretical basis of QM/MM embedding with the focus on solid state applications is introduced. Among other things, we discuss the nuts and bolts of the molecular mechanics description of solids, and the technicalities of coupling the QM and MM domains. This involves techniques to reproduce the electrostatic potential of the crystal background and the use of pseudopotentials in the QM/MM approach.

In the second part, all implementation work necessary for the QM/MM embedding approach is documented. We will discuss the implementation of norm-conserving pseudopotentials into the all-electron DFT code *FHI-aims*, including some details on efficient parallelization to allow for large scale computer simulations. Furthermore, we present a program which allows for automated *global* optimization of the force field parameters, tailored to achieve matching structural and dielectric properties of QM and MM levels.

In the third part we explain how to efficiently use the provided QM/MM infrastructure. In a manual-like fashion, we discuss all the ingredients needed to perform solid-state embedding calculations with our implementation, discussing the formats of all input files along the line. The actual applicability of QM/MM techniques and the challenges connected with it very much depend on the material addressed. One rather problematic case is, when the static dielectric properties cannot be described even through a state-of-the-art force field, which is the case in TiO_2 . We derive a best-practice approach to the setup and the actual calculation for such problematic materials. Furthermore, in order to gauge the accuracy of our QM/MM setup we benchmark our implementation as well as the derived best-practice approach on the example of the clean TiO_2 rutile (110) surface, and the adsorption of small molecules at this surface. In

doing so, we benefit from *FHI-aims*' ability to perform periodic and cluster calculations on the same numerical footing.

The last part of this thesis is dedicated to several applications of our QM/MM infrastructure, reporting new scientific insight and furthermore demonstrating the versatility of the provided infrastructure. First, we address the oxygen evolution reaction at the TiO_2 surface, one of the two half-reactions in the photocatalytic water splitting process. Being one promising approach to a future green economy, this reaction has especially been studied from first-principles in recent years. As a trade-off between computational expenses and accuracy most such studies were performed at the GGA-DFT level of theory. Exploiting efficient access to higher methods through our QM/MM approach, we perform a functional screening study from GGA up to double-hybrid functionals and discuss the predicted viability of TiO_2 as an oxygen evolution catalyst.

In a second demonstration of our embedding approach we study the oxygen vacancy at the TiO_2 surface, and assess its formation energy in the charge states 0, +1 & +2. The favored charge state and the concentration of defects potentially have great impact on the surface chemistry, not only considering the actual reaction energies and mechanisms but also with regards to conductivity, photon harvesting and photo electron-hole pair lifetime [6]. An experimental investigation of the charge state is fairly challenging and thus still under debate [7–9]. Therefore, prediction from first-principles are desired. Here, our QM/MM approach is of great advantage as it does not suffer from the same difficulties to describe charged defects as periodic calculations.

In a third study we investigate the stabilities of oxygen vacancies and interstitials at corner and step sites of the Magnesium Oxide (MgO) crystal. MgO is one of the most important classes of functional materials with wide applications in the field of catalysis, either as a catalyst by itself [10, 11] or as an active support for co-catalysts [12, 13]. Here, we exploit the QM/MM approach to effortlessly study such highly non-periodic systems which cannot be efficiently addressed in a periodic setup. Global optimization of the force field again allows for a most accurate coupling between the QM and MM domains and to calculate the *full* dielectric response explicitly.

Finally, our QM/MM embedding is used to study catalytic reactions in porous semi-covalent materials. Specifically, we address the $\text{Fe}^{3+/2+}$ reduction in the ion doped zeolite ZSM-5, applying different treatments of electron exchange and correlation up to double-hybrid functionals. As a second show-case, we address the catalytic methanol reduction to ethylene in the ZSM-5 zeolite. In support of experimental work in the group of Johannes Lercher, we aim to unravel the reaction mechanism and explore the thermodynamic feasibility of two proposed reaction path ways from first-principles.

Part I

**Methods and Theoretical
Background**

In this first part of this work the reader is introduced to the fundamental theoretical concepts this work is based on. The first chapter presents a short review of the quantum description of matter, specifically electronic structure theory in its ground state. Nomenclature and arguments closely follow the books of Martin [14] as well as Szabo and Ostlund [15]. For a more detailed description the reader is referred to these textbooks.

Electrons and nuclei are the fundamental particles determining the nature of matter in our daily lives: atoms, molecules and condensed matter. Interaction and fundamental “quantum behaviour” not only explain why electrons and nuclei can form stable matter, although being of opposite electric charge, they also determine electric, magnetic and optical properties of matter. Their collective description is given by the famous (time-independent)¹ Schroedinger equation [16]

$$\hat{H} |\Phi_i\rangle = E_i |\Phi_i\rangle \quad , \quad (1.1)$$

with \hat{H} being the time-independent Hamilton operator carrying all information about the system. The eigenspectrum of the Hamiltonian yields the (exact) solution of the system, i.e. all possible pure states. Technically, all possible states are superpositions of the pure states $|\Phi_i\rangle$. As real materials and chemical reactions involve many electrons, Eq. 1.1 refers to the many-body Schroedinger equation, determining the many-body wavefunctions and energetics.

Unfortunately, no analytic solution to Schroedinger’s equation exists for more than one electron, and exact numerical solution of Eq. 1.1 is beyond computational power even for a few electrons, calling for approximative methods. One of such approximative methods is *density functional theory*, which is - as the name implies - based on the electronic density rather than on explicit wavefunctions. Density functional theory (DFT) combines a reasonable level of accuracy for chemical applications with an excellent scaling behaviour with system size, establishing it as the most widely used and most successful approach in electronic structure theory [5]. DFT and its founding father, Walter Kohn, has been honored with the Nobel Prize for Chemistry in 1998.

In this chapter, we will discuss the nuts and bolts of Kohn-Sham DFT, which will be the main *work horse* in this thesis. Along these lines, we will compare different numerical concepts in terms of basis functions, boundary conditions and pseudopotentials.

In the second chapter a particularly efficient concept for the description of metal oxide solids involving coupling of quantum mechanical (QM) and molecular mechanical techniques (MM) will be presented. This hybrid concept is based on a hierarchical division of the system into a sequence of models with decreasing sophistication [17, 18].

Warshel, Levitt and Karplus were awarded the Nobel Prize in Chemistry in 2013 for their pioneer idea and further developments in QM/MM approaches. For an overview of hybrid QM/MM approaches the reader is referred to the reviews of Bernstein and Csanyi [19], Lin and Trular [20], and the references therein.

¹A time-dependent extension of Eq. 1.1 allows for explicit time-propagation and collective motion of electrons and nuclei. In this work, we focus on the stationary time-independent case.

2 Schroedinger Equation and Electronic Structure Theory

Our ultimate goal is to describe surface reactions involving many electrons and many nuclei. The fundamental equation determining such many-body problems is the deceptively simple appearing Schroedinger's equation (Eq. 1.1). All complexity of the system is, however, hidden in the many-body Hamiltonian ¹,

$$\hat{H} = \underbrace{-\frac{1}{2} \sum_i \nabla_i^2}_{\hat{T}_{el}} - \underbrace{\sum_{i,I} \frac{Z_I}{|\mathbf{r}_i - \mathbf{R}_I|}}_{\hat{V}_{ext}} + \underbrace{\sum_{i,j} \frac{1}{|\mathbf{r}_i - \mathbf{r}_j|}}_{\hat{V}_{int}} - \underbrace{\frac{1}{2M_I} \sum_I \nabla_I^2}_{\hat{T}_{nuc}} + \underbrace{\sum_{I,J} \frac{Z_I Z_J}{|\mathbf{R}_I - \mathbf{R}_J|}}_{\hat{V}_{nuc-nuc}} . \quad (2.1)$$

Electrons are denoted by lower case subscripts and symbols, while nuclei, with proton number Z_I and mass M_I , are indicated by upper case subscripts. From left to right, the terms represent the electronic kinetic energy operator, Coulomb potential between electrons and nuclei, Coulomb potential between electrons, kinetic energy operator for the nuclei and Coulomb potential among nuclei. An analytic solution is inaccessible already when more than one electron is involved. However, for a sound understanding of electronic structure theory, it is vital to start from such a complicated but exact expression and subsequently introduce approximations. ²

The first approximation arises from a separation of mass and time scales. In fact, nuclei are much heavier than electrons. The inverse mass of a nucleus $1/M_I$ can thus be considered as small. If we consider the approximation of letting the nuclear mass go to infinity, we can ignore its kinetic energy. This significantly simplifies the problem at hand, as it allows to separate the many-body wavefunction

$$|\Phi\rangle = |\Psi\rangle |\Pi\rangle . \quad (2.2)$$

into a product of the electronic $|\Psi\rangle$ and nuclear $|\Pi\rangle$ many-body wavefunctions. This is called the adiabatic Born-Oppenheimer approximation [22]. Pictorially, we can think of the electrons to instantaneously adapt to a given configuration of nuclei. In many cases, this approximation is perfectly valid. However, some interesting physical effects like electron-phonon interaction, BCS theory of superconductivity or proton-tunneling, require explicit treatment of the nuclear quantum effects, e.g. in a perturbative fashion. For the chemical applications we are aiming at here, separating out the nuclear motion is a decent approximation and we can focus on the Hamiltonian for the electrons, treating the nuclear positions as parameters. In the following we give a short introduction to such a treatment in the framework of DFT.

¹The equation is given in atomic units $\hbar = e = a_0 = 4\pi/\epsilon_0 = 1$, as defined in [21]. We follow this convention throughout this work, if not stated otherwise.

²At this point, we already neglect relativistic and quantum electrodynamic effects.

2.1 The Electronic Schroedinger Equation

In the Born-Oppenheimer approximation the electronic Hamiltonian can be written as

$$\hat{H} = \hat{T} + \hat{V}_{ext} + \hat{V}_{int} \quad , \quad (2.3)$$

following the notation in Eq. 2.1.

Evaluating this Hamiltonian yields the energy of electrons in an external potential. It does not include the Coulomb energy among nuclei. This term is not part of the electron problem and, thus does not have an effect on the spectrum of the electronic Hamiltonian. It does, however, contribute to the *total energy* of the system. The external potential here only includes the Coulomb term due to the nuclei. Yet, this term may be augmented by other external potentials, e.g. due to an external electric field or due to electrostatic embedding as will be discussed in Section 2.3 and explicitly in Section 3.4. Plugging Eq. 2.3 into the Schroedinger equation 1.1 now formulates the fundamental equation for electronic structure theory,

$$\hat{H}\Psi_i(\{\mathbf{r}_i\}) = E_i\Psi_i(\{\mathbf{r}_i\}) \quad , \quad (2.4)$$

determining the many-body wavefunctions for the electrons $\Psi_i(\{\mathbf{r}_i\}) = \Psi_i(\mathbf{r}_1, \mathbf{r}_2, \dots, \mathbf{r}_N)$.³

If the spectrum of many-body wavefunctions is known, then any many-body observable \mathcal{O} can be calculated as an expectation value. Dirac's *braket* nomenclature allows a very closed form:

$$\mathcal{O}_i = \frac{\langle \Psi_i | \hat{\mathcal{O}} | \Psi_i \rangle}{\langle \Psi_i | \Psi_i \rangle} = \frac{\int d\mathbf{r}_1 d\mathbf{r}_2, \dots, d\mathbf{r}_N \Psi_i^\dagger(\mathbf{r}_1, \mathbf{r}_2, \dots, \mathbf{r}_N) \hat{\mathcal{O}} \Psi_i(\mathbf{r}_1, \mathbf{r}_2, \dots, \mathbf{r}_N)}{\int d\mathbf{r}_1 d\mathbf{r}_2, \dots, d\mathbf{r}_N \Psi_i^\dagger(\mathbf{r}_1, \mathbf{r}_2, \dots, \mathbf{r}_N) \Psi_i(\mathbf{r}_1, \mathbf{r}_2, \dots, \mathbf{r}_N)} \quad . \quad (2.5)$$

A closed expression for the many-body wavefunction is, however, difficult to obtain. First, the electrons are explicitly correlated through the electron-electron Coulomb interaction \hat{V}_{int} — if one electron changes position (or state) it will effect all other electrons. Second, electrons are indistinguishable fermions and have to obey Pauli's exclusion principle. This manifests in the requirement of Ψ_i to be antisymmetric with respect to particle exchange

$$\Psi_i(\mathbf{r}_1, \mathbf{r}_2, \dots, \mathbf{r}_N) = -\Psi_i(\mathbf{r}_2, \mathbf{r}_1, \dots, \mathbf{r}_N) \quad . \quad (2.6)$$

Hence, the Ψ_i cannot be described as a simple product of *1-electron* wavefunctions, but through a full $3N$ dimensional object, with N being the number of electrons.

Storing the many-body wavefunction for a single oxygen atom, even on a very sparse grid with 10 grid points per dimension would require storage of $10^{3 \times 8}$ floating point numbers, which clearly exceeds any computational resources in terms of memory demand. Consequently, it is not possible to directly solve the many-body Schroedinger equation, which would contain the full information of the system.

Quantum mechanical particles also follow the *principle of least action*, known from classical mechanics. At zero temperature a quantum mechanical system will thus be in its ground state, i.e. there is no other state which would lead to a lower total energy than the one which is called the ground state of the system. Electronic excitations in atoms, molecules and in non-metallic solids on the other side typically afford an energy of the order of eV, which corresponds to orders of 10'000 K. For quantum chemistry applications, one is typically interested in temperature and pressure regimes which are not too far from standard conditions, e.g. a few hundred Kelvin. Under such conditions, thermal excitations can be neglected, which means that we can narrow down the problem to finding the electronic ground state.⁴

³Here, \mathbf{r} are generalized coordinates also incorporating the spin degree of freedom.

⁴Excitations can later be included *a posteriori* perturbatively.

Hartree-Fock Approximation

A historically very important approach to the many-electron system was elaborated by D.R. Hartree and V. Fock [21, 23]. In this approach the correlated many-electron problem is rephrased as a system of *non-interacting* electrons moving in an averaged Coulomb potential. The ingenious idea by V. Fock was to exactly account for electronic exchange through an antisymmetric many-body wavefunction constructed from the single-particle orbitals. This was not only a milestone by itself, but is the foundation of most modern quantum chemical methods.

Neglecting the electron-electron interaction \hat{V}_{int} in the many-body Hamiltonian yields a single-particle spectrum of eigenstates $\{\phi_i\}$ with eigenvalues ϵ_i for the non-interacting electron. Here, $\phi_i(\mathbf{r}_j, \sigma_j)$ are spin-orbitals, being a product of a function of the position $\varphi_i^{\sigma_j}(\mathbf{r}_j)$ and of a function of the spin variable $\alpha_i(\sigma_j)$. The simplest form of a many-body wavefunction obeying Pauli's principle is an antisymmetric product of such independent 1-electron wavefunctions $\phi_i(\mathbf{r}_j, \sigma_j)$ of electron j in the state i , the so-called *Slater determinant* [24]:

$$\Psi = \frac{1}{\sqrt{N!}} \begin{vmatrix} \phi_1(\mathbf{r}_1, \sigma_1) & \phi_2(\mathbf{r}_1, \sigma_1) & \cdots & \phi_N(\mathbf{r}_1, \sigma_1) \\ \phi_1(\mathbf{r}_2, \sigma_2) & \phi_2(\mathbf{r}_2, \sigma_2) & \cdots & \phi_N(\mathbf{r}_2, \sigma_2) \\ \vdots & \vdots & & \vdots \\ \phi_1(\mathbf{r}_N, \sigma_N) & \phi_2(\mathbf{r}_N, \sigma_N) & \cdots & \phi_N(\mathbf{r}_N, \sigma_N) \end{vmatrix} \quad (2.7)$$

Calculating the expectation value of the electronic many-body Hamiltonian (Eq. 2.3), while exploiting orthonormality conditions $\langle \phi_i | \phi_j \rangle = \delta_{ij}$, allows to write down an energy expression for the many-electron system expressed only through 1- and 2-particle operators

$$\begin{aligned} E = & \sum_{i,\sigma} \int d\mathbf{r} \varphi_i^{\sigma*} \left[-\frac{1}{2} \nabla^2 + V_{ext}(\mathbf{r}) \right] \varphi_i^{\sigma} + \\ & \frac{1}{2} \sum_{i,j,\sigma_i,\sigma_j}^N \int \int d\mathbf{r} d\mathbf{r}' \varphi_i^{\sigma_i*}(\mathbf{r}) \varphi_j^{\sigma_j*}(\mathbf{r}') \frac{1}{|\mathbf{r} - \mathbf{r}'|} \varphi_i^{\sigma_i}(\mathbf{r}) \varphi_j^{\sigma_j}(\mathbf{r}') \\ & - \frac{1}{2} \sum_{i,j,\sigma}^N \int \int d\mathbf{r} d\mathbf{r}' \varphi_i^{\sigma*}(\mathbf{r}) \varphi_j^{\sigma*}(\mathbf{r}') \frac{1}{|\mathbf{r} - \mathbf{r}'|} \varphi_j^{\sigma}(\mathbf{r}) \varphi_i^{\sigma}(\mathbf{r}') \quad . \end{aligned} \quad (2.8)$$

The first term refers to the kinetic energy of the independent electrons and the interaction with the external potential. The electron-electron interaction now separates into two integral terms of direct and exchange interactions among electrons. Since the electron density $n_i(\mathbf{r})$ of electron i is trivially related to the single-particle orbitals

$$n_i(\mathbf{r}) = \sum_{\sigma_i} \varphi_i^{\sigma_i*}(\mathbf{r}) \varphi_i^{\sigma_i}(\mathbf{r}) \quad (2.9)$$

the direct term is to be interpreted as the classic Coulomb interaction among electrons in terms of the electron density. This term is called the *Hartree term* and contains spurious self-interaction of electrons for $i = j$. The exchange term only acts between electrons with the same spin, and represents two physical effects: Pauli exclusion principle and cancellation of the self-interaction error in the Hartree term.

Applying Ritz' variational principle with respect to $\varphi_i^{\sigma_i*}(\mathbf{r})$ for each spin under the constraint of orthonormality of the single-particle orbitals allows to minimize Eq. 2.8 and to evaluate the

ground-state electronic energy. The resulting Schroedinger-like differential-integral equations determining the single-particle energies are called the *Hartree-Fock equations*

$$\left[-\frac{1}{2}\nabla^2 + V_{ext}(\mathbf{r}) + \sum_{j,\sigma_j} \int d\mathbf{r}' \frac{|\varphi_j^{\sigma_j}(\mathbf{r}')|^2}{|\mathbf{r} - \mathbf{r}'|} - \sum_j \int d\mathbf{r}' \frac{\varphi_i^{\sigma_i}(\mathbf{r}')\varphi_j^{\sigma_j*}(\mathbf{r}')}{|\mathbf{r} - \mathbf{r}'|} \right] \varphi_i^{\sigma}(\mathbf{r}) = \epsilon_i^{\sigma} \varphi_i^{\sigma}(\mathbf{r}) \quad . \quad (2.10)$$

The solutions φ_i^{σ} of this set of equations define states of quasi-independent electrons moving in a *mean effective* (nonlocal) potential. This effective potential depends on all orbitals, making Eq. 2.10 a coupled non-linear set of differential equations, which has to be solved iteratively. The resulting potential is then a so-called *self-consistent field* (SCF).

This approach incorporates electronic exchange in an exact way through the *ansatz* of Slater determinants. However, explicit electron-electron correlation is only incorporated through this mean effective potential, stemming from the fact that the many-body wavefunction is approximated through a single Slater-determinant. Several strategies have been proposed to cure for insufficient correlation effects, either based on a perturbative treatment (Møller-Plesset theory) or through systematic expansion of the many-body wavefunction in a basis of many Slater-determinants. For further reading in this direction the reader is referred to standard literature [15, 25, 26]. CCSD(T), one of these expansion based methods, is considered as the *gold standard* in quantum chemistry. However, a formal scaling of $\mathcal{O}(N^7)$ allows applications only for small molecules and not yet for solid state systems, although first attempts have been successfully made for very light crystals (LiH and BN) [27].

2.2 Density Functional Theory

Almost in parallel to Schroedinger and his work on his famous equation, Thomas and Fermi developed an alternative method to calculate the total energy of a many-electron system [28, 29]. In contrast to the Schroedinger equation the Thomas-Fermi method is not based on explicit wavefunctions but on the electronic density, which trivially relates to the normalized many-body wavefunction as

$$n(\mathbf{r}) = N \int d\mathbf{r}_2^3 \dots d\mathbf{r}_N^3 |\Psi(\mathbf{r}, \mathbf{r}_2, \mathbf{r}_3 \dots \mathbf{r}_N)|^2 \quad . \quad (2.11)$$

Thomas and Fermi approximated the total energy of an atom as an explicit functional of electron density

$$E[n] = T[n] + \int d^3r V_{ext}(\mathbf{r})n(\mathbf{r}) + \int d^3r d^3r' \frac{n(\mathbf{r})n(\mathbf{r}')}{|\mathbf{r} - \mathbf{r}'|} \quad , \quad (2.12)$$

simplified as non-interacting electrons, completely neglecting exchange and correlation between electrons. Furthermore, the density was approximated to be locally equal to the homogeneous electron gas. The ground state electron density and total energy can be found by minimizing Eq. 2.12 for all possible $n(\mathbf{r})$ constrained to conservation of the total number of electrons.

Although several correction terms have been proposed [30, 31], the Thomas-Fermi approximation is not able to reproduce chemical binding of molecules [32] due to the representation of the kinetic energy, which completely neglects contributions from electronic exchange and correlation. Thus, it is not a useful tool to predictively describe the electronic structure in chemical applications. Nonetheless, the failure of Thomas-Fermi theory for chemical systems is instructive, as it clearly points out the importance of electronic correlation to describe chemical binding. The work by Thomas and Fermi, moreover, can be considered a milestone in electronic structure theory paving the road for the *density functional theory*, which nowadays is the primary tool to describe the electronic structure of condensed matter.

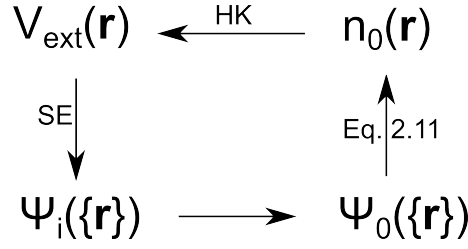


Figure 2.1: Illustration of the first Hohenberg-Kohn theorem. The external potential V_{ext} defines the spectrum of many-body wavefunctions ψ_i through Schroedinger's equation (SE), including the ground state wavefunction ψ_0 , which trivially relates to the ground state electron density n_0 . The Hohenberg-Kohn theorem (HK) states that n_0 in turn determines the external potential V_{ext} , completing the cycle.

Fundamentals of Density Functional Theory

Density functional theory (DFT) is one of the most popular and successful quantum mechanical approaches for the solution of many-body problems. It is an, in principle, exact many-body theory for systems described by a Hamiltonian such as

$$\hat{H} = -\frac{\hbar^2}{2m} \sum_i \nabla_i^2 + \sum_i V_{ext}(\mathbf{r}_i) + \frac{1}{2} \sum_{i \neq j} \frac{e^2}{|\mathbf{r}_i - \mathbf{r}_j|} . \quad (2.13)$$

DFT allows a huge versatility of applications from calculating atomic ground state energies and observables, e.g. bond-length, -angles and binding energies of molecules over to lattice constants, phonon spectra of solids and even in nuclear physics [33, 34].

In spite of its flexibility, DFT is based on a rigid conceptual framework, first proven by Hohenberg and Kohn [35] (for a detailed proof see e.g. [36, 37]). The external potential $V_{ext}(\mathbf{r})$ determines all states of the system ($\Psi_i(\{\mathbf{r}_i\})$) (including the ground state many-body wavefunction $\Psi_0(\{\mathbf{r}_i\})$) via the Schroedinger equation. The corresponding ground state density $n_0(\mathbf{r})$ is then described by Eq. 2.11. The first Hohenberg-Kohn theorem completes the cycle (see Figure 2.1, by proving that the ground state electron density $n_0(\mathbf{r})$, in turn, uniquely determines the external potential $V_{ext}(\mathbf{r})$, up to a constant. This means that also the ground state many-body wavefunction is determined by $n_0(\mathbf{r})$, and thus all ground state observables

$$\hat{O}_0 = \langle \Psi_0(\{\mathbf{r}_i\}) | \hat{O} | \Psi_0(\{\mathbf{r}_i\}) \rangle = \langle \Psi[n_0] | \hat{O} | \Psi[n_0] \rangle \quad (2.14)$$

are accessible through the ground state density.

Moreover, Hohenberg and Kohn, and in a more rigorous fashion Levy and Lieb [38, 39], proved the existence of an energy expression as a *universal functional* of the electron density, the infimum of which yields the ground state density (second Hohenberg-Kohn theorem). This functional is called universal because it is the same for all electron systems in any V_{ext} . For a particular V_{ext} , the exact ground state energy of the system is the global minimum of this functional, and the density $n(\mathbf{r})$ minimizing the functional is the exact ground state electron density $n_0(\mathbf{r})$.

Here, we briefly sketch out the proof by Levy and Lieb starting from the general energy expression in terms of the many body wavefunction Ψ (for further reading we refer to [36, 37]). In principle, the ground state can be found by minimizing the energy with respect to all variables in Ψ . However, Eq. 2.11 is not bijective, i.e. potentially more than one Ψ can lead to the same density. Let us first focus on all many-body wavefunctions, which have the same density $n(\mathbf{r})$.

For such a wavefunction the total energy can be written as

$$E = \langle \Psi | \hat{T} | \Psi \rangle + \langle \Psi | \hat{V}_{int} | \Psi \rangle + \int d^3r V_{ext}(\mathbf{r})n(\mathbf{r}) \quad . \quad (2.15)$$

If one now minimizes the energy over all wavefunctions Ψ with the same density $n(\mathbf{r})$, one obtains a unique lowest total energy for that density

$$\begin{aligned} E[n] &= \min_{\Psi \rightarrow n(\mathbf{r})} [\langle \Psi | \hat{T} | \Psi \rangle + \langle \Psi | \hat{V}_{int} | \Psi \rangle] + \int d^3r V_{ext}(\mathbf{r})n(\mathbf{r}) \\ &= F_{LL}[n] + \int d^3r V_{ext}(\mathbf{r})n(\mathbf{r}) \quad . \end{aligned} \quad (2.16)$$

A second minimization over all possible densities then defines the ground state electron density. $F_{LL}[n]$ is universally valid for all electron systems, as it is independent on any external information like $V_{ext}(\mathbf{r})$. It contains all problematic features of any many-body system, namely exchange and correlation terms. If an exact expression for $F_{LL}[n]$ would be known exactly all many-body ground state properties, e.g. susceptibilities or the Fermi surface, but also excitation energies were given correctly by this functional. So far, it only has been shown that a functional can be defined which yields the exact ground-state density and energy of the true interacting many-body system. It does, however, not propose any further strategy to find the functional other than through the original definition in terms of many-body wavefunctions.

The Hohenberg-Kohn theorem in its original proof requires the external potential to be local. A generalization, which also holds for nonlocal potentials, was given and proven by Gilbert [40].

Kohn-Sham Density Functional Theory

Density functional theory only became the most widely used method for electronic structure calculations because of the pioneering work by Kohn and Sham [41]. It is a disarmingly cheap approach to many-body systems, with its greatest asset being its easy numerical realization and implementation in computer codes.

The Kohn-Sham *ansatz* to DFT is to map the many-body problem onto an *auxiliary* system that can be solved more easily. The idea is to treat the system of interacting electrons as a system of non-interacting electrons in a mean effective potential V_{eff} , which includes the problematic many-body exchange and correlation terms. This approach is based on the assumption that the exact ground state electron density can be represented by a ground state electron density of the auxiliary system of non-interacting particle (see Fig. 2.2). This assumption has not yet been proven generally, valid in a mathematical rigorous way. Therefore, we have to proceed assuming its validity.

In order to make formulas more lucid we neglect electron spin in the following. Extending the theory to explicit spin treatment is straight-forward, if explicit relativistic effects like spin-orbit coupling are neglected. The density of the non-interacting system is given by the sum of squares of (occupied) single-particle orbitals

$$n(\mathbf{r}) = \sum_i^N |\Psi_i(\mathbf{r})|^2 \quad . \quad (2.17)$$

The first Hohenberg-Kohn theorem also holds for these non-interacting systems. This means the density of the non-interacting system defines the effective potentials. The effective potential, in turn, defines the single-particle orbitals $\Psi_{i=1,\dots,N}(\mathbf{r})$. If one finds a ground state density of the

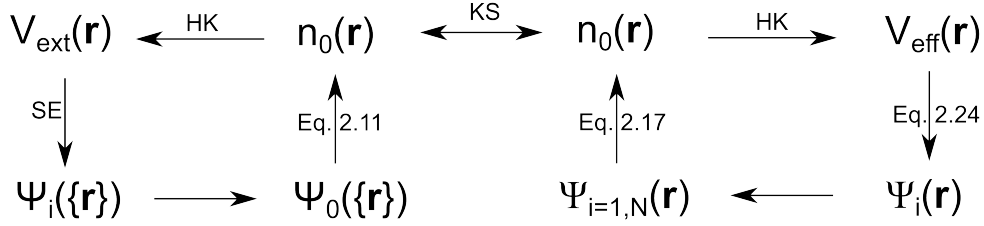


Figure 2.2: Illustration of the Kohn-Sham *ansatz*. The DFT descriptions of the many-body system (left) and the non-interacting *auxiliary* system (right) are connected through the assumption that the ground state densities of both systems are equal (arrow labeled KS), connecting any point to any other point. Therefore, all many-body properties are determined through solution of the Kohn-Sham auxiliary system of non-interacting electrons.

non-interacting system which is equal to the exact many-body ground-state density ⁵, solving the auxiliary system determines all properties of the many-body system.

The kinetic energy for independent particles T_s can be written as

$$T_s = -\frac{1}{2} \sum_i^N \langle \Psi_i | \nabla^2 | \Psi_i \rangle = \frac{1}{2} \sum_i^N \int d^3r |\nabla \Psi_i(\mathbf{r})|^2 \quad , \quad (2.18)$$

by partial integration.

The second problematic term in the many-body description, V_{int} in Eq. 2.15, is replaced by the classical interaction of the electron density $n(\mathbf{r})$ with itself

$$E_{Hartree} = \frac{1}{2} \int d^3r d^3r' \frac{n(\mathbf{r})n(\mathbf{r}')}{|\mathbf{r} - \mathbf{r}'|} \quad . \quad (2.19)$$

All many-body effects in the kinetic energy and the electron-electron potential are shifted into the exchange-correlation energy E_{xc} , completing the Kohn-Sham energy expression of DFT

$$E_{KS} = T_s[n] + E_{Hartree}[n] + \int d^3r V_{ext}(\mathbf{r})n(\mathbf{r}) + E_{xc}[n] \quad . \quad (2.20)$$

Comparing Eq. 2.20 and 2.16 shows that the exchange-correlation energy relates to the many-body description as

$$E_{xc}[n] = F_{LL}[n] - (T_s[n] + E_{Hartree}[n]) \quad . \quad (2.21)$$

An analytic expression for the exact exchange-correlation functional would allow exact calculation of all many-body ground state properties. So far, no analytic expression has been found. However, impressive work has been made in developing both meaningful and physically motivated approximations to the exchange-correlation energy functional. [42–44]

Before discussing approximations to the exact exchange-correlation functional, we should first describe how to solve the Kohn-Sham auxiliary system. Solution of Eq. 2.20 can be seen as a variational problem with respect to the density $n(\mathbf{r})$. The kinetic energy is a functional of the orbitals, while all other terms are functionals of the density. Due to relation 2.17 between orbitals and density, the variational problem can be written as a Rayleigh-Ritz variation of the orbitals $\langle \Psi_i | = \Psi_i^*$

$$\frac{\delta E_{KS}}{\delta \Psi_i^*} = \frac{\delta T_s}{\delta \Psi_i^*} + \left[\frac{\delta E_{Hartree}}{\delta n(\mathbf{r})} + \frac{\delta E_{ext}}{\delta n(\mathbf{r})} + \frac{\delta E_{xc}}{\delta n(\mathbf{r})} \right] \frac{\delta n(\mathbf{r})}{\delta \Psi_i^*} = 0 \quad (2.22)$$

⁵Although there is no rigorous proof for this assumption of representability, we have to proceed assuming it.

under constraint of orthonormality

$$\langle \Psi_i | \Psi_j \rangle = \delta_{ij} \quad . \quad (2.23)$$

Together with Eq. 2.17 and 2.18, we arrive at the Schroedinger-like Kohn-Sham equations,

$$\left(-\frac{1}{2}\Delta + V_{Hartree}(\mathbf{r}) + V_{ext}(\mathbf{r}) + V_{xc}(\mathbf{r}) \right) \Psi_i(\mathbf{r}) = \epsilon_i \Psi_i(\mathbf{r}) \quad , \quad (2.24)$$

a set of linear differential equations, with ϵ_i being the eigenvalue of state Ψ_i and the Hartree potential at every point in space integrated as

$$V_{Hartree}(\mathbf{r}) = \int d^3r' \frac{n(\mathbf{r}')}{|\mathbf{r} - \mathbf{r}'|} \quad . \quad (2.25)$$

The exchange-correlation potential V_{xc} at each point in space is defined as the functional derivative of the exchange-correlation energy functional

$$V_{xc}(\mathbf{r}) = \frac{\delta E_{xc}}{\delta n(\mathbf{r})} \quad . \quad (2.26)$$

These independent-particle equations are still coupled via the density – every (occupied) Kohn-Sham orbital Ψ_i contributes to the n – and through their constraint of orthogonality. Such a set of equations can be solved iteratively to find the self-consistent potential resulting in the self-consistent density. In practice, the density distribution, total energy or sum of eigenvalues are observed during the iterative process, and differences are compared with predefined convergence criteria. If their values $O^{(n)}$ from iteration n and iteration $n + 1$ deviate by less than the convergence criteria Δ_O ,

$$O^{(n+1)} - O^{(n)} < \Delta_O \quad , \quad (2.27)$$

the self-consistent field (SCF) cycle is considered to be converged⁶, i.e. the ground state electron density and total energy is found.

Approximations to the exact Functional

In the Kohn-Sham approach to many-body systems, exchange and correlation are extracted from the general many-body expressions for kinetic energy and internal potential and shifted into the exchange-correlation energy functional. Formally, nothing is won yet, as the explicit form of the exchange-correlation energy functional is unknown.

However, the knowledge of certain physical limits can be incorporated into the design of reasonable approximations. One observable for example, which is of key importance for the description of chemical binding, is the exchange (or Fermi) hole, which describes the possibility to find two electrons close together. In an adiabatic connection the exchange hole determines the exchange correlation energy density ϵ_{xc} [45].

One especially educative system is the homogeneous electron gas. In this approximation the positive charge of the nuclei is considered as a uniform background potential. The homogeneous electron gas is a reasonable "first-order" approximation to condensed matter, and in contrast to its simplicity was found to allow for a reasonably good description of simple metals. Therefore, the first family of approximations to the exchange-correlation energy functionals is based on

⁶Mathematically, this is not a proper criterion of convergence, as it does not exclude plateaus.

the idea that the electron density in a solid can be considered piecewise homogeneous. The corresponding exchange-correlation energy functional is then simply an integral over all space with the exchange and correlation energy density of the homogeneous electron gas

$$E_{xc}^{LDA}[n] = \int d^3r n(\mathbf{r}) \left[\epsilon_x^{homo}([n(\mathbf{r})], \mathbf{r}) + \epsilon_c^{homo}([n(\mathbf{r})], \mathbf{r}) \right] , \quad (2.28)$$

which is called the local density approximation (LDA).

In the non-interacting case, the exchange energy density for the homogeneous electron gas is known analytically ($\epsilon_x = -\frac{3}{4\pi}k_F$), even for the spin-polarized case [30, 46]. Unfortunately, there is no analytic form for the correlation energy density. Still, one has numerical access to this term by applying higher many-body methods, like the random phase approximation [47], self-consistent GW approximation [48] or most accurate ground state quantum Monte Carlo calculations [49–52], and fit an analytic form to these values. With that, one has a closed expression for the exchange-correlation energy density $\epsilon_{xc}^{homo}([n(\mathbf{r})], \mathbf{r})$ as a functional of the electron density. In this form, computational expenses for the exchange-correlation shows an $\mathcal{O}(N)$ scaling, with N being the number of electrons. It can therefore cheaply be applied to extended systems. Of course, assuming the electron density to be homogeneous in real systems is rather a precarious assumption, especially for atoms and molecules. But also localized d- and f- states, for example in transition metals, are only poorly described through LDA. On the other hand, LDA predicts the crystal structures surprisingly well, typically only deviating a few percent from the experimental values [14].

One way to improve the accuracy for more inhomogeneous systems is to incorporate information about the gradient of the density. This leads to the family of generalized-gradient approximation functionals (GGA), with a more flexible form

$$\begin{aligned} E_{xc}^{GGA}[n] &= \int d^3r n(\mathbf{r}) \epsilon_{xc}^{homo}(n, \nabla n, \dots) \\ &= \int d^3r n(\mathbf{r}) \epsilon_x^{homo} F_{xc}(n, \nabla n, \dots) \quad . \end{aligned} \quad (2.29)$$

F_{xc} is called the exchange enhancement factor. Numerous forms for F_{xc} have been proposed, with PBE [42], BLYP [53, 54] and rPBE [55] being prominent examples. All of them introduce one or more free parameters to include the gradient in the functional expression. Their values are either physically motivated, i.e. through enforced satisfaction of constraints and limiting behaviors, or simply fitted to obtain results which agree best with higher *ab-initio* methods (see [14] and citations within). GGAs do not necessarily lead to a consistent improvement over LDA, but perform in general much better for atoms or molecules. Incorporating higher-order derivatives of the density is one pursued attempt to improve accuracy [56]. This is however not a monotonic expansion, in the sense that high-order terms necessarily are less important. It rather only increases computational costs and introduces further empirical parameters. A different strategy of adding orbital-dependency [57] based on the Hubbard model can improve accuracy or rather may help to get the correct result, but introduces even more free parameters.

The main fault of LDAs and GGAs is the fact that they systematically contain a self-interaction in the Hartree term which leads to over-delocalization of electron density. Efforts were made to directly cure for that, by adding an approximative self-interaction correction term to the functional [58]. However, in the Hartree-Fock approximation the self-interaction is canceled *exactly* by the non-local exchange interaction, as described in Chapter 2.1. Making use of this fact, leads to the family of *hybrid* functionals, combining orbital dependent Hartree-Fock and explicit density functional theory. In hybrid functionals, the exact exchange E_x^{exact} is

computed in the basis of Kohn-Sham orbitals and mixed into the exchange-correlation energy functional

$$E_{xc}^{hybrids} = E_{xc}^{DFT} + a(E_x^{exact} - E_{xc}^{DFT}) \quad . \quad (2.30)$$

The E_x^{exact} is evaluated as the Fock-matrix in the basis of Kohn-Sham orbitals Ψ

$$E_x^{exact} = -\frac{1}{2} \sum_{ij} \int \int d^3r d^3r' \frac{\Psi_i^*(\mathbf{r}) \Psi_j^*(\mathbf{r}') \Psi_i(\mathbf{r}') \Psi_j(\mathbf{r})}{|\mathbf{r} - \mathbf{r}'|} \quad . \quad (2.31)$$

Given the variety of different choices of functionals determining E_{xc}^{DFT} and the fact that a is a free parameter, again leads to a zoo of hybrid functionals, with PBE0 [43] and B3LYP [59] being most widely used. In many cases, hybrid functionals present a huge improvement, e.g. for binding energies in molecules, and also for the prediction of band gaps of semiconductors. But there are also cases where hybrid functionals intrinsically fail: as Hartree-Fock always introduces an energy gap between highest occupied and lowest unoccupied Kohn-Sham state (band-gap), these functionals cannot describe metals.

Explicit evaluation of exact exchange is not a problem for molecules, yet still remains a challenge for solid-state systems, as evaluation of the Fock-matrix formally scales $\mathcal{O}(N^4)$ with the number of basis functions N ⁷. Developing new functionals is an active field of study. For example, incorporating range separation of the exact-exchange [44, 60] is not only physically motivated but also helps to reduce computational costs for hybrid functionals as the Fock-matrix may efficiently be truncated as the long-range part of the Fock-matrix is replaced by a functional expression of the density. Standard functionals are not able to capture van-der-Waals dispersion interaction, which can contribute significantly in adsorption processes on metal surfaces. Therefore several functionals have been developed which incorporate Van-der-Waals correction terms [61–63].

Some even more advanced approaches also try to be more precise on the correlation energy part of the functional E_c by treating it perturbative. These functionals are called double-hybrid functionals and show a very promising — yet computational very expensive — way towards chemical accuracy for molecules [64–66]. However, one should be aware of the fact that typically these approaches do not fulfill the conditions for the validity of the Hohenberg-Kohn theorem and are thus not based on rigid mathematical footing.

2.3 Basis sets and boundary conditions

In a numerical realization of DFT, the set of linear differential equations in 2.24 are to be solved self-consistently. Usually this is done in an iterative procedure, called the SCF-cycle. Solving the set of differential equations has two prerequisites: boundary conditions and a certain representation of the Kohn-Sham states (and potentials). In general, Kohn-Sham states can be represented on a real-space grid. This requires solving the differential equations on every grid point. A much more elegant and efficient detour is to expand the Kohn-Sham states Ψ_i in a certain basis set

$$\Psi_i(\mathbf{r}) = \sum_l c_{il} \varphi_l(\mathbf{r}) \quad , \quad (2.32)$$

with φ_l being the basis functions.

⁷In practice, the Kohn-Sham eigenstates are expanded in a certain basis (see Section 2.3), which governs the actual computational costs to evaluate the Fock matrix.

This transfers Eq. 2.24 into a generalized eigenvalue problem of the form

$$\sum_j h_{ij} c_{jl} = \epsilon_l \sum_j s_{ij} c_{jl} \quad , \quad (2.33)$$

where h_{ij} evaluates the independent-particle Hamiltonian

$$h_{ij} = \langle \varphi_i | \hat{h}_s | \varphi_j \rangle \quad , \quad (2.34)$$

with $\langle \mathbf{r} | \hat{h}_s | \mathbf{r} \rangle = -\frac{1}{2}\Delta + V_{Hartree}(\mathbf{r}) + V_{ext}(\mathbf{r}) + V_{xc}(\mathbf{r})$ defined in real-space and s_{ij} being the overlap between basis function i and j

$$s_{ij} = \langle \varphi_i | \varphi_j \rangle \quad . \quad (2.35)$$

For obvious reasons, the basis set is always finite. Therefore, the basis set size is the major parameter of convergence in a DFT calculation. Thorough convergence tests always have to be conducted to obtain a reasonable trade-off between accuracy and computational expenses.

An efficient choice for the boundary conditions as well as the basis set essentially depends on the structure, which is to be addressed. At this point, the communities of physicists and chemists typically go diametrically opposed ways, summarized in Table 2.3.

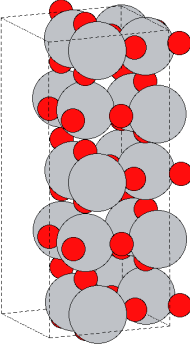
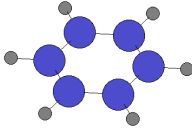
	Physics	Chemistry
Typical Setup		
Boundary Conditions	periodic	open
Electronic Structure	delocalized bands	localized orbitals
Basis set	$\varphi_{\mathbf{k}}(\mathbf{r}) \propto e^{i\mathbf{k}\mathbf{r}}$	$\varphi_{lm}(\mathbf{r}) = \frac{u(r)}{r} Y_{lm}(\Omega_{\mathbf{r}})$
k-point sampling	yes	no

Table 2.1: Comparison between the "Physicist's" and "Chemist's" numerical realization of DFT.

Originating from solid-state physics, DFT was first applied to solid state crystals. For something as periodic as a crystal, calculation of a Wigner-Seitz like *unit cell* together with Born-von Karmen periodic boundary conditions (PBC) are the natural choice [67, 68]. Basis functions which intrinsically match PBC and are able to describe the band-structure (*delocalized* in real-space) are plane waves

$$\varphi_{\mathbf{k}}(\mathbf{r}) = e^{i\mathbf{k}\mathbf{r}} \quad , \quad (2.36)$$

due to Bloch's theorem [68]. By doing this, translational symmetry is automatically exploited. Solving the infinite crystal, however, necessitates accurate sampling of the reciprocal (or \mathbf{k} -)

space. This can be done in an efficient way by discretization of the reciprocal space on a grid. Making use of time reversal and inversion symmetry reduces the number of grid points in k -space, e.g. following the strategy proposed by Monkhorst and Pack [69]. Still this, in turn, corresponds to solving many sets of Eq. 2.23, namely for every k -point which is to be sampled.

Plane waves also have some interesting advantages. First, plane waves constitute an orthogonal basis. This means Eq. 2.35 gives the identity matrix. Second, calculation of the kinetic energy of a plane wave is trivial ($E_k = \frac{\hbar^2 k^2}{2m}$). Third, there exist highly optimized *Fast Fourier Transform* algorithms to transform between reciprocal and real-space. Furthermore, plane waves are an extremely systematic basis set. This is convenient when checking convergence of any observable with respect to the basis set size, as \mathbf{k} is the only parameter defining a plane wave. However, plane waves cannot be used to describe the electronic structure in presence of the bare Coulomb potential of the nucleus, in an accurate and practicable way. The reason for that is the cusp in electron density at the position of a nucleus. The Fourier transform of a cusp, in principle, can not be truncated in k -space. This means, one would need an infinite number of plane waves to describe the proper electron distribution. For that reason, plane waves always have to be used together with the *pseudopotentials* approximation, applying effective potentials of the nucleus plus core-electrons, which ultimately remove the Coulomb singularity (see Section 2.4). By construction, this removes the core electrons from the DFT calculation which reduces the electronic degrees of freedom, however, makes observables connected to core electronic states inaccessible. For most applications, nonetheless, only the part of the electronic spectrum close to the Fermi level, e.g. high valence bands and low conducting band, is of interest.

The chemists' approach to DFT arises from a molecular orbital picture. A molecule in vacuum is not periodic. As molecular orbitals decay exponentially for large distances, the electronic states and all potentials can be defined on a finite real-space grid with *open* boundary conditions. Exploiting localization of electron density and Kohn-Sham orbitals through a localized basis set

$$\varphi(\mathbf{r}) = u(r)Y_{lm}(\Omega_{\mathbf{r}}) \quad (2.37)$$

allows for a most efficient representation, where Y_{lm} are spherical harmonics with angular respectively magnetic quantum numbers l and m . The radial part $u(r)$ can be any localized function like a linear combination of Gaussians or Slater-type function ($\propto e^{-\zeta r}$) or even a numerically tabulated orbital (NAO), all having their specific advantages. For example products and Fourier transforms of Gaussian functions can be calculated analytically, which is of great advantage when computing two-center integrals like Eq. 2.30. Slater-type orbitals on the other hand intrinsically incorporate the correct asymptotic behaviour. Ultimately, NAOs are most flexible in the radial part $u(r)$ allowing to dramatically reduce the number of basis functions involved in the DFT calculation compared to a plane wave calculation. Moreover, localized basis functions allow an explicit treatment of the core-electrons, which are not accessible with plane waves, for reasons discussed above. A localized basis set, on the other hand, is not universal in a sense that it is specific to a species and designed with *chemical intuition*. Also, in contrast to plane waves there is not only one parameter defining the basis function. This can lead to more erratic convergence behaviour. Therefore, a number of basis sets have been standardized [70–73] in order to establish a common sense for quality and level of convergence in the quantum chemistry community.

The sufficient number of plane waves in a calculation does not directly depend on the number of atoms in the periodic box. In a localized basis set approach every single atom carries its own basis functions, which leads to a systematic problem when calculating binding energies. If the species A is not sufficiently described with its own basis functions, it can be further stabilized through basis functions of the bonding partner B , and vice versa. In such a case, energies of A and B in vacuum are the wrong references for the binding energy, as these calculations miss

the basis functions of the respective other bonding partner, and therefore are not further stabilized. This is called the basis set superposition error (BSSE). Of course, the BSSE depends on the incompleteness and inability to describe the free atom. Especially NAOs allow for excellent description of the electron density of the free atom, due to their numerical flexibility in design. However, unoccupied states are typically described poorly since they are of delocalized nature. This leads to significant BSSE for methods involving unoccupied states like explicitly correlated methods, even for NAOs. The BSSE can be corrected for in terms of a counterpoise correction [74–76]. This involves calculation of both partners in the compound basis

$$\Delta E = E_A(A) - E_{AB}(A) + E_B(B) - E_{AB}(B) \quad . \quad (2.38)$$

ΔE is then added to the uncorrected binding energy with BSSE. The subscript denotes the basis set, $E_{AB}(A)$ is the total energy of species A calculated in the compound basis of A and B .

Meanwhile, there are *hybrid* versions of basis sets which attempt to combine advantages from localized and plane wave basis sets, like the *projector augmented wave* method [77] or strategies which augment a localized basis sets with a plane wave phase factor [78].

2.4 Pseudopotentials

The Coulomb potential of the bare nucleus and its respective singularity leads to issues when applying plane waves as described above. Is it, however, really necessary to explicitly describe *all* electrons in the system, even the energetically lowest-lying electrons, the so called *core electrons*? Closed core electron shells are very stable and their participation in chemical reactions are, in fact, negligible. Hence, for most applications only the valence electrons have to be described explicitly and accurately. The influence of the core electrons are incorporated through an effective potential for the nucleus and the core-electrons combined — the so called effective core potential or pseudopotential. Such pseudopotentials can in general be written as a sum of semi-local projector functions

$$\hat{V}_{SL}^{PP} = \sum_{lm} |Y_{lm}\rangle V_l(r) \langle Y_{lm}| \quad , \quad (2.39)$$

with Y_{lm} being spherical harmonics and $V_l(r)$ the radial potential or angular momentum state l . The prerequisite for the pseudopotential is, of course, that the valence electrons in the presence of the pseudopotential behave just like in an all-electron description.

A separation of core and valence electrons is justified when explicit correlation between core and valence electrons is negligible. Then, core and valence states reside in separable Hilbert spaces and the overall basis may be separated into a product basis. This reduces coupling terms between core and valence electrons to the classical Hartree potential.

The strength of exchange and correlation effects between two states is determined by their overlap in real and momentum space. If two states are spatially separated, hence their wavefunctions do not overlap, exchange and correlation between these states is indeed negligible.⁸ The same holds, if their wavefunctions do not overlap in momentum space but only in real space. The latter is a good approximation for the strongly bound core and weakly bound valence state in an atom. This allows to separate out the core states and density in order to reformulate the DFT problem in a description of the valence density in an effective core potential.

Most pseudopotentials in use nowadays are generated from all-electron calculations of atoms and are called “*ab-initio*“ pseudopotentials as they are derived from fundamental physics and

⁸It should be strictly zero if one neglects quantum entanglement effects.

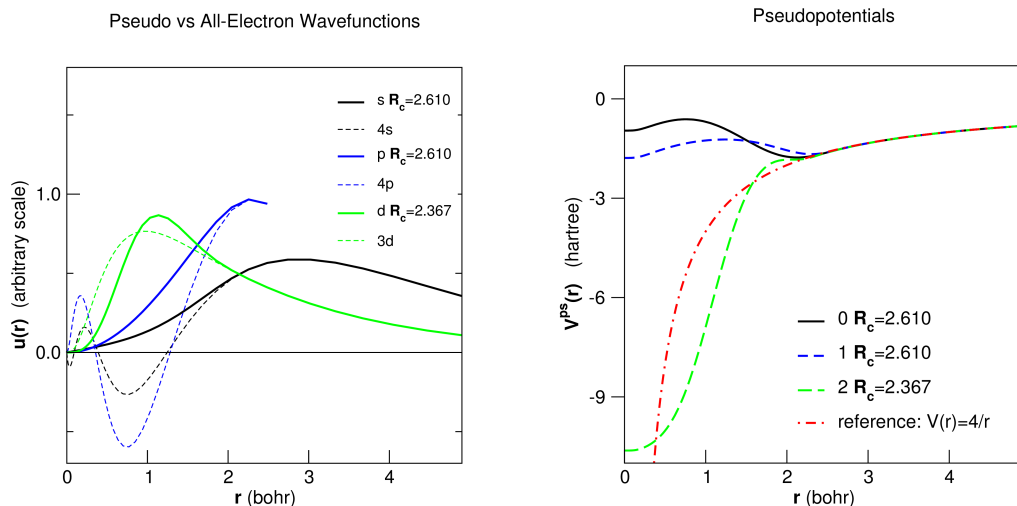


Figure 2.3: Illustrating an ionic pseudopotential and pseudo valence wavefunctions for Titanium with 18 core electrons generated with FHI98PP [80] using the procedure of Troullier and Martins. The left picture compares the pseudo valence wavefunctions (solid lines) with the all-electron wavefunctions (dashed lines). The pseudo valence wavefunctions do not have nodes in the core region, while coinciding with the all-electron wave function beyond the core radius R_c . The right picture shows the corresponding pseudopotentials V_l^{PP} for the s-, p-, and d-channel. Beyond R_c all V_l^{PP} are equal to the ionic reference potential, corresponding to the effective Coulomb potential of the nucleus ($Z = 22$) and core electrons ($Q_l = -18$).

not obtained empirically. This, in principle, allows to generate pseudopotentials consistent with the exchange-correlation functional the valence states are described with.

The aim is to generate a pseudopotential which yields the same valence states and eigenvalues as one would obtain from an all-electron description. Furthermore, this pseudopotential should not only work for the isolated atom but should be also *transferable* over a wide range of chemical environments. The list of mathematical requirements for an accurate and transferable ab-initio pseudopotentials is given by Hamann, Schlüter and Chiang [79]:

1. All-electron and pseudo valence eigenvalues agree for a given atomic reference configuration.
2. All-electron and pseudo valence wavefunctions agree outside a chosen core radius R_c .
3. Integrated charges within R_c agree for all-electron and pseudo valence states.
4. The logarithmic derivatives of the all-electron and pseudo valence states agree at R_c .
5. The first energy derivative of the logarithmic derivatives agree at R_c .

According to the first Hohenberg-Kohn theorem, a potential is uniquely determined by the ground state wavefunction up to a constant. The constant is determined through the actual eigenvalue. Consequently, criteria 1 and 2 mean that the pseudopotential and atomic potential have to agree outside the core radius R_c . Otherwise, the all-electron and pseudo valence states can not agree outside the core radius R_c . Inside R_c the pseudopotential and radial pseudo-orbital Ψ_l differ from their all-electron counterparts (see Fig. 2.3).

The total charge within the core region is simply the integral over the norm up to R_c

$$Q_l = \int_0^{R_c} dr r^2 |\Psi_l(r)|^2 \quad . \quad (2.40)$$

If the total charge in the core region is the same in the all-electron case, a possible potential offset between the atomic and pseudopotential necessarily vanishes, since the potential outside a spherical symmetric charge distribution only depends on the total charge.

We know from basic scattering theory that all scattering properties of a localized spherical potential can be expressed in terms of the energy dependent phase shift induced by the scattering potential. Since the logarithmic derivative are related to the phase shift [81], criterion 4 ensures the pseudopotential to induce a phase shift equal that of the all-electron potential outside R_c (modulus 2π).

Criterion 5 ensures transferability throughout different chemical environment. The first energy derivative of the logarithmic derivative relates to the core density

$$-\frac{1}{2}r^2|\Psi_l(\epsilon, r)|^2 \frac{d}{d\epsilon} \left[\frac{d}{dr} \ln \Psi_l(\epsilon, r) \right] \Big|_{r=R_c; \epsilon=\epsilon'} = \int d\Omega \int_0^{R_c} dr r^2 |\Psi_l(\epsilon', r)|^2 \quad , \quad (2.41)$$

where $\Psi_l(\epsilon, r)$ are the all-electron or pseudo valence wavefunctions at some energy ϵ . The norm-conservation then ensures, that the pseudopotential not only gives the proper scattering behaviour (logarithmic derivative) at some energy, but also in a certain energy window around the reference energy value ϵ' .

With these criteria in hand, constructing a pseudopotential from *ab-initio* is straightforward. The pseudopotential $V_l^{PP}(r)$ and the radial part of the pseudo valence wavefunction $u_l(r)$ ($u_l(r) = r\Psi_l(r)$) are generated for every angular momentum separately from an all-electron single-atom DFT calculation by inverting the Schroedinger equations, yielding

$$V_l^{PP}(r) = \epsilon - \frac{1}{2} \left[\frac{l(l+1)}{2r^2} - \frac{\frac{d^2}{dr^2} u_l(r)}{u_l(r)} \right] \quad . \quad (2.42)$$

The analytic form of $u_l(r)$ is typically $u_l(r) = e^{f(r)}$, $r < R_c$, with $f(r)$ being some kind of polynomial [82–84]. This allows to get a smooth form of the pseudo valence state within the core region⁹. Smoothness is extremely important when pseudopotentials are used together with a plane wave basis set, as wiggly fine-structured potentials would necessitate a larger number of plane waves to accurately resolve the potential. In Kohn-Sham DFT, the computational cost is dominated by diagonalizing the Hamiltonian. Since the size of the Hamiltonian matrix is $N_b \times N_b$, with N_b being the number of basis functions, overall computational cost is governed by the number of basis functions involved and not the number of electrons.

Since eigenvalues and orbitals, are required to be the same for the all-electron and pseudo case outside the core region, each potential $V_l^{PP}(r)$ equals the local (l -independent) Coulomb potential of the nucleus and core electrons $V(r) = -\frac{Z_{ion}}{r}$. Thus, all non-locality is confined in the core regions. It is often useful, to exploit that fact by separating the pseudopotential into a local and a nonlocal part

$$V^{PP}(r) = V_{loc}(r) + \delta V_l(r) \quad , \quad (2.43)$$

with $\delta V_l(r) = V_l^{PP}(r) - V_{loc}(r)$ containing all l -dependency. This allows real-space truncation of the nonlocal operator. More to this topic and how V^{PP} is evaluated will be discussed explicitly in Chapter 4.

⁹By loosening the constraint of norm-conservation even smoother, so called "*ultra soft*" pseudopotentials, can be generated [85].

3 Solid-state Embedding

The standard approach to address extended systems is to assume some kind of periodicity. While focusing the computational effort on the finite supercell, this approach elegantly captures e.g. long-range electrostatic effects and in particular the delocalized electronic bonding in metallic systems. Periodic boundary conditions (PBC) are no approximation in the limit of large supercells and can yield reasonable results if the supercell is sufficiently large, even for amorphous material or liquids [86]. For perfectly periodic systems this is of course no assumption and calculating the primitive unit-cell under PBC is no additional approximation. However, a very interesting family of systems are localized perturbations to the perfect crystal, e.g. interstitials or dopants in crystals, adsorbates on surfaces, or even charged defects. Computing such systems in PBC corresponds to a periodic array of defects. If one is interested in the single defect or adsorbate, one has to worry about unwanted interaction between the non-periodicity and its periodic replica, called *finite size effects*. This can be due to overlap of localized electronic states, elastic interactions like reorganization or pure electrostatic interaction. The general computational approach is to increase the size of the supercell until finite size effects can be corrected through extrapolation to the limit of large supercells. However, electrostatic interaction can be long-range and can even lead to a diverging Coulomb term in case of supercells carrying a net charge. Several correction schemes based on a multipole decomposition of the charge density in the supercell have been proposed to correct for the leading order terms [87–92]. These correction schemes work indeed well for cubical bulk unit cells. However, there is one subtle problem in the case of surfaces: The monopole term is compensated by a uniform charge background within the supercell in these schemes. The vacuum region in a surface supercell, which separates the periodic slabs, will therefore exhibit an attractive potential, leading to spurious bound states in the vacuum region, which again need to be corrected for *a posteriori* [93]. Other approaches suggest neutralization of the monopole term by scaling the nuclear charge accordingly [94], or adding a compensating point charge "somewhere" in the supercell [95]. Still, all correction schemes require structural reorganization to be negligible at the boundary of the supercell in order to be valid, which often necessitate prohibitively large supercells.

There exist several alternative approaches to extended systems, which allow to specifically avoid PBC. In such approaches the high-level description, e.g. quantum mechanical, is restricted to a small subsystem of special interest. Effects of the system remainder are then incorporated on a less sophisticated, but computationally less expensive level. Such *embedding* approaches can be divided into three categories with different fields of applications: solvation models, density embedding approaches and QM/MM models. Solvation models are a standard method in computational chemistry and are used to estimate solvation free energies of molecules. This involves electrostatic coupling of the quantum mechanical equations for the molecule to a dielectric continuum model for the solvent [96–98]. For more information on state-of-the-art solvation models the reader is referred to the review of Thomasi *et al.* [98], or the textbook by Cramer [99]. Density embedding methods are a much more elaborate approach typically aiming for very high accuracy, coupling high-level wave-function based quantum mechanical methods with density functional theory [100–102]. In this approach, the electron density of the entire sys-

tem is calculated and divided into a central subsystem A and system remainder B , by explicit orthogonalization of the Kohn-Sham orbitals in region A to those in region B . This allows to perform high-level quantum mechanical levels on a small subsystem. This method still requires solving the Kohn-Sham equations in PBC, as the electron density of the entire system needs to be computed limiting its applicability to solid-state systems.

The third family of embedding models, the QM/MM approach, allows solid-state applications while avoiding PBC and is therefore the focus of this thesis. In this approach the quantum mechanical calculation is reduced to a finite region, and the system remainder is treated on a molecular mechanical (MM) level of theory, which allows for a self-consistent polarization beyond continuum models.

For the electronic structure the vital condition is correct scattering at the QM/MM boundary. This makes the boundary “invisible” to the electrons, letting them behave like in the infinite crystal. Replacing point charges by pseudopotentials across the QM/MM boundary is a very good strategy to achieve that (at least for ionic materials), since pseudopotentials are specifically designed to restore such scattering behaviour. Second, the correct energetic alignment of electronic states with respect to vacuum energy is important to be able to compare to experiment or to address electrochemical problems. Here, the long-range electrostatics play an important role in terms of the Madelung potential of the infinite crystal. Because of the long-range nature of the Coulomb interaction it is in general not possible to reproduce the Madelung potential by a finite array of point charges. Therefore, the long-range electrostatics have to be evaluated in terms of an Ewald sum [103].

Throughout this work, computational coupling of QM and MM computer codes is outsourced to the computational chemistry package *ChemShell*. While discussing the general concept of solid-state QM/MM embedding in this chapter, the author therefore introduces *ChemShell* as an example for solid-state embedding infrastructure.

3.1 The QM/MM approach

The label QM/MM denotes hybrid simulation approaches, that combine two atomistic treatments: one explicitly quantum mechanical and one “molecular mechanical” based on a classical interatomic potential. The much more expensive quantum mechanical treatment is restricted to a certain region of interest whereas the influence of the surrounding is based on a classical description, where particles are represented by point charges interacting through interatomic potentials, so called *force fields*. With accurate coupling between QM and MM region, a relatively small embedded QM region is able to reproduce the electronic structure and thereby QM observables of the entire system.

Depending on the intended application, the QM/MM approach can be classified in two distinct branches. In the field of physical chemistry and biochemistry one is generally interested in the details of chemical reactions of solutes or of ligands at the active sites of proteins [104–107]. The focus here is more on the dynamical aspect necessary to map out configurational entropic contributions to the reaction, or on a high-level wavefunction based resolution of the electronic structure [108]. Karplus, Levitt and Warshel shared the 2013 Nobel Prize in Chemistry for their leading work in this field. Typically, the molecules or reactants of interest together with a few solvent molecules are treated quantum mechanically, embedded in a sea of force field based solvent molecules, usually based on point charges augmented with a short range potential [109]. Biochemical simulations are not the scope of this thesis. For further reading along these lines we refer to the the review of Zhang *et. al.* [110].

In the field of solid state physics and surface chemistry, the understanding of QM/MM

is slightly different. Here, the setup typically is a crystal structure divided into a quantum mechanical cluster *embedded* in the crystal remainder, which poses a different challenge to the description of the MM region and the coupling between QM and MM regions. The rationale is simply to avoid periodic boundary conditions in order to reduce computational costs and to allow to address overall charged systems in an efficient and flexible way.

Typical applications are the study of adsorption processes at surfaces, or formation energies of defect states. This necessitates the calculation of differences in total energies. The total energy (E^{tot}) of the QM/MM system is given by a simple additive definition:

$$E^{\text{tot}} = E^{\text{QM}} + E^{\text{MM}} \quad . \quad (3.1)$$

E^{QM} is the total energy of the QM-region, in this work assessed through DFT. E^{QM} is, in principle, given through Eq. 2.20, augmented with an additional potential V^{MM} accounting for the interaction of QM electrons with embedding MM particles,

$$E^{\text{QM}} = \langle \Psi | \hat{H}^{\text{QM}} + \hat{V}^{\text{MM}} | \Psi \rangle + E_{\text{nuc}}^{\text{QM}} + E_{\text{nuc}}^{\text{QM/MM}} \quad . \quad (3.2)$$

It additionally contains Coulomb interaction between nuclei within the QM region $E_{\text{nuc}}^{\text{QM}}$ as well as Coulomb interaction between such nuclei and the embedding MM particles $E_{\text{nuc}}^{\text{QM/MM}}$. For solid state applications \hat{V}^{MM} is typically not only the Coulomb potential of embedding point charges, but also contains non-electrostatic terms, discussed in Section 3.2.

In an MM description a nucleus and its electrons are treated as an effective atom. Their total energy is decomposed in an expansion of one-body, two-body, three-body interaction terms (and higher)

$$E^{\text{MM}} = \sum_i U_i + \frac{1}{2} \sum_i \sum_j U_{ij} + \frac{1}{6} \sum_i \sum_j \sum_k U_{ijk} \dots \quad , \quad (3.3)$$

which is an exact expansion if high enough orders are included. If we assume that contributions from higher orders get progressively smaller, the expansion can be truncated. In a state-of-the-art MM description for solids all terms higher than two-body interactions are neglected.

U_i is the self-energy of particle i and only introduces a constant shift in energy. Therefore, this term is of no interest in a QM/MM approach, as it does not induce a force. Although the actual value of the total energy loses its meaning, differences of total energies remain unaffected if U_i is neglected. The two-body interaction potential U_{ij} is dominated by the Coulomb interaction in ionic materials, which typically makes up about 90% of the two-body term. Non-electrostatic terms like Pauli repulsion or many-body dispersion interaction are further important features in a realistic description even in ionic materials. Such effects can be accounted for through a short-range potential, for example a Buckingham potential

$$U_{ij}^{\text{buck}} = Ae^{-r_{ij}/\rho} - C/r_{ij}^6 \quad . \quad (3.4)$$

The attractive r_{ij}^{-6} term mimics dispersion interaction, while the exponential term is a reasonable choice to account for Pauli repulsion. A , ρ and C are species dependent parameters.

Polarizability can be an important property, e.g. in oxide materials. In such a case, usually the point charge representing an oxygen ion is replaced by two point charges – the core and shell – adding up to the same amount of charge. Both point charges interact via a spring potential

$$U_{ij}^{\text{spring}} = \frac{1}{2} kr_{ij}^2 \quad . \quad (3.5)$$

Anharmonicities can be included by either adding a term quartic in r_{ij} or replacing the spring by a cosh-potential

$$U_{ij}^{cosh} = kd^2 \cosh\left(\frac{r}{d} - 1\right) \quad , \quad (3.6)$$

adding k and d to the set of parameters.

The total energy of the system (Eq. 3.1) then gives rise to forces on atoms, described by the Hellmann-Feynman theorem [111]

$$\mathbf{F}_i = -\nabla_i E^{\text{tot}} \quad (3.7)$$

for every particle i in the QM and MM region. Here, ∇_i denotes the gradient with respect to the coordinates of particle i . This allows for geometry optimization of the QM region, but also to calculate the *self-consistent* polarization response from the MM region.

3.2 *Seamless* coupling for solid-state embedding

QM/MM is a multi-scale approach, connecting methods for different length scales. Such approaches always require special attention to the coupling between both domains. Discontinuities in the description of (dynamic) material properties are to be avoided when crossing the domain boundaries, in order to guarantee perfect *seamless* coupling between both methods. Perfect matching of all properties is, of course, not possible given the huge difference in sophistication between the QM and MM description. Therefore, seamless coupling has to be approximated by focusing only on matching a *few* important properties, which are accessible in both methods. The typical approach is to further reduce complexity by focusing on matching bulk properties.

The most basic and easy to adjust properties are the lattice parameters. For more complex crystallographic structures, this should include matching the internal degrees of freedom within the unit cell. Mismatches in structural parameters lead to a long-range stress field in the QM region, escalating in unpredictable perturbations. Another important property to be matched for seamless coupling is the dielectric response tensor ϵ , as it immediately affects the self-consistent polarization response with the active MM region. Incorrect polarization of the MM region has, in turn, spurious effects on the electronic structure and geometry in the QM regions. An automated global optimization strategy for interatomic potential parameters will be discussed in Section 5.

A further issue is given at the transition between QM and MM region in terms of how the electronic degrees of freedom couple to the MM region. This immediately defines the boundary conditions for solving the differential equations in the QM region (Eq. 2.24). Open boundary conditions and direct linkage to point charges in the MM regions, have two dramatic effects: First, point charges act as Coulomb singularities, which lead to spurious charge leakage out of the QM-region. Second, open boundary conditions, similar to a cluster in vacuum, lead to dangling bonds at the QM region boundary, which will perturb the electronic structure in an unpredictable way.

Saturation of dangling bonds on the exterior of the QM region with “link”-atoms, e.g. through hydrogen termination, is a commonly used methodology [18, 112]. Such a setup is sufficient for strongly covalent materials with directional bonds. This approach, however, breaks down in the case of heteropolar semiconductors and ionic insulators like TiO_2 or MgO .¹

¹There are no clear and directed bonds in such materials. To our experience, hydrogen termination of TiO_2 clusters leads to spurious states within the band gap and even to metallic behavior.

Electrons in the QM-region should neither spill out of the QM-region, nor should they be artificially enclosed. Optimal boundary conditions would provide the correct phase-shift to mimic extended Bloch-like states. In this case, electrons would behave exactly like in the infinite crystal. Optimal boundary conditions are not accessible in a practicable way, and need to be approximated. One very important boundary condition for the differential equation describing electrons in the QM region is orthogonality of electronic states across the QM-region boundary, i.e. valence states in the QM-region not only have to be orthogonal to core states within the QM-region but also to *virtual* core states on the other side of the QM-region boundary. Replacing point charges by norm-conserving pseudopotentials (see Section 2.4) will automatically fulfill this condition. The nonlocal part, i.e. the projector functions, of such pseudopotentials ensures this orthogonality, thus providing the correct boundary condition. Hence, the embedding potential \hat{V}^{MM} can be written as

$$\hat{V}^{\text{MM}} = \hat{V}_{PC}^{\text{MM}} + \hat{V}^{\text{PP}} \quad , \quad (3.8)$$

where the first term refers to the Coulomb potential of embedding point charges and the second summarizes all pseudopotentials. Aforementioned orthogonality constraints effectively localize electrons within the QM region, correct for termination effects on the band gap, and compensate for missing short-range forces in the QM-MM interface.

For the lack of anionic pseudopotentials (e.g. O^{2-}) only positively charged point charges can be replaced by pseudopotentials. The non-electrostatic term for anions is, therefore, neglected. Keeping the negatively charged point charges is still a very good approximation. Being repelled by negatively charged point charges, electrons are unlikely to overlap with the core region of a possible anionic pseudopotential. Electrons are therefore only subject to the local ionic potential which is equal to the potential of a point charge, $-2/r$ in the example of O^{2-} (compare with Figure 2.3).²

3.3 Reproducing the long-range Electrostatic Potential

Correct level alignment on an absolute scale is only possible when the full long-range electrostatic potentials are properly accounted for. This is not only important for the calculation of the work function, but also when modeling atomic and electronic processes involving a change in the charge (oxidation) state or comparing systems in different charge states. For example, calculated formation energies of charged defects in semiconductors and insulators directly depend on the overall electrostatic potential, as this defines the electronic chemical potential. Another example is given by complementary oxidation-reduction cycles in acid-base and redox chemistry that involve ions or electrons to be removed or added to the system from remote locations.

For a periodic structure the zero-reference potential is the long-range electrostatic potential of the infinite crystal, i.e. the Madelung potential. In the solid-state embedding approach, correct level alignment is a peculiar issue, as it is generally impossible to reproduce the Madelung potential of the infinite crystal background through a finite field of point charges [113].

One remedy is to calculate the exact Madelung potential from a periodic structure and incorporate that information into the embedded cluster setup by adding point charges to exactly reproduce the Madelung potential within the physically relevant region of interest [114–116], which will be explained in the following.

²We tested this assumption in a TiO_2 benchmark setup (see Chapter 7). Replacing the anionic point charges by smeared out potentials of the shape $\text{erf}(r/\sigma)/r$ did not have a significant effect on the band gap or adsorption energies of small molecules, as long as σ is not pathologically large.

In general, the Madelung potential is not accessible through a straightforward summation of the Coulomb potential, as infinite sums of $1/r$ -terms are only conditionally convergent. Rather, it has to be computed using an Ewald-like summation technique [103] or as a Parry sum for the 2D surface periodicity [117, 118]. In the following the general concept of the Ewald summation and the trick to incorporate this reference potential in the solid-state embedding approach will be discussed. For a more rigorous and detailed description of the mathematical aspects of the Ewald summation the author refers to the review by Lipkowitz and Cundari [119].

The electrostatic potential of N ions in a cubic unit cell in periodic boundary conditions is defined through the electrostatic energy

$$E = \frac{1}{2} \sum_i^N q_i \Phi_{[i]} \quad . \quad (3.9)$$

$\Phi_{[i]}$ denotes the electrostatic potential generated by the N ions in the cubic unit cell together with their periodic images except ion i in the first unit cell, to avoid self-interaction.

In atomic units, $\Phi_{[i]}$ can be written as

$$\Phi_{[i]}(\mathbf{r}) = \sum_{\mathbf{n}} \sum_{j=1}^N \frac{q_j}{|\mathbf{r} - \mathbf{r}_j + \mathbf{nL}|} - \frac{q_i}{|\mathbf{r} - \mathbf{r}_i|} \quad . \quad (3.10)$$

The summation goes over an infinite number of periodic images, enumerated by the vector \mathbf{n} , and is only conditionally convergent. Ewald's clever idea was to reformulate the problem by adding and subtracting a compensating Gaussian charge distribution $G_\sigma(\mathbf{r}) = \frac{1}{\sqrt{2\pi\sigma^2}^3} e^{-\frac{r^2}{2\sigma^2}}$ for every point charge

$$\begin{aligned} \rho_i(\mathbf{r}) &= \rho_i^S(\mathbf{r}) + \rho_i^L(\mathbf{r}) \\ \rho_i^S(\mathbf{r}) &= q_i \delta(\mathbf{r} - \mathbf{r}_i) - q_i G_\sigma(\mathbf{r}) \\ \rho_i^L(\mathbf{r}) &= q_i G_\sigma(\mathbf{r}) \quad . \end{aligned} \quad (3.11)$$

This does not change the overall density, but it allows to split up the potential into a long-range and short-range part

$$\Phi_{[i]}(\mathbf{r}) = \Phi_{[i]}^S(\rho^S(\mathbf{r})) + \Phi_{[i]}^L(\rho^L(\mathbf{r})) \quad , \quad (3.12)$$

exploiting the superposition principle in electrostatics. After some straightforward and simple arithmetics $\Phi_{[i]}^S$ and $\Phi_{[i]}^L$ can be written as

$$\begin{aligned} \Phi_{[i]}^S(\mathbf{r}) &= \sum_{\mathbf{n}} \sum_{j=1}^N \frac{q_j}{|\mathbf{r} - \mathbf{r}_j + \mathbf{nL}|} \operatorname{erfc}\left(\frac{|\mathbf{r} - \mathbf{r}_j + \mathbf{nL}|}{\sqrt{2}\sigma}\right) - \frac{q_i}{|\mathbf{r} - \mathbf{r}_i|} \operatorname{erfc}\left(\frac{|\mathbf{r} - \mathbf{r}_i|}{\sqrt{2}\sigma}\right) \\ \Phi_{[i]}^L(\mathbf{r}) &= \sum_{\mathbf{n}} \sum_{j=1}^N \frac{q_j}{|\mathbf{r} - \mathbf{r}_j + \mathbf{nL}|} \operatorname{erf}\left(\frac{|\mathbf{r} - \mathbf{r}_j + \mathbf{nL}|}{\sqrt{2}\sigma}\right) - \frac{q_i}{|\mathbf{r} - \mathbf{r}_i|} \operatorname{erf}\left(\frac{|\mathbf{r} - \mathbf{r}_i|}{\sqrt{2}\sigma}\right) \quad . \end{aligned} \quad (3.13)$$

Here, we used that the potential of a Gaussian charge distribution G_σ is proportional to $\operatorname{erf}(r/\sqrt{2}\sigma)/r$. Since the integrated charge of each $\rho_i^S(\mathbf{r})$ is zero, $\Phi_{[i]}^S(\mathbf{r})$ can be summed up in real space. The complimentary error function $\operatorname{erfc}(x) = 1 - \operatorname{erf}(x)$ efficiently truncates the potential at large distances, which ensures fast convergence of the sum in $\Phi_{[i]}^S$. The long-range potential, on the other hand, cannot be evaluated as a finite sum in real space, as it is still only conditional convergent. However, one can exploit the fact that the Fourier transform of ρ_i^L is

a Gaussian distribution in reciprocal space. As contributions from higher k -values decay with e^{-k^2} , $\Phi_{[i]}^L$ can be evaluated as a finite sum in reciprocal space

$$\Phi_{[i]}^L(\mathbf{r}) = \frac{1}{V} \sum_{\mathbf{k}} \tilde{\Phi}^L(\mathbf{k}) - \frac{q_i}{|\mathbf{r} - \mathbf{r}_i|} \operatorname{erf}\left(\frac{|\mathbf{r} - \mathbf{r}_i|}{\sqrt{2}\sigma}\right) \quad , \quad (3.14)$$

with $\tilde{\Phi}^L(\mathbf{k}) = \int_V d^3r e^{-i\mathbf{k}\mathbf{r}} \Phi^L(\mathbf{r})$ being the Fourier transform of $\Phi_{[i]}^L + \Phi_i^L$ and V the volume of the unit cell.

After solving the Poisson equation in reciprocal space and applying Fourier back-transformation into real space, the long-range potential can be written as

$$\Phi_{[i]}^L(\mathbf{r}) = \frac{4\pi}{V} \sum_{\mathbf{k} \neq \mathbf{0}} \sum_j^N \frac{q_j}{k^2} e^{i\mathbf{k}\mathbf{r}_j} e^{-\frac{\sigma^2 k^2}{2}} - \frac{q_i}{|\mathbf{r} - \mathbf{r}_i|} \operatorname{erf}\left(\frac{|\mathbf{r} - \mathbf{r}_i|}{\sqrt{2}\sigma}\right) \quad . \quad (3.15)$$

The apparently diverging long-wavelength limit term ($\mathbf{k} = \mathbf{0}$) vanishes for neutral unit cells with sufficiently small macroscopic dipole, as shown by Lipkowitz and Cundari [119].³ The sum of $\Phi_{[i]}^L$ and $\Phi_{[i]}^S$ is now the overall electrostatic potential of the infinite crystal serving as the target potential which needs to be reproduced in the embedded cluster model. Note, that the first term in Eq. 3.15 is not a function of r and thus a constant potential offset, which is often referred to as the *Madelung constant*.

In the embedded cluster setup, the finite number of point charges q_i in the MM region alone cannot reproduce the reference potential. It basically misses a constant potential offset. This can be corrected for by adding additional point charges, placed sufficiently far away to approximate a constant potential. Furthermore, although the MM region can be chosen to be charge neutral, the finite number of point charges potentially leads to other non-vanishing electrostatic moments. This strongly depends on the geometry of the MM region. To compensate for spurious electric moments, further added point charges are placed around the MM region. If the MM region is large enough terms higher than the dipole can be neglected [115].

The values of all added charges can be determined through least-square fitting to the reference potential, which can be solved on a grid extending over the QM and active MM region. If positions are fixed but only charges are subject to fitting, the optimization problem is reduced to solving a set of linear equations $\mathbf{A}\mathbf{q} = \mathbf{M}$. Here, A is a coefficient matrix, q the vector of charges and M carries the information of the reference Madelung potential. Hereby, if the number of charges is not too large, linear dependencies of the set of equations can be avoided and the Madelung potential can accurately be reproduced up to 10^{-4}V [115]. However, one needs to be aware that the encounter of linear dependencies poses limitations to the size of the active MM region.

Ultimately, the finite MM region and the fitted point charges together reproduce the correct reference potential of the infinite crystal background, without evoking spurious electric fields. This is independent of charge neutrality and specific shape of the MM region.

3.4 Solid-state embedding with ChemShell

The concept of solid-state embedding has found application for almost three decades by various groups with different levels of sophistication. Computational approaches which allow for self-consistent polarization of ionic materials, necessitate explicit coupling between QM and MM

³The importance of this term for charged unit cells is one of the reasons why correction methods like those proposed by Makov and Payne [87] or Lany and Zunger [89] potentially miss a shift in the overall electrostatic potential.

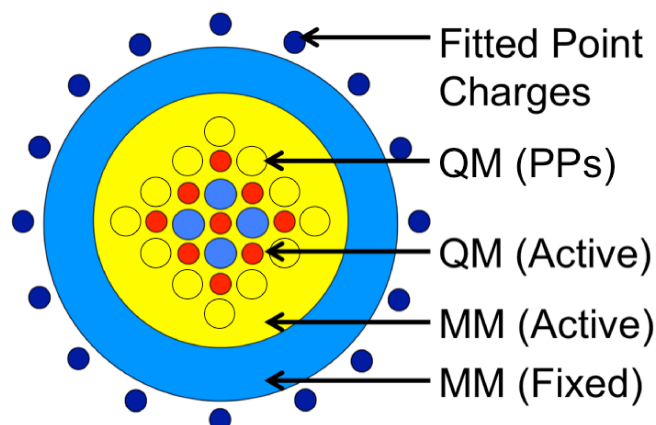


Figure 3.1: Schematic representation of the embedded-cluster models used in the QM/MM calculations: The central QM atoms, represented by individual red and blue circles, is surrounded by regions of active (yellow) and frozen (light blue) MM atoms. If necessary, such as in ionic systems, an additional embedding potential (yellow circles) is included around the QM region in the form of atom-centered pseudopotentials (PPs). The outer shell of point charges (dark blue) is fitted to ensure reproduction of the correct long-range electrostatic potential within the active region.

calculations. Computational infrastructure which also accounts for matching the long-range electrostatic potential has been made available in the QUASI project [115, 120], through the *ChemShell* simulation package.

Besides infrastructure that couples QM and MM driver, *ChemShell* provides routines to generate consistent embedded cluster setups from an periodic input structure. The embedded-cluster models used in the QM/MM *ChemShell* calculations generally consist of multiple concentric regions, each of which is described using more approximate methods as one moves further from the center of the cluster, as illustrated in Figure 3.1. The central region of the embedded cluster is described quantum mechanically, with the applied level of theory being DFT, Hartree-Fock (HF) or higher post-HF as offered by the employed QM calculator. Atoms in the outer MM regions are treated at the level of interatomic potentials and are represented within the QM calculations as external point charges. The MM region is typically divided into an inner “active” part, where atoms are allowed to relax their positions and polarize, and an outer part where atoms are constrained to their lattice positions. The latter is needed to suppress artifacts from the spurious electric field originating from the outer boundary of the MM region. Shell model potentials can be employed in the MM region for an accurate treatment of polarizable materials (see Section 5). A final exterior shell of point charges is added to the embedded cluster, with the point charges fitted to reproduce the full electrostatic embedding potential of an infinite bulk or surface reference calculation within the regions of physical and/or chemical interest (the “active” region) as discussed in the previous section.

ChemShell manages the properties of an embedded cluster during calculations, outsourcing the calculation of energy and force terms to the varied QM and MM interfaces. The program couples a number of quantum chemistry and classical forcefield software packages: In a given geometry the QM driver computes the energy as given in Equation 3.2, and the forces acting on all particles (atoms, PPs and point charges). Evaluation of energy and forces will be discussed in detail in Chapter 4. The forcefield software then evaluates further forces on the embedding point charges. This involves Coulomb interaction between all embedding point charges and

pseudopotentials. Further, all short-range interaction among point charges, QM-atoms and point charges, and pseudopotentials and point charges are calculated. In case of polarizable media, this also involves evaluation of core-shell interactions. With all force terms at hand propagation of particles can be performed. *ChemShell* updates the geometry input file and again invokes the QM-driver for energy and force evaluation. Geometry optimization of QM-atoms is performed using the *DL-FIND* routine [121]. Iteratively, this leads to self-consistent embedding and polarization.

Many MM software packages are available, linked to the *ChemShell* package. The General Utility Lattice Program (*GULP*) offers comprehensive MM functionality, especially in the implementations for strongly polarizable materials such as ionic oxides [122, 123]; an alternative such as *DL-POLY* provides excellent parallelization of larger molecular dynamics problems, and contains forcefield implementations more suited for semi-covalent systems [124].

3.5 Charged QM-region in the dilute limit

In contrast to periodic boundary conditions, addressing net charged systems is unproblematic, which is one of the greatest assets of the QM/MM approach. However, only the QM-region and the active part of the MM region are able to respond to the net charge. Therefore, a post-correction in the Mott-Littleton defect model is necessary to capture the long-range polarization response to extrapolate to the dilute limit, in order to mimic the polarization response of the infinite crystal background [125].

Chemical reactions with changes in oxidation state or formation energies of charged defects are assessed through differences in total energies of the system in different charge states. Charging the QM region changes the total energy of the overall system through the QM energy E^{QM} and MM energy E^{MM} . Effects on the QM energy comprise the change in electron-electron interaction as well as electron-nuclei interaction. This will lead to structural changes in the QM-region, which in turn lead to a different polarization response in the MM regions. Second, there is the direct Coulomb interaction of the net-charge with the MM region. Through coupling with the shell degrees of freedom this interaction can be accounted for through self-consistent polarization response. However, shells are only polarizable within a finite region of radius R by construction, as the MM region is finite. Since the Coulomb potential of the net charge decays with $1/r$, polarization of the system remainder beyond R cannot be neglected.

In principle, the MM-region beyond R would polarize, and induced dipoles and higher order multipoles would explicitly couple back to the QM-region. Since the field of a dipole falls off with $1/r^3$ we can neglect explicit effects on the QM region, if R is large enough, and correct the total energy by a post correction. By further neglecting structural details of the outer MM-region, one can retain the energy correction from a continuum solvation model (Fig. 3.2).

The QM-cluster is to be constructed such that the charge is localized in its middle. The inner MM-region can then adapt to that charge through a polarization response, according to the dielectric constant of the MM region. Let us further assume that the dielectric constants of the QM and inner MM-region match. The picture is then reduced to that of a charged sphere with dielectric constant ϵ in a continuum with dielectric constant ϵ' (see Fig. 3.2 b). The system remainder is not able to polarize outside the active region with radius R , i.e. ϵ' is 1 there. Thus, the missing energy term is the polarization energy of the region outside the active region, which can be found by integrating the polarization energy density outside the sphere

$$E^{\text{pol}} = \frac{1}{8\pi} \int d\Omega \int_R^\infty dr r^2 \left(\mathbf{E} \cdot \mathbf{D} - \mathbf{E}_0 \cdot \mathbf{D}_0 \right) \quad , \quad (3.16)$$

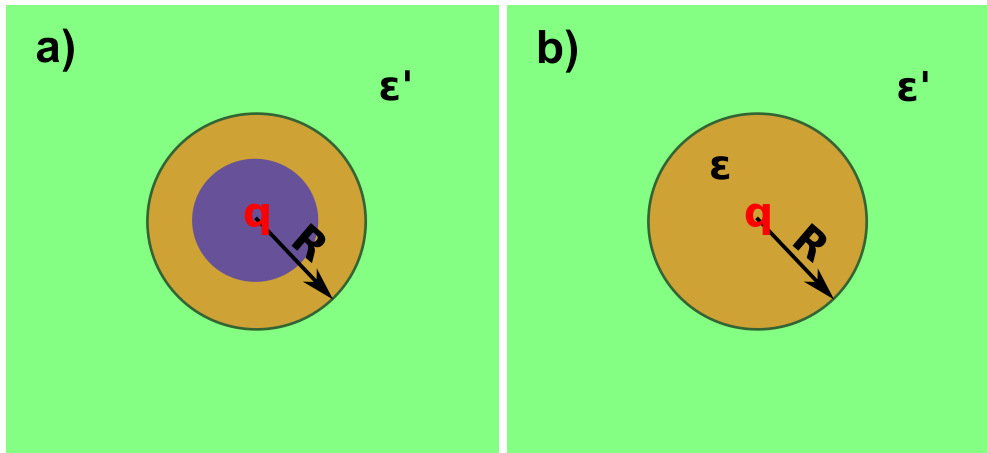


Figure 3.2: QM/MM and Continuum Solvation Model. Left: The QM region (purple) hosting a net charge q is surrounded by the inner MM-region (brown), which allows for explicit polarization. Beyond a radius R the system's remainder (green) is treated as an isotropic continuous medium with dielectric constant ϵ' . Right: A sphere with radius R , dielectric constant ϵ and charge q localized at the center of the sphere is surrounded by a continuum with dielectric constant ϵ' .

with \mathbf{E}_0 and \mathbf{D}_0 being the electric field and displacement in vacuum. The electric field within the sphere is $\mathbf{E}(r) = \frac{Q}{\epsilon r^2} \hat{\mathbf{e}}_r$, with $\hat{\mathbf{e}}_r$ being the radial unit vector. Together with $\mathbf{D} = \epsilon \mathbf{E}$ and the boundary conditions for the normal component of \mathbf{D} at the interface, the correction term can be calculated for the bulk case as

$$E_{bulk}^{pol} = -\frac{Q^2}{2R} \left(1 - \frac{1}{\epsilon}\right) \quad . \quad (3.17)$$

In case the charge is not located in the bulk but at a surface — or in general at a dielectric interface — an analogous formula can be derived. At an interface between two media with dielectric constant ϵ and ϵ'' the electric field is effectively reduced through image charges in the two media. This manifests through an effective dielectric constant for the medium

$$\tilde{\epsilon} = \frac{2}{\epsilon + \epsilon''} \quad , \quad (3.18)$$

following directly from the boundary conditions at the interface [126]. In case the $\epsilon' = 1$ the interface corresponds to the situation of a surface. Plugging Eq. 3.18 into Eq. 3.16 an analogous formula can be found for a surface

$$E_{surf}^{pol} = -\frac{Q^2}{2R} \frac{\epsilon - 1}{\epsilon + 1} \quad , \quad (3.19)$$

which follows from the boundary conditions for the electric field and displacement at the interface [115]. Finally, E^{pol} needs to be added to Eq. 3.1 to sum up to the corrected total energy of the system.

The polarization correction is zero for neutral systems, however, can easily be of the order of eVs for charged systems.

Part II

Implementation

This part documents new implementations carried out during the dissertation. For this work, we opted to employ *FHI-aims* [127] as a QM-driver for the QM/MM calculations, and created the interface to the *ChemShell* package (see Chapter 3.4). This work has been carried out in collaboration with Alexey Sokol and Andrew Logsdail (University College London) and Volker Blum (Duke University). Along these lines, a major part has been the implementation work of Kleinman-Bylander pseudopotentials into the all-electron electronic structure package *FHI-aims*. This work has been published in the *Journal of Chemical Physics* [128]. The implementation is part of the release version of *FHI-aims* (since August 2013), and is used by several groups [129]. Detailed documentations for usage of this implementation can be found in the manual of *FHI-aims*.

The importance of *seamless* coupling between QM and MM region has been discussed in the previous Chapter. To allow for matching QM and MM material properties we, furthermore, wrote a short program for the optimization of force field parameters. This program employs evolutionary algorithms from the python package *Inspyred* for *global* optimization, and is available for public use via the homepage of the Reuter group (TUM).

4 Implementation of Pseudopotentials

FHI-aims is a full-potential all-electron electronic structure theory package providing both DFT and "beyond-DFT" functionality [127, 130, 131]. Notably, this comprises efficient treatments beyond standard semi-local DFT, such as bare or screened single-determinant exchange; quantum-chemical perturbation theory for the Coulomb interaction, e.g., second-order Møller-Plesset (MP2) perturbation theory, bare (MP2) or screened (GW) self-energies for single-electron excitation energies; or the random-phase approximation (RPA) in the adiabatic connection fluctuation dissipation theorem.

It is based on hierarchical sets of all-electron atom-centered NAO basis functions of the form

$$\langle \mathbf{r} | \phi_\alpha \rangle = \phi_\alpha(\mathbf{r}) = \frac{u_l(r)}{r} Y_{lm}(\Omega) \quad , \quad (4.1)$$

where $Y_{lm}(\Omega)$ are the spherical harmonics, and the radial functions $u_l(r)$ are numerically tabulated and therefore fully flexible. Each basis function is strictly localized inside a given radius, which enables a highly efficient computation of both finite and (within PBCs) infinite systems within the same numerical framework. The regular basis set levels (called tiers, i.e. tier1, tier2, ...), as well as the recent valence-correlation consistent NAO-VCC-nZ basis sets for light elements [132] are constructed to enable systematic accuracy improvements from fast, but qualitative to meV per atom. Radial functions are integrated on a dense one-dimensional grid with logarithmic spacing. Global integration is efficiently achieved on a sparser three-dimensional concatenation of atom-centered grids [133, 134] (see ref. [135] for details of the present implementation). Conversion between logarithmic and global integration grid is done by using cubic splines. When working with embedding potentials (particularly, bare point charges) within the range of other integrands (e.g. the Kohn-Sham Hamiltonian matrix elements), these singularities must be integrated accurately, e.g. by placing an additional atom-centered grid on the site of the embedding potential.

With analytic forces provided, the major effort in the interfacing of *FHI-aims* with the *ChemShell* environment is the implementation of PP-functionality to describe cations at the boundary between the QM and MM region. For reasons of numerical efficiency described below, we opt for normconserving pseudopotentials (PP) of Kleinman-Bylander type [136]. In general, PPs are constructed to replace the atomic all-electron potential such that core states are eliminated and the then missing orthogonalization constraint of valence and core wavefunctions is achieved through appropriate scattering properties of the PP [80, 137]. In a real-space representation conveniently used together with localized basis sets, this energy-dependent scattering is expressed by a dependence on the angular momentum,

$$\hat{V}^{\text{PP}} = \sum_{lm} |Y_{lm}\rangle V_l(r) \langle Y_{lm}| \quad . \quad (4.2)$$

For every angular momentum l up to a maximum l_{max} , usually 2 or 3, there is thus a different

spherically-symmetric PP channel $V_l(r)$ with corresponding eigenfunctions

$$\langle \mathbf{r} | \psi_{lm} \rangle = \psi_{lm}(\mathbf{r}) = \frac{v_l(r)}{r} Y_{lm}(\Omega) \quad . \quad (4.3)$$

The radial functions $v_l(r)$ as well as the potentials $V_l(r)$ are commonly tabulated on a logarithmic grid. Our implementation is specifically tailored to read the tabulated format of the *.cpi PP files provided with the *FHI98PP* package [80, 138]. In principle, any kind of PP can be used though, as long as it is made available in the *.cpi format of *FHI98PP*. An almost complete database of PPs is e.g. available on the *abinit* webpage [139].

Mimicking an ion with a net charge, all PP channels $V_l(r)$ must embody the same Coulomb behaviour and are thus independent of the angular momentum in the far field, i.e. all $V_l(r)$ are the same outside the core radius r_{core} of the PP by construction. One channel can thus be chosen to embody all ionic long-range behavior. This local potential $V^{\text{loc}}(r)$ then acts on all electrons independent of their angular momentum, while the remaining channels $\delta V_l = V_l(r) - V^{\text{loc}}(r)$ are now short-ranged with $\delta V_l(r) = 0$ for $r > r_{\text{core}}$. Mathematically, the choice of the local component is hereby arbitrary. In practice a proper choice is crucial for the performance and transferability of the PP [140]. For instance, the routine *pswatch* in the *FHI98PP* package provides full analysis capabilities according to rigorous criteria by Gonze *et al.* [140].

Numerically, it is most convenient to further transform the PP into the fully separable form of Kleinman-Bylander, where the short-ranged part δV^{KB} is a fully nonlocal operator in \mathbf{r} -space [136]

$$\begin{aligned} \langle \mathbf{r} | \hat{V}^{\text{PP}} | \mathbf{r}' \rangle &= \langle \mathbf{r} | \hat{V}^{\text{loc}} | \mathbf{r}' \rangle + \langle \mathbf{r} | \hat{V}^{\text{KB}} | \mathbf{r}' \rangle \\ &= V^{\text{loc}}(r) \delta(\mathbf{r} - \mathbf{r}') + \sum_{l=0}^{l_{\text{max}}} \sum_{m=-l}^l \langle \mathbf{r} | \chi_{lm} \rangle E_l^{\text{KB}} \langle \chi_{lm} | \mathbf{r}' \rangle \quad . \end{aligned} \quad (4.4)$$

Here, the projector functions $|\chi_{lm}\rangle$ are defined as

$$|\chi_{lm}\rangle = \frac{1}{\sqrt{\langle \psi_{lm} | (\delta V_l)^2 | \psi_{lm} \rangle}} \delta V_l |\psi_{lm}\rangle \quad (4.5)$$

with energies

$$E_l^{\text{KB}} = \frac{\langle \psi_{lm} | (\delta V_l)^2 | \psi_{lm} \rangle}{\langle \psi_{lm} | \delta V_l | \psi_{lm} \rangle} \quad . \quad (4.6)$$

4.1 Energy Evaluation

FHI-aims evaluates the total energy in terms of the Harris energy functional [141]

$$\begin{aligned} E_{\text{tot}}^{\text{QM}} &= \sum_k^{N_{\text{states}}} f_k \epsilon_k - \int d^3r n(\mathbf{r}) V_{\text{xc}}[n(\mathbf{r})] + \int d^3r n(\mathbf{r}) \epsilon_{\text{xc}}[n(\mathbf{r})] \\ &\quad - \frac{1}{2} \int d^3r n(\mathbf{r}) V_{\text{H}}[n(\mathbf{r})] + E_{\text{nuc-nuc}} \quad , \end{aligned} \quad (4.7)$$

with f_k the occupation number of Kohn-Sham state ϵ_k and V_{H} the Hartree potential. The eigenvalues ϵ_k are hereby obtained in the standard manner via diagonalization of the Hamiltonian of the Kohn-Sham system, $\hat{h}_{\text{KS}} = \hat{t}_{\text{s}} + \hat{v}_{\text{ex}} + \hat{v}_{\text{es}} + \hat{v}_{\text{xc}}$. Here, \hat{t}_{s} is the kinetic energy operator, \hat{v}_{ex} the external potential, \hat{v}_{es} the electrostatic potential, and \hat{v}_{xc} the xc potential for the single

electrons as described in Eq. 2.23.¹ For the implementation of pseudopotentials, \hat{h}_{KS} is now augmented by the Kleinman-Bylander operator as written in Eq. 4.4. This involves computation of the local and nonlocal potential part.

The local potential part is straightforward to implement. It is mapped from the (finite) logarithmic grid around the PP center onto the global integration grid with the help of cubic splines [127, 134], and its long-range part beyond the limits of the atom-centered grid is extrapolated by its Coulombic behavior (formal charge over distance). In the evaluation of the Hamiltonian matrix, V^{loc} is then evaluated like all other local potentials

$$E_{\text{loc}} = \int d^3r n(\mathbf{r})V_{\text{loc}}(\mathbf{r}) \quad . \quad (4.8)$$

The general matrix expression of the nonlocal potential involves the evaluation of a sum over the projections of every basis function $|\phi_\alpha\rangle$ on to every Kleinman-Bylander projector function $|\chi_{lm}\rangle$

$$\langle\phi_\alpha|\hat{V}^{\text{KB}}|\phi_\beta\rangle = \sum_{l=0}^{l_{\text{max}}} \sum_{m=-l}^l \langle\phi_\alpha|\chi_{lm}\rangle E_l^{\text{KB}} \langle\chi_{lm}|\phi_\beta\rangle \quad . \quad (4.9)$$

For a given geometry, this matrix is computed once before entering the SCF cycle and is added to the Hamiltonian matrix $H_{\alpha\beta}$ in every iteration in the self-consistent field (SCF) cycle. The nonlocality in Eq. 4.9 is hidden in the fact, that basis functions ϕ_α, ϕ_β are centered on the atoms (not necessarily the same) while χ_{lm} are centered on the pseudopotentials.

The strength of the Kleinman-Bylander formalism lies generally in its scaling behavior. Rather than having to evaluate and store all $\langle\phi_\alpha|\delta V_l|\phi_\beta\rangle$ matrix elements, resulting in $\mathcal{O}(N^2)$ scaling with the number of basis functions, the fully separable KB form only requires evaluation and storage of $N \times M$ projections with M the (small) number of KB projector functions. In case of atom-centered basis sets the projections $\langle\phi_\alpha^{(j)}|\chi_{lm}^{(i)}\rangle$ correspond furthermore to a two-center integral of basis function $|\phi_\alpha^{(j)}\rangle$ of atom j at \mathbf{R}_j and $|\chi_{lm}^{(i)}\rangle$ of PP i at \mathbf{R}_i . The explicit expression to be evaluated is then:

$$\langle\phi_\alpha^{(j)}|\chi_{lm}^{(i)}\rangle = \frac{1}{\int dr (\delta V_l(r)v_l(r))^2} \int d\mathbf{r} \phi_\alpha(\mathbf{r} - \mathbf{R}_j) \frac{\delta V_l(|\mathbf{r} - \mathbf{R}_i|)v_l(|\mathbf{r} - \mathbf{R}_i|)}{|\mathbf{r} - \mathbf{R}_i|} Y_{lm}\left(\frac{\mathbf{r} - \mathbf{R}_i}{|\mathbf{r} - \mathbf{R}_i|}\right) \quad . \quad (4.10)$$

This term is most efficiently computed with the help of spherical Bessel transformations [142–144] already implemented in *FHI-aims* [130]. The radial functions $v_l(r)$ and the potential $V_l(r)$, respectively potential differences $\delta V_l(r)$ of the projector are tabulated in *.cpi format and provided as input for each relevant element. The total number of overlap integrals that needs to be computed at all is further reduced by locality, as overlap integrals are exactly zero if the distance of the involved atom centers exceeds a maximum value. This maximum value is given by the maximum extension of any basis function plus the maximum extension of any KB projector function, and is typically in the range of 8 Å.

Eqs. 4.8 and 4.9 are implemented in a general way, such that they can be evaluated also for the Hartree-Fock and generalized Kohn-Sham theory (hybrid functionals). This allows to employ pseudopotentials and with that the whole QM/MM infrastructure in all flavors of DFT. Thereby, all post-DFT methods available in *FHI-aims* are now also accessible for solid-state embedding.

¹The treatment of xc-energy and -potential may appear a bit confusing. The xc-potential is needed to get an effect on the Kohn-Sham states. The second term compensates for the energy associated due to the change in KS-eigenvalues ϵ_k , because the actual physical quantity contributing to the total energy is the xc-energy $E_{xc}[n]$ (compare with Eq. 2.20 and 2.26).

4.2 Force Evaluation

For geometry optimization, molecular dynamics or vibrational analysis, forces acting on the pseudopotentials but also additional contributions to the forces on all-electron atoms need to be evaluated. Hellman-Feynman contributions arise from the embedding of the pseudopotential with formal charge q_i centered at position \mathbf{R}_i into the electrostatic fields of the electron density and all other nuclei in the QM region at positions \mathbf{R}_j and with charges Z_j

$$\mathbf{F}_i^{\text{loc}} = - \sum_j^{n_{\text{atoms}}} \frac{Z_j q_i}{|\mathbf{R}_j - \mathbf{R}_i|^3} (\mathbf{R}_j - \mathbf{R}_i) - \int d^3 r \rho(\mathbf{r}) \nabla_i V^{\text{loc}}(\mathbf{r}) \quad . \quad (4.11)$$

Here, $\nabla_i V^{\text{loc}}(\mathbf{r})$ is the gradient of V^{loc} with respect to the position \mathbf{R}_i and is needed on every global integration grid point. This is efficiently computed from a cubic spline interpolation of V^{loc} created before entering the SCF cycle. Analogous to the first term in Eq. 4.11, the Coulomb interaction between nuclei and PPs gives rise to a force term of the same shape that complements the general QM-force expression for atoms in *FHI-aims* (Eqs. (69) and (71-75) in Ref. [127]). As written and implemented, Eq. 4.11 will work only for non-periodic geometries. A formalism analogous to Eq. (70) in Ref. [127] would have to be adopted in order to employ pseudopotentials for periodic geometries.

The overlap, Eq. 4.10, between any basis function and a KB-projector function $|\chi_{lm}^{(i)}\rangle$ of the PP i at \mathbf{R}_i is an explicit function of \mathbf{R}_i . This gives rise to a force acting on the PP,

$$\begin{aligned} \mathbf{F}_i^{\text{KB}} = & - \sum_k f_k \sum_{j,h}^{n_{\text{atoms}}} \sum_{\alpha \in \mathcal{J}, \beta \in \mathcal{H}} \\ & c_{k\alpha} c_{k\beta} \sum_{\chi \in \mathcal{I}} \sum_{lm} \left[\left(\frac{\partial}{\partial \mathbf{R}_i} \langle \phi_\alpha^{(j)} | \chi_{lm}^{(i)} \rangle \right) E_l^{\text{KB}} \langle \chi_{lm}^{(i)} | \phi_\beta^{(h)} \rangle + \langle \phi_\alpha^{(j)} | \chi_{lm}^{(i)} \rangle E_l^{\text{KB}} \left(\frac{\partial}{\partial \mathbf{R}_i} \langle \chi_{lm}^{(i)} | \phi_\beta^{(h)} \rangle \right) \right] \quad , \end{aligned} \quad (4.12)$$

where f_k is the occupation number of Kohn-Sham state k , and $c_{k\alpha} c_{k\beta}$ is the density matrix. \mathcal{I}, \mathcal{J} and \mathcal{H} are the subspaces of projectors respectively basis functions belonging to PP i and atoms j and h , respectively. Again, derivatives of overlaps only have to be calculated for those pairs of functions, which have a non-zero overlap. Since the overlap, Eq. (4.10), is also a function of the position of atom j , this gives reciprocally rise to a negative force acting on atom j complementing the general force expression on atoms.

In order to compute the Hartree potential, *FHI-aims* follows the strategy of an atom-centered multipole (MP) decomposition as introduced by Delley [134]. Here, the density difference to a sum-over-free-atom density is partitioned into atom-centered components on the integration grid shells centered around individual atoms [127]. Applying an MP decomposition to these atom-centered components leads (together with the known MPs of the free-atom density components) to the total MP components of the Hartree potential [127, 134]. Although the ionic PPs do not introduce any electron density of their own, they do act as integration grid centers and are thus included into the partitioning. As a result, some electron density components are assigned to the PPs, even when no basis functions are centered at the position of the PP. The MP expansion always introduces an error $\rho(\mathbf{r}) - \rho_{\text{MP}}(\mathbf{r})$ though, as the expansion is truncated beyond a maximum angular momentum $l_{\text{MP}}^{\text{max}}$. This error leads to a net force [127],

$$\mathbf{F}_i^{\text{MP}} = - \int d^3 r [\rho - \rho_{\text{MP}}] \nabla_i V^{\text{loc}}(\mathbf{r}) \quad (4.13)$$

as the missing multipole terms move with the position of the center.

4.3 Parallelization

FHI-aims allows for massive parallelization with almost perfect scaling with the number of processors. For all operations on the global integration grid, this is achieved by distributing equal-sized batches of grid points over the processors. This infrastructure is exploited in full functionality for the energy and force evaluation of the local potential.

The nonlocal matrix can be relatively sparse in larger systems, especially when PPs are solely used to saturate the QM cluster in the embedded cluster setup. To save memory, only the none-zero entries together with a map of these entries to the corresponding indexing in the Hamiltonian is stored. Energy and force evaluation of the nonlocal potential is equally distributed over all processors using basic MPI commands.

Localization of basis functions in *FHI-aims* can be heavily exploited not only for integrations on the global grid, but also through block distribution of the Hamiltonian across all processors.² For a certain computational overhead, which becomes worth to pay for systems with a few hundred atoms, the Hamiltonian can be constructed in form of blocks for every atom only containing relevant basis functions with potential overlap. This allows for block distribution of the Hamiltonian over all processors, minimizing memory demand and work load per processor. The nonlocal operator (Eq. 4.9), however, allows interaction between basis functions which do not directly overlap. Hence, pseudopotential infrastructure cannot exploit this efficient block Hamiltonian functionality in *FHI-aims*, which limits practicableness of pseudopotentials for systems with a large number of QM atoms.

At this side, the present implementation leaves room for optimization. For example, the Hamiltonian block construction could be used with a slightly different distance criterion: in case two atoms are separated by more than

$$d_{cut} = r_{max}^{(i)} + r_{max}^{(j)} + 2r_{core} \quad , \quad (4.14)$$

not only the overlap matrix, but also their entries in the nonlocal energy matrix and consequently in the Hamiltonian have to be zero. $r_{max}^{(i)}$ and $r_{max}^{(j)}$ are the maximum extension of basis function of atom i and j , and r_{core} is the core radius of the pseudopotential. Further, a threshold for entries in the nonlocal energy matrix can be introduced suppressing very small values and the need to store them. This would also allow for block construction and block distribution, now with slightly larger blocks than in the highly optimized implementations without pseudopotentials.

For extensive studies of large clusters beyond the semilocal local level of DFT we recommend to extend our implementation along these lines.

4.4 Towards “full” pseudopotential functionality

In the QM/MM-context the PP-functionality is exclusively used to prevent overpolarization of the QM charge due to immediately adjacent MM cationic monopoles. As such, the monopole term of the cation is replaced by a bare ionic PP with equal formal charge. In contrast, when using the PP in regular electronic structure calculations, valence electrons would need to be considered for the pseudoized atom and would then contribute to the total electronic energy. Under these circumstances, the basis set of NAOs, which are usually used in *FHI-aims*, is not a good choice. Such NAOs were optimized for a completely different purpose, namely to represent electrons in the bare coulomb potential of a nucleus. Thus, standardized Gaussian basis functions

²Using the keywords *packed_matrix_format* and *use_local_index* one can exploit locality of the basis functions by sorting the Hamiltonian, Fock matrix and overlap matrix (and integration grid batches) in local blocks. In this way, not every processor needs to store the full matrices, which can be a bottle neck for extended systems.

would be a better choice. However, one could also generate new NAOs optimized specifically for the PP in hand. A minimal basis is always given in terms of the pseudo valence wavefunction in the pseudopotential *cpi file. It is straightforward to extend the *FHI98PPs* capabilities towards generating and printing a larger set of pseudo wavefunctions beyond the minimal basis. This should allow for a cheap and accurate description of the valence electrons throughout various chemical environments.

Second, as the xc-energy and -potential are not additive with respect to the electron density, a non-linear core correction (NLCC) [145, 146] may be required to make up for the missing core density of the pseudoized atom and therewith allow to properly capture the xc contribution of the added valence electrons. The essential idea of the NLCC is to simply add the core density ρ_{core} of a free atom to the calculation of the pertinent parts of the total energy expression.

As discussed above, *FHI-aims* calculates the total energy in a form given in Eq. 4.7. The NLCC correspondingly affects the first three terms in Eq. 4.7, which are thus replaced as follows:

$$\begin{aligned}
 E_{\text{xc}}^{\text{NLCC}}[\rho + \rho_{\text{core}}] &= \sum_i^{N_{\text{states}}} f_i \langle \psi_i | \hat{v}_{\text{xc}}[\rho + \rho_{\text{core}}] | \psi_i \rangle \\
 &- \int d^3r \rho V_{\text{xc}}[\rho + \rho_{\text{core}}] \\
 &+ \int d^3r (\rho + \rho_{\text{core}}) \epsilon_{\text{xc}}[\rho + \rho_{\text{core}}] \quad .
 \end{aligned} \tag{4.15}$$

Even though not of concern for the QM/MM focus, this expression was also implemented into *FHI-aims* for testing purposes. Thus, if an "empty" site (without nucleus and electrons, but including basis functions and integration grids) is placed atop a PP in *FHI-aims*, our present implementation also allows to perform norm-conserving PP calculations in *FHI-aims*. As smoothness of the core density is not an issue for NAO basis sets and integration grids designed for an all-electron code, we hereby employ the full atomic core density ρ_{core} and not a smoothed auxiliary representation as is commonly done in plane-wave codes [80].

As the added core density is atom centered, a Pulay-type force term on the pseudoized atom i arises when adding the NLCC [147–149]. Differentiating Eq. 4.15 determines this term as

$$\begin{aligned}
 \mathbf{F}_i^{\text{NLCC}} &= - \frac{\partial E_{\text{xc}}^{\text{NLCC}}[\rho]}{\partial \mathbf{R}_i} \\
 &= - \int \frac{\delta((\rho + \rho_{\text{core}}) \epsilon_{\text{xc}}[\rho + \rho_{\text{core}}])}{\delta(\rho + \rho_{\text{core}})} \frac{\partial \rho_{\text{core}}}{\partial \mathbf{R}_i} \\
 &= - \int dr^3 V_{\text{xc}}[\rho + \rho_{\text{core}}] \frac{\partial \rho_{\text{core}}}{\partial \mathbf{R}_i}
 \end{aligned} \tag{4.16}$$

at the level of LDA. For GGA functionals the complimentary gradient terms are still to be implemented.

As a showcase for the use of pseudopotentials, Figure 4.1 shows the dissociation curve of an Na_2 molecule with a pseudoized and an all-electron atom on the level of LDA. Compared to a fully all-electron calculation, accuracy even with a Gaussian-basis set for hydrogen is very good. Forces are computed consistent with the total energy (lower panel in Fig. 4.1). *FHI-aims* can be used as a pseudopotential code for single-point calculations. For full-pseudopotential functionality the PP-PP interaction still needs to be implemented. In the QM/MM setup, *ChemShell* expects this contribution to be outsourced to the MM-calculator. While in a given geometry this term is only a constant it is, however, vital in geometry optimizations.

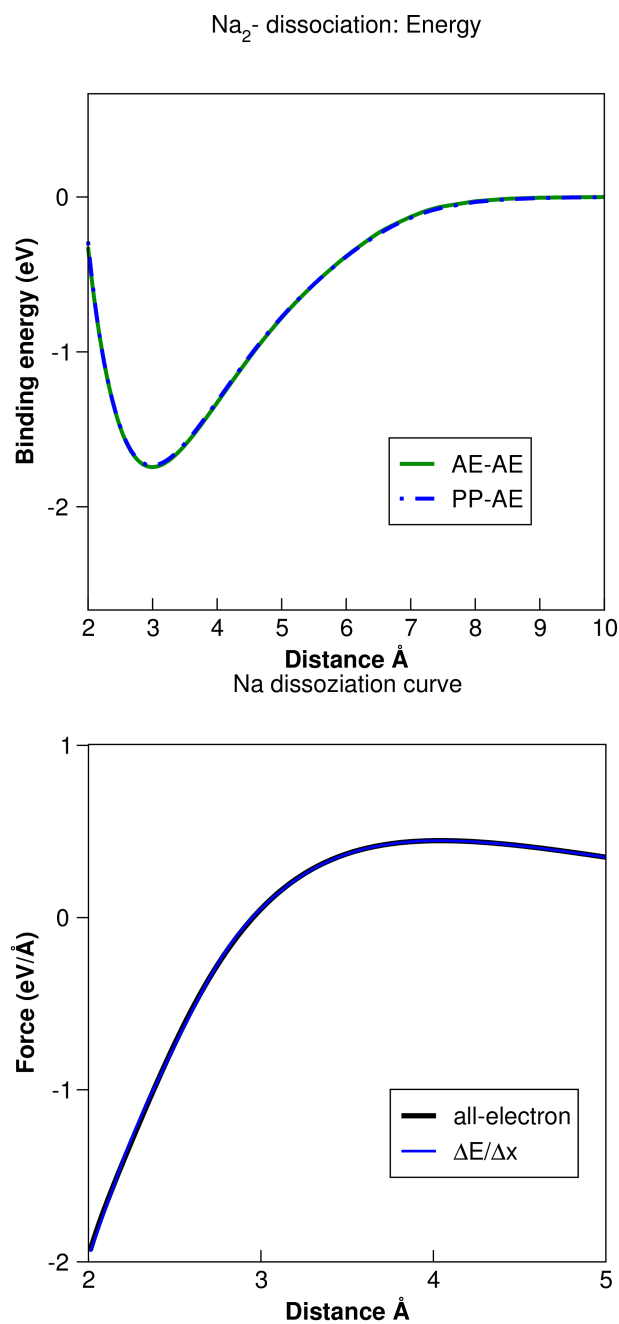


Figure 4.1: Accuracy of pseudopotentials on the level of LDA. The upper plot shows the dissociation between a pseudoized sodium atom (PP) and an all-electron (AE) sodium atom (green curve), compared to the reference curve between two AE atoms (blue). PP comprises an ionic sodium Na⁺-pseudopotential (incl. NLCC) augmented with an *aug-cc-pVTZ*-Gaussian basis set for hydrogen. The lower plot shows the computed forces in the PP-AE curve, referenced against the differential quotient of $\Delta E/\Delta x$.

5 Force Field Optimization with Evolutionary Algorithms

Force fields essentially are coarse-grained representations of the potential energy landscape. As such they depend on a set of parameters, which in combination determine all MM material properties. In order to achieve seamless coupling in the QM/MM setup these parameters need to be optimized to get matching properties, e.g. lattice parameters and dielectric constants. However, a straightforward optimization by divide and conquer of parameter space is tedious for three reasons. First, the number of parameters are easily in the order of 8-10. Second, all these parameters are coupled non-trivially via the equations determining the materials properties. Third, some observables of interest like the dielectric constant can have an extremely rough landscape in parameter space. To tackle these difficulties, we make use of global optimization routines to explore parameter space for optimized material properties. The source code of our potential optimization program is attached in the appendix to this work (Appendix A).

The quality of a force field can in general be assessed through a combined observable, a so called cost function, which measures the deviation to some reference values, in our case determined through the QM region. Since the different observables can have very different values, it is more meaningful to use the normalized deviation of MM from DFT observables

$$F = \sqrt{a \sum_i \left(\frac{L_i^{MM} - L_i^{DFT}}{L_i^{DFT}} \right)^2 + b \sum_j \left(\frac{\epsilon_j^{MM} - \epsilon_j^{DFT}}{\epsilon_j^{DFT}} \right)^2} \quad , \quad (5.1)$$

with L_i being the lattice constants, and ϵ_j the diagonal entries of the dielectric tensor, static and/or high-frequency, of the bulk unit cell. In an MM-description, the static dielectric tensor $\epsilon_{\alpha\beta}$ is computed from the Cartesian second derivative matrix with respect to all particles, $D_{\alpha\beta}$, and the vector \mathbf{q} containing the charges of all particles:

$$\epsilon_{\alpha\beta} = \delta_{\alpha\beta} + \frac{4\pi}{V} \mathbf{q} D_{\alpha\beta}^{-1} \mathbf{q} \quad , \quad (5.2)$$

and V being the volume of the unit cell. The expression for the high frequency dielectric tensor is determined in analogous fashion, only that the $D_{\alpha\beta}$ solely contains components of the shells. Thus, the static dielectric tensor describes the dielectric response of all particles, whereas the high frequency tensor gives the response only of the shells. For a core-only model the high frequency tensor equals the unity matrix. Parameters a and b can be used to emphasize the importance of specific observables.¹

The cost function is now subject to minimization with respect to all force field parameters. Here, we employ a differential evolutionary algorithm [150] from the Python package *Inspyred 1.0* [151]. First, the algorithm generates a set of “agents” with randomized force field parameters,

¹For example we found that for TiO₂ matching lattice parameter are more important for seamless coupling and also much easier to match than the dielectric constant. Therefore, a useful choice of parameter for such materials is $a = 1$ and $b = 100$.

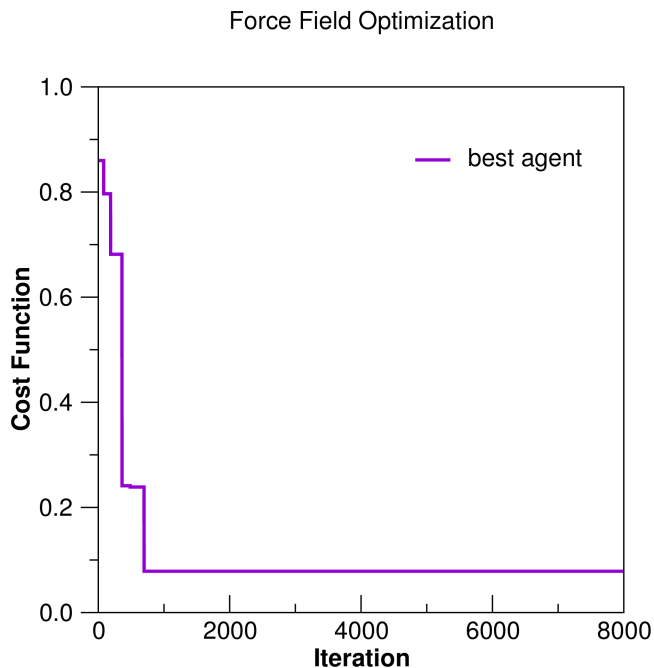


Figure 5.1: Convergence of cost function with the number of iterations for an MgO force field. The cost function (Eq. 5.1) was evaluated with equally weighted observables ($a = b = 1$). A number of 1000 agents with a mutation rate of 0.15 were used.

which explore the whole parameter space. For every agent, an input file for a bulk unit cell optimization is written and executed. In general any MM driver can be linked to our optimization program. Here, the format of the input file is designed for use of *GULP*, matching our general QM/MM setup.

The resulting observables L_i and ϵ_j are read from the output. According to their respective value of the cost function, agents can either be dismissed or kept. If the cost functions suggest the set of parameters was not too bad, the set is slightly “*mutated*”. In this way, parameter space is explored iteratively. It can be useful to reduce the domains the parameters are randomly picked from to some meaningful subdomain to avoid sampling of the whole real numbers \mathbb{R} , which would not provide physically meaningful parameters.

The algorithm does not guarantee to find the optimum in parameter space in a finite number of iterations. However, we are confident about the performance of this routine, as obtained minima were always reproducible, even with randomized values for the initial set. In contrast to the dimensionality of parameter space, the optimum is found quickly as can be seen in Fig. 5.1 and with an average cost of 0.05s per *GULP* calculation, it is also a relatively cheap approach.

Part III

Best-Practice and Benchmark

In this part, we will explain how to set up and perform an embedded cluster calculation and carefully benchmark our implementation against PBC reference calculations. We will thoroughly highlight how the different embedding ingredients affect observables in the QM region. In particular, we will discuss the importance of (norm-conserving) pseudopotentials and the influence of the embedding force field on the density of states (DOS) and the binding energies of small molecules.

In the first chapter of this part, all files necessary for an embedded cluster calculation using *ChemShell*, *FHI-aims* and *GULP* are described. General documentations of the *ChemShell* program can be found on the Internet [152], including a tutorial to solid state embedding [153].

Although the embedded cluster approach has been successfully applied to wide-gap ionic material, no clear guidelines have been formulated, so far. Specifically, documentation on how the MM region, especially the structural and dielectric parameters, affect observables in the QM region is scarce. In the second chapter of this part, we try to shed some light on that. We demonstrate embedding influences on the rutile TiO_2 surface, because titania not only has a very large, but also highly anisotropic dielectric tensor. This makes embedding extremely challenging as well as extremely sensitive to the different ingredients, which means that the embedded TiO_2 cluster is a very sensitive “device” to measure the quality of our embedding approach. This allows to clearly nail down the strengths and shortcomings of the embedding approach, and derive a clear best-practice embedding guideline for such materials. The density of states (DOS) here serves as sensitive observable for the clean surface. On top of that, binding energetics and local charging upon adsorption of the O, OH and OOH, representative for a wide range of chemically relevant processes, are benchmarked against PBC.

6 General Input Structure

Embedded cluster calculations with *ChemShell* are controlled with a set of files. A central processing script is needed to assign the given files. It contains the paths to the QM and MM program binaries, and provides other general information and specifies the actual calculation (single point, polarization response, geometry optimization, etc.). Detailed information on the syntax of this script and a description of all control flags can be found in [154]. Second, the geometry input in the *ChemShell* format (see again [154]) is required containing all structural information, i.e. atom coordinates and their assignment to QM, active or inactive MM region. How to generate the *ChemShell* geometry input is explained exemplary for a TiO₂ surface in Section 6.1. During the *ChemShell* iterations, the geometry input file is translated for the QM and MM drivers. Further input for the actual QM and MM calculations are required. The input files for *FHI-aims* and *GULP* are explained in Section 6.2 and 6.3.

6.1 *ChemShell* geometry input

ChemShell requires a general geometry input file, providing coordinates, species and charges of all particles. Therein, particles are allocated to the different QM/MM domains (QM region, active or inactive MM region) through a suffix to the species names (species name + "region number"). In principle, one can manually edit such a file for any kind of structure. *ChemShell* accepts the geometry input file provided in the *ChemShell* format (see [153]).

In solid state applications, the system is typically periodic. The *ChemShell* package provides routines allowing to construct the *ChemShell* geometry input from a periodic supercell exploiting periodicity of the underlying crystal. Among others, this includes a fitting routine for embedding point charges to reproduce the long-range electrostatic potential as discussed in Section 3.3.

For such periodic systems, the crystal structure of QM and MM region are defined through a common supercell. This common supercell contains all information about the structure, e.g. lattice parameters and internal atomic positions. Furthermore, every particle is assigned with a species and a particle charge. In this way, the long-range electrostatic potential of the infinite crystal is completely defined. From this common supercell, the *ChemShell* routine *c.create_coords* creates a periodic array of supercells according to the lattice parameters. As a next step, the routine *construct_cluster* generates a spherical cut from this array comprising the QM region, active and fixed MM region. This requires specification of the central atom of the system, the overall system size, and size of active region - QM and polarizable MM region (yellow circle in Fig. 3.1).

These parameters ultimately also define the fitted charges (dark blue spheres in Figure 3.1), to reproduce the Madelung potential within the active region, as discussed in Section 3.3. The optimal choice for the density of fitted charges as well as their distance from the fixed MM region depend on the overall system size. These parameters can be optimized such that deviations to the exact periodic Madelung potential are in the order of 10^{-4} Ha. For MM regions with a radius larger than 50 Å the least-square routine starts to get linearly dependent. This, ultimately limits the system size in this approach.

For a given choice of overall MM region size, the surrounding point charges are fitted to generate a potential equal to the exact Madelung potential with the active MM region. This procedure does not introduce any free parameters to the setup, as the Madelung potential is calculated consistently only from the charge distribution and lattice parameters of the input surface supercell. Hence, the actual thickness of the fixed MM region has no effect on observables in the QM region, since the long-range electrostatic embedding potential is always the same. Nonetheless, the choice for the thickness of the fixed MM region is not indiscriminate and has to be larger than the cutoff of the short-range MM potentials (typically 12 Å), to avoid spurious polarization at the outer active MM region. The overall system size, however, affects the computational cost for both the QM and the MM calculation. A thickness equal to the cutoff length of the short-range potential is, hence, recommended.

At this point an intermediate file has been generated defining the geometry. However, particles are not yet assigned to specific regions. At first, QM particles have to be labeled as such by adding the suffix “1” to their species name, e.g. Ti1 or O1. Now, the routine *cluster_partition* can be used to further assign all other particles to the active and fixed MM regions, by adding suffixes 3 and 4, respectively. The output of *cluster_partition* is a list sorted by distance to the central atom of the QM cluster.

As a final step, the pseudopotentials (PPs) need to be marked manually, by adding the suffix 2. In principle, all cations with possible overlap with QM basis functions need to be replaced by PPs. This, of course, is specific to the material as it reflects interior bonding behaviour. In practice, we found it sufficient ¹ to only replace the first shell of cations, at least for TiO₂ and MgO, which is in perfect agreement to an earlier study [155].

Of particular interest for solid-state QM/MM applications are periodic host systems which contain a non-periodicity, e.g. a defect or a molecule of cluster adsorbed to the surface. Here, the strategy is to generate the *ChemShell* geometry input for the periodic substrate and add the non-periodicity in a second step by editing the geometry input file. In this way, the single non-periodicity can be studied in the dilute limit.

The embedded cluster approach leaves only two major freely controllable parameters regarding the geometry, namely the size of the QM region and the size of the active MM region. Convergence of any QM observable with respect to the geometry input, hence, only needs to be checked in terms of these two parameters.

6.2 FHI-aims input

FHI-aims requires a geometry input file (*geometry.in*) and a control file (*control.in*). In a *ChemShell* calculation the former is generated from the *ChemShell* geometry input file in the *FHI-aims* format ².

For accurate integration across the QM region boundary, nearby point charges should in principle be augmented with an integration grid. Grid points which coincide with an embedding point charge are excluded. However, if the point charge is very close to a grid point, this point enters the global integration with an extreme potential. This can be a source of numerical noise. In *FHI-aims*, the global integration grid can be extended by adding a so-called *empty-site* at a certain position in space. Such an *empty-site* corresponds to a radial logarithmic grid and excellently suits the accurate integration of nearby point charges when centered at their position.

¹In the TiO₂ system discussed below, adsorption energies (of O, OH and OOH) and KS-eigenvalues converge within 1 meV, already with only replacing the next-neighbored cations.

²QM atoms are specified as *atom*, PP as *pseudocore* and embedding point charges as *multipole* with order zero [156].

ChemShell automatically adds an empty-site on top of every nearby positive point charge in the *geometry.in* file, based on a distance criterion. The negative point charges effectively repel electrons and therefore do not complicate global integrations. However, in single-point SCF calculations we never encountered a change the QM total energy by more than 30 meV or more than 2 meV in adsorption energies due the usage of *empty*-sites. On the other hand, forces on embedding point charges can be quite noisy in calculations without empty sites, which can in turn lead to very poor convergence of the self-consistent polarization response.

The *control.in* consists of a header, which contains all general information (i.e. level of theory, mixing parameters, convergence criteria, etc.) followed by all species specific information (i.e. basis sets, integration grids, potential cutoff, ...). In *FHI-aims* PPs are allocated as independent species. Therefore, a species section needs to be supplied for the PP containing all general information such as integration parameters, cutoff, charge etc. Although the PP is not augmented with basis functions for the actual calculation, a minimal basis is needed to solve the free atom properties in order to generate integration weights for global integrations [127]. The integration parameters as well as the minimal basis can be taken from the default species settings of the pseudoized species (Ti for a titanium PP). To avoid the minimal basis to enter the SCF cycle, the flag *include_min_basis* has to be set to false. In addition a few flags need to be added containing the name of the PP file (Ti.cpi), the angular momentum channel which serves

```
[...]
species      Ti_pseudo

nucleus      22
mass         47.867

pseudo       Ti.cpi
pp_charge    4.
pp_local_component  1
nonlinear_core .false.

include_min_basis .false.
[...]
```

Figure 6.1: Species data for a pseudoized titanium atom. Starting from the default settings of the pseudoized species only a few flags need to be edited (documented in [156]). Furthermore, the default species integration parameters and the minimal basis (accept the minimal basis) need to be appended.

as local potential and the charge of the PP. A nonlinear-core correction is not available for GGA or hybrid functionals. However, nonlinear core correction is not expected to have a significant impact in QM/MM applications, as electron density should effectively be pushed away from the core region due to the nonlocal projector functions. An example input section for a pseudo-atom is given in Fig. 6.1.

Analogously, independent species information also has to be provided for *empty*-sites. Here, the integration grid can be relatively sparse. Default *light* settings of a Helium atom without any basis functions (again, except the minimal basis, which is needed to generate the integration weights) is found to give sub-meV convergence of the total energy.

The PP file itself needs to be provided in a separate file in the *.cpi format of FHI98PP [80]. In our approach the PP should have a long-range potential according to the formal charge of the ion.

In the case of Titania this corresponds to a Ti^{+4} pseudopotential, providing pseudoized $3d$ and $4s$ valence states. One controllable parameter for the PP is the number of angular momentum channels. For titanium and magnesium studied here, a number of three channels were found to be sufficient for sub-meV convergence of total energies in QM/MM applications. Furthermore it is essential that the PP does not introduce spurious ghost states through an inappropriate choice for the local potential channel. The eigenspectrum of the PP should therefore be tested, which can be done with the routine *pswatch* provided by FHI98PP (or equivalent).

Further information for the specific QM/MM and pseudopotential input parameters for *FHI-aims* can be found in the manual of *FHI-aims* [156].

6.3 GULP input

The task for the MM driver is to evaluate those energy and force contributions, which are not covered by the QM driver. These are Coulomb and short-range interactions among embedding monopoles, short-range interactions between embedding point charges and QM atoms, short-range interactions between embedding point charges and PPs and finally the core-shell spring interaction of MM oxygen. A file containing all force field interaction parameters has to be provided in a suitable format for the MM driver. An exemplary *GULP* input file can be found on the *ChemShell* web page [153].

In principle, *GULP* requires a specific list of all interacting species together with their specific short-range potential parameters. Here, the *ChemShell* nomenclature for species need to be satisfied. Hence, all species with their suffixes have to be considered, further distinguishing between MM cores and MM shells. In a QM/MM context, a QM atom is only assigned as a single core. The QM atom, however, also interacts via the short-range contribution of the respective shell. Consequently, the pair O1 core - O3 shell interacts with the same potential as the pair O3 shell - O3 shell.

All interactions among the fixed MM region and between fixed MM region and fitted point charges can be omitted in order to speed up the calculation. This, solely, affects the total energy in form of a constant shift (Eq. 3.1). Thus, differences in total energy, the QM and MM structure or any QM observable are not affected.

Detailed explanation for every *GULP* input parameter can be found on the *GULP*-homepage [157]. We found that the geometry optimizer is very sensitive to its input parameters, which can lead to oscillations of the shells resulting in very poor convergence of the self-consistent polarization response. To avoid such oscillatory behaviour and guarantee convergence we recommend a maximum step length of not more than 0.2 \AA , when using weak spring potentials.

7 Benchmark against PBC: the TiO₂(110) surface

In this Chapter, we show how exactly to perform an embedded cluster calculation using our implementation. As an example the (110) surface of rutile TiO₂ is studied, and benchmarked against the conventional supercell approach using periodic boundary conditions.

We first discuss specific challenges for solid state embedding with high dielectric constants, such as TiO₂. In Section 7.2 we present a detailed best-practice guideline how to create a *ChemShell* geometry input for such material. This closely follows instructions given in the supplementary material of Reference [158].

With the best-practice setup in hand, we perform careful benchmarking against periodic boundary conditions exploiting *FHI-aims*' capability of treating periodic as well as cluster calculations on identical numerical footing (same integration parameters, same basis sets), allowing benchmarking specifically targeting the strength and shortcomings of solid state embedding.¹ For all calculations in this part, a *tier2* basis set with default *tight* settings are used throughout. These settings were found to yield band-gaps, work functions and adsorption energies converged within less than 10 meV. Electronic exchange and correlation on the QM description are approximated at the GGA level of theory. Here, we opt for the rPBE functional for its presumably improved description of hydrogen over other GGA functionals.

In Section 7.3, the influence of the high-frequency dielectric constant of the MM region on the DOS of the clean TiO₂(110) surface is discussed. Furthermore, the effect of the self-consistent polarization response on the neutral cluster is studied in a series of differently sized clusters.

In Section 7.4, the adsorption of the O, OH and OOH molecules at the TiO₂(110) surface is studied. Adsorption of these radicals on rutile TiO₂ is not only a well studied system because of its relevance in photocatalytic watersplitting process, it also represent a wide range of the *chemical spectrum* due to the very different electronegativities and dipole moment.

Here, binding energies and Mulliken charges of the adsorbates are observed for different cluster sizes and varying high-dielectric constant in the MM region.

7.1 Challenges with TiO₂

Wide-gap insulators like MgO or NaCl have been extensively and successfully studied in embedded cluster approaches for decades. Such materials are very ionic. Hence, each ion is in a very stable closed shell configuration, making the cluster tolerant against imperfect scattering at the QM cluster boundary. Furthermore, using embedding point charges with formal charges is a very good representation of the actual charge state of ions. The dielectric constant in these materials is typically quite low (MgO: $\epsilon_0 \approx 10$), ultimately reducing polarization effects between QM and MM region. On the MM level, the structural properties and the static dielectric

¹The QM package *Dmol³* is also able to perform molecular as well as periodic calculations on the same numerical footing, however *FHI-aims* is the only QM driver which has this handy feature also available for hybrid functionals.

constant can be accurately described in a rigid ion model, allowing for seamless embedding. Here, MM particles are described as unpolarizable ions interacting via long-range Coulomb and short-range Buckingham potentials.

Embedding semi-covalent semi-conductors like TiO₂, however, still remains a huge challenge, as discussed in the following. One reason is its very high static dielectric constant ($\epsilon_0 \approx 180$ [159]), leading to strong electrostatic coupling between QM and MM region.

In TiO₂ the valence band formally consists of oxygen 2*p* states and the conduction band of titanium 4*s* and 3*d* states. This can be confirmed by projecting the density of states onto these orbitals. Assuming the ions to be in the formal oxidation state is, therefore, well motivated, i.e. the crystal consists of Ti⁺⁴ and O⁻² ions. In contrast to that, UV photoelectron spectroscopy suggest that the Ti 3*d* states contribute significantly to the O 2*p* valence states [160]. Furthermore, first-principle charge analysis support skepticism of formal charges. According to Mulliken analysis [161] titanium is charged +1.3, and Hirshfeld analysis [162] even results in a charge of +0.6. Thus, it is arguable that a fully ionic representation is suited.

The charge values for embedding particles are, ultimately, determined through available pseudopotentials terminating the cluster region boundary. Norm-conserving pseudopotentials are only defined for integer charge values. Generation of such pseudopotentials requires the electronic spectrum of an atom to be separable into core and valence states. Since the fully occupied 4*s* and twofold occupied 3*d* states are not separable, norm-conserving pseudopotentials for titanium have at least the charge +4. Approaches using other, less ionic PPs are not an option, as they would provide wrong scattering at the QM cluster region boundary. For example Ca²⁺ as employed by Sanz *et al.* [163] and Ammal and Heyden [164] lead even to a break-down of the HOMO-LUMO gap [163, 164]. For a consistent description across the MM region, all titanium and oxygen ions need to have formal charges.

Oxygen ions in TiO₂ are highly polarizable, and are in fact intrinsically polarized in the rutile structure. The electric field at the position of the oxygen atoms in the rutile structure is essentially non-zero. Using as interatomic potential a simple rigid ion model with +4 and -2 charges does not capture this physics. Applying such a rigid ion model for our embedding purposes leads to overpolarization at the cluster region boundary, making the cluster too ionic [155, 163–168], which in turn potentially has significant effects on adsorption processes at the embedded cluster.

The rigid ion model can be straightforwardly be extended to the polarizable core-shell model by Dick and Overhouser [169, 170], which has been recently applied for embedded clusters to study bulk properties of TiO₂ by Scanlon *et al.* [158]. In the core-shell model, the oxygen ion in the MM region is described by two charges — summing up to the formal charge — connected via a spring potential.² In an harmonic description, this mimics polarizability of the valence electron cloud with respect to the nucleus in the high-frequency limit. The polarizability of cations is typically negligible. Hence, the MM region for TiO₂ consists of Ti⁺⁴ ions, but instead of O⁻² one uses an oxygen shell O_{shell}^{-2-X} and an oxygen core O_{core}^X, with *X* being a small positive number. In practice, *X* can be subject to force field optimization. In a polyatomic environment, the shell separates from the core due to the electrostatic potential, which we will call *intrinsic polarization*. The degree of polarization can be tuned by the choice of spring potential together with the collective force field parameters. In the limit of zero core-shell separation this model equals the rigid core model. However, when allowed to relax the shells reduce the overall electrostatic potential, as they partly compensate the potential of the Ti⁺⁴ ions. Using a core-shell model thus not only introduces polarizability to the MM region, but also potentially reduces the effective charges in the system. Hence, this strategy allows to use Ti⁴⁺ PP and account for polarization response in the MM region, without overestimating the ionizity of the material.

²In the core-shell model, Coulomb interaction between oxygen core and its shell is excluded.

Within this approach, the MM region is described through eight interatomic potentials parameters: three parameters for the Buckingham potential between titanium and oxygen shells, three parameters for the Buckingham potential among oxygen shells, one parameter for the spring potential between oxygen core and shell, and one parameter for the charge offset X associated with the oxygen shell. Since all non-classical interactions like the Pauli repulsion are associated with the oxygen shell, Buckingham potentials involving oxygen cores are omitted. Furthermore, non-classical interactions between Ti cores are neglected. Equilibrium structural parameters and all dielectric properties are now completely determined through the combined set of interatomic potentials. For QM/MM applications these properties have to be reproduced simultaneously to allow for seamless coupling between QM and MM region.

For TiO₂ in its rutile structure this has been shown to be impossible by Catlow *et al.* [170]. Using formal charges, they found a set of potential parameters which could reproduce both the static and the high frequency dielectric constants, but completely failed to reproduce the lattice parameters.

Even when applying our program for global optimization of the interatomic potentials (described in Section 5), we were also not able to reproduce the lattice parameters together with the static dielectric constant. The best set of parameters — corresponding to a cost function (Eq. 5.1) of 0.28 — yield lattice parameters of $a = 3.886$ and $c = 3.216$ while reproducing the dielectric constants ($\epsilon_0^a = 149$ and $\epsilon_0^c = 228$). More precisely, it is the ratio of lattice parameters which poses the challenge. As the employed force fields tend towards cubic unit cell rather than reproducing the stretch of the DFT unit cell [170]. Strikingly, we found this misbehavior is not owed to the constraint of formal charges. Including the charge of the Ti cores (and O cores) as subject to force field optimization does not improve the performance, as optimized core charge values are in fact $+4/-2-X$.

On the MM level, the high-frequency dielectric response is mimicked through displacements of shell while the full static response also includes ionic displacements. This corresponds to solely electronic respectively full structural relaxation in the QM description. In the QM/MM approach, the dielectric constant enters in two ways. Most obviously, it enters through the self-consistent polarization response in the active MM region. For the clean TiO₂ surface, a neutral QM cluster can always be chosen to serve for embedding, e.g. by a Ti _{n} O _{$2n$} stoichiometry, with n being an integer value. In this case, dipole-dipole interactions between QM and MM region are the first non-vanishing term which are a direct function of the dielectric constant in the MM region. Since this term decays with $1/R^3$ with distance between dipoles, the cluster size serves as a controllable parameter of convergence for observables in the QM region. In the limit of large clusters, the dielectric response from the MM region is thus negligible. This also holds for neutral adsorbates, following the rationale, that relaxation effects for neutral adsorbates can be truncated at large distances.³

In a second, more subtle way, the dielectric properties constant defines the equilibrium geometry at the surface, as they define surface reconstruction due the electric field at the interface to the vacuum. Furthermore, surface atoms always have a non-vanishing dipole moment perpendicular to the surface. In the case of the (110) surface the bridging oxygen atoms will experience the strongest polarization. On the QM level — both in the reference slab calculation and also the QM region in the embedding setup — the surface QM atoms adapt through displacement of nuclei and quenching of the electron density.

On the MM level, the surface equilibrates through displacements of MM particles (static di-

³Polarization response for charged QM clusters requires an accurate representation of the static dielectric constant, involving a further energy correction for long-range polarization effects as described in Section 3.5. Applications are discussed in Chapter 10. Charged TiO₂ clusters without the full polarization response are addressed in an approximate way in Chapter 9.

electric response) and core-shell displacements (high frequency dielectric response). The aforementioned inability of force fields to reproduce the huge difference between static and high frequency dielectric constants of TiO₂ — and arguably of all high dielectrics — poses a specific challenge in the context of QM/MM. If full surface relaxation is allowed on the MM level, wrong static dielectric constants will lead to MM structures which are very different from their DFT counterparts. Even with force field parameters which allow very good structural representation of the bulk unit cell, MM atoms at a surface easily experience displacements in the order of 1 Å with respect to the QM atom positions in the reference slab calculation. This mismatch, in turn, yields a massive distortion of the embedding potential causing erroneous stress on the QM cluster. This stress can be avoided by fixing the core position in the MM region, and reducing relaxation to the shells. This is equivalent to reducing the general dielectric response to that of the high frequency limit (ϵ_∞).

Such an approach, proposed by Sokol *et al.* [115] has been applied to bulk TiO₂ recently [158]. In specific, they were able to accurately predict the band alignment in bulk rutile and anatase TiO₂, which is of utter importance in photocatalytic application. However, a clear best-practice guideline to generate the setup is desirable, as detailed discussion and benchmark tests are scarce.

7.2 Best practice setup for high-dielectrics

As discussed above, the inability to describe the static dielectric constant in high dielectrics poses a challenge to the QM/MM approach. In this Section, a consistent work-around for such materials, which neglects the static but fully embraces the high frequency dielectric constant, is proposed as a *best practice* approach. This is done in form of a *walk-through* following a step-by-step procedure summarized in Figure 7.1 Along the way, a relaxed surface supercell is generated on the DFT level, which later serves as input for the PBC reference calculation.

The *ChemShell* cluster cutting routine requires a surface supercell as input, as discussed in Section 6.1. It periodically replicates the supercell geometry in two dimension as the underlying crystal structure. From this structure the embedded cluster geometry is excised. To reproduce the electrostatic potential of the infinite slab, additional point charges are fitted and placed around the finite cluster. This setup is then divided into QM region as well as active and fixed MM region. Consequently, the input supercell determines the starting geometry for both the MM and QM region.

To ensure consistent surface reconstruction in the QM and MM region, the input surface supercell needs to be optimized on the DFT level before entering the *ChemShell* cluster cutting routine. This will determine the position of all MM atoms throughout the calculations, as further relaxation in the MM region is suppressed. Construction of such an input surface supercell follows the standard procedure with the bulk unit cell as the starting point. Structural properties can be quite different for different exchange-correlation functionals. To avoid erroneous stress, the bulk unit cell should be optimized on the level of DFT using the functional one later addresses the embedded cluster with. The resulting structural bulk properties for the rPBE functional are summarized in Table 7.1.

Based on the bulk unit cell a surface slab is generated and relaxed on the consistent level of theory. The (110) surface of the rutile structure results in a layered structure with O-Ti₂O₂-O trilayer building blocks. Here, a slab of 5 O-Ti₂O₂-O trilayers is chosen to resemble the surface. According to previous studies, such a setup yields converged electronic structure, surface energies and adsorption behavior with respect to slab thickness [172, 173]. In z-direction periodic slabs are separated by 50 Å of vacuum to avoid spurious interaction between them. The top and bottom

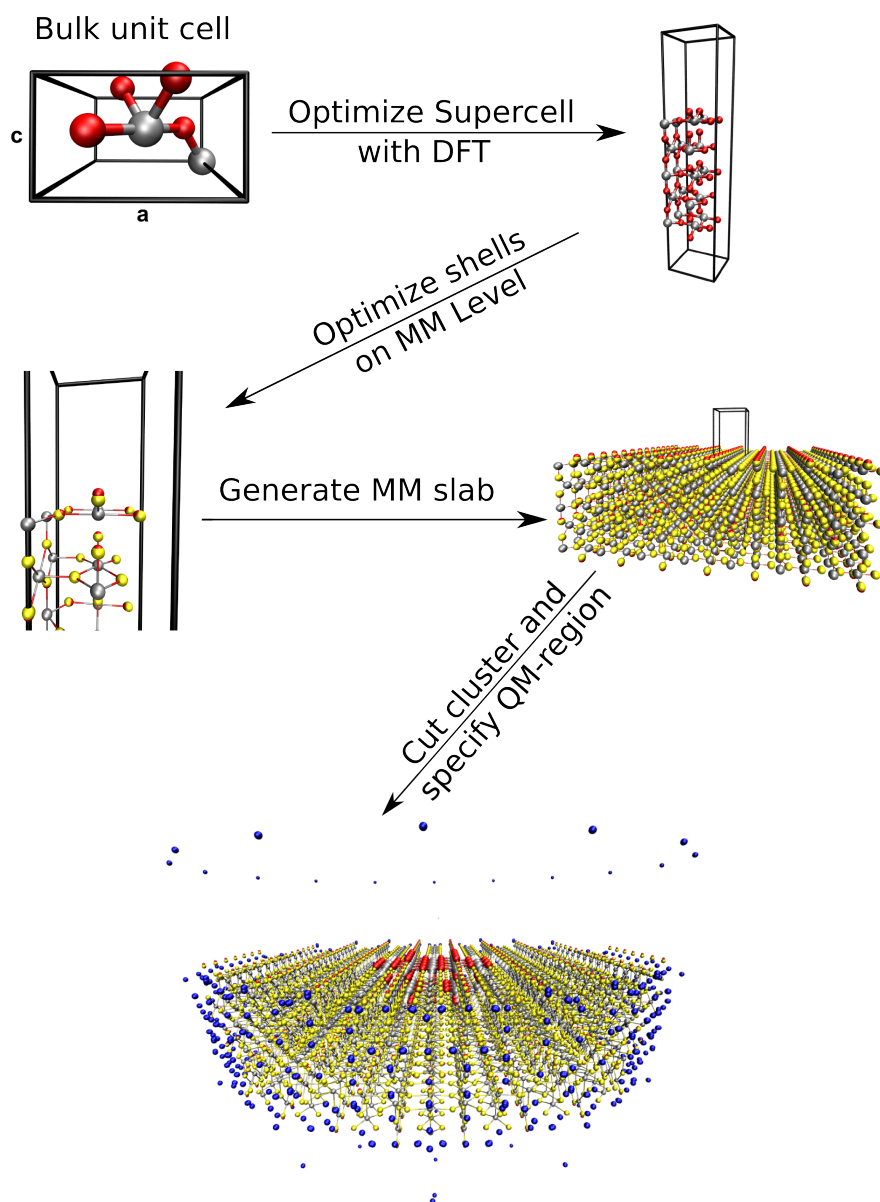


Figure 7.1: Sketching the steps from the optimized bulk unit cell to the final embedded cluster setup. Silver spheres depict titanium atoms, red spheres are oxygen QM atoms or MM cores and yellow spheres are oxygen shells. Blue spheres surrounding the MM region reproduce the Madelung potential in the QM region. See text for a detailed description.

two trilayers are fully relaxed to avoid odd-even oscillations with the number of trilayers [174]. Predominantly, this leads to relaxation of the top (respectively bottom) layer towards the central trilayer of the slab by 0.2 Å.

The resulting structure of the surface supercell defines the positions of all atoms in the embedded cluster calculation, also in the MM region. More specifically, it determines the position of MM titanium and oxygen cores. The position of the oxygen shells are yet undefined. Physically, the equilibrium positions of the oxygen shells are determined through the high frequency dielectric constant. In a polyatomic system, shells always equilibrate away from their cores,

bulk	$a(\text{\AA})$	$c(\text{\AA})$	u
rPBE	4.690	2.974	0.305

(110) surface	$E_{gap}(\text{eV})$	ϵ_{VBM}
rPBE	1.56	-7.67

Table 7.1: Important material properties of rutile TiO₂ calculated with DFT-rPBE. The structure of the bulk rutile TiO₂ unit cell is given by the lattice parameters a and c and the internal parameter u defining the position of oxygen atoms [171]. The electronic structure of the corresponding (110) surface is characterized through values for the band gap $E_{Gap}(\text{eV})$ and the eigenvalue of the valence band maximum ϵ_{VBM} with respect to the vacuum level, determined in the middle of the vacuum between slabs. The unit cell and surface supercell are optimized with the BFGS algorithm until residual forces are below 0.001 eV/Å. Reciprocal space has been thoroughly sampled on a $8 \times 8 \times 8$ k-grid for the bulk unit cell, respectively a $4 \times 8 \times 1$ k-grid for the primitive (1x1) surface supercell. Tight settings and the tier 2 basis set have been used.

leading to the aforementioned intrinsic polarization.⁴ This intrinsic polarization should also be enforced in the fixed MM region, to minimize later dependence on the size of active MM region. Hence, the equilibrium shell positions have to be calculated for a given configuration of MM cores. Applying the MM driver *GULP*, this can be accomplished in a shell-only optimization under the constraint of constant volume. Optimized shell positions are then to be appended to the input surface supercell entering the *ChemShell* cluster cutting routine. Consequently, this intrinsic shell polarization also affects the overall electrostatic potential, as the Madelung potential of the MM supercell and with that the fitted charges surrounding the MM region depend on the shell positions in the surface supercell. Following the argumentation above, the MM supercell with formal charges but displaced shells effectively corresponds to something less ionic than an assembly of rigid formal charges. This results in a weaker long-range electrostatic potential, which in turn affects the ionization energy of an embedded cluster.

The input supercell with optimized shells can now enter the *ChemShell* cluster cutting routine. For that, the center and radius of the active MM region needs to be defined. Here, the five-fold coordinated surface titanium atom (see Fig. 7.2) is chosen as the center of the cluster, since it is the adsorption site for the study in Section 7.4.

The major convergence parameter in the embedded cluster setup is, of course, the size of the QM cluster. Artifacts due to imperfect description of the MM region can be minimized through the use of large clusters. We therefore perform benchmark tests on four different clusters suggested by Heyden *et al.* [164], namely a Ti₁₇O₃₄, Ti₂₉O₅₈, Ti₃₃O₆₆ and Ti₅₄O₁₀₈ clusters (Fig. 7.2). Replacing nearby MM titanium cores with Ti⁴⁺ norm-conserving pseudopotentials finally completes setup.

Before conducting actual benchmark tests against the periodic reference setup, the influence of pseudopotentials and the influence of the intrinsic polarization shall first be clarified. Moreover, a safe choice for the size of active region has to be determined. In this way, only the QM cluster size and the high frequency dielectric constant are left as parameters which potentially affect any QM observables in the benchmark test.

⁴Only for a high frequency dielectric constant of 1 (vacuum) shells are not elongated. This equals an MM description without core-shell model.

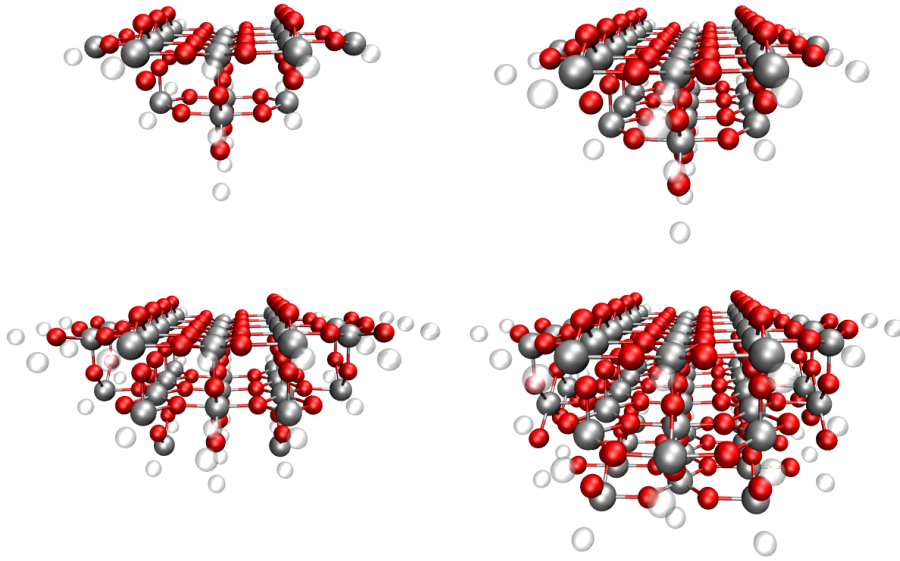


Figure 7.2: Perspective view of the $\text{Ti}_{17}\text{O}_{34}$, $\text{Ti}_{29}\text{O}_{58}$, $\text{Ti}_{33}\text{O}_{66}$ and $\text{Ti}_{54}\text{O}_{108}$ clusters, exposing at their top center the fivefold coordinated Ti adsorption site of the $\text{TiO}_2(110)$ surface. Ti atoms are shown as large white spheres, O atoms as small red spheres, and semi-transparent grey spheres mark the positions where PPs represent the immediately surrounding Ti-cations.

Necessity of pseudopotentials

In order to study the influence of the pseudopotentials, it is revealing to first calculate the bare QM cluster in vacuum and step by step go towards correct embedding by adding point charges and pseudopotentials. Here, only single point calculations are performed neglecting intrinsic polarization and a polarization response.

The resulting DOS of the bare cluster in vacuum does not show a gap between occupied and unoccupied states. This even holds for the already quite large $\text{Ti}_{54}\text{O}_{108}$ cluster, as can be seen in Fig. 7.3 (upper panel). The bare cluster, hence, predicts TiO_2 as a metal. However, TiO_2 is known to be a semiconductor, which is also reproduced by the periodic reference slab calculation (see Table 7.1). Consequently, the bare cluster clearly fails to even qualitatively reproduce the electronic structure of the surface.

As a next step, the QM cluster is embedded in a field of point charges using the strategy described above, but without replacing nearby Ti cores by pseudopotentials. As can be seen in Fig. 7.3 (b) the DOS looks quite different, compared to the one of the bare cluster. Predominantly the Fermi energy – the border between occupied and unoccupied states – is significantly shifted to lower energies. Again, there is no gap between occupied and unoccupied states. Hence, embedding without PPs fails to reproduce the electronic structure of the surface. In fact, the presence of nearby positive point charges causes spurious electron spill-out into the MM region. This is efficiently prevented by replacing the nearby Ti cores by PPs. Figure 7.4 shows the difference of electron density of a $\text{Ti}_{17}\text{O}_{34}$ cluster embedded with and without saturation with PPs. One can clearly see electron density accumulating at the cluster boundary. As a consequence, the central cluster regions suffers from electron depletion (red region in Fig. 7.4), which leads to overbound electronic states and a significantly reduced Fermi-level.

Replacing nearby Ti cores by PPs in the embedded cluster setup not only prevents electron spill-out, but it also introduces the desired gap between occupied and unoccupied states, as can

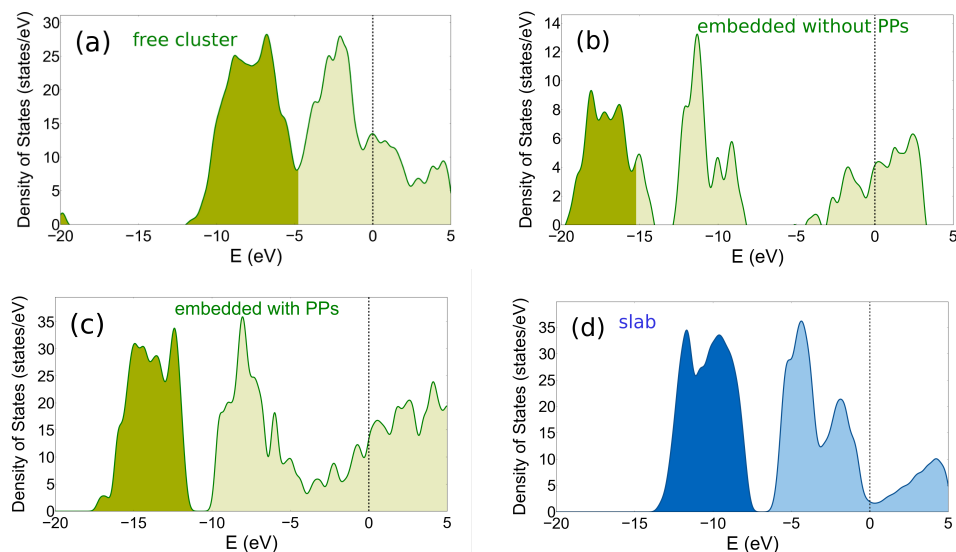


Figure 7.3: Total density of states (DOS) of the $\text{Ti}_{54}\text{O}_{108}$ cluster in vacuum (a), the $\text{Ti}_{17}\text{O}_{34}$ cluster embedded in a field of point charges without using pseudopotentials to saturate the QM cluster (b) and the same cluster with nearby MM cations replaced by Ti^{4+} norm-conserving pseudopotentials. The DOS of the reference slab calculation is shown in (d). The resulting band structure is sampled very accurately in reciprocal space on a $40 \times 40 \times 1$ k-grid to converge the DOS. The vacuum level represents the zero reference throughout, in the slab defined as the potential in the middle of the vacuum between slabs. Filled states are depicted in darker color.

be seen in Fig. 7.3 (c). In principle, all cations with potential overlap with electronic density have to be replaced by PPs. This, in turn, depends on the choice of basis set. Diffuse basis functions extend further out and therefore require further replacement of Ti cores with PPs. We found that for the basis sets applied here, (*tier2* for Ti and O), only next-neighbored titanium cores need to be replaced with PPs, to have the total energy converged within a few meV in a single point calculation of the $\text{Ti}_{17}\text{O}_{34}$ cluster. Due to our efficient evaluation of energy and force contribution of the PPs (see Chapter 4), the computational cost scales linearly with the number of pseudopotentials, with small prefactor. To avoid further convergence tests with respect to the number of PPs in the following, all cations in the second row are replaced as well.

Here, the cluster is embedded in an unpolarizable MM region without intrinsic polarization. When comparing the DOS of the embedded cluster in Figure 7.3 (c) with the reference slab calculation (d), the Fermi levels are shifted to each other by a few eV. This is due to the missing intrinsic polarization as will be discussed in the following.

Intrinsic Shell polarization

As a next step, the embedding model shall now include intrinsic polarization of the MM region. This requires shell optimization of the surface supercell on the MM level. The intrinsic polarization can be quantified in terms of shell displacement of the bridging surface oxygen atom. If shell displacements are not too large, i.e. shells are not too close to other MM particles except their own core, polarization and polarizability are dominated by the spring potential between core and shell. In the harmonic regime the spring potential energy is proportional to the polarization

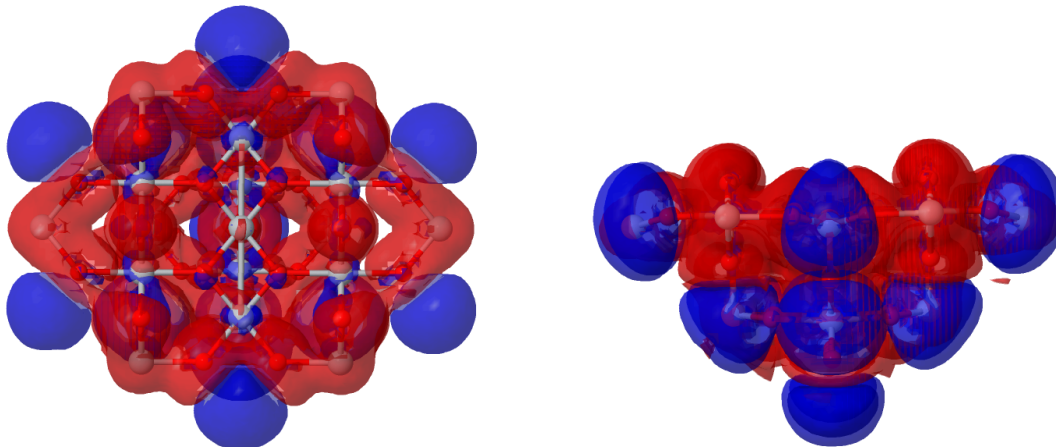


Figure 7.4: Difference of electron density of an $\text{Ti}_{17}\text{O}_{34}$ cluster embedded with and without pseudopotentials (isodensity surface 0.01), in top (left) and side view (right). Without pseudopotentials higher density accumulates at the cluster boundary (blue regions), leading to a slight electron depletion in the center of the cluster (red region).

energy [126]

$$\frac{1}{2}kd^2 \propto \epsilon_\infty |\mathbf{E}^2| \quad , \quad (7.1)$$

which yields a cubic dependence of the shell displacement d from the high frequency dielectric constant ϵ_∞ . While this should be true for all shells in the system, it not necessarily has to be fulfilled for surface atoms, since there is no clear definition for the dielectric constant at surfaces. Still, one observes exactly this correlation when plotting the shell displacement against the bulk dielectric constant (see Fig. 7.5). For larger displacements, the shell interactions with other MM particles get more and more noticeable. In case of very weak spring potentials, this leads to unstable polarization up to a complete detachment of the shells from their cores, limiting the high frequency polarizability in the core-shell model. Incidentally, this prohibits to mimic the static dielectric response through shell polarization only, as the spring potential would need to be extremely weak to reproduce a dielectric constant of 180.

To show the effect of the intrinsic shell polarization on the electrostatic potential, a set of embedded cluster ($\text{Ti}_{17}\text{O}_{34}$) calculations were performed with varying high frequency dielectric constants. The well established force field parameters by Jentys and Catlow were used [175]. The spring potential of the core-shell interaction was modified over the whole stable range to vary the high-frequency constant. To observe the pure effect of the intrinsic polarization, the self-consistent polarization response is not included here.

As can be seen in the left plot in Fig. 7.5, the high-frequency dielectric constant can systematically be tweaked between 1 and 6 by modifying the spring potential. However, for spring constants lower than $35 \text{ eV}/\text{\AA}^2$ one runs into aforementioned shell instabilities prohibiting usage in a QM/MM context. The effect on the overall electrostatic potential is measured in terms of the resulting ionization potential — highest occupied Kohn-Sham level in QM/MM — which systematically depends on the intrinsic polarization as can be seen in the right plot in Fig. 7.5. Embedding without intrinsic polarization corresponds to infinitely strong springs, a.k.a $\epsilon_\infty = 1$. Such a setup, indeed, leads to a massively overestimated work function. Only embedding in a force field with appropriate ⁵ high frequency dielectric constant leads to an ionization energy

⁵In principle, it is possible to calculate the dielectric constants even on a GGA level of DFT. One could apply

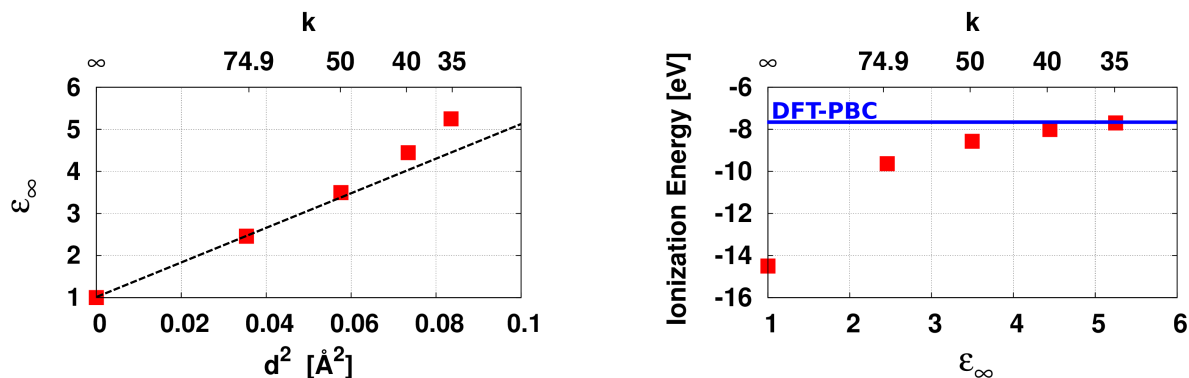


Figure 7.5: The high-frequency dielectric constant ϵ_∞ , intrinsic core-shell separation and their effect on the ionization energy. The left plot shows ϵ_∞ of the MM bulk unit cell plotted against the square of the core-shell displacement of bridging surface oxygen atom d in the MM slab. For a weak spring potential, shell displacements leave the harmonic regime (dashed line). The right plot shows resulting ionization potentials, a.k.a. the highest occupied orbital, of a $\text{Ti}_{17}\text{O}_{34}$ cluster embedded with different spring potentials. The blue line corresponds to the valence band maximum of a periodic DFT slab calculation.

which matches the valence band maximum of a periodic reference DFT calculation (see the right plot in Fig. 7.5).

Size of active MM region

In QM/MM, the self-consistent polarization according to the high-frequency dielectric constant can only be addressed within a finite active MM region. This introduces the radius of the active region as a further controllable parameter. In principle, convergence of any observable with respect to this parameter needs to be checked. In practice, this is only important in calculations with charged QM regions. For such cases, interaction with the embedding background is long-range, as discussed in Section 3.5. In case of neutral QM regions, the active region can be chosen relatively small, since the dominant term in the polarization energy decays with $1/R^3$ (see above).

At this stage, we determine a safe value for the setup used in our benchmark tests. For this, a $\text{Ti}_{17}\text{O}_{34}$ cluster is embedded in an active MM region, again with varying spring potentials. Within an active region of radius $25 a_0$ (bohr), the shell displacement of the self-consistent polarization response is measured relative to the shell positions of the intrinsic polarization, and plotted against the distance to the central atom of the QM cluster. The innermost shell has a distance of $11 a_0$, and represents the onset of the active MM region.

As can be seen in Fig. 7.6, the shell displacements are significant within the first $5 a_0$, then fall off quickly and are almost negligible after $9 a_0$, even for the "softest" core-shell potential. Displacements strongly depend on the spring potentials. As expected, weak springs lead to the largest displacements.

a sawtooth potential and measure the electronic response in a supercell. This functionality is not yet available in *FHI-aims*. Unfortunately, also no reference value could be found for the rPBE functional in the literature. Therefore, we can only roughly estimate the dielectric constant from other GGA functionals [176, 177]. For PBE it is about 7.

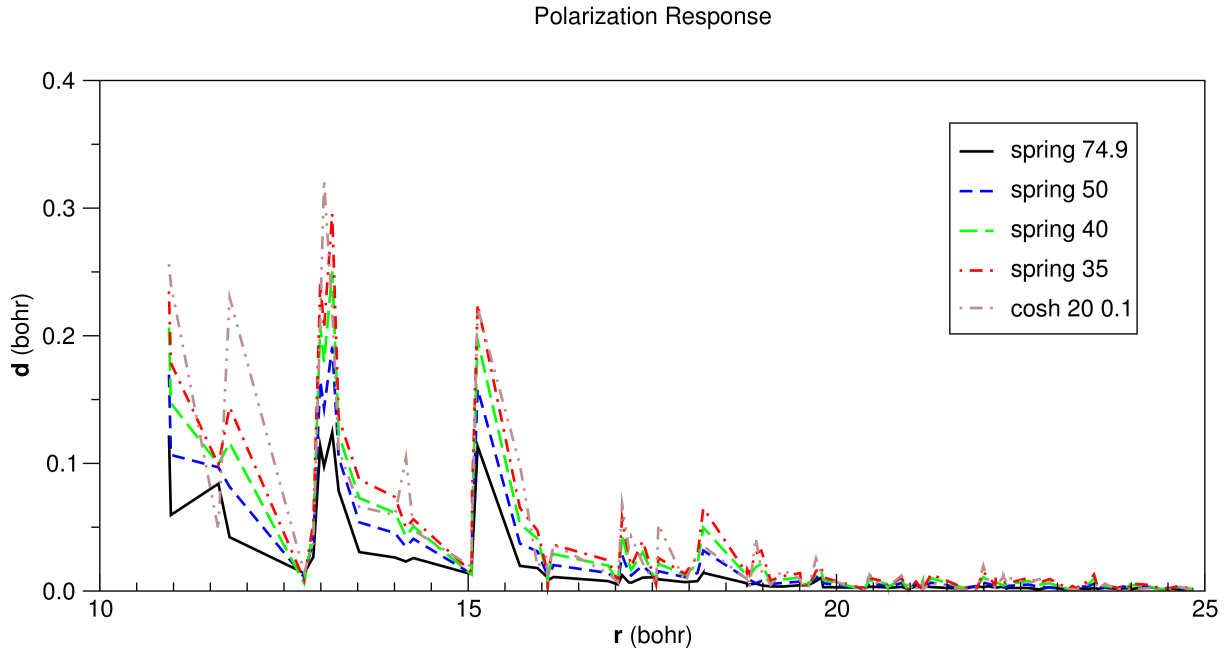


Figure 7.6: Self-consistent shell displacements in the embedded cluster calculation as a function of distance to the cluster center. A charge neutral $\text{Ti}_{17}\text{O}_{34}$ cluster with 151 PPs is embedded in an active MM region with 25 bohr radius. Together with the fixed MM region and fitted background charges a total number of 9203 point charges are used. The short range parameters and shell charges are taken from Jentys and Catlow [175], the core-shell spring potential was modified as labeled in the legend.

Hence, we can conclude that the self-consistent polarization response for neutral QM clusters decays indeed quickly. For such a system, a thickness of the active MM region of $9 a_0$ is found to be sufficient and is thus chosen throughout this work if not stated differently. The radius of the active region depends on the cluster size, defined as the radius of the QM cluster plus the thickness of the active MM region.

7.3 Benchmark: the clean surface

With this best-practice setup in hand, we now perform benchmark tests against the corresponding periodic reference calculation of the clean TiO_2 surface. For such a charge neutral QM region relaxation of the QM cluster is neglected. Again the force field parameters by Jentys and Catlow together with a modified spring potential between oxygen core and shell are used. Here, we opt for a *cosh-spring* potential with parameters $k=20$ and $d=0.15$ (see Eq. 3.6), which yield a good description of the high frequency dielectric tensor, including its anisotropy ($\epsilon_\infty^a = 5.8$, $\epsilon_\infty^c = 9.8$).

At the first stage, polarization response from the MM region is neglected, *i.e.* the electronic structure of the QM cluster is determined in presence of a fixed but intrinsically polarized MM region. The resulting density of states (DOS) is plotted for two cluster sizes, the $\text{Ti}_{17}\text{O}_{34}$ cluster and the $\text{Ti}_{54}\text{O}_{108}$ cluster.

As can be seen in Fig. 7.7, the DOS of embedded and slab calculation are not identical, however, their agreement of overall shape is indeed very good already for the $\text{Ti}_{17}\text{O}_{34}$ cluster. For

the quite large $\text{Ti}_{54}\text{O}_{108}$ cluster the agreement is almost perfect, both for the occupied and also the unoccupied states. This agreement extends not only to the band gap i.e. relative difference of highest occupied molecular orbital (HOMO) and lowest unoccupied molecular orbital (LUMO), but also to the absolute band edge positions. The ionization energy – the eigenvalue of the highest occupied molecular orbital (HOMO) – agrees within a few tens of meV. This means the overall electrostatic potential matches the one in the slab calculation, specifically the long-range electrostatics are well reproduced by the fitted point charges surrounding the MM region ⁶.

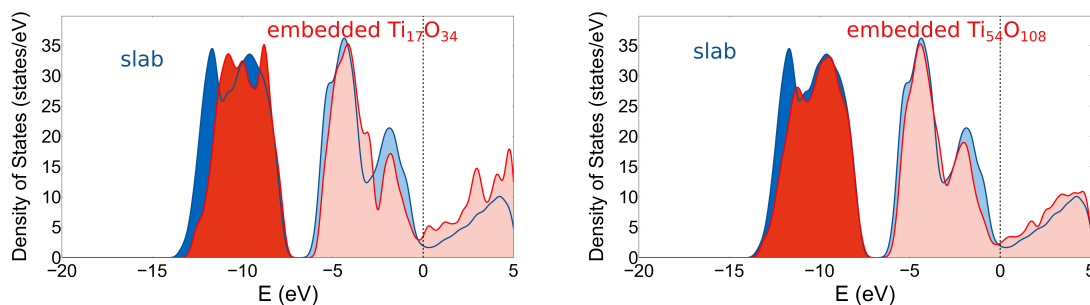


Figure 7.7: Comparison of the total density of states (DOS) without polarization response: Even a relatively small embedded $\text{Ti}_{17}\text{O}_{34}$ cluster (left panel) recovers important features from the reference slab calculation (in blue colors). Finite cluster artifacts can further be reduced, when increasing the cluster size. The embedded $\text{Ti}_{54}\text{O}_{108}$ cluster achieves almost perfect agreement with the corresponding PBC supercell calculations (right panel), in particular in the valence and lower conduction band region. Again, the vacuum level represents the zero reference throughout, and filled states are depicted in darker color.

As next step, also the self-consistent polarization response of the oxygen shells is included. Iteratively, the oxygen shells may adapt to the electrons in the QM region: in any given shell geometry *FHI-aims* solves the electronic structure and calculates forces on shells. Then, *GULP* adds short-range and spring forces. Shells are then propagated according to the total forces. This results in a new embedding potential acting on the QM region. The polarization response is considered to be converged when forces on shells do not change more than 10^{-3} eV/Å between iterations. As can be seen in Fig. 7.8 the occupied states are only little effected by the polarization response. However, the density of unoccupied states changes noticeably. Being of delocalized nature such states tends towards higher overlap across the cluster boundary and are thus more sensitive to the polarization response. In general, it leads to a slight lowering of the HOMO-LUMO gap, which is more pronounced in the small clusters.

In our QM/MM model, the self-consistent polarization response of the MM region is reduced to that of the dipole response of polarizable oxygen. The full response, however, would include higher moments. This is one reason why the band gap is reduced below the slab reference when including polarization response. In general, the mismatch obtained here reveals the discrepancy of the dielectric constant, which is defined only in a continuum model, mimicked through displacement of point charges. Furthermore, the real dielectric response is a function of the frequency. In our model, only the high frequency limit is incorporated. Consequently, including

⁶In case of very large MM regions, one can run into instabilities of the *ChemShell* charge fitting routine (see Section 3.3). Then, the fitted charges are not able to accurately reproduce the long-range electrostatics. In principle, this potential can always be tweaked by modifying the values of the fitted point charges, e.g. by symmetrically adapting values for the outermost charges. This, however, is not a self-consistent approach anymore.

the self-consistent polarization response not necessarily improves agreement of the DOS of the neutral embedded cluster with that of the periodic reference.

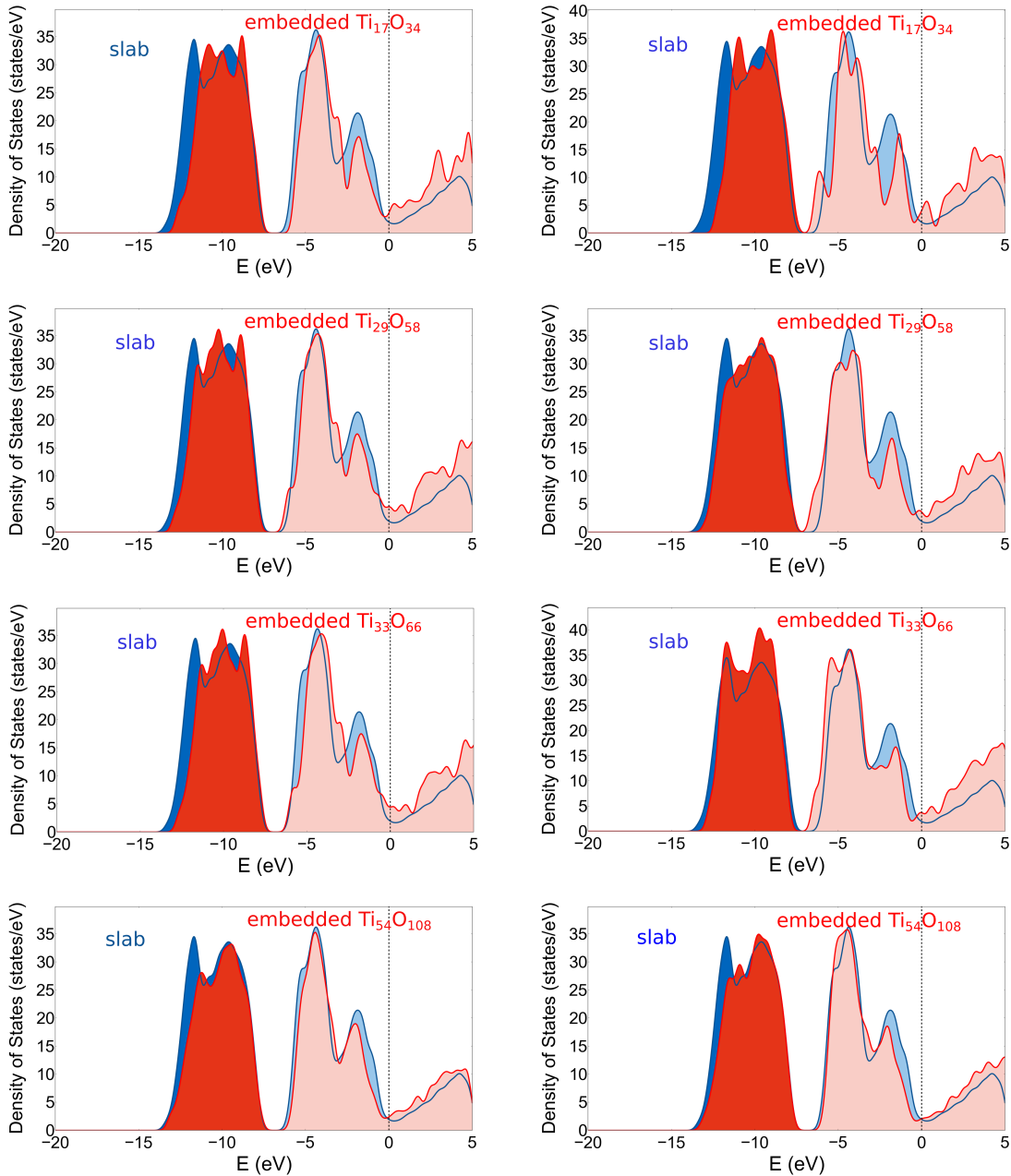


Figure 7.8: Total density of states with (right) and without (left) polarization response. The short-range parameters from Jentys and Catlow were used together with a cosh-spring for the oxygen core-shell interaction ($k=20$, $d=0.15$), which yield an acceptable description of the high frequency dielectric tensor ($\epsilon_{\infty}^a = 5.8$, $\epsilon_{\infty}^c = 9.8$).

7.4 Benchmark: Adsorption of small molecules

As a further benchmark test, the adsorption of small molecules on the surface, namely O, OH & OOH, is studied in the embedded cluster setup and compared to results from the corresponding periodic reference calculations. Adsorption of these radicals on rutile TiO₂ is not only a well studied system, because of their relevance in the photocatalytic watersplitting process, they also represent a wide range of the *chemical spectrum* due to their very different electronegativities, electronic structures and dipole moments.

The embedded cluster setup represents the low-coverage limit in that only a single molecule is adsorbed at a time, whereas the periodic setup corresponds to a much higher coverage by construction. There, every supercell hosts (at least) one adsorbate. In PBC, the low-coverage limit is therefore only approximately accessible. We determine the reference low-coverage adsorption energies through extrapolation of results from the (1 × 2), (2 × 4) and a (3 × 5) supercell.

The coverage, in general, also affects the adsorption geometry, both of the adsorbate as well as the substrate. To have a clear reference, the same adsorbate geometries for all supercell sizes and embedded cluster setups are used. Furthermore, relaxation of the surface upon adsorption is neglected. The effect of surface relaxation will be discussed in Chapter 8. Here, the adsorption geometries of the three adsorbates are determined⁷ in a 2×1 surface slab calculations. For the single molecule adsorption study in the QM/MM setup, one adsorbate is placed at the central five-fold coordinated titanium atom of the embedded TiO₂ cluster, in the slab-optimized geometry. To confirm stability of the adsorption geometry in the cluster setup, forces on the adsorbates in the QM/MM setup were calculated. Indeed, all forces were smaller than 10⁻³ eV/Å.

Computationally, surface chemical reactions are typically addressed through a thermodynamic approach [179–181]. For such approaches, accurate calculation of binding energies is of key importance. Hence, binding energies are the primary observable in this benchmark. The binding energies are computed as differences of total energies

$$E_b[X] = E^{\text{tot}}[X@TiO_2] - E^{\text{tot}}[TiO_2] - E^{\text{tot}}[X] \quad . \quad (7.2)$$

Here, $E^{\text{tot}}[X@TiO_2]$ and $E^{\text{tot}}[TiO_2]$ are the total energies of the TiO₂(110) surface with and without adsorbate X , respectively, and $E^{\text{tot}}[X]$ is the total energy of the isolated adsorbate. The accurate calculation of $E^{\text{tot}}[X]$ may be a challenge in DFT. For example describing the correct spin state of the free oxygen atom in vacuum is a well known problem of GGA-DFT. For this benchmark test, this is not a problem, as $E^{\text{tot}}[X]$ are identical for QM/MM and the slab.

In this test case, the adsorbing molecules are not charged. Thus the first nonvanishing interaction term between adsorbate and its copy in a periodic calculation is a dipole-dipole term. In the case of molecular orbitals of the adsorbate not overlapping with their periodic copy, the interaction is purely electrostatic and decays with $1/L^3$ [87], with L being box size of the periodic cell. Adsorption energies of one molecule per supercell are computed in the 2×1 and 4×2 supercell, and extrapolated to the low coverage limit according to the expected $1/L^3$ behaviour. Extrapolated values match those from a very extensive 5×3 supercell. These values are now the reference for the embedded cluster study.

As can be seen in Tab. 7.2, the adsorption energies of O and OH are well converge red with respect to the unit cell size in the 2×1 supercell. In other words, adsorbed O and OH molecules

⁷The adsorption site is the fivefold coordinated titanium atom. We start from the adsorption geometry documented by Valdéz *et al.* [178], and reoptimize the structure. However, the adsorption geometry here is not important on an absolute scale. It merely needs to be identical in both approaches.

do not interact significantly already in the 0.5 ML coverage. Being the largest adsorbate with also the highest dipole moment, the interaction of adsorbed OOH is apparently of more long-range character.

Again, references for a free cluster in vacuum and the embedded cluster without PPs are considered. Although, both setups were not even remotely able to reproduce the DOS from the slab calculation, the effect on adsorption energies of such an incomplete setup is not known *a priori*. Binding energies calculated for both setups using a $\text{Ti}_{17}\text{O}_{34}$ cluster do not reproduce the slab results. Compared to the PBC reference the free cluster surprisingly achieves good agreement of adsorption energies for O and OH. However, the description of the OOH molecule deviates by almost 300 meV and is even predicted to be unbound. Results from the embedded cluster without pseudopotentials deviate even more dramatically. Here, adsorption energies are consistently overestimated by up to 1 eV compared to the PBC reference as can be seen in Tab. 7.2. This reflects aforementioned electron depletion (see Fig. 7.4) within the central region of the cluster due to charge spill-out at the cluster region boundary. Therefore, binding energies are affected differently, depending on the number of electrons in the adsorbing molecule, with a maximum derivation from slab calculations for OOH.

E_b	O	OH	OOH
PBC			
(2×1)	-0.46	-0.53	-0.17
(4×2)	-0.46	-0.52	-0.26
(5×3)	-0.47	-0.52	-0.27
free cluster			
$\text{Ti}_{17}\text{O}_{34}$	-0.52	-0.51	0.01
QM/MM without PP			
$\text{Ti}_{17}\text{O}_{34}$	-0.58	-0.76	-1.28

Table 7.2: Calculated rPBE binding energies (in eV) of O, OH and OOH on the rutile $\text{TiO}_2(110)$ surface. Compared are results from slab calculation with different unit cells, with a free cluster calculation and the embedded cluster without using PPs.

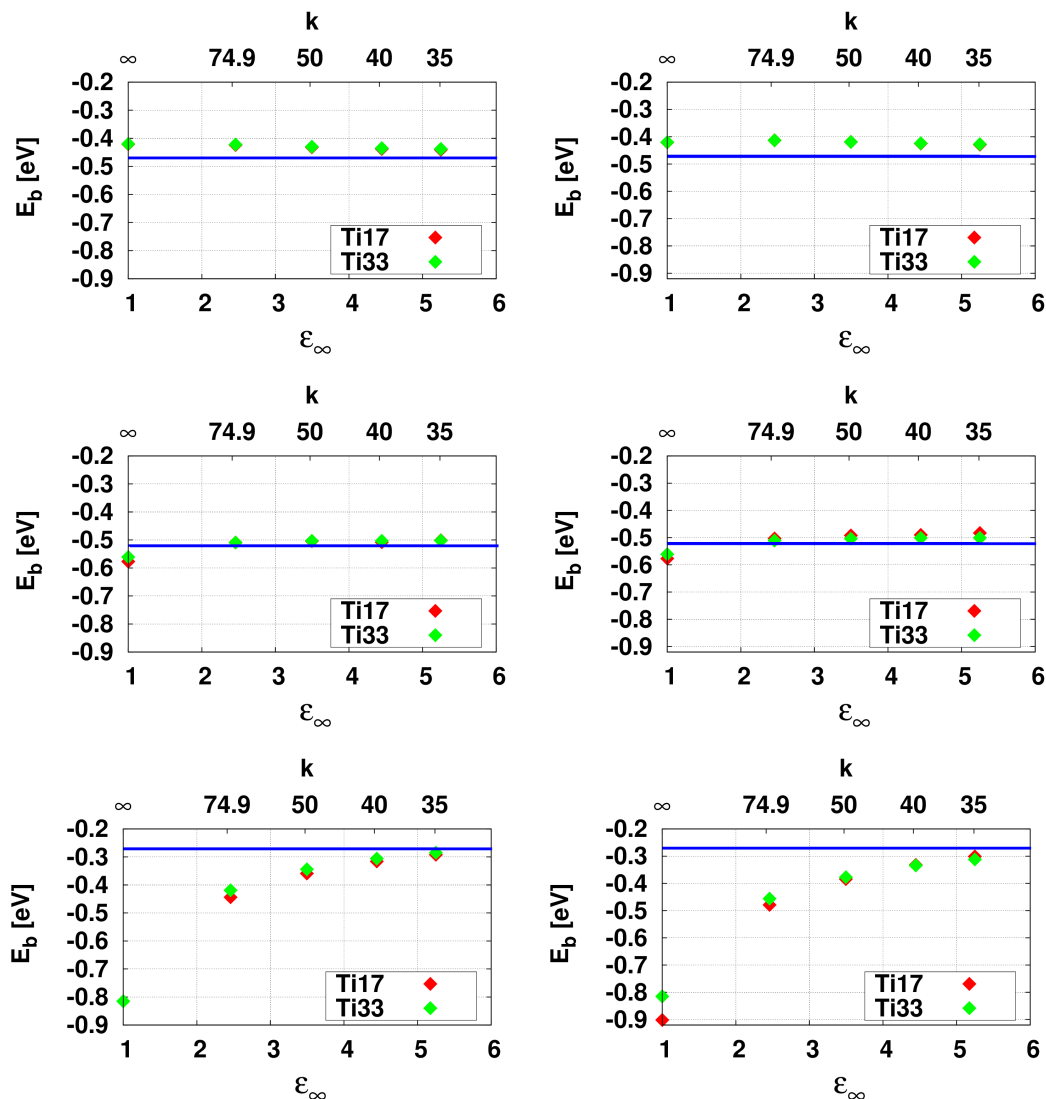


Figure 7.9: Binding energy of O (top), OH (middle) and OOH (bottom) with (right) and without (left) self-consistent polarization response. The $\text{Ti}_{17}\text{O}_{34}$ and the $\text{Ti}_{33}\text{O}_{66}$ cluster were embedded in the force field by Jentys and Catlow with modified spring constant k . The blue lines correspond to respective results from the 5×3 supercell calculation.

Finally, the adsorption energies are calculated in the embedded cluster setups. For that the adsorption geometries were taken from the reference slab calculations, and added to the clean embedded cluster setup from last chapter.

As discussed above, the high-frequency dielectric constant has a significant effect on the overall level alignment through the long-range part of the electrostatic background potential of the crystal. This long-range part corresponds to a constant shift in the potential. Adsorption energies are, however, invariant to a constant shift in potential and thus independent of the absolute level alignment. However, the high-frequency dielectric constant also induces short-range contributions through the intrinsic polarization, which can couple to electrostatic moments of the adsorbates. It is, hence, revealing to study the adsorption energies in the embedded cluster approach with different high-frequency constants for the MM region. For this we used again the force field parameters by Jentys and Catlow and varied the spring potential. Convergence with

respect to the QM cluster size is tested by comparing adsorption energies from the $\text{Ti}_{17}\text{O}_{34}$ and $\text{Ti}_{33}\text{O}_{66}$ cluster.

Resulting binding energies for the different cluster embedding setups are summarized in Fig. 7.9. As can be seen, adsorption energies converge rapidly with cluster size and are converged to within a few meV already for $\text{Ti}_{17}\text{O}_{34}$ cluster, at least if surface relaxation is neglected. This ultimately allows — in terms of computational cost — application of double-hybrid functionals, which will be discussed in Chapter 8.

Moreover, the self-consistent polarization response has only marginal influence on the adsorption energies. Thus, neglecting the polarization response is justified for adsorption studies, if QM cluster and adsorbates are charge neutral. The binding energies for O and OH depend only very little on the MM region and agree with the periodic reference within 60 meV for all choices of the spring potential. Here, the adsorption energy of O is systematically below the PBC reference. This is most likely due to difficulties of the description of the oxygen at the GGA-level of DFT, especially in PBC. The oxygen at the surface tends to be metallic even in the (5×3) supercell.

The binding energetics of OOH are much more sensitive to the MM region. Variation of the spring constant resulted in differences in binding energies of up to 700 meV for the strongest spring. However, if a spring potential is used which consistently reproduces the dielectric constant of the DFT calculation, also the binding energy of OOH matches the periodic reference result. As discussed before, the spring potential affects the ionizity of the MM background as oxygen shells tend to compensate the strong electrostatic potential of the Ti^{4+} cations. Formal charges lead to overpolarization at the QM region boundary, leading to slight electron depletion in the center of the QM cluster. Consequently, the level of depletion and, in turn the binding energy, correlates with the spring constant. Having the largest number of electrons OOH is again affected the most.

This is confirmed through a charge analysis, as it directly reveals how much electron density of the adsorbate is drawn into the substrate (or vice versa). Here, the Mulliken charge [161] of the three adsorbates in the embedded cluster calculation are compared to those of the slab reference. The Mulliken analysis integrates the charge from the density matrix, i.e. the population of molecular orbitals and their composition from atomic orbitals. This approach can lead to a strong dependence on the actual choice of basis set. Therefore, these numbers should be compared to results of other codes only with caution. However, as we use exactly the same basis set in the periodic as well as the cluster calculation, it is a valid means of benchmarking our solid-state embedding approach. Results for the embedded $\text{Ti}_{17}\text{O}_{34}$ and the $\text{Ti}_{33}\text{O}_{66}$ clusters are compiled in Fig. 7.10.

The Mulliken charges of the adsorbed molecules are converged to within 0.01 e already for the $\text{Ti}_{17}\text{O}_{34}$. Moreover, self-consistent polarization response does not have a notable influence on the charges. Adsorbates are systematically more cationic in the embedded cluster approach, whereas again significant dependence on the spring potential can be observed.

These results reinforce the analysis that formal charges, which correspond to a spring of $k=\infty$, yield a much too *ionic* embedding potential, and confirms the interpretation of the adsorption and its dependence on the spring potential. By using a weaker spring potential much of the ionic character can be reduced, leading to a very good agreement with periodic reference calculations. Differences were in the order of 0.01 e for the oxygen radical and even an order of magnitude less in the case of OOH. Again the spring potential leading to the best agreement with the calculations corresponds to a high-frequency constant which roughly matches the DFT calculations.

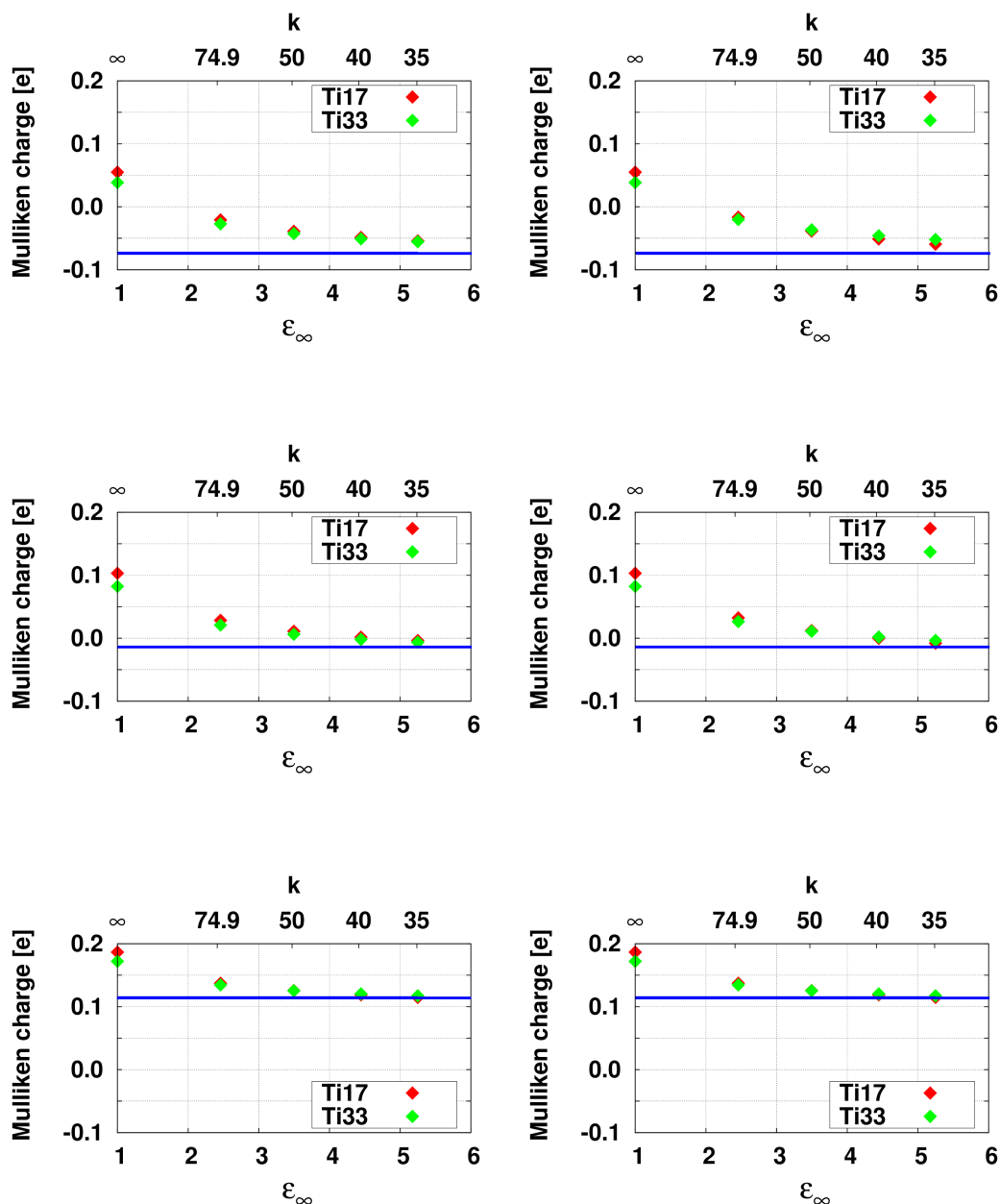


Figure 7.10: Mulliken charges of adsorbed O (top), OH (middle) and OOH (bottom) with (right) and without (left) self-consistent polarization response. The $\text{Ti}_{17}\text{O}_{34}$ and $\text{Ti}_{33}\text{O}_{66}$ clusters were embedded in the force field by Jentys and Catlow [175] with modified spring constant k . Blue lines correspond to respective results from the 5×3 supercell calculation.

One further observable to characterize bonding is the hybridization of the molecular orbitals with those of the substrate. Here we discuss this in terms of the relative ⁸ energetic position of the frontier orbitals (HOMO) in the compound system (cluster with adsorbate), which is most involved in the chemical bonding. In the periodic reference calculation, the valence band maximum strongly depends on the coverage of adsorbates, as can be seen in the left plot in Fig. 7.11. In the QM/MM approach, the dependence on the cluster size is comparatively small.

⁸Relative means the difference with respect to the position of the HOMO of the clean surface.

All clusters yield a consistent picture for each molecule, suggesting consistent description of hybridization through bonding. Already the numbers for the $\text{Ti}_{17}\text{O}_{34}$ cluster compare very well with those from the 5×3 reference, when using a spring potential with appropriate dielectric constant for the embedded cluster approach.

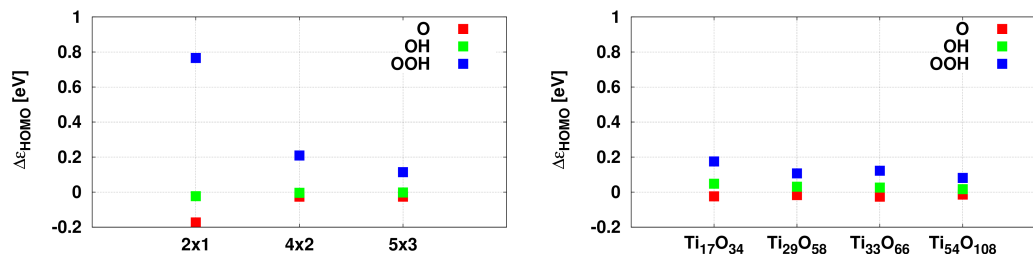


Figure 7.11: Energetic position of the HOMO for the O, OH and OOH, relative to the HOMO energy of the clean surface, as a function of the coverage. Calculations were performed in different supercells (left) and with different embedded cluster sizes (right) using the force field by Jentys and Catlow with a spring constant of $k=35$. Self-consistent polarization is neglected.

Are *nonlocal* pseudopotentials really necessary?

Replacing nearby embedding titanium MM point charges with pseudopotentials was proven necessary to reproduce the DOS and the adsorption energies. In fact, the DOS could already be reproduced on simple removing the Coulomb singularity. We test this by using only the local part of the pseudopotential and neglecting nonlocal projector functions.

E_b	O	OH	OOH
$\text{Ti}_{54}\text{O}_{108}$			
with nonlocal	-0.46	-0.52	-0.32
$\text{Ti}_{17}\text{O}_{34}$			
with nonlocal	-0.45	-0.50	-0.33
without nonlocal	0.01	-0.49	-0.26

Table 7.3: Comparing binding energies (in eV) for embedding with local and fully nonlocal pseudopotentials. The embedded $\text{Ti}_{54}\text{O}_{108}$ cluster serves as reference for the low coverage limit.

However, when comparing binding energies, again of O, OH and OOH, unsystematic deviations from the reference calculation with full nonlocal pseudopotentials are obtained (see Table 7.3). This may reflect the different electrostatic electron affinities of the different radicals. The system involving the oxygen radical, being the chemically most reactive one, shows largest deviations, of almost 0.5 eV. Neglecting the nonlocal PP part does not affect the multiplicity, however. Spin states are the same as in the calculation with full nonlocal pseudopotential. Thus, the above results clearly show that for a generally valid embedding scheme it is not enough to simply remove the Coulomb singularities at the QM region boundary, but also to reproduce the correct scattering behaviour through the use of nonlocal pseudopotentials.

Part IV

Applications

In the last part of this thesis, we present several applications of our QM/MM implementation. We studied three important materials of heterogeneous catalysis, namely TiO_2 , MgO and ZSM-5.

At first, we investigated the oxygen evolution reaction at the TiO_2 (110) surface, one of the two half reactions of photocatalytic watersplitting [178, 182]. Here, we study the performance of various levels of theory from GGA up to double-hybrid functionals, exploiting the efficiency of such methods through our embedded cluster approach in combination with numerical atomic orbitals. Parts of this chapter have been published in the *Journal of Chemical Physics* [128].

As a second application, the bridging oxygen vacancy at the TiO_2 (110) surface in charge states 0, +1 & +2 is studied. In particular, we address the energetic position of the defect states, and the formation energies of the vacancy in its three charge states. Formation energies essentially determine the defect concentration which in turn regulates reactivity and conductivity of the TiO_2 surface. Most of the computational studies of electro- and photocatalytic application of TiO_2 focus on the pristine surface. Addressing defects in periodic boundary conditions requires very large surface supercells to suppress spurious finite site effects. This is even aggravated in the case of charged defects. Additionally, treatment of electronic exchange-correlation on the hybrid functional DFT level is necessary to properly account for charge localization at the defect site. For periodic boundary conditions this results in CPU time and memory demands which still exceed most available supercomputing resources. In our embedded cluster approach, we again exploit efficient access to hybrid functionals and address the surface vacancy also in the charged states for the first time. A publication of this chapter is currently in preparation.

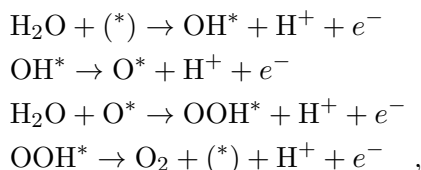
As a further project, stability of oxygen vacancies and interstitials on corner and step sites of the MgO crystal in their various charge states are addressed with *ab initio* thermodynamical methods. Not being limited by long range periodicity, the QM/MM approach allows for most efficient access to such aperiodic systems. With the help of global force field optimizations, we find a set of interatomic potentials which simultaneously reproduces structural parameters and both the high frequency and static dielectric constant. This allows to directly account for the full dielectric response in the MM region, which is not possible in TiO_2 . This project is conducted in collaboration with Saswata Bhattacharya, Luca Ghiringhelli, Sergey Levchenko and Matthias Scheffler from the Fritz-Haber Institute in Berlin. A joint publication for submission to *Physical Review Letters* is currently in preparation.

In the last chapter of this part, we apply solid state embedding in a porous material, namely ZSM-5 zeolites. For such a material, a slightly different embedding protocol is required in the form of cluster termination with hydrogen. To establish the accuracy of such an approach we initially performed benchmarks against periodic reference calculations. Then we address the $\text{Fe}^{3+/2+}$ reduction potential of Fe doped ZSM-5 and the catalytic reduction of methanol to ethylene in the ZSM framework. The latter project is ongoing work supporting experiments performed by the group of Johannes Lercher (TUM).

8 Photocatalytic watersplitting at the pristine TiO₂ surface - Dependence on the xc-functional

Among many other applications, the TiO₂ surface is particularly known for its ability to oxidize water using light [183–185]. The desire for a molecular-level understanding of this intriguing property motivates detailed mechanistic studies unraveling the chemical steps involved. Of the various known phases and many different facets the rutile (110) surface has been studied most thoroughly [183, 186], with recent theoretical work considering reaction mechanisms including an OOH intermediate on a defect-free surface [178, 187]. Characteristically for the field of surface catalysis, these calculations were performed at the semi-local DFT level, specifically with the rPBE [55] functional. Arguably because of its acceptable description of hydrogen bonds, this functional has been frequently employed in the context of water dissociation and photocatalysis at TiO₂ [178, 182, 188–190], but of course as a GGA functional it still suffers from the well-known electron delocalization problems [191]. The possibility to perform hybrid and double-hybrid level calculations efficiently with our QM/MM setup offers therefore an ideal platform to assess how much these shortcomings of GGA level DFT affect the predicted reaction energetics. Along these lines, we aim to disentangle these effects into electronic and structural contributions. First, we construct a setup with GGA lattice parameters and bond distance of the adsorbed molecules. In this geometry, binding energies are computed with different xc-treatment. Second, we construct a setup with lattice parameters and bond distances optimized on the hybrid functional level, and discuss the influence on the binding energies.

Following earlier theoretical work [178, 187, 192] we assume the water oxidation pathway at defect-free TiO₂(110) to proceed along four electron-coupled proton transfer steps:



where the asterisk stands for the five-fold coordinated Ti centers offered by the catalytic surface (*) and particles attached to them (e.g. O*), respectively. Central energetic quantities for this pathway are correspondingly the binding energies of the three reaction intermediates O, OH and OOH, defined as

$$E_b[X] = E^{\text{tot}}[X@\text{TiO}_2] - E^{\text{tot}}[\text{TiO}_2] - E^{\text{tot}}[X] \quad . \quad (8.2)$$

Here, $E^{\text{tot}}[X@\text{TiO}_2]$ and $E^{\text{tot}}[\text{TiO}_2]$ are the total energies of the TiO₂(110) surface with and without adsorbate X , respectively, whereas $E^{\text{tot}}[X]$ is the total energy of the isolated adsorbate.

In the last Section 7.4, the clean surface has been carefully benchmarked against reference slab calculations with the rPBE functional. We found that adsorption energies of the three

molecules addressed quickly converge with respect to the cluster size. In fact, already the Ti₁₇O₃₄ cluster (see Fig. 7.2) yields essentially converged binding energies. Hence, all calculations in this section are done with an embedded Ti₁₇O₃₄ cluster.

8.1 Electronic contributions

The dependence of the binding energies on the xc-functional is investigated with the embedded cluster constructed on the basis of optimized rPBE lattice positions, following the best-practice approach discussed in the previous Chapter. First, lattice parameters are optimized in a bulk unit cell (see Table 7.1). Based on these parameters, a 5 O-Ti₂O₂-O trilayer slab is constructed and fully optimized. The adsorption geometries are determined in a (1 × 2) supercell applying a (4 × 4 × 1) Monkhorst-Pack k-point grid [69]. For the latter, surface relaxation upon adsorption is neglected to suppress any dependence on the coverage.

A Ti₁₇O₃₄ cluster was constructed from the optimized surface supercell. Intrinsic polarization on the MM level, as described in the previous Chapter, was allowed for by applying the well-established polarizable TiO₂ forcefield from Ref. [175], where only the spring potential between oxygen shell and oxygen core has been modified to $V = kd^2(\cosh(\frac{r}{d}) - 1)$ with $k = 20 \text{ eV}/\text{\AA}^2$ and $d = 0.1 \text{ \AA}$. This improves the representation of the dielectric constant of the MM region when setting it up with the DFT lattice parameters, with high frequency dielectric constants ($\epsilon_\infty^a = 5.8$, $\epsilon_\infty^c = 9.8$) along axes a and c. For the neutral systems studied here, further geometry optimization and self-consistent polarization of the MM region in response to the adsorbates is neglected. The position of the adsorbates on top of the central fivefold-coordinated Ti site in the QM region, cf. Fig. 7.2, are taken from the periodic supercells.

At the hybrid and double-hybrid functional levels, identical spin states are obtained in corresponding QM/MM and slab calculations. At the semi-local level, which suffers significantly from self-interaction, this needed to be explicitly ensured by fixing the spin states to those of the higher-level calculations, i.e. doublet for OH and OOH, and triplet for O. This is an important issue, as most semi-local functionals yield the wrong spin-polarization for the O adsorbate, and already due to this result in a large deviation of the corresponding binding energy with respect to the higher-level calculations [192]. The *tier2* basis sets readily converge all E_b to within 10 meV at the semi-local and hybrid level, while at the double-hybrid level the valence-correlation consistent NAO-VCC-4Z basis set for all O atoms together with a counterpoise correction [193] was required to reach the same level of convergence.

In the last Chapter, the effect of the MM region and its intrinsic polarization of the electronic spectrum of the embedded cluster were discussed in detail. It was found, that an MM environment with oxygen shells fixed in the positions of ideal surface polarization allows for a very good reproduction of the surface band structure. This not only holds for occupied, but in particular also for the unoccupied bands. The latter do not contribute to the total energy on the GGA and hybrid level, however enter the PT2 term in the double-hybrid functional. In studying the differences in energy and electronic structure between functionals, we can therefore neglect an additional self-consistent polarization response of the MM region here.

Table 8.1 compiles the results obtained at GGA, hybrid and double-hybrid level. Generally, we observe a somewhat larger scatter among the three GGAs tested as compared to the group of hybrid and double-hybrid functionals. As commonly observed in literature [178, 195], in particular the PBE functional seems to be more on the overbinding side. Interestingly, hybrid and double-hybrid xc-functionals reduce the bond strength of the O adsorbate and increase the bond strength of the OOH intermediate as compared to the semi-local description. Together with its overall weaker binding, rPBE mimics this best, which to some extent seems to support

E_b	O	OH	OOH	E_b^{SHE}	O	OH	OOH
rPBE	-0.45	-0.49	-0.26	rPBE	4.80	2.43	4.60
BLYP	-0.60	-0.62	-0.30	BLYP	4.75	2.34	4.59
PBE	-0.71	-0.79	-0.43	PBE	4.90	2.34	4.61
B3LYP	-0.36	-0.56	-0.35	B3LYP	4.86	2.37	4.78
PBE0	-0.39	-0.64	-0.41	PBE0	4.92	2.36	4.86
HSE06	-0.41	-0.66	-0.43	HSE06	4.87	2.32	4.84
XYG3	-0.36	-0.64	-0.53	XYG3	4.88	2.39	4.89

Table 8.1: Calculated binding energies (in eV) of O, OH and OOH on the rutile $\text{TiO}_2(110)$ surface. Results are obtained for an embedded $\text{Ti}_{17}\text{O}_{34}$ cluster at different levels of theory (GGA, hybrid and double-hybrid), see text. The right hand table shows results referenced against the standard hydrogen electrode (SHE) following Eqs. (10-12) of Ref. [194].

the arguments made in its favor in preceding work at the semi-local level. The inclusion of PT2 correlation in the XYG3 double-hybrid functional primarily changes the most polarization-affected OOH binding compared to its parent B3LYP hybrid functional.

Notwithstanding, these differences are primarily due to the description of the bare radical in the gas phase, which is used as reference in the definition of E_b in Eq. 8.2 and which is, of course, most sensitively affected by a varying degree of electron localization achieved at the different xc-levels. To circumvent this, adsorption energies in photoelectrochemical calculations are often given with respect to the computational standard hydrogen electrode (SHE) [187]. The right hand table in Table 8.1 reproduces the same binding energies of the left table with respect to this reference and demonstrates that this indeed removes most of the scatter and leads to consistent trends at all xc-functional levels studied. Under the above described constraint that the GGA functionals are enforced to yield the correct spin polarization, our results thus suggest that despite the known electron localization problems, a description at the semi-local level seems indeed sufficient for computational screening work relying on trends and correlations between reaction intermediate binding energies [194, 196], rather than quantitative differences within 0.2 eV [194]. Of course, this may be quite different when addressing adsorption at defects, in charged states, or when calculating reaction barriers – with the present QM/MM-setup then forming an ideal tool to conduct higher-level calculations either directly for production or as reference.

8.2 Structural contributions

All single-point calculations in the last section were carried out on top of the geometry generated at the GGA level. Since the geometry is affected by the specific treatment of exchange-correlation, single point calculations should be performed on top of a self-consistent geometry. Geometry optimization on the hybrid level is, however, very expensive. Therefore, it is common practice to perform hybrid calculations on the geometry obtained on the GGA level.[197] Here, we will investigate how much the binding energies of O, OH and OOH depend on the underlying geometry. For this a $\text{Ti}_{17}\text{O}_{34}$ embedded cluster setup in the the consistent HSE06 geometry is generated, again following the best-practice strategy discussed in Chapter 7. Bulk unit cell optimization was performed with a *tier2* basis set, default *tight*-settings and a k-grid of $(6 \times 8 \times 8)$ for accurate sampling of reciprocal space. Obtained lattice constants were found to agree very well with experimental results (see Table 8.2).

Embedded clusters were again constructed from a fully optimized 5 trilayer supercell, which

was also used for the periodic benchmark calculations, and to determine the adsorption structures. Ultimately, we also want to account for relaxation of the QM-cluster upon adsorption. This necessitates specific force field optimization to reduce artifacts from coupling the QM and MM regions, in terms of structural stress and mismatch in dielectric properties. We apply our force field fitting program (see Appendix A) to generate parameters, which specifically match the observables from a HSE06 bulk unit cell calculation listed in Table 8.2.

It has been shown that larger ratios a/c are a peculiar difficulty for the type of force field applied [170]. Compared to rPBE the ratio of lattice constants a/c is smaller in the HSE06 bulk unit cell. This makes it easier to achieve matching structural parameters between force field and QM observables, facilitating more flexibility when optimizing the high frequency dielectric constant. The latter shows excellent agreement, both in absolute value and anisotropy.

Buckingham	A	ρ	C
$\text{O}_s - \text{O}_s$	23550	0.2113	38.55
$\text{Ti}_c - \text{O}_s$	1838	0.3207	26.62
cosh spring	k	d	O_c charge
$\text{O}_c - \text{O}_s$	23.67	0.098	0.9332

	a	c	ϵ_∞^a	ϵ_∞^c
MM	4.587	2.950	5.755	6.726
HSE06	4.588	2.950		
HSE06 ref. [177]	4.588	2.951	5.74	6.77
Exp.	4.587 [198]	2.954 [198]	6.84 [199]	8.43 [199]

Table 8.2: Force field parameters for HSE06 and their resulting unit cell properties, lattice parameters a and c as well as high frequency dielectric constants along the axes. Parameters were optimized under the constraint of $u = 0.305$, with u being the internal parameter of the rutile unit cell. Results are compared to experiments and another first-principle study also applying HSE06.

The generated force field parameters give indeed a very good description of the intrinsic polarization of the surface. This can be seen when comparing the density of states and specifically the position of the HOMO for the clean embedded cluster, with a reference slab calculation. The slab calculation predicts a band gap of 3.15 eV. The valence band maximum (VBM) lies at the -8.65 eV. Both values are significantly different from the rPBE results, and much closer to experimental values. The embedded $\text{Ti}_{17}\text{O}_{34}$ -cluster accurately reproduces the VBM with a HOMO position of -8.62 eV, as shown in Fig. 8.1. The band gap is slightly overestimated with 3.8 eV, reflecting known difficulties to accurately describe the unoccupied states in any finite cluster approach.

With sufficiently validated hybrid DFT embedding we now compare the consistent rPBE and HSE06 results, i.e. rPBE on top of the geometry optimized with rPBE (rPBE@rPBE) and HSE06 on top of the geometry optimized with HSE06 (HSE06@HSE06), respectively. The periodic reference for the HSE06 functional was calculated in a 2×1 supercell. A (4×2) supercell is in principle yet extremely costly in terms of computing time. One relaxation step takes 10'000 CPU*h on Intel Xeon Sandy Bridge-EP. However, we can estimate the finite size effect in the 2×1 supercell, on the level of rPBE (compare with Tab. 7.2). Thus, the finite size effect for OOH is approximately 100 meV and about 10 meV for O and OH. When adding this finite size correction to the slab results ($(4 \times 2) \cdot n$ in Table 8.3), the adsorption energies show very good

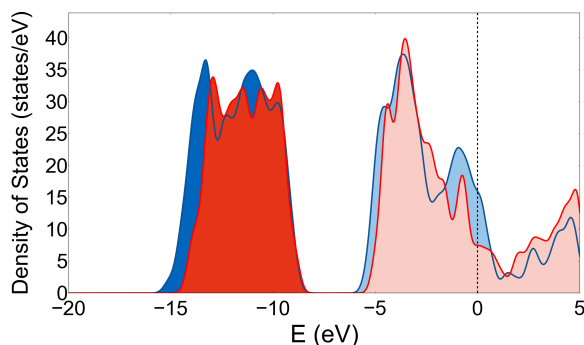


Figure 8.1: Density of states (DOS) of the ideal $\text{TiO}_2(110)$ surface as calculated with the embedded $\text{Ti}_{17}\text{O}_{34}$ cluster (red) and with a supercell geometry (blue). The valence band maximum is used as zero reference and filled states are depicted in darker color. A Gaussian smearing ($\sigma = 0.1$) is applied.

E_b	O	OH	OOH
PBC (2×1)			
rPBE@rPBE (2×1)	-0.46	-0.52	-0.26
HSE06@HSE06 (2×1)	-0.64	-0.67	-0.39
HSE06@HSE06 (4×2)*	-0.64	-0.66	-0.49
QM/MM			
rPBE@rPBE	-0.45	-0.49	-0.26
HSE06@rPBE	-0.41	-0.66	-0.43
HSE06@HSE06	-0.64	-0.71	-0.53

Table 8.3: Binding energies (in eV) of O, OH and OOH with different underlying geometries, without relaxation upon adsorption. An embedded $\text{Ti}_{17}\text{O}_{34}$ cluster represents the QM region in the QM/MM approach. Slab calculations with the HSE06 calculation were performed on a 2×1 supercell. Finite size effects are estimated from rPBE results, adding up to results labeled (4×2)* (see text).

agreement with the embedded cluster calculation.

Slab and embedded cluster calculations show a consistent picture: all adsorbates bind stronger when using the HSE06 functional as can be seen in Table 8.3. This is either due to the differences in the electronic levels or changes in the underlying geometry. These two effects can be disentangled when applying the HSE06 on the rPBE geometries. For the OH and OOH molecule the difference is mostly due to differences in the electronic structure (≈ 200 meV). On the other hand, in the case of the oxygen radical, the situation is reversed. There, differences are mostly due to changes to the geometry, which stems from the inaccuracy of GGA functional when dealing with single oxygen atoms.

8.3 Conclusion

We addressed the oxygen evolution reaction on TiO_2 with different regularly used functionals up to the double-hybrid level. The level of xc-treatment affects binding energies though electronic as well as structural contributions. In order to disentangle these two contributions, we first

fixed the geometry and observed the electronic contribution by varying the xc-functional. Here, we found that all functionals applied predict free energies which agree within 200 meV, when referenced against the standard hydrogen electrode. For the latter, no reference calculations of molecules in vacuum are needed, removing the associated error. In particular, binding energies of O and OH are already well described on the GGA level. For the OOH molecular, however, hybrid functionals are required to achieve agreement with the double-hybrid reference calculation. We further investigated the structural contribution of the xc-functional to the binding energies. For that we calculated binding energies on top of the rPBE and HSE06 structure, using the same functional for the single-point calculation. We found that an inconsistent underlying structure can lead to errors of 200 meV, showing that the xc-treatment significantly affects the binding energies not only through electronic contribution but also through changes in the geometry.

In all cases, the scatter of binding energies due to different xc-treatment of different structures were significantly larger than possible inaccuracies induced through the solid state embedding approach.

9 Surface oxygen vacancy at the TiO₂ rutile surface

As discussed in the previous chapter, the TiO₂ surface is particularly known for its ability to photocatalytically split water [183–185]. So far, especially theoretical studies have mostly focused on idealized, defect free model systems, where the reaction takes place on a stoichiometric surface. Initial results seemed to indicate that such a perfect surface is able to oxidize water—the generally agreed on determining half-reaction—with photo-generated electron-holes [178]. Yet, experimental evidence [186, 200–203] and indeed very recent theoretical studies [192] suggested that clean TiO₂ surfaces are thermodynamically unable to split water even considering the relatively high energy of photo-generated holes due to the wide band-gap of TiO₂ of 3.1eV.

Recent UHV STM experiments show that, rather than the pristine surface, defects associated to bridging oxygen vacancies are the active sites for the oxygen evolution [200, 204]. Furthermore, surface defects may act as charge trapping centers for photo-excited holes [205, 206], can lead to increased conductivity [6, 207] or may act as possible anchor sites for co-catalysts [208].

This demonstrates the importance of a fundamental and detailed understanding of catalyst structure and stoichiometry on a microscopic scale. Yet, in spite of their significance, very little is known about the thermodynamically favored charge state of the surface oxygen vacancies in TiO₂. This already starts with the fact that oxygen vacancy and the protonated bridging oxygen give almost indistinguishable signals in STM pictures.

For bulk defects, the current model is that upon oxygen vacancy (V_O^0) formation the two defect electrons reduce the two next neighboring titanium atoms (Ti^{4+}/Ti^{3+}), leaving an overall charge neutral vacancy complex or polaron [209]. The unpaired electron of the Ti^{3+} ion can be detected by means of electron paramagnetic resonance (EPR). Detection of Ti^{3+} ions has been, therefore equated to evidence for the charge neutral state of the oxygen vacancy. In 2009 Yang *et al.* further showed through EPS measurements that the V_O^0 and V_O^+ defect can be created from photoinduced electrons which are trapped in a V_O^{+2} [210]. This confirms that all three defect charge states play an important role in this material.

In this work, we study the oxygen vacancy in the charge states 0,+1 & +2 in terms of defect formation energies, and discuss the thermodynamic stability as a function of the oxygen partial pressure and doping conditions. Here, our QM/MM embedding infrastructure is of great advantage allowing efficient access to hybrid functionals, but also through the ability to explicitly account for long-range polarization effects of the charged defects.

9.1 Methodology

We describe the localized surface defects in a concentric solid-state embedding approach as sketched in Fig. 9.1. The immediate vicinity of the defect and the rehybridization induced through it is treated at the quantum mechanical (QM) level, and in particular through density-functional theory (DFT). This QM region is embedded into a much larger molecular mechanics (MM) region, which accounts for the longer-ranged dielectric properties of the TiO₂(110) surface

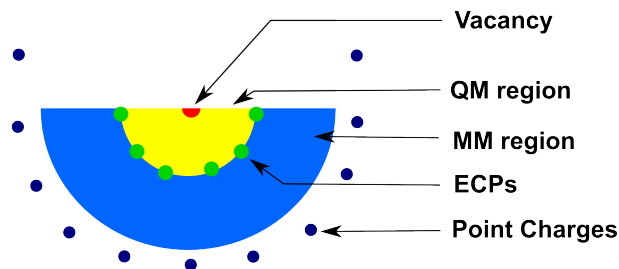


Figure 9.1: Schematic representation of the employed concentric solid-state embedding approach. A quantum-mechanical (QM) region hosting the oxygen vacancy is surrounded by a molecular mechanics (MM) region represented by a polarizable force field. Spurious charge leakage out of the QM region is prevented through a transition shell, in which cations are described with effective core potentials (ECPs). The full electrostatic potential of the infinite crystal surface is reproduced by placing point charges with fitted values around the MM region.

on the level of a polarizable force field. In a transition shell at the QM/MM boundary, cations are described by effective core potentials (ECPs) to prevent a spurious overpolarization of the electron density (aka charge leakage). These ECPs recover the long-range electrostatics of a point charge, but also have a repulsive short-range contribution which effectively mimics Pauli repulsion of core electrons. A final exterior shell of point charges is added at the outer boundary of the finite MM region. These point charges have values that are fitted to reproduce the full electrostatic potential of the infinite surface inside the QM region [115]. The following sections provide details of the DFT calculations, the force field parametrization, and the employed surface models within this overall approach.

Density-functional theory calculations

All DFT calculations have been performed with the full-potential, all-electron framework *FHI-aims* [127, 130]. Electronic exchange and correlation (xc) is treated at the level of screened hybrid-DFT, applying the HSE06 functional with the default mixing of 25% exact exchange and the default screening parameter of 0.2 \AA^{-1} [44]. Systematic test calculations showed that the *tier2* numerical atomic orbital basis set and the default *tight* settings for the atom-centered integration grids ensure a numerical convergence of the calculated defect formation energies within 10 meV. Spin polarization is included throughout. As ECPs for the transition shell we employ *FHI98PP*-generated [80] Ti^{4+} Kleinman-Bylander pseudopotentials [136] with non-local projector functions expanded up to the *d*-states. Further details of these potentials and their implementation into *FHI-aims* can be found in Ref. [128].

The finite clusters describing the QM region are constructed using optimized bulk lattice parameters and relaxed positions of surface atoms at the ideal $\text{TiO}_2(110)$ surface as obtained from periodic boundary condition supercell calculations. The calculated lattice parameters of rutile TiO_2 are listed in Table 9.1 and agree very well with preceding calculations at HSE06 level [177] and with experiment [198]. The surface calculations employed symmetric 5 O- Ti_2O_2 -O trilayer slabs, a $c(4 \times 2)$ surface unit-cell, a 40 \AA vacuum, and a $(4 \times 4 \times 1)$ Monkhorst-Pack k-point sampling [69]. The surfaces were fully relaxed until residual forces fell below 10^{-3} eV/\AA . Within periodic boundary conditions the zero reference of the electrostatic potential is not uniquely defined [211]. Notwithstanding, in surface calculations, the vacuum level can be assigned as the

	a [in Å]	c [in Å]	ϵ_o^a	ϵ_o^c	ϵ_∞^a	ϵ_∞^c
Exp. [159, 198, 199]	4.587	2.954	111	257	6.84	8.43
HSE06 [177]	4.588	2.951	278	402	5.74	6.77
HSE06 (this work)	4.588	2.951				
MM (this work)	4.587	2.950	3	12	5.76	6.73

Table 9.1: Rutile TiO_2 lattice constants a and c , as well as its static (ϵ_o^a , ϵ_o^c) and high-frequency (ϵ_∞^a and ϵ_∞^c) dielectric constants along the corresponding axes. Literature data from experiment [159, 198, 199] and DFT-HSE06 calculations [177] are compared against our own calculations at the DFT-HSE06 level and with the parametrized force field for the MM region (see text).

electrostatic potential at the middle of the vacuum separating the slabs. This provides access to the work function and the absolute position of the valence band maximum (VBM) at the surface, $\text{VBM}_{\text{surf}} = -8.2$ eV. To also access the bulk VBM position, VBM_{bulk} , we computed the layer-resolved Ti_{1s} core-level positions in an 11 trilayer thick (1×1) slab. These positions indicate a negligible band bending of the order of 30 meV for the here ideal stoichiometric $\text{TiO}_2(110)$ surface. This finding is confirmed by additional calculations with up to 27 trilayer thick slabs using the PBE xc functional [42]. For the purposes of this work we therefore use $V_{\text{bulk}} = V_{\text{surf}}$, and henceforth refer only to the VBM.

Force field parametrization

The HSE06 functional achieves a reliable account of the electronic contribution to the bulk dielectric properties of rutile TiO_2 , evidenced by the close match of the high-frequency dielectric constants ϵ_∞^a and ϵ_∞^c in Table 9.1. In contrast, it fails largely to describe the dominant lattice contribution additionally contained in the large static dielectric constants ϵ_o^a and ϵ_o^c , which has been traced back to its deficiencies in describing the intricate soft phonon modes of this material [177]. In order to achieve a seamless embedding the employed interatomic potential in the MM region should generally match the dielectric properties of the xc functional employed in the QM region. In the present case this would mean that the QM/MM approach then exhibits the same shortcomings with respect to the static dielectric properties; a point to which we will return in the discussion part below. In addition to the dielectric properties, the MM potential also has to match the QM lattice constants, to avoid artificial confinement stress in particular when geometric relaxation of the QM region is to be considered. These demands highly challenge any existing interatomic potential [170, 212]. In the present case, the situation is further aggravated by the necessity to saturate the QM region with norm-conserving pseudopotentials. For consistency, the remaining MM region then also has to employ formal charges +4 and -2 on Ti cations and O anions, respectively.

Oxygen ions in TiO_2 are highly polarizable, and are in fact intrinsically polarized in the rutile structure. Using as interatomic potential a simple rigid ion model with formal charges does not capture this physics. In the QM/MM context, such potentials lead to an overpolarization at the QM cluster region boundary and an overestimation of the electrostatic potential [163, 165]. In contrast, oxygen polarizability can be modeled efficiently within a polarizable shell-model [169], as has recently been demonstrated for TiO_2 by Scanlon *et al.* [158]. Here, the oxygen anion is described by two point charges: A “core” charge representing the nuclei and closed-shell core electrons, and a “shell” charge simulating the valence electron cloud. Mimicking electronic

polarizability, the oxygen core (c) and its shell (s) interact via a spring potential

$$V_{c-s} = k_{c-s} d_{c-s}^2 \left[\cosh \left(\frac{r_{c-s}}{d_{c-s}} \right) - 1 \right] , \quad (9.1)$$

where d_{c-s} is the distance between the core and shell charge, and k_{c-s} and r_{c-s} are parameters defining the potential. In this model [169], the dominant Coulomb interaction between different oxygen shells (s-s) and between oxygen shells and Ti point charges (s-Ti) is furthermore augmented by Buckingham potentials

$$V_{s-s} = A_{s-s} \exp \left(-\frac{d_{s-s}}{\rho_{s-s}} \right) - \frac{C_{s-s}}{d_{s-s}^6} \quad (9.2)$$

and

$$V_{s-Ti} = A_{s-Ti} \exp \left(-\frac{d_{s-Ti}}{\rho_{s-Ti}} \right) - \frac{C_{s-Ti}}{d_{s-Ti}^6} , \quad (9.3)$$

to provide some effective account of dispersive interactions and Pauli repulsion. Here, d_{s-s} and d_{s-Ti} are the distance between oxygen shells and between oxygen shell and Ti, respectively, and A , ρ and C are potential parameters. Restricting the interaction between MM Ti cations to the mere formal charge electrostatics, the model is thus defined through a set of nine parameters: [k_{c-s} , r_{c-s} , A_{s-s} , ρ_{s-s} , C_{s-s} , A_{s-Ti} , ρ_{s-Ti} , C_{s-Ti} , q_s], with a final parameter q_s for the charge on the oxygen shell.

For a seamless matching between QM and MM region we perform a global optimization of these force field parameters to yield bulk DFT-HSE06 lattice and dielectric constants. Specifically, we employ a differential evolutionary algorithm [150] from the Python package *Inspyred 1.0* [151] to minimize the dimensionless cost function (see Appendix A)

$$F = \sqrt{\sum_i \left(\frac{L_i^{\text{MM}} - L_i^{\text{DFT-HSE06}}}{L_i^{\text{DFT-HSE06}}} \right)^2} \quad (9.4)$$

with $L_i = [a, c, \epsilon_o^a, \epsilon_o^c, \epsilon_\infty^a, \epsilon_\infty^c]$ and using the DFT-HSE06 values from ref. [177] (cf. Table 9.1), as target values. In the corresponding MM calculations, the internal lattice parameter u is always kept at its DFT-HSE06 value (0.305), and the static and high-frequency dielectric tensors are determined from the second derivative matrix of all MM particles or only of the shells, respectively [122].

	k_{c-s} [in eV/Å ⁻²]	r_{c-s} [in Å]	q_s [in e]
	23.67	0.098	-2.9332
	A [in eV]	ρ [in Å]	C [in eV Å ⁶]
s - s	23550	0.2113	38.55
s - Ti	1838	0.3207	26.62

Table 9.2: Interatomic potential parameters, optimized to reproduce the bulk TiO₂ DFT-HSE06 lattice parameters and high-frequency dielectric constants, see text.

The best parameter sets generated this way still exhibit rather large errors, with $F \geq 0.33$. They typically exhibit substantial deviations in the lattice constants. This agrees not only with the observation of Catlow *et al.* [170] who assigned the inability to reproduce both lattice and static dielectric constants to missing many-body terms in this class of interatomic potentials. It is also consistent with the finding of Lee *et al.* [177] that deficiencies in the description of

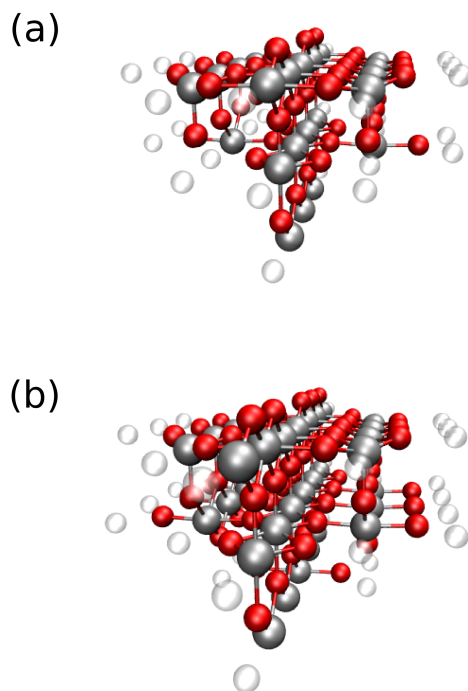


Figure 9.2: Perspective view of the employed clusters: (a) $\text{Ti}_{22}\text{O}_{43}$, (b) $\text{Ti}_{32}\text{O}_{63}$, each exhibiting a surface O vacancy in their central bridging O atom row. Ti atoms are shown as large white spheres, O atoms as small red spheres, and semi-transparent gray spheres mark the positions where ECPs represent the immediately surrounding Ti-cations.

the TiO_2 soft phonon modes (and therewith static dielectric constants) can be effectively cured through the use of different lattice constants. In the present context, an accurate representation of the lattice constants is indispensable though to avoid artificial stress on the QM region. We therefore removed the static dielectric constants from the training set and immediately obtain parameter sets with significantly reduced cost functions. The best parameter set exhibits an $F = 0.007$ and is used in all QM/MM calculations reported below. It is compiled in Table 9.2 and yields highly accurate lattice parameters and high-frequency dielectric constants as shown in Table 9.1. Notwithstanding, its largely erroneous representation of the static dielectric properties (which is about as wrong as the one obtained with HSE06 itself) is a concern and we discuss in Section III how this is addressed in our defect calculations.

QM/MM setup

In order to assess the convergence with respect to the employed QM region all calculations are done for a sequence of two embedded cluster models, originally suggested by Ammal and Heyden [164]. As shown in Fig. 9.2, both clusters, $\text{Ti}_{22}\text{O}_{43}$ and $\text{Ti}_{32}\text{O}_{63}$, are centered on a bridging oxygen row, from where the central O atom will be removed to create the surface vacancy. Only the smaller cluster is of approximately hemispherical shape, while the $\text{Ti}_{32}\text{O}_{63}$ is rather hemi-ellipsoidal, owing to the specifics of the rutile structure. Each cluster is embedded into an MM region that extends hemispherically up to a constant outer radius of 25 Å. For the smaller cluster this translates to a total number of 3029 MM atoms, while for the larger one this yields 2999 MM atoms. Every MM cation within 6 Å vicinity of the QM cluster is

replaced by ECPs to suppress spurious charge leakage out of the QM region. All MM cores are placed at positions according to those of the fully relaxed DFT supercell reference calculation for the stoichiometric TiO₂(110) surface. All O shells are initialized to the fully relaxed state within a corresponding MM supercell reference calculation with the MM cores at exactly the same positions. Thus, an initial guess for the MM region is the fully *intrinsically polarized* surface as discussed in Chapter 7. A final exterior shell of 64 point charges around the MM region is then added, with charges fitted to reproduce the full electrostatic embedding potential of an infinite TiO₂(110) surface [115]. Finally, for every QM cluster all MM shells and QM atom positions are fully relaxed. This setup defines what will henceforth be referred to as the ideal TiO₂(110) surface. The surface defect setups are created from this reference setup, either without subsequent geometry relaxation ("non-relaxed" geometries) or with full geometry relaxation of all QM atoms except those at the QM region boundary until residual forces are below 10⁻³ eV/Å ("relaxed" geometries).

Test calculations increasing the outer radius of the MM region up to 30 Å show full convergence of the formation energy and electronic structure in the case of the neutral defect. In case of a net-charged QM region the polarization response is much longer ranged though ($\propto q/(\epsilon R)$). Fortunately, the missing polarization energy outside of the finite MM region can be reliably captured through an analytical correction. For a hemisphere with radius R in a continuum with a dielectric constant ϵ and carrying a charge q at its center this analytic correction can be derived as [115] (cf. Section 3.5)

$$\Delta E_{\text{pol}}(q) = -\frac{q^2}{2R} \frac{\epsilon - 1}{\epsilon + 1} . \quad (9.5)$$

Using the high-frequency dielectric constant in this expression as further discussed below, we validated that after a corresponding post-correction also the formation energies of charged defects are fully converged with respect to the size of the MM region. Technically, we hereby use as isotropic dielectric constant the average over the diagonal entries of the bulk dielectric tensor, $\epsilon = 1/3(2*\epsilon_{\infty}^a + \epsilon_{\infty}^c)$. As radius R we simply set the outer radius of the MM region and variations of R by ± 1 Å have a negligible effect on the calculated formation energies. As an approximate method we also use the analytical correction directly outside the QM region (*vide infra*). Here the choice of the radius is more critical and we determine it by measuring the semi-principal axes of the hemi-ellipsoid defined by the atomic positions of the QM cluster. R is then taken as that of a hemisphere with identical volume. Uncertainties of $\pm 5\%$ in the thus determined radius translate in this case into an uncertainty of ± 0.2 eV for $E(\text{V}_{\text{O}}^{+2})$ and of ± 0.05 eV for $E(\text{V}_{\text{O}}^{+1})$.

The actual QM/MM calculations for the thus defined setup are performed within the *ChemShell* environment [115, 120] with the interface described in detail before [128]. We specifically use *GULP* [122] for the MM force calculations and the *DL-FIND* routine [121] for the geometry optimizations. Self-consistent polarization, a.k.a. shell optimization, within the MM region as a response to an updated QM geometry is hereby calculated in an inner loop of the optimization process.

Defect formation energies

Neglecting vibrational entropic contributions in the solid state and neglecting defect-defect interactions in the dilute limit we define the formation energy to create a surface O vacancy in charge state q as [213]

$$\begin{aligned} \Delta E^{\text{f}}(\text{V}_{\text{O}}^q) &= E(\text{V}_{\text{O}}^q) - E(\text{TiO}_2(110)) + \\ &+ \mu_{\text{O}} + qE_{\text{F}} + \Delta E_{\text{pol}}(q) . \end{aligned} \quad (9.6)$$

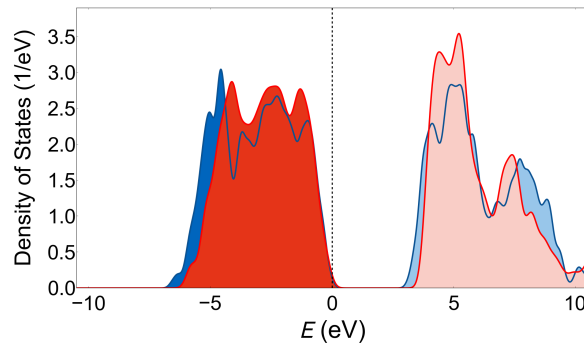


Figure 9.3: Density of states (DOS) of the ideal $\text{TiO}_2(110)$ surface per TiO_2 formula unit as calculated with the embedded $\text{Ti}_{32}\text{O}_{66}$ cluster (red) and with a supercell geometry (blue). The valence band maximum is used as zero reference and filled states are depicted in darker color. A Gaussian smearing ($\sigma = 0.1$) is applied.

Here, $E(\text{TiO}_2(110))$ and $E(\text{V}_\text{O}^q)$ are the total energies of ideal $\text{TiO}_2(110)$ and of $\text{TiO}_2(110)$ with the defect as obtained from our QM/MM calculations, respectively. μ_O is the chemical potential of oxygen and E_F is the Fermi energy. In our sign convention a positive formation energy implies a cost to create the defect. Correspondingly, the charge state exhibiting the lowest formation energy will be the thermodynamically stable state.

μ_O represents the energy of the reservoir where the O atom that is removed from the crystal is placed into. It is generally a variable, e.g. dependent on temperature and O_2 pressure, if the reservoir is a surrounding gas phase. Limits for μ_O can, however, be derived [214]. In the extreme O-rich limit

$$\mu_\text{O}(\text{O} - \text{rich}) = 1/2E(\text{O}_2) \quad , \quad (9.7)$$

with $E(\text{O}_2)$ the total energy of an isolated O_2 molecule. The opposite O-poor (Ti-rich) limit can be assessed from the stability condition of bulk TiO_2 against decomposition into Ti_2O_3 , $\mu_\text{O} > -\Delta E^\text{f}(\text{Ti}_2\text{O}_3) + 2\Delta E^\text{f}(\text{TiO}_2)$, where $\Delta E^\text{f}(\text{Ti}_2\text{O}_3)$ and $\Delta E^\text{f}(\text{TiO}_2)$ are the formation energies of bulk Ti_2O_3 and TiO_2 , respectively. At the HSE06 level this yields [215]

$$\mu_\text{O}(\text{Ti} - \text{rich}) = \mu_\text{O}(\text{O} - \text{rich}) - 4.07\text{eV} \quad . \quad (9.8)$$

The Fermi energy E_F is the energy of the reservoir where electrons released from the charged defects move to. We use the valence band position as zero reference. To obtain a better error cancellation, we specifically use for every QM cluster size the VBM_surf position at the ideal surface that is calculated with the same cluster size. Also E_F is a variable that can e.g. be changed through doping. Below we correspondingly report results up to $E_\text{F} = 3.36\text{eV}$, which corresponds to the calculated bulk TiO_2 band gap at the HSE06 level.

This value agrees well with preceding calculations at the HSE06 level (3.36 eV [216], 3.39 eV [217]), as does the calculated absolute VBM position, which we find at -8.2 eV.

9.2 Results

$\text{TiO}_2(110)$ electronic structure

We begin our investigation by demonstrating the high quality representation of the surface electronic structure obtained with our QM/MM setup, which could generally not be achieved

	Self-consistent MM electr. polarization		
	$\text{Ti}_{22}\text{O}_{43}$	$\text{Ti}_{32}\text{O}_{63}$	Slab
V_{O}^0	5.60	5.65	5.59
V_{O}^{+1}	2.70	2.87	
V_{O}^{+2}	2.99	3.25	
	Analytic correction for electr. polarization		
	$\text{Ti}_{22}\text{O}_{43}$	$\text{Ti}_{32}\text{O}_{63}$	
V_{O}^0	5.61	5.66	5.59
V_{O}^{+1}	2.69	2.87	
V_{O}^{+2}	2.99	3.25	

Table 9.3: Unrelaxed surface defect formation energies in the oxygen-rich limit and for a Fermi-level position at the VBM. Shown are results for the two different QM clusters and, in the case of the neutral defect, from the supercell reference calculation. Upper rows correspond to a QM/MM setup, in which the electronic polarization response to the defect is treated through self-consistent relaxation of the MM shells. Lower rows correspond to a QM/MM setup, where this response is approximately obtained through an analytical polarization correction approach (see text).

without the consistent parametrization of the MM potentials. Figure 9.3 compares the density of states (DOS) for the ideal $\text{TiO}_2(110)$ surface obtained with the embedded $\text{Ti}_{32}\text{O}_{66}$ cluster against the results from the slab reference calculation. Good agreement is achieved for both filled and empty states. Furthermore, the agreement extends not only to the band gap — i.e. relative difference of VBM and conduction band minimum (CBM) position — or to the width of the occupied band. Both are reproduced within 0.2 eV and 0.5 eV, respectively.

Indeed, also more subtle features within the bands are properly reflected in our embedding calculations. Equivalent findings are obtained for the neutral defect, where a straightforward comparison to supercell calculations is also possible. For both the ideal and the neutral defect case the DOS calculated with the smaller QM clusters also agrees well with the reference calculations. Due to the much smaller number of electrons, intra-band features are slightly different, but the band gap or the width of the occupied band varies each time by less than 0.4 eV.

Formation energies of unrelaxed vacancies

For a systematic assessment of the convergence of the defect formation energies with respect to the size of the QM region we concentrate on the $\Delta E^f(V_{\text{O}}^q)$ in the O-rich limit and using the VBM as Fermi-level position. Table 9.3 compiles the corresponding defect formation energies computed with both QM clusters, when initially not considering geometric relaxation due to the creation of the surface vacancy. In this particular case, neither the QM atoms nor MM cores are allowed to move and, correspondingly, the deficiency of the MM potential with respect to the lattice polarization as expressed by the largely wrong static dielectric properties does not matter. Additionally included in the table is the reference value for the neutral defect as obtained from supercell calculations. As the O shells can self-consistently adapt to the created defect, the full electronic polarization response of the material is accounted for within the MM region. Outside the MM region this is captured through the analytical correction $\Delta E_{\text{pol}}(q)$, cf. Eq. (9.5). The data reveals good convergence with respect to the size of the QM region, even for the doubly charged surface defect where the polarization response of the material is largest. Already the far-field $\Delta E_{\text{pol}}(+2)$ ($\Delta E_{\text{pol}}(+1)$) alone amounts to -1.95 eV (-0.49 eV),

which highlights the necessity to use a dedicated polarizable embedding scheme to reliably determine the defect formation energies of charged defects. Comparing the values for both clusters shows that formation energies to a minor extent depend on the shape of the cluster, which is more pronounced for the charged defects. However, as this occurs also for the neutral cluster it indicates that the shape not only affects the long-range polarization, but also the electronic structure in the QM cluster. The larger cluster has a more elliptical shape exhibiting a larger surface at the QM/MM interface, and particular a larger surface to volume ratio. This allows for more interaction between the QM and MM region, and is slightly more influenced through imperfect QM/MM coupling. The neutral defect has also been addressed in a reference slab calculation again neglecting relaxation. The calculated formation energy agrees very well already for the small cluster, showing that the electronic effects of defect formation are already well captured within there.

Table 9.3 also compiles results obtained with a more approximate method, where the entire electronic polarization response of the material is accounted for through the analytic correction equation (Eq. 9.5). Here, the O shells in the MM region are not allowed to relax after the creation of the defect. Instead, the analytical correction equation is employed with a radius R that no longer corresponds to the outer radius of the MM region, but to the outer radius of the QM cluster. This method is numerically more advantageous as it does not need to achieve self-consistency between the MM shell polarization and the QM cluster. On the other hand, it is more approximate, as it describes the polarization only at the isotropic continuum level. Also the outer boundary of the QM clusters is less well approximated by a hemisphere than the outer boundary of the much larger MM region. Nevertheless, the data in Table 9.3 demonstrates a convergence behavior and absolute values for the defect formation energies that are very well comparable to the ones obtained with the fully self-consistent MM electronic polarization. Here, the radii of QM clusters are determined through the positions of outer QM atoms, plus an additional parameter accounting for the extension of the electron density beyond the atomic positions. The value of these parameters is chosen to reproduce the self-consistent polarization. With 0.7 - 0.9 Å larger than the radii from atomic positions, these values are very reasonable. This approach is of course much more phenomenological than the self-consistent approach, however, the fact that the formation energies for *both* charge states are accurately reproduced, shows that such a method can be applied without further systematic errors.

Formation energies of relaxed vacancies

As pointed out in previous studies, relaxation, especially for charged defects, is significant [215, 218]. Due to the aforementioned inability of the force field to reproduce the static dielectric response of TiO_2 , relaxation in the MM region cannot be addressed explicitly. However, relaxation is fully accounted for within the QM region, with atomic positions directly at the boundary to the MM region fixed to minimize spurious short-range artifacts from the QM/MM coupling. This gives a first estimate of local lattice relaxations within a few shells of QM atoms, which is about the size addressed in current supercell calculations.

The first rows in Table 9.4 (a) compile our results with relaxed QM region together with electronic response in the MM region. Relaxation of the neutral cluster is minute, lowering the energy by 0.2 eV for all cluster sizes. The charged defects are, however, drastically stabilized. V_{O}^+ gains 1 & 1.2 eV and the V_{O}^{+2} even 3.6 & 4.3 eV in energy, respectively, which can be explained from the huge static dielectric constant and are in good agreement with a previous study addressing bulk defects [215]. Furthermore, relaxation effects for the two charged defects is in good agreement with fundamental electrostatics considerations, as polarization of the environment is proportional to the square of charge. Primarily, next neighboring titanium atoms

(a)	Self-consistent ϵ_∞	
	$\text{Ti}_{22}\text{O}_{43}$	$\text{Ti}_{32}\text{O}_{63}$
V_{O}^0	5.40	5.38
V_{O}^{+1}	1.69	1.69
V_{O}^{+2}	-0.59	-1.06
(b)	Analytic correction ϵ_∞	
	$\text{Ti}_{22}\text{O}_{43}$	$\text{Ti}_{32}\text{O}_{63}$
V_{O}^0	5.40	5.38
V_{O}^{+1}	1.49	1.42
V_{O}^{+2}	-0.50	-1.06
(c)	Analytic correction ϵ_0	
	$\text{Ti}_{22}\text{O}_{43}$	$\text{Ti}_{32}\text{O}_{63}$
V_{O}^0	5.40	5.38
V_{O}^{+1}	1.19	1.16
V_{O}^{+2}	-1.71	-2.11
(d)	$\epsilon_0 - \epsilon_\infty$	
	$\text{Ti}_{22}\text{O}_{43}$	$\text{Ti}_{32}\text{O}_{63}$
V_{O}^0	0.00	0.00
V_{O}^{+1}	-0.30	-0.26
V_{O}^{+2}	-1.21	-1.05
(e)	Self-consistent MM + $\epsilon_0 - \epsilon_\infty$	
	$\text{Ti}_{22}\text{O}_{43}$	$\text{Ti}_{32}\text{O}_{63}$
V_{O}^0	5.40	5.38
V_{O}^{+1}	1.39	1.43
V_{O}^{+2}	-1.80	-2.11
(f)	Self-consistent MM + $\epsilon_0 - \epsilon_\infty$, final correction	
	$\text{Ti}_{22}\text{O}_{43}$	$\text{Ti}_{32}\text{O}_{63}$
V_{O}^0	5.40	5.38
V_{O}^{+1}	1.28	1.33
V_{O}^{+2}	-2.17	-2.5

Table 9.4: Relaxed surface defect formation energies for the two different QM clusters in the O-rich limit and using the VBM as Fermi-level position. Upper rows (a) correspond to a QM/MM setup, in which only the electronic polarization response to the defect is treated through self-consistent relaxation of the MM shells. The next rows show results without MM polarization but the analytic correction ((b) ϵ_∞ in Eq. 9.5), then full ((c) ϵ_0 in Eq. 9.5). Rows (e) and (f) compile the results for the (a) together with the analytic correction for the static response (ϵ_0) (see text).

relax away from the defect allowing to strengthen their bond to other atoms, which leads to the aforementioned gain in energy. The obtained displacements are up to 0.4 Å (20 % of their former bond distance to the vacancy), which is in good agreement to the findings of Janotti *et al.* for the bulk defect [215].

Lattice relaxations of the direct defect vicinity in the $\text{Ti}_{22}\text{O}_{43}$ and the $\text{Ti}_{32}\text{O}_{63}$ cluster agree within 0.1 Å, showing that the near-field lattice reconstruction is already well converged. Relaxation patterns decay quickly with increasing distance to the defect. However, displacement

of outermost atoms are still up to 0.05 Å, hence non-negligible. Analogously to the electronic response outside the MM region in the previous chapter, we account for these missing long range relaxation effects through Eq. 9.5, however now with the static dielectric constant and the effective QM radii determined above (Table 9.4 (c)). Double counting of the high-frequency response within the MM region is removed by subtracting the high-frequency polarization energy within the MM region of the same radii (see Table 9.4). As outermost QM atoms are fixed, the radii for the full static polarization should be actually smaller. Hence, by still taking the QM radii of the electronic polarization we underestimate the polarization correction. We can gauge this error by calculating the difference between the full and electronic response between the QM radii and the slightly smaller radii where relaxation is fully accounted for, using Eq. 9.5. This yields another correction energy of -0.37 eV (-0.09 eV) for the $\text{Ti}_{22}\text{O}_{43}$ in charge state +2 (+1), respectively -0.39 eV (-0.1 eV) for the $\text{Ti}_{32}\text{O}_{63}$ cluster. Table 9.4 (f) then gives the final calculated formation energies.

Eq. 9.5 is relatively robust against an inaccurate description of large dielectric constants, i.e. using the experimental static dielectric constant manifests only in 0.03 eV (0.01 eV) lower total energies for the doubly (singly) charged defect. Hence, the inability of HSE06 to describe the static dielectric constant has only minute influence the final formation energies

9.3 Discussion

Defect formation energies are not yet accessible experimentally. Furthermore, the surface oxygen vacancy in its charged states has not been addressed with the HSE06 functional before and the comparison with previous studies using other functionals is difficult, as calculated values strongly depend on the applied xc-functional. Moreover, very little literature is available addressing charged vacancies, even less addressing charged vacancies at the surface.

GGA's have been shown unable to stabilize V_{O}^0 and V_{O}^{+1} , at least when lattice relaxation is included [215]. The widely varying formation energies for the neutral defect of 2-4.6 eV published in literature are therefore debatable [219, 220].

Correcting for on-site Coulomb interaction, the GGA + U method pushes the defect state below the band gap and thus yields a stabilization of the defect. Resulting formation energies for V_{O}^0 are 3.7 eV (with $U = 4.2$ eV) [221], while still significantly underestimating the band gap (2.2 eV) and the energetic position of the defect state.

Hybrid functionals with their different amounts of exact exchange report varying band gap, defect level positions and thus defect formation energies. For example Bredow and Pacchioni calculate the formation energy of V_{O}^0 as 4.7 eV using the B3LYP functional [167]. As they referenced the chemical potential of the oxygen not against the oxygen molecule but the single oxygen atom, they calculate the formation energy as 7.27 eV. Recalibration to our reservoir reference results in 4.7 eV [222]. However, direct comparison is difficult as they used a different embedded cluster approach without pseudopotentials but hydrogen termination, which most certainly leads to a distorted electronic structure for rather ionic materials like TiO_2 .

Recently, the vacancy stabilities in bulk TiO_2 have been addressed with the HSE06 functional by Janotti *et al.* [215]. They found formation energies of 5.5 eV (V_{O}^0) 2.4 eV (V_{O}^{+1}) and -1.4 eV (V_{O}^{+2}) for O-rich conditions, also predicting the V_{O}^{+2} vacancy being the most stable over a wide range of electrochemical conditions. While the formation energy of their neutral bulk vacancy compares very well with our predicted value for the surface, the formation energy for both charged defects are higher in energy by 1 eV, surprisingly independent of their charge. Bjørheim *et al.* studied the energy difference between the surface and bulk V_{O}^{+2} vacancy on TiO_2 with PBE. They found that this defect is 1.1 eV more stable at the surface. Assuming that this

additional stabilization is largest for the V_{O}^{+2} and less pronounced for the other two charge states potentially resolves the disagreement with Janotti *et al.*, within the expected accuracy.

Fig. 9.4 finally compiles the calculated formation energies (bottom rows in Table 9.4) as a function of the electron chemical potential, here normalized to the valence band maximum. This allows us to discuss the defect stability over a wide range of doping conditions. Over the full range from p-type (0 eV) to n-type doping (3 eV), the V_{O}^{+2} shows the lowest formation energy and is thus thermodynamically favored. This means that the bridging oxygen vacancy at the TiO₂ in the dilute limit is predicted to always favor the charge state +2 over the +1 or neutral charge state. For oxygen-poor conditions (Fig. 9.4 (b)), the defect formation energy is negative for all electrochemical potentials within band gap. This is in very good agreement with experiments which showed that defect concentrations under realistic conditions are considerable [183, 185, 200, 223]

Under extreme oxygen-rich conditions (Fig. 9.4 (a)), that is high oxygen partial pressures, and an electron chemical potential above 1.3 eV the V_{O}^{+2} defect formation energy, however, gets positive. Since TiO₂ is intrinsically an n-type semiconductor — i.e. without additional doping the Fermi energy is close to the VBM — the oxygen vacancy should not be present under oxygen rich conditions.

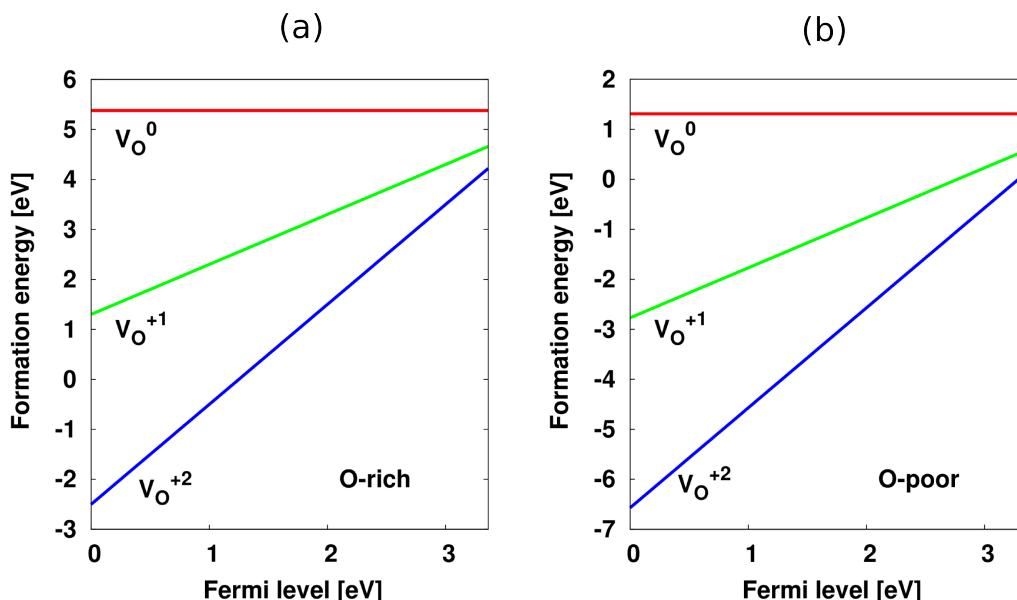


Figure 9.4: Calculated formation energies of the relaxed surface oxygen vacancy in oxygen rich (left) and oxygen poor conditions (right). The Fermi energy is normalized to the valence band maximum.

The energetic position of the defect state is predicted to be 0.7 eV below the CBM. Charging the defect corresponds to depopulating this defect state. This is in excellent agreement with other theoretical studies [218, 224], and experiments e.g. with electron energy loss spectroscopy experiments (0.75 eV below the CBM) [225], two-photon photo-emission spectroscopy (0.6 eV below the CBM) [226], and metastable impact electron spectroscopy (0.9 eV below the CBM) [227].

Finally, we have a remark on the multiplicity of the defect state and electron paramagnetic resonance experiments (EPR). We can not confirm the presence of two energetically separated defect states [206]. Further, we cannot confirm that spin polarization has an effect either on

the geometry or the electronic spectrum [218], suggesting a closed-shell singlet state.¹ At first glance, this is in contradiction to EPR measurements [210, 228, 229], which associate a measured triplet state to the V_O^0 defect, but is in perfect agreement with a previous theoretical study applying screened exchange [230]. In fact, it was shown by Deák *et al.* that the triplet and singlet defect states are energetically degenerated in large enough supercell sizes [206]. Hence, the defect state is present in a singlet as well as a triplet. Since the closed shell state is however invisible to EPR, there is no contradiction to experiment.

9.4 Summary/Conclusion

We studied oxygen vacancies at the rutile TiO_2 surface. We applied an embedded cluster setup using the hybrid density functional HSE06. Force field parameters were optimized to give matching structural parameters and high frequency dielectric constants, minimizing artifacts from QM/MM coupling.

Analysis of the resulting electronic structure revealed that the defect state lies about 0.7 eV below the CBM, which is in very good agreement with experiments. We further calculated the formation energies of the vacancy in its charge states 0, +1 and +2. Our results show that V_O^{2+} has the lowest formation energy for all Fermi levels within the band gap, suggesting that bridging oxygen vacancies are in the charge state +2, if present. With increasing oxygen pressure the defect formation energies gets positive for n-type TiO_2 . However, even under such oxygen rich partial pressure the oxygen vacancy can be stabilized through significant doping.

¹Here, the spin moment was initialized with 0.01 for every atom in order to break the symmetry.

10 MgO - oxygen vacancies and interstitials at corner and step sites

Magnesium Oxide (MgO) is one of the most important functional materials in the field of catalysis. It has a wide range of applications, either by itself [10, 11] or as an active support for co-catalysts [12, 13]. On such a surface, especially defects are of great interest due to their enhancement of catalytic activities [231]. The properties of such surface defects are markedly different from those of their bulk counterparts. An extensive body of work exists concerning the atomic and electronic structure of point defects in the bulk and at surfaces of oxides [232–235]. While the electron-rich O-vacancy is believed to play the key role in catalysis at oxide surfaces [231, 236, 237], also other kind of defects, such as O/O₂-interstitial, are promising catalytically active sites [238, 239]. Determining the stabilities of these defects (such as O-vacancies) on an extended MgO surface is an active field of research [129, 240], yet much less is known regarding formation and stability of defects at corners and steps. Significant controversy still exists regarding their defect formation energy, charge state and stability. Experimental determination of these defect properties at realistic conditions (T , p , and doping) is generally very challenging. There, theory can provide an invaluable support for understanding the role defects play in the catalytic function of oxides. In light of this, a systematic theoretical study is indeed needed in order to understand the stability of defects (namely, O-vacancy and O/O₂-interstitial) at the corners and steps of an MgO surface. Bhattacharya *et al.* have recently shown that unexpectedly the highly O-rich state is thermodynamically favored for small and medium sized neutral Mg_MO_x clusters ($1 \leq M \leq 15$) [241]. Such clusters predominantly expose corner and edge sites, and hence suggest that the O-rich state is also favored at the corners and steps of the MgO surface. We address this question and study the stability of both O-rich defects (e.g. O/O₂-interstitial) vs. the O-vacancy at corners and steps of the extended MgO surface and thereby screen for the thermodynamically most favored charge state. We address the relative defect stabilities at realistic T , p_{O_2} , and doping conditions of such defects using Density Functional Theory (DFT) and *ab initio* atomistic thermodynamics [214, 242]. At this stage, the doping is considered only indirectly as means of fixing chemical potential of electrons (μ_e).

10.1 Introduction

In a previous study towards a detailed understanding of the relative defect stabilities, Bhattacharya *et al.* studied a set of medium-size parallelepipedal [Mg_NO_(n+N)]^q clusters at various sizes [$N = 18, 24, 32, 108$] with a defect at one of the corners [$n = -1$ (O-vacancy), 0(pristine), 1(O-interstitial), 2(O₂-interstitial)]. The charge state q is varied from -2 to +2 [$q = -2, -1, 0, 1, 2$]. Using the massively-parallel cascade genetic algorithm implementation [cGA] [241, 243] allowing for global structure optimization, it was found that the corners of such parallelepipedal clusters are the most active sites for defect creation [See Fig. 10.1 (b) (upper panel)]. At realistic temperatures and pressures (e.g. $T = 300\text{K}$, $p_{\text{O}_2} \sim 1 \text{ atm}$) O or O₂-interstitial states at the

oxygen corners of pristine $[(\text{MgO})_N]^q$ clusters are favored at all studied charge states, over a wide range of electronic chemical potential μ_e . In fact, the interstitials are stable even at some values of μ_e , for which O-vacancies are preferred at flat (100) surfaces of doped MgO.

Previously, the charge neutral MgO surface has been simulated through finite clusters embedded in a simple static field of point charges. Surprisingly the electronic structure of the MgO surface could be well reproduced and adsorption processes of small gold cluster simulated on such simply embedded clusters show very good agreement with experiment [244]. Such a simple setup is, however, insufficient for the case for charged systems, as discussed in the following.

In a first attempt, the parallelepipedal $[\text{Mg}_N\text{O}_{(n+N)}]^q$ clusters were embedded in a static bulk truncated field of point charges in order to mimic the corner of the MgO surface. At such a corner of the rock salt structure the electric field is significant. This manifests in a non-negligible rearrangement of electron density within the QM cluster [245]. Even employing an almost exhaustively large $\text{Mg}_{102}\text{O}_{102}$ cluster as QM region could not achieve convergence with respect to the cluster size, for both the Mulliken charges of the corner site and defect formation energies [245]. The strong dipole field taxes the embedding approach of a static bulk truncated MM region, as it misses polarizability. This is even aggravated in the case of charged defects. Consequently, such simply embedded clusters are not viable models for the corner site of the surface.

10.2 Defects at the MgO surface

Here, our QM/MM approach shows its advantage in not only allowing for most efficient application of hybrid functionals, but also in its ability to capture long range polarization on the computationally much more feasible MM level. The latter ultimately allows to simulate the (charged) corner site of the surface through an embedded cluster approach.

We have created two embedded cluster model structures for the QM region ($\text{Mg}_{32}\text{O}_{32}$ and $\text{Mg}_{25}\text{O}_{25}$) depicted in Fig. 10.1 (b), (lower panel), embedded in a field of point charges. The corner and step setups are designed as shown in in Fig. 10.1 (c). Both systems do not exhibit long-range periodicity. Hence, a supercell and the corresponding Madelung potential cannot easily be defined. Therefore, the long range electrostatics are here converged by increasing the number of point charges. We found that a number of 7936 MM atoms for the corner and 12950 for the step site in both cases, adding up to a charge neutral system remainder, yield an electrostatic embedding potential converged to within 1 mV. In both setups, the self-consistent dielectric response was calculated for particles within 25 a_0 from the defect site.

k_{c-s} [in eV/Å ⁻²]	q_s [in e]
42.26	-2 .7089

	A [in eV]	ρ [in Å]	C [in eV Å ⁶]
$\text{O}_s - \text{O}_s$	21246.710	0.121	23.469
$\text{O}_s - \text{Mg}$	1262.651	0.309	18.560

Table 10.1: Interatomic potential parameters, optimized to reproduce the bulk MgO DFT-HSE06 lattice parameter and static and high-frequency dielectric constants (see Table 10.2).

As in the previous Chapter, we use a polarizable force field for the description of the MM region, with a spring potential between oxygen core (c) and its shell (s) (see Eq. 3.5) and

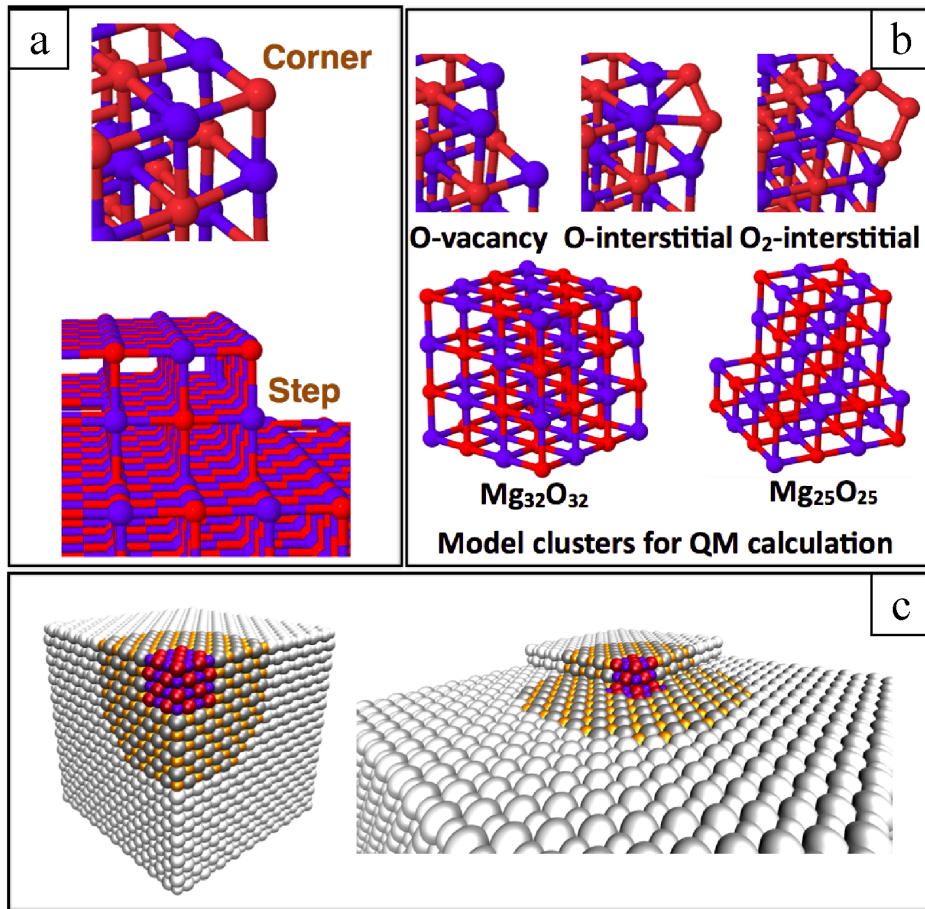


Figure 10.1: (a) Structural defects in an extended MgO surface (namely, corners and steps), (b) (upper panel) different types of defects (namely, O-vacancy, O-interstitial, O₂-interstitial) at the corners, (lower panel) model clusters Mg₃₂O_{32+n} (corner) and Mg₂₅O_{25+n} (step) to be used for the QM region of the embedded cluster model calculation, (c) and the full embedded cluster models (see text for details).

Buckingham short-range potential (see Eq. 3.4) for the interaction between magnesium core and oxygen shells and among oxygen shells that augments the Coulomb interaction. Using the differential evolutionary algorithm (c.f. Chapter 5) to find the global minimum in force field parameter space, we found a set of parameters (see Table 10.1) which simultaneously reproduces the structural and static and high-frequency dielectric constants (see Table 10.2). Unlike in TiO₂, this allows to account for the full dielectric response within the active MM region by explicit relaxation of MM cores. In doing this, the precarious electric fields at the corner site as well as the polarization response to charged defects are captured efficiently in a large volume, generally not affordable on a hybrid functional level of theory.

To extrapolate the defect concentration to the dilute limit, the long-range polarization energy beyond the active MM region is accounted for through an analytic formula, analogous to the Joost correction (see Chapter 3.5). The explicit formula depends on the geometry addressed. For the bulk and surface case analytic formulas are known [115], however not for the corner or step site. In general, the polarization energy has to be proportional to q^2 , with q being the charge of the defect. Furthermore it decays with $1/R$, with R being the distance to charge. For

	a [in Å]	ϵ_o	ϵ_∞
Exp.	4.212 [246]	9.8 [247]	3.0 [248]
HSE06	4.219		2.8 [249]
MM (this work)	4.217	10.7	2.95

Table 10.2: Lattice constant (a) as well as the static (ϵ_o) and high-frequency (ϵ_∞) dielectric constants of bulk MgO. Literature data from experiment [250] and DFT-HSE06 calculations [249] are compared against our own calculations at the DFT-HSE06 level and with the parametrized force field for the MM region (see Table 10.1).

radial symmetry, the dielectric constant and the actual geometry (bulk, surface, ...) are united a factor $f_{geo}(\epsilon)$ (compare with Eq. 3.17 and Eq. 3.19)

$$\Delta E_{pol}[q] = -\frac{q^2}{R} f_{geo}(\epsilon) \quad . \quad (10.1)$$

The energy correction $\Delta E_{pol}[q]$, which extrapolates to the dilute limit, is determined through least square fitting to a series of calculations with increasing active MM region, and added to the total energy of the system. All QM calculations were carried out using *FHI-aims* [127, 130] with *tight* settings and the *tier2* basis set. For the corner as well as the step site, convergence of calculated formation energies with respect to the QM cluster size and basis set was tested for the +2 charge state. Systematically increasing the QM cluster size and basis set showed that formation energies even for this most sensitive charge state are well converged to within 0.1 eV.

As a next step, we used the above described QM/MM setup to calculate the formation energies of the vacancy and O/O₂-interstitial in the charge states -2, -1, 0, 1 & 2 and applied the *ab initio* atomistic thermodynamics approach [180, 242] to understand their thermodynamic stability for given parameters T, p_{O_2}, μ_e . When adding/removing n O-atoms to the pristine cluster or to the surface of a material, the chemical potential with respect to a reservoir needs to be defined. Here, we use the gas phase of O₂ molecules as the reservoir, which is characterized by an oxygen chemical potential μ_{O_2} (and $\mu_O = \frac{1}{2}\mu_{O_2}$).

Vibrational contributions (harmonic and beyond) could, in principle, play a significant role in the phase diagram, especially at high temperatures. A previous study on neutral Mg_MO_n clusters, however, showed that although the change in vibrational free-energy is in general non-negligible, the effect on the phase diagrams is hardly visible for such systems [241]. Essentially, the configurational/vibrational contributions of the defected systems are to a large extend compensated by contributions of the pristine system, as only relative free energies have to be considered. Hence, these contributions are neglected in the following. For embedded clusters [Mg_NO_(N+n)]^q with n number of oxygen defects (vacancy/interstitial) at a charge state q , the difference in Gibbs free energy [$G_f^q(T, p_{O_2})$] of formation with respect to the host (pristine neutral embedded cluster [(MgO)_N]^{q=0}) is thus given by

$$G_f^q(T, p_{O_2}) = E_{defect}^q - E_{host}^{q=0} - n\mu_O(T, p_{O_2}) + q\mu_e \quad . \quad (10.2)$$

E_{defect}^q and $E_{host}^{q=0}$ are the total energies of the clusters with defect at charge state q and without defect at neutral state, respectively. The dependence of μ_O on T and p_{O_2} is calculated using the ideal (diatomic) gas approximation with the same DFT functional as for the clusters. μ_{O_2} is expressed with respect to μ_{ref} which is $E_{O_2}^{DFT} - \frac{h\nu_{OO}}{2}$. The latter term is the zero point energy (ZPE) of the O₂ molecule, calculated as 0.1 eV with HSE06. Therefore, $\Delta\mu_O$ is expressed as:

$$\Delta\mu_O(T, p_{O_2}) = \frac{1}{2} \left(\mu_{O_2}(T, p_{O_2}) - E_{O_2}^{DFT} - \frac{h\nu_{OO}}{2} \right) \quad (10.3)$$

More details on the technicalities of this procedure can be found in Ref. [243]. μ_e is the chemical potential of electrons, here referenced against the vacuum level. Therefore, the value of q that minimizes Eq. 10.2 at given (T, μ_{O_2}, μ_e) will be the preferred charge state at these experimental conditions.

Recently, it has been shown that the HSE06 [44] functional yields a good description of the level alignment and electron transfer in MgO [129]. Taking this into account, we have used the HSE06 functional to calculate the total energies in determining E_{defect}^q and $E_{host}^{q=0}$ as shown in Eq. 10.2. Furthermore, dispersion corrections to the formation energies of the clusters are included through the Tkatchenko-Scheffler scheme [63].

Geometry relaxation is significant for the charged clusters and is allowed for all atoms within the QM region. Furthermore, all MM particles within 25 a_o distance to the defect site were optimized in inner loop after every QM geometry optimization until all residual forces were less than $10^{-3} \text{eV}/\text{\AA}$.

The calculated defect stabilities are compiled in phase diagrams shown in Fig. 10.2. Only a limited area of these phase diagrams is experimentally accessible (area within the yellow box in Fig. 10.2). Experiments are limited in the applicable pressure regime. Furthermore, the electron chemical potential is limited through the band gap of bulk MgO ($\approx 8 \text{ eV}$). Within this area of the phase diagram, differences between the corner and step site are minute. Only for very low pressures the +1 pristine state becomes stable at the corner site. Furthermore, raising the electron chemical potential, e.g. by doping, stabilizes the neutral pristine state. The experimentally accessible areas of both phase diagrams compare very well with the one of the free cluster [243], showing that charge stabilization through long range polarization is hardly visible on such a scale. Both phase diagrams (embedded-corner and step) confirm the extra stability of O/O₂-interstitial defects over O-vacancies for a wide range of temperature and oxygen partial pressure regimes, around a chemical potential corresponding to the bulk Fermi energy (-7.5 eV).

It is known that introducing charge carriers into MgO via p -type doping greatly reduces the formation energy of oxygen vacancies in the bulk and at the (100) surface [129, 233]. The vacancies are stabilized by trapping the holes at the defect state thus lowering their energy. It is therefore unexpected that at corners of the MgO surface O-interstitials rather than O-vacancies are the dominating defect at realistic conditions.

The stability of the interstitials over vacancies and pristine corners can be explained by a competition between bond-breaking, bond-making, and charge-carrier trapping. For the latter, the gain in energy when charging the defect, can be discussed on the basis of electronic spectra as shown in Fig. 10.3. As the HOMO position of the system with the neutral vacancy is higher in energy than that of the system with the interstitial, the gain in energy of removing one electron into the electron reservoir (green line at -7.5eV is the Fermi level as computed from HSE06+vdW for bulk MgO) is larger for the vacancy than for the interstitial by 1.8 eV. However, the calculated formation energy of the oxygen vacancy (5.07 eV) is substantially higher than that for the formation of an O-interstitial (0.17 eV). This shows that the corner site much more favors bond-making instead of bond-breaking, leaving an overall favored interstitial even for the singly positively charged state. Apparently, in the competition between bond breaking and electron transfer, O-interstitials win over O-vacancies.

In order to make a quantitative analysis of defect conditions at the extended MgO surface, we compare the concentrations of different kinds of defects. As described above, the formation energy $\Delta G_n[q]$ of the n^{th} type of defect in charge state q is given by Eq. 10.2. Therefore, if N_n is the number of such defected corners out of N neutral pristine corner sites, we obtain

$$N_n = (N - \sum_{m \neq n} N_m) \times \frac{1}{e^{\frac{\Delta G_n}{k_B T}} + 1} \quad , \quad (10.4)$$

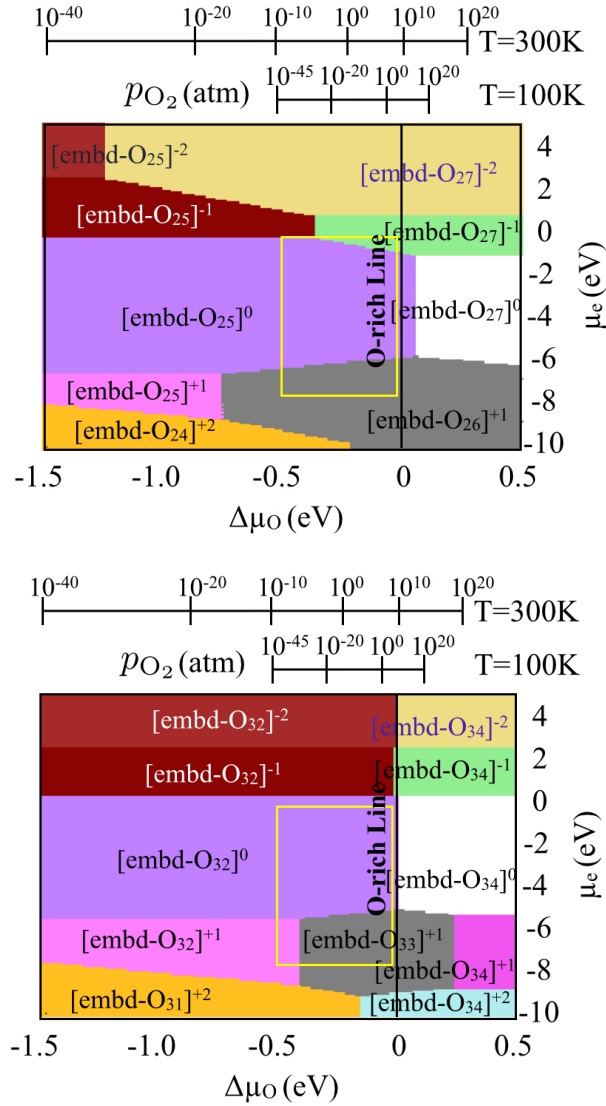


Figure 10.2: Phase diagram for embedded $\text{Mg}_{25}\text{O}_{(25+n)}$ (step) and embedded $\text{Mg}_{32}\text{O}_{(32+n)}$ cluster (corner) with O-vacancy ($n = -1$), pristine ($n = 0$), O-interstitial ($n = 1$), O_2 -interstitial ($n = 2$) clusters in the oxygen atmosphere. Geometry optimization and total energies are calculated with HSE06+vdW. The yellow box highlights the experimentally accessible regime.

where N_m is the number of other types of defects occupying corner sites. Boltzmann statistics does not reflect the quantum nature of such defects, and in fact would result in defect concentrations above 100%. Therefore, Fermi statistics $\frac{1}{e^{\frac{\Delta G_m}{k_B T}} + 1}$ has to be applied [245].

Similarly, for a different kind m of defect the expression for N_m is

$$N_m = (N - \sum_{l \neq m} N_l) \times \frac{1}{e^{\frac{\Delta G_m}{k_B T}} + 1} . \quad (10.5)$$

Dividing Eq. 10.4 and 10.5, we obtain

$$N_m = N_n \times e^{\frac{\Delta G_n - \Delta G_m}{k_B T}} . \quad (10.6)$$

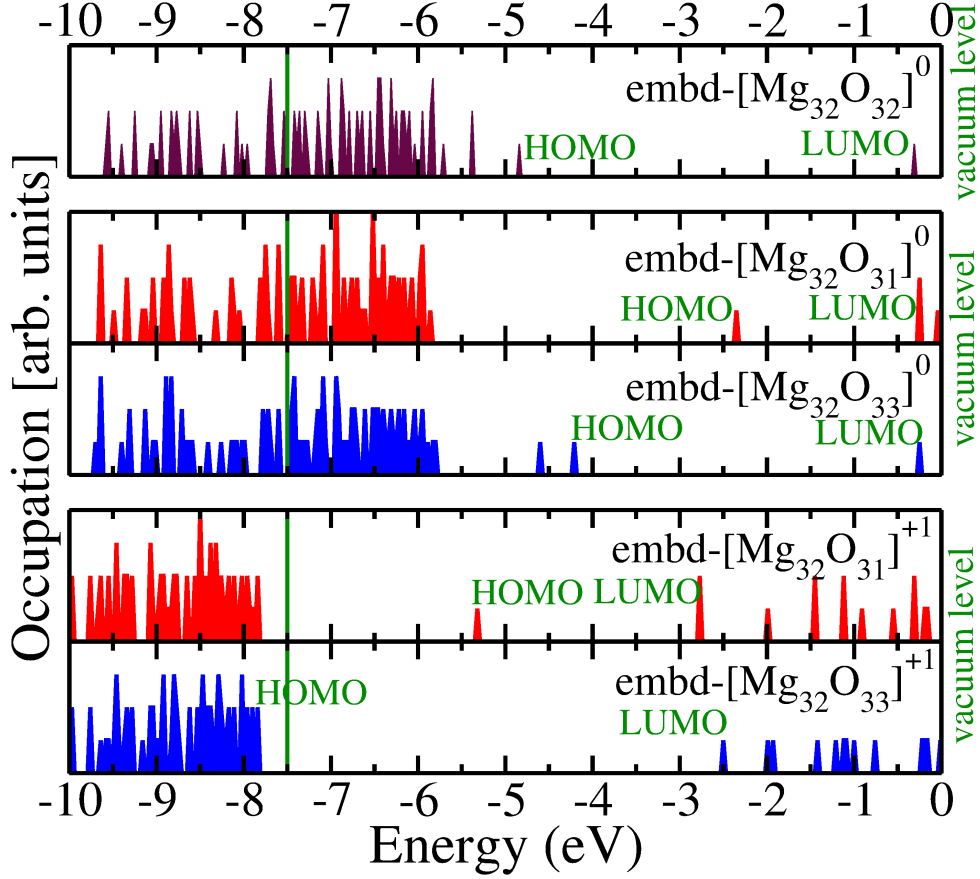


Figure 10.3: Kohn-Sham spectrum of embedded-[Mg₃₂O_{32+n}]^q [$n = 0, -1, 1$ with $q = 0, 1$] clusters. Competition between bond breaking and electron transfer.

From Eq. 10.4 and 10.6 the final expression for the defect concentration percentage is derived as

$$\frac{N_n}{N} \times 100\% = \frac{1}{e^{\frac{\Delta G_n}{k_B T}} + 1} \times \frac{100\%}{1 + \frac{e^{\frac{\Delta G_n}{k_B T}} \times \sum_m e^{-\frac{\Delta G_m}{k_B T}}}{e^{\frac{\Delta G_n}{k_B T}} + 1}} \quad (10.7)$$

The calculated defect concentrations at $\mu_e = -7.5$ eV as a function of temperature are shown in Fig. 10.4. There is clear abundance of singly positively charged O-interstitial at the corners of MgO-surface. With increasing temperature singly positively charged pristine corners also compete with O-interstitials, most prominent at low oxygen partial pressures. While at low temperature the percentage of singly positively charged O-interstitials is almost 100%, the same kind of defect at high temperature gets reduced to 50% abundance while the remaining 50% are singly positively charged pristine corners. Note that at very high temperature and low pressure, we obtain small traces of O-vacancies whose concentration is increasing at the cost of decreasing concentration of O₂-interstitial.

10.3 Conclusion

In summary, we studied the relative stability of O-vacancies and O/O₂-interstitials at the corner and step sites of the MgO crystal surface as a function of T , p_{O_2} , and doping conditions, using

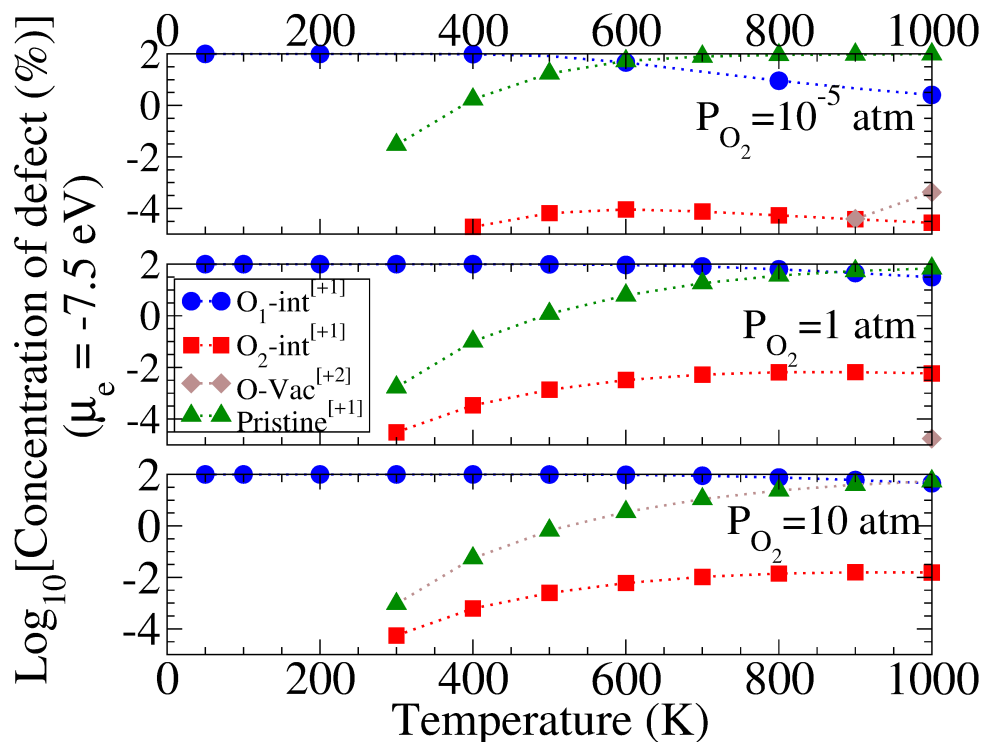


Figure 10.4: Concentration of O-vacancies and O/O₂-interstitials at the corner sites of the MgO crystal at various temperatures and pressures at $\mu_e = -7.5$ eV.

DFT with the HSE06 hybrid exchange-correlation functional and *ab initio* atomistic thermodynamics. We found that QM/MM embedding can only mimic the corner sites of the MgO crystal when applying a polarizable MM region. We find that over a wide range of experimentally realistic temperatures and pressures (e.g. around $T = 300$ K, $p_{O_2} \sim 1$ atm) O-interstitials in the charge state +1 are clearly favored. In fact, interstitials are stable even at some values of μ_e for which oxygen vacancies are preferred at flat (001) surfaces of doped MgO [233]. For a quantitative estimate we calculated the defect concentration and found that the concentration of oxygen interstitials is almost 100% for most experimentally accessible temperatures and oxygen partial pressures.

11 Catalytic reactions in ZSM-5 zeolites

As a further application, we used our QM/MM implementation to study catalytic reactions in ZSM-5 zeolites. Belonging to the MFI structural family, ZSM-5 is a porous aluminum silicate framework (SiO₂ building units with Al-substitutions) [251], which is an important catalyst for a range of important reactions [252–254]. These frameworks can further be doped with catalytically active transition metals such as Fe and Ti [255], either enhancing already present catalytic reactivity or opening up many new possible catalytic reaction pathways.

A detailed understanding of reaction mechanisms and the elementary processes involved is essential when aiming to improve the overall reactivity of any catalyst. Quantifying the reaction energetics is then an obvious milestone on the route to improved catalyst design. In many cases, several possible reaction pathways can be postulated from *chemical intuition* and narrowed down by experiment. However, the actual reaction mechanism and the reaction energetics of distinct pathways are difficult if not impossible to measure. Computational studies have proven to be useful, as the reaction energetics of all possible mechanisms can be calculated and compared [256, 257].

Here, we investigate two important reactions in ZSM-5. First, we study the Fe^{3+/2+} reduction potential of Fe doped ZSM-5. Accurate quantification of this reduction potential is essential to describe possible chemical reactions. Accurate calculations of corresponding potentials, even in the static picture, have proven to be problematic though, due to the difficulty in accounting for both the extended bulk framework and the electron localization around the active site. As semi-local DFT does not appropriately accomplish the latter [258, 259], calculations at hybrid xc level are required. This in turn is hardly feasible in periodic boundary conditions, leaving our QM/MM embedding infrastructure as the only practicable approach. The first part of this chapter has also been published in JCP [128]. Within this part, our QM/MM implementation for covalent materials is benchmarked against the Quantum Chemistry package *Gamess-UK* [260].

As a second example, we investigate the reduction of methanol to ethylene in pristine ZSM-5, which is one of the key reactions in zeolite catalysis. Ethylene is one of the most industrially used basic chemicals with vast utilization in polymerization, alkylation and general oxidation reactions. With a world-wide production of 140 million tons per year in 2011 [261], ethylene production — typically done by conventional steam cracking — is a major consumer of energy. Needless to say, alternative catalytic production methods with reduced energetic costs are highly desirable. ZSM-5 is able to catalytically reduce methanol to ethylene [262], however the reaction mechanism has not yet been fully understood [263–265]. There is still a debate about whether the reaction involves a decarbonylation (splitting off CO) or a decarboxylation (splitting off CO₂) step. Complementary to experiments conducted by the group of Prof. Johannes Lercher at TU München, we aim to address this question through first-principles calculations. This collaboration is ongoing, and no final discussion can be made yet, as latest experiments showed that even further possible reaction pathways need to be considered. At this point we therefore address two preliminary questions for a follow-up extensive sampling study of possible

reaction pathways. First, we determine the QM cluster size necessary to reproduce results of computationally exhaustive periodic reference calculations, independent from the investigated reaction pathways. Second, we compare results of GGA and hybrid-functional DFT to determine the necessary level of theory for such reactions in the zeolite framework. Here, we do this by studying the decarbonylation and decarboxylation route. For a detailed description of organic molecules and reaction mechanisms involved the author refers to standard literature [266].

11.1 Embedding in covalent material

Zeolites are (semi-)covalent materials, which means that atoms in the material are only weakly charged. Therefore, the embedding scheme with pseudopotentials described in Chapter 3 is not applicable as it requires formal charges for embedding cations. Embedding with formal charges and pseudopotentials would lead to strong overpolarization at the QM region boundary. Thus, one has to follow a different approach to allow for seamless embedding here.

Covalent materials have directed chemical bonds, therefore greatest artifacts of the finite cluster treatment arise from unsaturated dangling bonds (open valencies) at the QM-region boundary. Here, we follow the common procedure of saturating the QM cluster with hydrogen atoms. For a review on this method we refer to Vayssilow *et al.* and literature within [267]. The system remainder again is treated on a molecular mechanics level of theory. Yet, to recover the rather complex zeolite structure, an elaborate force field is needed. Throughout this chapter we use the well-tested force field by Hill and Sauer [268]. This force field includes bond and torsion angle dependent terms, which are not implemented in *GULP*. Forces and energies were therefore calculated with the *DL_POLY*-package [269], as it provides infrastructure for such comprehensive force fields.

For the problems of current interest, it is essential to describe the time averaged response in a zeolite system to a perturbation near the center of the cluster, which is accounted for already by the current model. Long-range polarization effects here are less important than in many other classes of dielectric materials due to their relatively low static permittivity ($\epsilon \sim 4$) and low density. The local electronic and ionic polarization fields are fully captured within the QM part of the total system. For charged QM regions as such addressed in the next section, the smaller static dielectric response from the MM vicinity can be included through relaxation of the point charges in the MM region.

11.2 $\text{Fe}^{3+/2+}$ reduction potential of Fe doped ZSM-5

ZSM-5 can be doped by replacing the tetrahedral Si atom (T-sites) e.g. with transition metals. The zeolite structure provides several non-equivalent active T-sites, which potentially have differing reduction potentials. Here, we compare three different active sites : a T-site at a straight channel (M7-T1), at a sinusoidal channel (Z6-T4) and at a channel intersection (I2-T12), cf. Fig. 11.1. We construct three different embedded clusters from the undoped parent MFI framework, each centered on a tetrahedral Si atom of differing structural nature within a framework active site [120].

Around this central atom the QM region includes all other members of the active site, as well as any extra Si atoms that are first neighbors to the active site, and all the corresponding linking oxygen atoms. All incomplete bonds from the oxygen atoms are saturated with H link-atoms, and a bond-dipole correction is added to the MM representation [270]. Concentric regions of MM atoms are then added; first an active region up to a radius of 10.58 Å (20 Bohr) and then

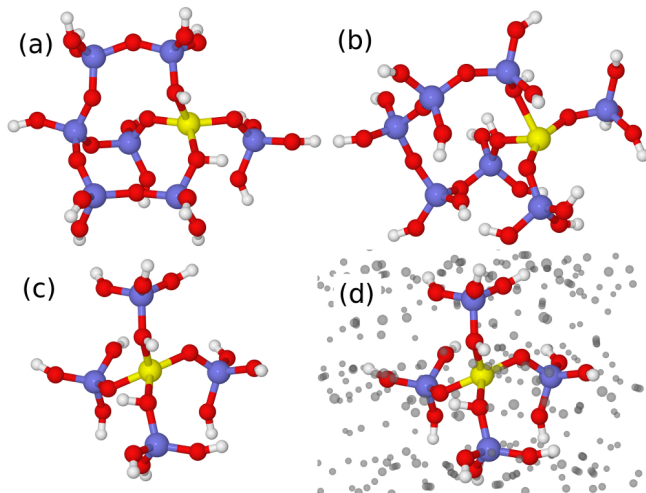


Figure 11.1: Illustration of the QM clusters used in our calculations of Fe-ZSM-5: (a) M7-T1; (b) Z6-T4; and (c) I2-T12. Fe, Si, O and H atoms are represented in yellow, mauve, red and white, respectively. The extended embedding environment included in the QM calculation of (c) is illustrated in (d), with the MM point charges represented in grey.

a fixed region up to a radius of 21.17 \AA (40 Bohr). This results in a total number of atoms in the embedded clusters in the range 2155 – 2180.

The accuracy of the *FHI-aims-ChemShell* coupling is validated by calculating the same embedded clusters also with *Gamess-UK* as QM calculator, and using the same TZVP Gaussian basis sets of Ahlrichs and Taylor [271] in both QM codes. At the PBE [42] xc level of theory and using converged integration grid settings in both codes differences in total energies are below 18 meV for each cluster, while forces on QM atoms differ by less than 0.05 eV/\AA . This clearly demonstrates the validity of our QM/MM implementation for (semi-) covalent materials.

With this confidence, production calculations with *FHI-aims* are henceforth performed with the code’s own numerical basis sets. For the three embedded clusters at PBE level, already *tier1* leads to total energies lower by 1 eV than for the TZVP basis set, demonstrating the better description of e.g. the near-nuclear potential and kinetic energy integrals by the purposely designed NAO basis sets. The Fe^{3+} active center is introduced to the embedded clusters by replacing the central Si atom. The reduced Fe^{2+} state is described by coordinating an additional H atom to an O atom directly adjacent to the central Fe species. The reduction potential can then be defined as

$$E^{\text{Red}}(\text{Fe}^{3+/2+}) = E^{\text{tot}}(\text{Fe}^{2+}\text{-MFI}) + \frac{1}{2}E^{\text{tot}}(\text{H}_2) - E^{\text{tot}}(\text{Fe}^{3+}\text{-MFI}),$$

where $E^{\text{tot}}(\text{H}_2)$ is the energy of a gas-phase hydrogen dimer. Calculations are performed for the semi-local PBE and BLYP, for the hybrid PBE0 and B3LYP, as well as for the double-hybrid XYG3 functionals [42, 43, 53, 272–275]. All geometries are fully relaxed at the corresponding semi-local level, with hybrid and double-hybrid calculations performed on these geometries. Hereby, we ensure consistency in the correlation treatment, i.e. single-point B3LYP and XYG3 calculations were performed on the BLYP geometry, respectively PBE0 on the PBE geometry. The XYG3 calculations are furthermore performed post-SCF on the optimized B3LYP Kohn-Sham orbitals. At *tier2* basis set level the obtained reduction potentials are already numerically converged to within 1 meV for the semi-local and hybrid functionals. At the double hybrid-level a sufficient convergence to within $\pm 20 \text{ meV}$ can instead only be reached using the *tier3* basis

	M7-T1	Z6-T4	I2-T12
$E_{\text{PBE}}^{\text{Red}}(\text{Fe}^{3+/2+})$	-0.18	-0.16	-0.18
$E_{\text{BLYP}}^{\text{Red}}(\text{Fe}^{3+/2+})$	-0.29	-0.39	-0.17
$E_{\text{PBE0}}^{\text{Red}}(\text{Fe}^{3+/2+})$	-0.05	0.04	-0.03
$E_{\text{B3LYP}}^{\text{Red}}(\text{Fe}^{3+/2+})$	-0.09	0.01	-0.02
$E_{\text{XYG3}}^{\text{Red}}(\text{Fe}^{3+/2+})$	-0.34	-0.20	-0.18

Table 11.1: Computed reduction potentials (in eV) for $\text{Fe}^{3+/2+}$ embedded intra-framework within an MFI siliceous structure. Active sites are modeled as the M7-T1, Z6-T4 and I2-T12 sites shown in Fig. 11.1. Calculations performed using semi-local and hybrid functionals used the *tier2* basis level for all atoms; at the double hybrid-level the NAO-VCC-4Z basis set was used for all atoms except Fe, for which — due to the lack of Fe VCC basis set — a *tier3* basis set was used.

set for Fe and for all other (light) species the NAO-VCC-4Z basis set that specifically converges the sums in the unoccupied-space [132]. The more diffuse functions contained in this basis set require an ensuing counterpoise correction [193] though.

The efficiency of this QM/MM approach can be seen by comparing the computational cost for one SCF iteration with that of the reference PBC setup. The I2-T12 cluster geometry comprises 21 atoms, while the MFI unit cells consists of 288 atoms. On the level of PBE, the average SCF iteration for the QM/MM setup takes 30 s using 4 CPUs(AMD Opteron Processor 250, 2393 MHz), compared to 1200 s for the periodic calculation (k-grid reduced to Γ -point) on the same machine. Periodic references on the hybrid and double hybrid level, moreover, demand a prohibitive amount of memory. Such levels of theory are thus only accessible through a QM/MM approach.

Table 11.1 compiles the obtained reduction potentials for Fe at the three structural sites in the MFI framework. At all levels of theory the differences between these three sites are very small, indicating a low structure sensitivity for the catalytic properties of the active center. This structure insensitivity warrants a direct comparison to previous experimental voltammetry by Pérez-Ramírez *et al.*, which gave very small reduction energies for intra-framework Fe^{3+} of the order $0.05 \text{ eV} \geq V_{\text{Red}}(\text{Fe}^{3+/2+}) \geq -0.15 \text{ eV}$ [276]. There is, thus, a huge effect induced by the siliceous framework, when considering that the corresponding reduction potential of Fe^{3+} in a hexagonally coordinated $[\text{Fe}(\text{H}_2\text{O})_6]^{3+}$ complex was for instance calculated as 1.07 eV at PBE level [277]. This framework effect is well captured on essentially all xc levels studied, which in good overall agreement with the experimental findings yield small reduction potentials scattered around zero. More specifically, the majority of the xc-treatments agrees that the reduction potential is negative, indicating stability for Fe(II) in the material. Interestingly, the double-hybrid functional XYG3 yields reduction potentials closer to the ones at the semi-local (BLYP) level, and thus makes up for most of the change observed at the hybrid (B3LYP) functional level. At least within the small scatter of Table 11.1 there is thus no clear trend in the calculated reduction potentials that would prominently reflect the allegedly gradually increasing electron localization achieved in the sequence $\text{BLYP} \rightarrow \text{B3LYP} \rightarrow \text{XYG3}$.

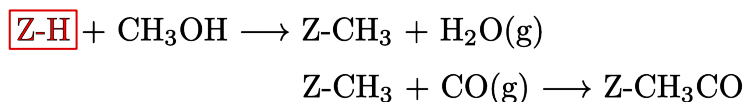
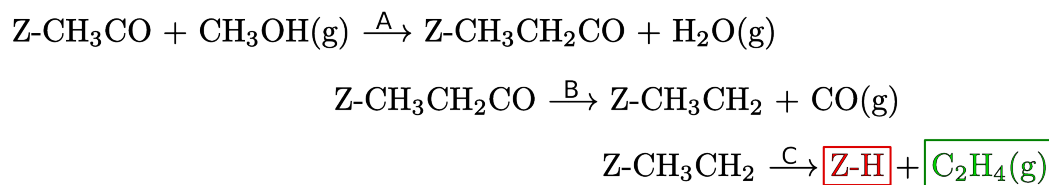


Figure 11.2: Adsorption and carbonylation of methanol at the zeolite acid site (red).

Figure 11.3: *Decarbonylation route*. The CH_3CO group adsorbed at the zeolite acid site (Z) is methylated and then decarbonylated. Desorption of ethylene (green) leaves the protonated acid site (red).

11.3 Catalytic reduction of methanol to ethylene

Synthesizing ZSM-5 from the MFI, i.e. substituting a silicon atom with aluminum, leads to protonation of the neighboring oxygen atom for charge compensation [251]. This oxygen atom, the Brønsted *zeolite acid site*, is catalytically active [256, 278]. One of the possible applications, is the catalytic reduction of methanol to ethylene, a reaction of major interest for the chemical industry. Here, the motivation is to gain a detailed and accurate understanding of the reaction mechanism. Based on that information one can then aim to improve the performance of the catalyst for example through specific doping.

The reaction is already relatively complex due to the number of atoms involved and the large number of possible reaction pathways. Previous experimental and computational studies addressed different aspects of the interplay between zeolites and various reaction intermediates, however, the complete reaction mechanism for the methanol to ethylene reaction has not been determined. There is strong evidence that the reaction starts with the adsorption of a gas phase methanol molecule to the clean (protonated) zeolite acid site Z-H under elimination of one water molecule [263–265, 279]. In a second step, the adsorbed methyl-group is carbonylated with carbon monoxide (see Fig. 11.2). The further reaction pathway is not yet determined experimentally. Here, Lercher and co-workers found evidence for two possible and competing reaction mechanisms starting from the adsorbed CH_3CO molecule [280], explained in the following. Experimental results of this specific reaction mechanism to compare our results with are not yet available ¹.

The proposed reaction mechanisms describe the pathway through the reaction interstitials. Intermediate reaction products imply meta-stable activated complexed along the transition state pathway. The first mechanism, shown in Fig. 11.3, involves methylation with gas phase methanol under elimination of one further water molecule followed by decarbonylation and final desorption leaving the initially protonated zeolite acid site. This so called *decarbonylation route* only requires one additional carbon monoxide molecule.

The second proposed reaction mechanism, the so called *decarboxylation route*, starts with

¹to be published

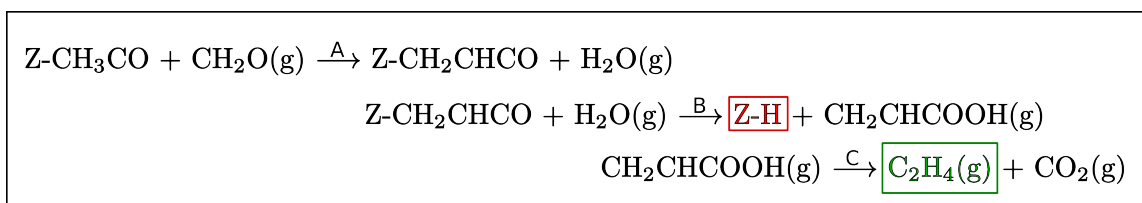


Figure 11.4: *Decarboxylation route*. Formaldehyde is added to the CH_3CO group adsorbed at the zeolite acid site (Z) creating an aldol. Upon reaction with a gas phase water molecule, 2-propanoic acid is formed and desorbed, leaving the protonated zeolite acid site (red). Final decarboxylation yields gas phase ethylene (green).

the adsorption of formaldehyde under elimination of water, followed by adding a water molecule and subsequent desorption of the formed 2-propanoic acid. In the gas phase reaction the 2-propanoic acid is decarbonylated through elimination of carbon decarbonylationdioxide leaving ethylene as the final product. This reaction pathway involves the reaction with gas phase formaldehyde and water. Aside from the energetic reaction barrier, this circumstance already affects the reaction rate due to basic Bayesian probability estimations, as *two* reactants (instead of one in the decarbonylation route) have to meet the reaction partner at the zeolite acid site. Furthermore, it requires abundance of formaldehyde. Formation of formaldehyde from methanol is endothermic and has to be included in the assessment of this reaction pathway.

Providing access to energy barriers of specific reactions steps, first-principle calculations are of great aid in comparing both proposed reaction mechanisms. In this work, we will calculate reaction energetics for every proposed reaction step along the pathways. We will then assess the thermodynamic feasibility by comparing the overall energy record and the reaction barriers along the given reaction paths.

While bond lengths of organic molecules and the structure of the zeolite can correctly be predicted in the semi-local level of DFT, total energies are typically described very inaccurately. To allow for an accurate account of the reaction energetics, hybrid functionals are required. The unit cell of the zeolite structure comprises 289 atoms, ultimately prohibiting application of hybrid functionals in periodic boundary calculations. Not being tied to such a large number of QM atoms involved, our QM/MM implementation provides most efficient access to the reaction energetics.

Analogous to the previous Section, the QM/MM setup is generated from the ZSM-5 unit cell with the experimental lattice parameters of 20.022, 19.899 and 13.383 Å [281]. Two clusters with 22 (Cluster I) and 74 (Cluster II) QM atoms are generated (Fig. 11.5) terminated with 13, respectively 25 hydrogen atoms according to the force field by Hill and Sauer [268]. The clusters are surrounded by an MM region comprising 1484 point charges for the small and 1481 for the large cluster. Long-range electrostatic contributions in the zeolite structure can have significant influence on reactions barriers [282]. In the embedded cluster calculation the overall electrostatic potential is reproduced by adding fitted point charges, following the procedure described in Sec. 3.3. Given that the dielectric constant of ZSM-5 is very small ($\epsilon \sim 4$) and only neutral QM clusters are studied, self-consistent dielectric response is neglected here.

Geometry optimization in each reaction step was performed on the GGA-level of electronic exchange-correlation (BLYP [53, 54]). To prevent boundary effects in the small cluster only the adsorbate and the central Al together with its neighboring oxygen atom in the zeolite structure were allowed to relax, while full geometry optimization was performed in the large cluster and the PBC reference calculations. Total energies in these structures were then calculated also

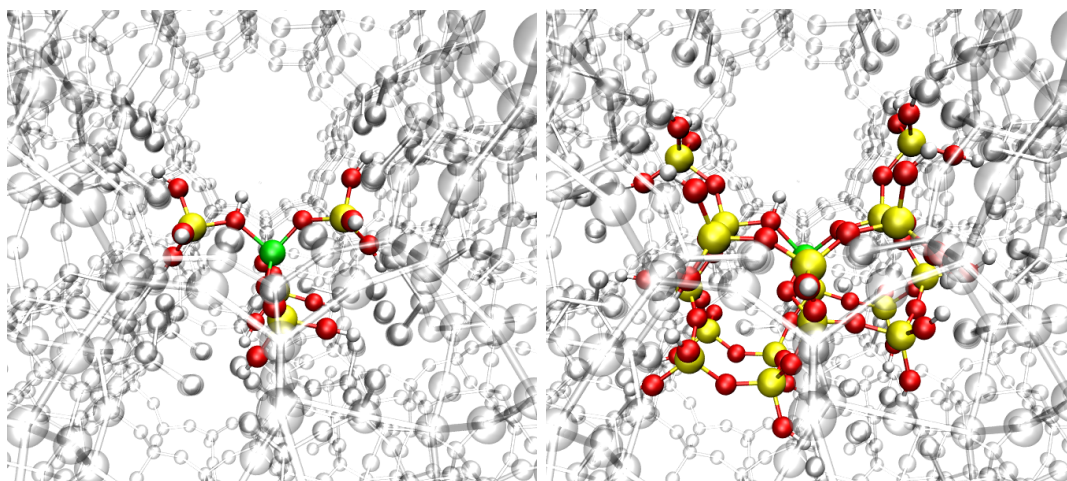


Figure 11.5: Perspective view on the two QM clusters centered around the aluminum atom (green). The small $\text{AlSi}_4\text{O}_{16}\text{H}$ cluster shown on the left is terminated with 13 hydrogen atoms, the large $\text{AlSi}_{17}\text{O}_{48}\text{H}$ cluster (right) with additional 25 hydrogen atoms for cluster termination. Silicon atoms are marked as yellow, oxygen as red spheres. Terminating hydrogen and embedding point charges are white.

on the hybrid-level of theory using the B3LYP functional [272, 273]. The BLYP and B3LYP functional are missing van der Waals interactions, which are significant in the description of organic molecules. To correct for the missing physics, a post-correction to the total energies according to Tkatchenko and Scheffler [63] was applied throughout.

All calculations were performed using *FHI-aims* with default *tight* setting for the basis set and integration grids. The level of convergence provided by these settings is investigated for the total energy of the gas phase CH_2CHCOOH molecule, where numbers are converged within 12 meV compared to complete basis set limit. Calculated *relative* total energies of the large zeolite system can be expected to be of the same order.

All reaction steps considered here are of type



In our case experiments were performed in the gas phase, where no solvation effects influence the reaction. Thus, configurational entropic effects are indeed not expected to contribute significantly to the free energies. In principle, also vibrations contribute to the reaction free energies, and should be included for a proper discussion of the reaction barriers. To most extent such contributions arise from different vibrational spectra of the molecules in vacuum and the adsorbed state. Also the vibrational spectrum of the zeolite framework is slightly perturbed upon adsorption. Due to the low dielectric response, this should be a local effect. The size of the QM cluster therefore has minimal effect on vibrational contributions to differences in the free energies [282]. Hence, vibrations can be neglected here for this preparatory study. Reactions are then assessed by calculating the differences of total energies between educts A and B and products C and D

$$\Delta E^{\text{tot}} = E^{\text{tot}}(A) + E^{\text{tot}}(B) - E^{\text{tot}}(C) - E^{\text{tot}}(D) \quad , \quad (11.2)$$

which typically already account for the most important physics and trends [283]. These energies are valid for all reaction conditions like temperature and partial pressures of all the reactants, and

do not allow direct thermodynamic comparison of the two reactions at given reaction conditions. However, pointing out the rate determining step — the one with the largest barrier — is already very important information.

Avoiding periodic boundary conditions for an exhaustive study of such a system has two major advantages: first, the unit cell is relatively large, making the electronic structure calculations cumbersome already on the GGA level of theory. Second, the large number of degrees of freedom severely challenges the geometry optimizer (here we apply the *BFGS* algorithm [284]). This is further enhanced when studying adsorption of molecules with several torsion angles, with many shallow local minima. In most of the periodic calculations the optimizer detects inconsistencies between forces and the total energy: a structural minimum is characterized through vanishing forces in all directions. In a stepwise procedure the *BFGS* algorithm propagates the structure according to evaluated forces, leading to a lower-energy structure. In the case of the large zeolite unit cells, the algorithm detects an inconsistency that forces and differential quotient of the total energy do not have the same orientation, a.k.a. propagating according to the forces raises rather than lowers the total energy. This inconsistency could not be resolved by increasing the integration grids or basis set, and terminates the geometry optimizer. This not only shows that studying these reactions in a periodic setup is extremely challenging, but it also makes it difficult to benchmark our QM/MM setup. Here, the latter can only be done for the two periodic setups with the most reliable structure, *Z-H*, the initial state of the preceding carbonylation reaction (Fig. 11.3). In this structure the aforementioned inconsistency only occurred when all forces were already converged below $0.02 \text{ eV}/\text{\AA}$. Hence, with a grain of salt these structures can be taken as fully optimized. The overall electrostatic potential is well reproduced within the embedded cluster model. This can be seen when comparing the highest occupied KS-orbital. For example for the protonated acid site *Z-H* the energy of the HOMO in Cluster II agrees very well with VBM of the periodic calculation within 60 meV. As furthermore can be seen in Fig. 11.6, the predicted bond distance between the acid site (bridging oxygen atom between aluminum and silicon) and the hydrogen atom agree for all three setups. The intra-zeolite bonds (Al-O and O-Si) are underestimated only by up to 0.05 \AA already in the small cluster, and converge towards the PBC limit with increasing cluster size. In cases of the acetylated acid site we detect massive deviations for the small cluster, e.g. the bond distance to the acid site is overestimated by 0.8 \AA , only leading to a quasi-bonded compound state. In particular, also the orientation of the molecule is the same in the large cluster and the PBC reference. The large cluster on the other hand reproduced this bond length within 0.03 \AA compared to the PBC reference. Furthermore, reorganizations of the intra-zeolite bonds upon acetylation of $0.02\text{-}0.03 \text{ \AA}$ exactly reproduce the PBC reference. The same holds for the C-C bond within the adsorbed acetyl-group (1.48 \AA).

Calculated reaction energies ΔE^{tot} for the carbonylation reaction sketched in Fig. 11.2 are consistent within the three setups. In particular, the larger cluster (Cluster II) shows very little deviation from the PBC reference by 10 meV. Deviations in the smaller cluster are slightly larger, predicting the reaction as too exothermic. This agrees with observations by van Santen [285], that relaxations within the zeolite are essential for the accurate description of the Brønsted acid site, and are not captured within the small cluster. Following calculations are thus all performed with the Cluster II.

As expected, the reaction energetics calculated at the hybrid functional level differ significantly from GGA results, by up to 300 meV. This shows that the well-known delocalization error of GGA functionals has a significant effect on the reaction energetics in such systems. Here, our QM/MM approach exhibits its great asset as computational expenses of hybrid functionals are tremendously reduced compared to periodic calculation. Although results from hybrid functionals are in principle more reliable, we will report results from both functionals. The scatter among results from different functionals is an estimate for the systematic errors of DFT. The

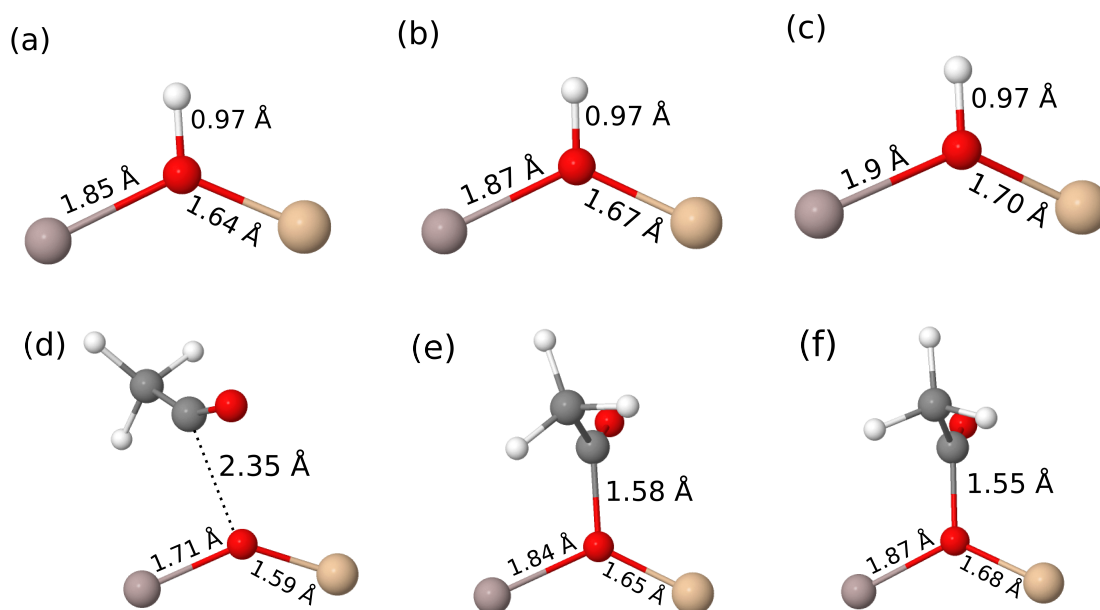


Figure 11.6: Bond distances at the protonated and acetylated acid site, calculated in Cluster I (a) & (d), Cluster II (b)&(e) and the periodic setup (c)&(f). The aluminum atom is silver, silicon is beige, oxygen is red and hydrogen is white.

ΔE^{tot} [eV]	Carbonylation reaction
BLYP	
PBC	-1.33
Cluster I	-1.46
Cluster II	-1.34
B3LYP	
Cluster I	-1.12
Cluster II	-1.04

Table 11.2: Relative energy differences of educts and the final products of the carbonylation reaction shown in Fig. 11.2 (sum of both steps). Results from the two embedded clusters are compared with periodic reference results (PBC) on the BLYP-level of xc-functional. Further, results for Cluster I and II using the hybrid functional B3LYP are listed.

validated QM/MM model is now used to study the energetics of the decarbonylation (Fig. 11.3) and the decarboxylation route (Fig. 11.4).

Table 11.3 compiles the calculated relative total energies for both routes. For assessment of both reaction mechanisms for their thermodynamical feasibility the most important observable is the overall energy consumption, the sum of the energy of all steps involved in one pathway. The decarbonylation route is endothermic by 1.38 eV with BLYP and 0.96 eV with B3LYP. The decarboxylation route is exothermic by -0.47 eV, respectively -0.76 eV with B3LYP. The difference in energy consumption reflects the fact that the decarboxylation route requires an abundance of formaldehyde. If this is not fed in as an additional educt, gas phase formation from methanol — $\text{CH}_3\text{OH} \rightarrow \text{CH}_2\text{O} + \text{H}_2$ — has to be included when discussing reaction energetics. This reaction is endothermic by 1.18 eV with BLYP and 1.21 eV with B3LYP. When

ΔE^{tot} [eV]	Decarbonylation route			
	Step A	Step B	Step C	Σ
BLYP				
BLYP	-0.68	0.91	1.16	1.38
B3LYP	-0.66	0.77	0.85	0.96
ΔE^{tot} [eV]	Decarboxylation route			
	Step A	Step B	Step C	Σ
BLYP	-0.55	0.20	-0.11	-0.47
B3LYP	-0.66	0.09	-0.20	-0.76

Table 11.3: Energetics of the decarbonylation and decarboxylation route as described in Fig. 11.3 and Fig. 11.4 and calculated in the embedded $\text{AlSi}_{17}\text{O}_{48}\text{H}$ cluster. ΔE^{tot} is shown for every reaction step and as the sum of all steps Σ . Step C of the decarboxylation route is a gas phase reaction and thus calculated in absence of the zeolite framework.

including this number, also the decarboxylation route is endothermic by 0.72 eV, respectively 0.45 eV for B3LYP. Still, from this calculated relative energies the decarboxylation route is significantly favored (BLYP: 0.66 eV, B3LYP: 0.51 eV), even with the additional cost for the gas phase formation of formaldehyde. This is due to the fact, that both pathways end up with different side products, namely CO and H_2O in the decarbonylation route and CO_2 and H_2 (due to formation of formaldehyde) in the decarboxylation route. In fact the differences in energy exactly corresponds to the energy balance of the water-gas shift reaction.²

For a practicable catalyst the reaction rate is of great importance, as it determines the maximum turn-over. The reaction rate, however, not only depends on the energy consumption but also on the reaction barriers of the intermediate steps. In principle, transition rates can be determined from *ab-initio* calculated transition states through transition state theory. However, explicit sampling of the transition pathways is cumbersome for system sizes discussed here, and goes beyond the purpose of this study. For future studies, our QM/MM implementation is readily available to perform *ab-initio* transition state searches, as *ChemShell* provides such infrastructure in form of the nudged elastic band algorithm [286]. Here, the transition states of the two routes are approximated through the meta-stable states resulting from the intermediate reaction steps.

The largest barrier in the decarboxylation route is the final desorption (Step C) with 1.16 eV, respectively 0.85 eV (B3LYP). The reaction at the zeolite acid site in the decarboxylation route itself are small throughout, however, the gas phase formation of formaldehyde is predicted to be the rate determining step, with aforementioned ≈ 1.2 eV.

²Calculation of the water-gas phase reaction ($\text{H}_2\text{O} + \text{CO} \rightarrow \text{CO}_2 + \text{H}_2$) in terms of differences of total energies exactly yields 0.66 eV for BLYP and 0.51 eV for B3LYP.

Conclusion

We studied the reaction energetics of the decarbonylation and decarboxylation route, two proposed reaction mechanisms in the catalytic methanol reduction to ethylene, in the QM/MM approach. We found that hybrid functional level is required to accurately assess reaction energetics, prohibiting periodic calculations because of the relatively large unit cell of the ZSM-5 zeolite. The $\text{AlSi}_{17}\text{O}_{48}\text{H}$ cluster is shown to reproduce the electronic structure of the much more expensive periodic reference calculation. We found that even with the required gas phase formation of formaldehyde the decarboxylation route is energetically more favored by ≈ 0.5 eV. This difference can be explained by the difference in side products (CO and CO_2) and the related energy needed for conversion (water-gas shift reaction). The whole mechanism is, however, "adiabatically slaved" to the gas phase formation of the formaldehyde as this reaction yield the largest barrier. An external feed of formaldehyde would erase this barrier, and furthermore make the decarboxylation route exothermic.

12 Conclusion & Outlook

The increasing world population and increased standards of living in developing countries are predicted to result in a massive increase of energy demand in the next decades. Catalysis and photocatalysis are promising technologies to save and produce energy and fuels for a sustainable energy future. However, existing photocatalytic devices are far from operating on a level of efficiency, which is economically feasible for large scale energy production. To improve existing catalysts, extend their scope of applications or find new nanostructured compound catalysts, present theoretical models need to be revisited with fundamental research.

Computational approaches have been established as a powerful method to study such catalytic reaction from first-principles. Due to their favorable scaling with system size, the by far most widely used methods are such based on *density functional theory*. Due to subsequent progress in theory and numerical realization during the last 50 years these approaches have gained predictive power and are almost universally applicable from molecules to solid state materials. Particularly for addressing photocatalytic processes, where localized photoinduced charges and possible nanostructuring or defects complicate the standard periodic approach, QM/MM embedding is a most efficient alternative.

In this work, we implemented norm-conserving pseudopotentials to facilitate novel QM/MM functionalities for solid-state applications connecting the all-electron quantum chemistry package *FHI-aims* with the general QM/MM environment *ChemShell*. Efficiently exploiting the localized character of chemical processes, the expensive quantum mechanical description is reduced to the central chemically active region. Long range electrostatic interactions with the system remainder are accounted for on a classical level through adequate interatomic potentials. The norm-conserving pseudopotentials here are used to remove spurious charge leakage and overpolarization at the QM/MM boundary. We moreover provided global optimization functionalities to parametrize the embedding force field to achieve almost seamless coupling between QM and MM domains. In particular, this allows to explicitly account for the dielectric response of the surrounding crystal, a significant contribution for charged systems and charge-transfer processes. Furthermore, the relatively small number of electronic degrees of freedom allow for application of very accurate high-level quantum mechanical methods, such as hybrid and even double-hybrid density functionals. Exploiting *FHI-aims*' ability to calculate both cluster and periodic calculations on the same footing, we benchmarked our implementations against the standard approach with periodic boundary conditions. In doing so we discovered that accurate matching of QM and MM properties, especially of the high-frequency dielectric constant, is of utter importance to reproduce the work function and adsorption energies. Overall, we found that our QM/MM approach is well able to reproduce the electronic structure of the periodic calculation, with only minute overestimation of the band gap, and suggest it as powerful computational tool to study heterogeneous catalysis at oxide surfaces. Our implementations, both in *FHI-aims* and *ChemShell*, are available in the respective release versions.

We also considered first applications of our embedding framework to three distinct (photo-) catalytic materials. These materials are chemically very different, and require different embedding strategies, showing the flexibility of our implementation. Among many other applications,

the TiO₂ surface is particularly known for its ability to photocatalytically split water. However, the actual reaction mechanism, and in particular the role of defects and co-catalysts are far from being understood. Here, fundamental research is of utter importance. As a first step, we addressed the photocatalytic oxygen evolution reaction at the TiO₂ surface specifically questioning the necessary level of theory for predictive calculations. Allowing for most efficient application of second-order perturbation theory to solid-state materials through our QM/MM embedding, we conducted a screening study of different levels of exchange-correlation treatment up to the double-hybrid functionals. We found significant differences between semi-local and hybrid density functional theory, while further increasing the level to a double-hybrid description did not change the picture. In an ongoing follow-up collaboration with Prof. Frank Neese (MPI Mühlheim) we will further climb up the ladder of accuracy and address surface chemical reactions at TiO₂ through *coupled cluster* theory. This will then ultimately answer the question of the necessary level of theory.

In a second step, we addressed the bridging oxygen vacancy at the TiO₂ surface. There is strong experimental evidence that this type of defect is the key element of the photocatalytic potential of TiO₂. It not only provides a distinguished reaction site, it also acts as a charge trap for photo-excited holes. Thermodynamic stability of such defects in its various charge states is not yet really known. We addressed this question and found that over a wide range of electrochemical potentials and oxygen partial pressures, formation of the vacancy in the +2 charge state is favored. Here, stabilization through long-range dielectric response is found to play a significant role. This is important information for the theoretical TiO₂ community, which so far only considers the charge neutral defected or pristine surfaces. As the surface defect is also known to act as an anchor point for noble-metal nanoclusters, our findings pose a sensible starting point to investigate their applicability in photocatalytic water splitting as co-catalysts in future studies. The charge flexibility of the QM/MM approach will ultimately also allow to study charge-transfer processes and non-electron-proton-coupled reaction mechanisms from first principles.

In a third study we investigated the corner and step sites of the Magnesium Oxide (MgO) crystal, one of the most important classes of functional materials with wide application in the field of catalysis. Such corner and step sites present very little studied, yet promising reaction sites for novel catalytic applications. Here, we applied our QM/MM approach together with *ab-initio* thermodynamic techniques to compare stabilities of the O-vacancies and O/O₂-interstitials in several charge states. We found that polarizability of the MM region is very important to cope with the strong electric fields of the corner geometry. Surprisingly we also found that the concentration of O-interstitial defects at corner or step sites is almost 100% percent, over a wide range of oxygen partial pressures and temperature regimes. Such a corner site with O-interstitials possibly provides rich catalytic applications, especially of oxidative reactions.

In a last application, we showed the flexibility of our implementation to also treat porous materials. Specifically, we studied the ZSM-5 zeolite, a widely used catalyst in the petrochemical industry. Here, we investigated the catalytic reduction of methanol to ethylene. With a worldwide production of 140 million tons per year in 2011, ethylene production typically done by conventional steam cracking is a major consumer of energy. The ZSM-5 is a very promising candidate for an industrial catalyst for this very reaction. In an ongoing project together with the group of Prof. Johannes Lercher (TU München), we try to unravel the reaction energetics from experiment as well as theory. Here, we studied the proposed *decarbonylation* and *decarboxylation* reaction routes and compared relative total energies along the reaction pathway. We found that the *decarboxylation* is overall energetically favored. This difference can be explained by the difference in side products (CO and CO₂) and the related energy needed for conversion. The overall reaction rate is, however, hindered by the gas phase formation of formaldehyde as this

reaction yield the largest barrier of all steps. An external feed of formaldehyde would erase this barrier, and furthermore make the decarboxylation route exothermic. Further competing reaction mechanisms are to be assessed in the future.

In all these, chemically very different, catalyst materials only our QM/MM solid state embedding approach allowed to apply levels of theoretical accuracy not otherwise achievable. Furthermore, only through our embedding we were able to study defected and charged systems without computational artifacts inherent to standard periodic calculations.

Appendices

A Force Field generator

As discussed in Section 5, optimizing the force field parameters is crucial for seamless coupling of QM and MM region. Here, we present a *python* program based on the the differential evolutionary algorithm [150] from the python package *inspyred* [151]. Only a *python* version of at least 2.7 together with the *inspyred*-package needs to be installed before executing the program.

First, a set of “agents” with random force field parameters is spawned (*generateTrial*). It can be very useful to generate these random numbers within a physical motivated subspace (ParMin, ParMax), as the parameters can cover very different ranges. For every agent, the routine *getObj* writes an input file for the MD program of choice, executes and finally reads the observable the force field should be optimized for. An example routine generating an MgO input for *GULP* and reading the lattice constant and high frequency dielectric constant is given below (Fig. A.3). The cost function is calculated as the deviation of the specified observables (lattice parameters and dielectric constants)to specified target values (routine *evaluatePotSO*). From to the collective knowledge of the agents about the cost functions landscape, new agents with mutated force field parameters get spawned. Agents in unfavorable regions of parameter space get dismissed. By doing this iteratively, agents can explore the whole parameter space and find optimal force field parameters which minimize the cost function.

In principle, other optimization algorithms can be used as well, to explore surprisingly rough the landscape of the fitness function. We, however, found the differential evolutionary algorithm yielding fastest convergence to the global minimum.

```
#!/usr/bin/env python
# -*- coding: utf-8 -*-

from random import Random
from math import sqrt
from inspyred import ec
from inspyred.ec import terminators
from inspyred.ec import emo
import os, argparse, pylab, time

Nparam=8
Nobj=2

ParMin=[500., 0.10,0.0, 10000, 0.10, 10.0, 25.0, 0.33302]
ParMax=[2500., 0.40, 30.0, 35000., 0.40, 40., 79.00, 1.16902]
targets=[4.217,10.70 ]

def getObj(inp):
    [...]
```

Figure A.1: Program for force field optimization based on evolutionary algorithms, Part I.

```
def generateTrial( random, args):
    inp = [round(random.uniform( ParMin[i], ParMax[i]),10) for i in range( Nparam)]
    return inp

@ec.evaluators.evaluator
def evaluatePotSO( candidate, args):
    observables=getObj(candidate)
    fitness=0.
    for i in range( Nobj):
        fitness+=( observables[i]-targets[i])*( observables[i]-targets[i])
    fitness=sqrt( fitness)
    return fitness

def optimiseSO( max_eval, p_size, m_rate, verb = False, graph = False):
    rand = Random()
    rand.seed( int( time.time()))
    es = ec.DEA( rand)
    es.terminator = terminators.generation_termination
    es.observer = []
    final_pop = es.evolve(generator=generateTrial, evaluator=evaluatePotSO,
        pop_size=p_size, maximize=False, boulder=ec.Boulder(ParMin, ParMax),
        max_evaluations=max_eval, mutation_rate=m_rate,max_generations=max_eval)
    final_pop.sort( reverse=True)
    print( final_pop[0])

def main():
    par = argparse.ArgumentParser( description="Potential Optimiser utilising GULP.")
    par.add_argument( "-p", "--pop", dest="p_size", type=int, default=1000,
        help="Popularity size")
    par.add_argument( "-N", "--Nsteps", dest="max_eval", type=int, default=10000,
        help="Maximum number of iterations")
    par.add_argument( "-m", "--mutation", dest="m_rate", type=float, default=0.15,
        help="Mutation rate [0.0,1.0]")
    par.set_defaults( method_so=False, verb=False, graph=False)
    args = par.parse_args()

    optimiseSO( args.max_eval, args.p_size, args.m_rate, args.verb, args.graph)

if __name__ == "__main__":
    main()
```

Figure A.2: Program for force field optimization based on evolutionary algorithms, Part II.

```

def getObj(inp):
    observables=[0. for i in range( Nobj)]

    gulp_in=open('run.gin','w')

    gulp_in.write('opti prop comp ' + "\n" )
    gulp_in.write('cell' + "\n" )
    gulp_in.write('  4.2  4.2  4.2  90.0  90.0  90.0' + "\n" )
    gulp_in.write('frac' + "\n" )
    gulp_in.write('Mg core 0.0 0.0 0.0 2.0' + "\n" )
    gulp_in.write('Mg core 0.0 0.5 0.5 2.0' + "\n" )
    gulp_in.write('Mg core 0.5 0.5 0.0 2.0' + "\n" )
    gulp_in.write('Mg core 0.5 0.0 0.5 2.0' + "\n" )
    gulp_in.write('O core 0.5 0.5 0.5 {0:8f}'.format(inp[7])+ "\n" )
    gulp_in.write('O core 0.5 0.0 0.0 {0:8f}'.format(inp[7])+ "\n")
    gulp_in.write('O core 0.0 0.5 0.0 {0:8f}'.format(inp[7])+ "\n")
    gulp_in.write('O core 0.0 0.0 0.5 {0:8f}'.format(inp[7])+ "\n")
    gulp_in.write('O core 0.5 0.5 0.5 {0:8f}'.format(inp[7])+ "\n" )
    gulp_in.write('O core 0.5 0.0 0.0 {0:8f}'.format(-2-inp[7])+ "\n")
    gulp_in.write('O core 0.0 0.5 0.0 {0:8f}'.format(-2-inp[7])+ "\n")
    gulp_in.write('O core 0.0 0.0 0.5 {0:8f}'.format(-2-inp[7])+ "\n")
    gulp_in.write('buck ' + "\n")
    gulp_in.write('{0:24} {1:12f}{2:12f}{3:12f}{4:13}'.format(
        'O shel 0 shel ',inp[3],inp[4],inp[5], ' 12.00')+ "\n")
    gulp_in.write('{0:24} {1:12f}{2:12f}{3:12f}{4:13}'.format(
        'Mg core 0 shel ',inp[0],inp[1],inp[2], ' 10.00')+ "\n")
    gulp_in.write('spring ' + "\n")
    gulp_in.write('{0:13} {1:8f}'.format('O ', inp[6])+ "\n")
    gulp_in.write('stepmax 0.1'+ "\n" )

    gulp_in.close()

    os.popen('gulp run & sleep 0.2 ; kill $! 2>/dev/null')

    #####EXTRACT#OBSERVABLES#####
    try:
        gulp_out=open('run.gout','r')
        foo=gulp_out.read()
        a= float(foo[foo.find('Final Cart')+53:foo.find('Final Cart')+65].strip())
        diel_inf_a=float(foo[foo.find('High freq')+253:foo.find('High freq')+264].strip())

        print a, diel_inf_a

    except ValueError:
# in case GULP runs into an error, dismiss walker
        [a, diel_inf_a] = [-1., -10]

    observables=[a, diel_inf_a]

    return observables

```

Figure A.3: Script to write an file input for GULP, execute and extract observables for the example of MgO. This parts of the code needs to be adapted when used with a different MD calculator or for a different material.

List of Figures

2.1	Illustration of the first Hohenberg-Kohn theorem. The external potential V_{ext} defines the spectrum of many-body wavefunctions ψ_i through Schroedinger's equation (SE), including the ground state wavefunction ψ_0 , which trivially relates to the ground state electron density n_0 . The Hohenberg-Kohn theorem (HK) states that n_0 in turn determines the external potential V_{ext} , completing the cycle.	13
2.2	Illustration of the Kohn-Sham <i>ansatz</i> . The DFT descriptions of the many-body system (left) and the non-interacting <i>auxiliary</i> system (right) are connected through the assumption that the ground state densities of both systems are equal (arrow labeled KS), connecting any point to any other point. Therefore, all many-body properties are determined through solution of the Kohn-Sham auxiliary system of non-interacting electrons.	15
2.3	Illustrating an ionic pseudopotential and pseudo valence wavefunctions for Titanium with 18 core electrons generated with FHI98PP [80] using the procedure of Troullier and Martins. The left pictures compares the pseudo valence wavefunctions (solid lines) with the all-electron wavefunctions (dashed lines). The pseudo valence wavefunctions does not have nodes in the core region, while coinciding with the all-electron wave function beyond the core radius R_c . The right pictures shows the corresponding pseudopotentials V_l^{PP} for the s-, p-, and d-channel. Beyond R_c all V_l^{PP} are equal to the ionic reference potential, corresponding to the effective Coulomb potential of the nucleus ($Z = 22$) and core electrons ($Q_l = -18$).	22
3.1	Schematic representation of the embedded-cluster models used in the QM/MM calculations: The central QM atoms, represented by individual red and blue circles, is surrounded by regions of active (yellow) and frozen (light blue) MM atoms. If necessary, such as in ionic systems, an additional embedding potential (yellow circles) is included around the QM region in the form of atom-centered pseudopotentials (PPs). The outer shell of point charges (dark blue) is fitted to ensure reproduction of the correct long-range electrostatic potential within the active region.	32
3.2	QM/MM and Continuum Solvation Model. Left: The QM region (purple) hosting a net charge q is surrounded by the inner MM-region (brown), which allows for explicit polarization. Beyond a radius R the system's remainder (green) is treated as an isotropic continuous medium with dielectric constant ϵ' . Right: A sphere with radius R , dielectric constant ϵ and charge q localized at the center of the sphere is surrounded by a continuum with dielectric constant ϵ'	34

4.1	Accuracy of pseudopotentials on the level of LDA. The upper plot shows the dissociation between a pseudoized sodium atom (PP) and an all-electron (AE) sodium atom (green curve), compared to the reference curve between two AE atoms (blue). PP comprises an ionic sodium Na^+ -pseudopotential (incl. NLCC) augmented with an <i>aug-cc-pVTZ</i> -Gaussian basis set for hydrogen. The lower plot shows the computed forces in the PP-AE curve, referenced against the differential quotient of $\Delta E/\Delta x$	45
5.1	Convergence of cost function with the number of iterations for an MgO force field. The cost function (Eq. 5.1) was evaluated with equally weighted observables ($a = b = 1$). A number of 1000 agents with a mutation rate of 0.15 were used.	48
6.1	Species data for a pseudoized titanium atom. Starting from the default settings of the pseudoized species only a few flags need to be edited (documented in [156]). Furthermore, the default species integration parameters and the minimal basis (accept the minimal basis) need to be appended.	55
7.1	Sketching the steps from the optimized bulk unit cell to the final embedded cluster setup. Silver spheres depict titanium atoms, red spheres are oxygen QM atoms or MM cores and yellow spheres are oxygen shells. Blue spheres surrounding the MM region reproduce the Madelung potential in the QM region. See text for a detailed description.	61
7.2	Perspective view of the $\text{Ti}_{17}\text{O}_{34}$, $\text{Ti}_{29}\text{O}_{58}$, $\text{Ti}_{33}\text{O}_{66}$ and $\text{Ti}_{54}\text{O}_{108}$ clusters, exposing at their top center the fivefold coordinated Ti adsorption site of the $\text{TiO}_2(110)$ surface. Ti atoms are shown as large white spheres, O atoms as small red spheres, and semi-transparent grey spheres mark the positions where PPs represent the immediately surrounding Ti-cations.	63
7.3	Total density of states (DOS) of the $\text{Ti}_{54}\text{O}_{108}$ cluster in vacuum (a), the $\text{Ti}_{17}\text{O}_{34}$ cluster embedded in a field of point charges without using pseudopotentials to saturate the QM cluster (b) and the same cluster with nearby MM cations replaced by Ti^{4+} norm-conserving pseudopotentials. The DOS of the reference slab calculation is shown in (d). The resulting band structure is sampled very accurately in reciprocal space on a $40 \times 40 \times 1$ k-grid to converge the DOS. The vacuum level represents the zero reference throughout, in the slab defined as the potential in the middle of the vacuum between slabs. Filled states are depicted in darker color.	64
7.4	Difference of electron density of an $\text{Ti}_{17}\text{O}_{34}$ cluster embedded with and without pseudopotentials (isodensity surface 0.01), in top (left) and side view (right). Without pseudopotentials higher density accumulates at the cluster boundary (blue regions), leading to a slight electron depletion in the center of the cluster (red region).	65
7.5	The high-frequency dielectric constant ϵ_∞ , intrinsic core-shell separation and their effect on the ionization energy. The left plot shows ϵ_∞ of the MM bulk unit cell plotted against the square of the core-shell displacement of bridging surface oxygen atom d in the MM slab. For a weak spring potential, shell displacements leave the harmonic regime (dashed line). The right plot shows resulting ionization potentials, a.k.a. the highest occupied orbital, of a $\text{Ti}_{17}\text{O}_{34}$ cluster embedded with different spring potentials. The blue line corresponds to the valence band maximum of a periodic DFT slab calculation.	66

7.6	Self-consistent shell displacements in the embedded cluster calculation as a function of distance to the cluster center. A charge neutral $\text{Ti}_{17}\text{O}_{34}$ cluster with 151 PPs is embedded in an active MM region with 25 bohr radius. Together with the fixed MM region and fitted background charges a total number of 9203 point charges are used. The short range parameters and shell charges are taken from Jentys and Catlow [175], the core-shell spring potential was modified as labeled in the legend.	67
7.7	Comparison of the total density of states (DOS) without polarization response: Even a relatively small embedded $\text{Ti}_{17}\text{O}_{34}$ cluster (left panel) recovers important features from the reference slab calculation (in blue colors). Finite cluster artifacts can further be reduced, when increasing the cluster size. The embedded $\text{Ti}_{54}\text{O}_{108}$ cluster achieves almost perfect agreement with the corresponding PBC supercell calculations (right panel), in particular in the valence and lower conduction band region. Again, the vacuum level represents the zero reference throughout, and filled states are depicted in darker color.	68
7.8	Total density of states with (right) and without (left) polarization response. The short-range parameters from Jentys and Catlow were used together with a cosh-spring for the oxygen core-shell interaction ($k=20$, $d=0.15$), which yield an acceptable description of the high frequency dielectric tensor ($\epsilon_{\infty}^a = 5.8$, $\epsilon_{\infty}^c = 9.8$).	69
7.9	Binding energy of O (top), OH (middle) and OOH (bottom) with (right) and without (right) self-consistent polarization response. The $\text{Ti}_{17}\text{O}_{34}$ and the $\text{Ti}_{33}\text{O}_{66}$ cluster were embedded in the force field by Jentys and Catlow with modified spring constant k . The blue lines correspond to respective results from the 5×3 supercell calculation.	72
7.10	Mulliken charges of adsorbed O (top), OH (middle) and OOH (bottom) with (right) and without (right) self-consistent polarization response. The $\text{Ti}_{17}\text{O}_{34}$ and $\text{Ti}_{33}\text{O}_{66}$ clusters were embedded in the force field by Jentys and Catlow [175] with modified spring constant k . Blue lines correspond to respective results from the 5×3 supercell calculation.	74
7.11	Energetic position of the HOMO for the O, OH and OOH, relative to the HOMO energy of the clean surface, as a function of the coverage. Calculations were performed in different supercells (left) and with different embedded cluster sizes (right) using the force field by Jentys and Catlow with a spring constant of $k=35$. Self-consistent polarization is neglected.	75
8.1	Density of states (DOS) of the ideal $\text{TiO}_2(110)$ surface as calculated with the embedded $\text{Ti}_{17}\text{O}_{34}$ cluster (red) and with a supercell geometry (blue). The valence band maximum is used as zero reference and filled states are depicted in darker color. A Gaussian smearing ($\sigma = 0.1$) is applied.	85
9.1	Schematic representation of the employed concentric solid-state embedding approach. A quantum-mechanical (QM) region hosting the oxygen vacancy is surrounded by a molecular mechanics (MM) region represented by a polarizable force field. Spurious charge leakage out of the QM region is prevented through a transition shell, in which cations are described with effective core potentials (ECPs). The full electrostatic potential of the infinite crystal surface is reproduced by placing point charges with fitted values around the MM region.	88
9.2	Perspective view of the employed clusters: (a) $\text{Ti}_{22}\text{O}_{43}$, (b) $\text{Ti}_{32}\text{O}_{63}$, each exhibiting a surface O vacancy in their central bridging O atom row. Ti atoms are shown as large white spheres, O atoms as small red spheres, and semi-transparent gray spheres mark the positions where ECPs represent the immediately surrounding Ti-cations.	91

9.3	Density of states (DOS) of the ideal $\text{TiO}_2(110)$ surface per TiO_2 formula unit as calculated with the embedded $\text{Ti}_{32}\text{O}_{66}$ cluster (red) and with a supercell geometry (blue). The valence band maximum is used as zero reference and filled states are depicted in darker color. A Gaussian smearing ($\sigma = 0.1$) is applied.	93
9.4	Calculated formation energies of the relaxed surface oxygen vacancy in oxygen rich (left) and oxygen poor conditions (right). The Fermi energy is normalized to the valence band maximum.	98
10.1	(a) Structural defects in an extended MgO surface (namely, corners and steps), (b) (upper panel) different types of defects (namely, O-vacancy, O-interstitial, O_2 -interstitial) at the corners, (lower panel) model clusters $\text{Mg}_{32}\text{O}_{32+n}$ (corner) and $\text{Mg}_{25}\text{O}_{25+n}$ (step) to be used for the QM region of the embedded cluster model calculation, (c) and the full embedded cluster models (see text for details).	103
10.2	Phase diagram for embedded $\text{Mg}_{25}\text{O}_{(25+n)}$ (step) and embedded $\text{Mg}_{32}\text{O}_{(32+n)}$ cluster (corner) with O-vacancy ($n = -1$), pristine ($n = 0$), O-interstitial ($n = 1$), O_2 -interstitial ($n = 2$) clusters in the oxygen atmosphere. Geometry optimization and total energies are calculated with HSE06+vdW. The yellow box highlights the experimentally accessible regime.	106
10.3	Kohn-Sham spectrum of embedded- $[\text{Mg}_{32}\text{O}_{32+n}]^q$ [$n = 0, -1, 1$ with $q = 0, 1$] clusters. Competition between bond breaking and electron transfer.	107
10.4	Concentration of O-vacancies and O/ O_2 -interstitials at the corner sites of the MgO crystal at various temperatures and pressures at $\mu_e = -7.5$ eV.	108
11.1	Illustration of the QM clusters used in our calculations of Fe-ZSM-5: (a) M7-T1; (b) Z6-T4; and (c) I2-T12. Fe, Si, O and H atoms are represented in yellow, mauve, red and white, respectively. The extended embedding environment included in the QM calculation of (c) is illustrated in (d), with the MM point charges represented in grey.	111
11.2	Adsorption and carbonylation of methanol at the zeolite acid site (red).	113
11.3	<i>Decarbonylation route.</i> The CH_3CO group adsorbed at the zeolite acid site (Z) is methylated and then decarbonylated. Desorption of ethylene (green) leaves the protonated acid site (red).	113
11.4	<i>Decarboxylation route.</i> Formaldehyde is added to the CH_3CO group adsorbed at the zeolite acid site (Z) creating an aldol. Upon reaction with a gas phase water molecule, 2-propanoic acid is formed and desorbed, leaving the protonated zeolite acid site (red). Final decarboxylation yields gas phase ethylene (green).	114
11.5	Perspective view on the two QM clusters centered around the aluminum atom (green). The small $\text{AlSi}_4\text{O}_{16}\text{H}$ cluster shown on the left is terminated with 13 hydrogen atoms, the large $\text{AlSi}_{17}\text{O}_{48}\text{H}$ cluster (right) with additional 25 hydrogen atoms for cluster termination. Silicon atoms are marked as yellow, oxygen as red spheres. Terminating hydrogen and embedding point charges are white.	115
11.6	Bond distances at the protonated and acetylated acid site, calculated in Cluster I (a) & (d), Cluster II (b)&(e) and the periodic setup (c)&(f). The aluminum atom is silver, silicon is beige, oxygen is red and hydrogen is white.	117
A.1	Program for force field optimization based on evolutionary algorithms, Part I.	127
A.2	Program for force field optimization based on evolutionary algorithms, Part II.	128
A.3	Script to write an file input for GULP, execute and extract observables for the example of MgO. This parts of the code needs to be adapted when used with a different MD calculator or for a different material.	129

List of Tables

2.1	Comparison between the "Physicist's" and "Chemist's" numerical realization of DFT.	19
7.1	Important material properties of rutile TiO_2 calculated with DFT-rPBE. The structure of the bulk rutile TiO_2 unit cell is given by the lattice parameters a and c and the internal parameter u defining the position of oxygen atoms [171]. The electronic structure of the corresponding (110) surface is characterized through values for the band gap $E_{\text{Gap}}(\text{eV})$ and the eigenvalue of the valence band maximum ϵ_{VBM} with respect to the vacuum level, determined in the middle of the vacuum between slabs. The unit cell and surface supercell are optimized with the BFGS algorithm until residual forces are below $0.001 \text{ eV}/\text{\AA}$. Reciprocal space has been thoroughly sampled on a $8 \times 8 \times 8$ k-grid for the bulk unit cell, respectively a $4 \times 8 \times 1$ k-grid for the primitive (1x1) surface supercell. Tight settings and the tier 2 basis set have been used.	62
7.2	Calculated rPBE binding energies (in eV) of O, OH and OOH on the rutile $\text{TiO}_2(110)$ surface. Compared are results from slab calculation with different unit cells, with a free cluster calculation and the embedded cluster without using PPs.	71
7.3	Comparing binding energies (in eV) for embedding with local and fully nonlocal pseudopotentials. The embedded $\text{Ti}_{54}\text{O}_{108}$ cluster serves as reference for the low coverage limit.	75
8.1	Calculated binding energies (in eV) of O, OH and OOH on the rutile $\text{TiO}_2(110)$ surface. Results are obtained for an embedded $\text{Ti}_{17}\text{O}_{34}$ cluster at different levels of theory (GGA, hybrid and double-hybrid), see text. The right hand table shows results referenced against the standard hydrogen electrode (SHE) following Eqs. (10-12) of Ref. [194].	83
8.2	Force field parameters for HSE06 and their resulting unit cell properties, lattice parameters a and c as well as high frequency dielectric constants along the axes. Parameters were optimized under the constraint of $u = 0.305$, with u being the internal parameter of the rutile unit cell. Results are compared to experiments and another first-principle study also applying HSE06.	84
8.3	Binding energies (in eV) of O, OH and OOH with different underlying geometries, without relaxation upon adsorption. An embedded $\text{Ti}_{17}\text{O}_{34}$ cluster represents the QM region in the QM/MM approach. Slab calculations with the HSE06 calculation were performed on a 2×1 supercell. Finite size effects are estimated from rPBE results, adding up to results labeled $(4 \times 2)^*$ (see text).	85

9.1	Rutile TiO ₂ lattice constants a and c , as well as its static (ϵ_o^a , ϵ_o^c) and high-frequency (ϵ_∞^a and ϵ_∞^c) dielectric constants along the corresponding axes. Literature data from experiment [159, 198, 199] and DFT-HSE06 calculations [177] are compared against our own calculations at the DFT-HSE06 level and with the parametrized force field for the MM region (see text).	89
9.2	Interatomic potential parameters, optimized to reproduce the bulk TiO ₂ DFT-HSE06 lattice parameters and high-frequency dielectric constants, see text.	90
9.3	Unrelaxed surface defect formation energies in the oxygen-rich limit and for a Fermi-level position at the VBM. Shown are results for the two different QM clusters and, in the case of the neutral defect, from the supercell reference calculation. Upper rows correspond to a QM/MM setup, in which the electronic polarization response to the defect is treated through self-consistent relaxation of the MM shells. Lower rows correspond to a QM/MM setup, where this response is approximately obtained through an analytical polarization correction approach (see text).	94
9.4	Relaxed surface defect formation energies for the two different QM clusters in the O-rich limit and using the VBM as Fermi-level position. Upper rows (a) correspond to a QM/MM setup, in which only the electronic polarization response to the defect is treated through self-consistent relaxation of the MM shells. The next rows show results without MM polarization but the analytic correction ((b) ϵ_∞ in Eq. 9.5), then full ((c) ϵ_0 in Eq. 9.5). Rows (e) and (f) compile the results for the (a) together with the analytic correction for the static response (ϵ_0) (see text).	96
10.1	Interatomic potential parameters, optimized to reproduce the bulk MgO DFT-HSE06 lattice parameter and static and high-frequency dielectric constants (see Table 10.2).	102
10.2	Lattice constant (a) as well as the static (ϵ_o) and high-frequency (ϵ_∞) dielectric constants of bulk MgO. Literature data from experiment [250] and DFT-HSE06 calculations [249] are compared against our own calculations at the DFT-HSE06 level and with the parametrized force field for the MM region (see Table 10.1).	104
11.1	Computed reduction potentials (in eV) for Fe ^{3+/2+} embedded intra-framework within an MFI siliceous structure. Active sites are modeled as the M7-T1, Z6-T4 and I2-T12 sites shown in Fig. 11.1. Calculations performed using semi-local and hybrid functionals used the <i>tier2</i> basis level for all atoms; at the double hybrid-level the NAO-VCC-4Z basis set was used for all atoms except Fe, for which — due to the lack of Fe VCC basis set — a <i>tier3</i> basis set was used.	112
11.2	Relative energy differences of educts and the final products of the carbonylation reaction shown in Fig. 11.2 (sum of both steps). Results from the two embedded clusters are compared with periodic reference results (PBC) on the BLYP-level of xc-functional. Further, results for Cluster I and II using the hybrid functional B3LYP are listed.	117
11.3	Energetics of the decarbonylation and decarboxylation route as described in Fig. 11.3 and Fig. 11.4 and calculated in the embedded AlSi ₁₇ O ₄₈ H cluster. ΔE^{tot} is shown for every reaction step and as the sum of all steps Σ . Step C of the decarboxylation route is a gas phase reaction and thus calculated in absence of the zeolite framework.	118

Bibliography

- [1] *International Energy Outlook 2014: US Department of Energy*, <http://www.eia.gov/forecasts/ieo/>, Accessed: 2014-11-1 (cit. on p. 1).
- [2] A. Fujishima and K Honda, *Electrochemical Photolysis of Water at a Semiconductor Electrode*, *Nature* **238**, 37 (1972), (cit. on p. 1).
- [3] J. Yang, D. Wang, H. Han, and C. Li, *Roles of Cocatalysts in Photocatalysis and Photoelectrocatalysis*, *Acc. Chem. Res.* **46**, 1900 (2013), (cit. on p. 1).
- [4] W. Kohn, A. D. Becke, and R. G. Parr, *Density Functional Theory of Electronic Structure*, *J.Phys.Chem.* **100**, 12974 (1996), (cit. on p. 1).
- [5] A. D. Becke, *Perspective: Fifty years of density-functional theory in chemical physics*, *J. Chem. Phys.* **140**, – (2014), (cit. on pp. 1, 7).
- [6] W.-T. Kim, C.-D. Kim, and Q. W. Choi, *Sub-band-gap photoresponse of TiO_{2-x} thin-film electrolyte interface*, *Phys. Rev. B* **30**, 3625 (1984), (cit. on pp. 3, 87).
- [7] C. M. Yim, C. L. Pang, and G. Thornton, *Oxygen Vacancy Origin of the Surface Band-Gap State of TiO₂(110)*, *Phys. Rev. Lett.* **104**, 036806 (2010), (cit. on p. 3).
- [8] S. Wendt, R. Bechstein, S. Porsgaard, E. Lira, J. O. Hansen, P. Huo, Z. Li, B. Hammer, and F. Besenbacher, *Comment on “Oxygen Vacancy Origin of the Surface Band-Gap State of TiO₂(110)”*, *Phys. Rev. Lett.* **104**, 259703 (2010), (cit. on p. 3).
- [9] C. M. Yim, C. L. Pang, and G. Thornton, *Yim, Pang, and Thornton Reply*: *Phys. Rev. Lett.* **104**, 259704 (2010), (cit. on p. 3).
- [10] L. Giordano, J. Goniakowski, and J. Suzanne, *Partial Dissociation of Water Molecules in the (3 × 2) Water Monolayer Deposited on the MgO (100) Surface*, *Phys. Rev. Lett.* **81**, 1271 (1998), (cit. on pp. 3, 101).
- [11] C. A. Scamehorn, N. M. Harrison, and M. I. McCarthy, *Water chemistry on surface defect sites: Chemidissociation versus physisorption on MgO(001)*, *J. Chem. Phys.* **101**, 1547 (1994), (cit. on pp. 3, 101).
- [12] L. M. Molina and B. Hammer, *Theoretical study of CO oxidation on Au nanoparticles supported by MgO(100)*, *Phys. Rev. B* **69**, 155424 (2004), (cit. on pp. 3, 101).
- [13] C. R. Henry, *Surface studies of supported model catalysts*, *Surf. Sci. Rep.* **31**, 231 (1998), (cit. on pp. 3, 101).
- [14] R. M. Martin, *Electronic structure: basic theory and practical methods*, Cambridge university press, 2004, (cit. on pp. 7, 17).
- [15] A. Szabo and N. S. Ostlund, *Modern Quantum Chemistry: Introduction to Advanced Electronic Structure Theory*, Dover Publications, Mineola, New York, 1996, (cit. on pp. 7, 12).
- [16] E. Schrödinger, *Quantisierung als Eigenwertproblem*, *Ann. Phys.* **385**, 437 (1926), (cit. on p. 7).

- [17] A. Warshel and M. Levitt, *Theoretical studies of enzymic reactions: Dielectric, electrostatic and steric stabilization of the carbonium ion in the reaction of lysozyme*, J. Mol. Biol. **103**, 227 (1976), (cit. on p. 7).
- [18] M. J. Field, P. A. Bash, and M. Karplus, *A combined quantum mechanical and molecular mechanical potential for molecular dynamics simulations*, J. Comput. Chem. **11**, 700 (1990), (cit. on pp. 7, 28).
- [19] N. Bernstein, J. R. Kermode, and G. Csányi, *Hybrid atomistic simulation methods for materials systems*, Rep. Prog. Phys. **72**, 026501 (2009), (cit. on p. 7).
- [20] H. Lin and D. Truhlar, *QM/MM: what have we learned, where are we, and where do we go from here?*, Theor. Chem. Acc. **117**, 185, (cit. on p. 7).
- [21] D. R. Hartree, “The Wave Mechanics of an Atom with a Non-Coulomb Central Field. Part I. Theory and Methods”, 1928, (cit. on pp. 9, 11).
- [22] M. Born and R. Oppenheimer, *Zur Quantentheorie der Molekeln*, Ann. Phys. **389**, 457 (1927), (cit. on p. 9).
- [23] V. Fock, *Näherungsmethode zur Lösung des quantenmechanischen Mehrkörperproblems*, Z. Phys. **61**, 126 (1930), (cit. on p. 11).
- [24] J. C. Slater, *The Theory of Complex Spectra*, Phys. Rev. **34**, 1293 (1929), (cit. on p. 11).
- [25] C. J. Cramer, *Essentials of Computational Chemistry*, John Wiley and Sons, Chichester, 2002, (cit. on p. 12).
- [26] F. Jensen, *Introduction to computational chemistry*, John Wiley & Sons, 2007, (cit. on p. 12).
- [27] G. H. Booth, A. Grüneis, G. Kresse, and A. Alavi, *Towards an exact description of electronic wavefunctions in real solids*, Nature **493**, 365 (2013), (cit. on p. 12).
- [28] L. H. Thomas, *The calculation of atomic fields*, Math. Proc. Cambridge Philos. Soc. **23**, 542 (1927), (cit. on p. 12).
- [29] E. Fermi, *Un metodo statistico per la determinazione di alcune priorieta dell’atome*, Rend. Accad. Naz. Lincei **6**, 32 (1927), (cit. on p. 12).
- [30] P. A. M. Dirac, *Note on Exchange Phenomena in the Thomas Atom*, Math. Proc. Cambridge Philos. Soc. **26**, 376 (1930), (cit. on pp. 12, 17).
- [31] C. Weizsäcker, *Zur Theorie der Kernmassen*, Z. Phys. **96**, 431 (1935), (cit. on p. 12).
- [32] E. Teller, *On the Stability of Molecules in the Thomas-Fermi Theory*, Rev. Mod. Phys. **34**, 627 (1962), (cit. on p. 12).
- [33] M. Bender, P.-H. Heenen, and P.-G. Reinhard, *Self-consistent mean-field models for nuclear structure*, Rev. Mod. Phys. **75**, 121 (2003), (cit. on p. 13).
- [34] J. Erler, N. Birge, M. Kortelainen, W. Nazarewicz, E. Olsen, A. M. Perhac, and M. Stoitsov, *The limits of the nuclear landscape*, Nature **486**, 509 (2012), (cit. on p. 13).
- [35] P. Hohenberg and W. Kohn, *Inhomogeneous Electron Gas*, Phys. Rev. **136**, B864 (1964), (cit. on p. 13).
- [36] R. M. Dreizler and E. K. Gross, *Density functional theory*, Springer, 1990, (cit. on p. 13).
- [37] H. Eschrig, *The fundamentals of density functional theory*, Springer, 1996, (cit. on p. 13).
- [38] M. Levy, *Universal variational functionals of electron densities, first-order density matrices, and natural spin-orbitals and solution of the v -representability problem*, PNAS **76**, 6062 (1979), (cit. on p. 13).

-
- [39] E. H. Lieb, *Density functionals for coulomb systems*, Int. J. Quantum Chem. **24**, 243 (1983), (cit. on p. 13).
- [40] T. L. Gilbert, *Hohenberg-Kohn theorem for nonlocal external potentials*, Phys. Rev. B **12**, 2111 (1975), (cit. on p. 14).
- [41] W. Kohn and L. J. Sham, *Self-Consistent Equations Including Exchange and Correlation Effects*, Phys. Rev. **140**, A1133 (1965), (cit. on p. 14).
- [42] J. P. Perdew, K. Burke, and M. Ernzerhof, *Generalized Gradient Approximation Made Simple*, Phys. Rev. Lett. **77**, 3865 (1996), (cit. on pp. 15, 17, 89, 111).
- [43] C. Adamo and V. Barone, *Toward reliable density functional methods without adjustable parameters: The PBE0 model*, J. Chem. Phys. **110**, 6158 (1999), (cit. on pp. 15, 18, 111).
- [44] J. Heyd, G. E. Scuseria, and M. Ernzerhof, *Hybrid functionals based on a screened Coulomb potential*, J. Chem. Phys. **118**, 8207 (2003), (cit. on pp. 15, 18, 88, 105).
- [45] J. Harris, *Adiabatic-connection approach to Kohn-Sham theory*, Phys. Rev. A **29**, 1648 (1984), (cit. on p. 16).
- [46] U. von Barth and L. Hedin, *A local exchange-correlation potential for the spin polarized case. i*, J. Phys. C: Solid State Phys. **5**, 1629 (1972), (cit. on p. 17).
- [47] L. Hedin and S. Lundquist, *Solid state physics*, Academic Press, New York, 1969, (cit. on p. 17).
- [48] B. Holm, *Total Energies from GW Calculations*, Phys. Rev. Lett. **83**, 788 (1999), (cit. on p. 17).
- [49] D. Ceperley, *Ground state of the fermion one-component plasma: A Monte Carlo study in two and three dimensions*, Phys. Rev. B **18**, 3126 (1978), (cit. on p. 17).
- [50] D. M. Ceperley and B. J. Alder, *Ground State of the Electron Gas by a Stochastic Method*, Phys. Rev. Lett. **45**, 566 (1980), (cit. on p. 17).
- [51] G. Ortiz and P. Ballone, *Correlation energy, structure factor, radial distribution function, and momentum distribution of the spin-polarized uniform electron gas*, Phys. Rev. B **50**, 1391 (1994), (cit. on p. 17).
- [52] Y. Kwon, D. M. Ceperley, and R. M. Martin, *Effects of backflow correlation in the three-dimensional electron gas: Quantum Monte Carlo study*, Phys. Rev. B **58**, 6800 (1998), (cit. on p. 17).
- [53] A. D. Becke, *Density-functional exchange-energy approximation with correct asymptotic behavior*, Phys. Rev. A **38**, 3098 (1988), (cit. on pp. 17, 111, 114).
- [54] J. P. Perdew and Y. Wang, *Accurate and simple analytic representation of the electron-gas correlation energy*, Phys. Rev. B **45**, 13244 (1992), (cit. on pp. 17, 114).
- [55] B. Hammer, L. B. Hansen, and J. K. Nørskov, *Improved adsorption energetics within density-functional theory using revised Perdew-Burke-Ernzerhof functionals*, Phys. Rev. B **59**, 7413 (1999), (cit. on pp. 17, 81).
- [56] Y. Zhao and D. Truhlar, *The M06 suite of density functionals for main group thermochemistry, thermochemical kinetics, noncovalent interactions, excited states, and transition elements: two new functionals and systematic testing of four M06-class functionals and 12 other functionals*, Theor. Chem. Acc. **120**, 215 (2008), (cit. on p. 17).

- [57] V. I. Anisimov, A. I. Poteryaev, M. A. Korotin, A. O. Anokhin, and G. Kotliar, *First-principles calculations of the electronic structure and spectra of strongly correlated systems: dynamical mean-field theory*, J. Phys. Condens. Matter **9**, 7359 (1997), (cit. on p. 17).
- [58] J. P. Perdew and A. Zunger, *Self-interaction correction to density-functional approximations for many-electron systems*, Phys. Rev. B **23**, 5048 (1981), (cit. on p. 17).
- [59] G. E. Scuseria and V. N. Staroverov, *Progress in the development of exchange-correlation functionals*, 2005 (cit. on p. 18).
- [60] R. Baer, E. Livshits, and U. Salzner, *Tuned Range-Separated Hybrids in Density Functional Theory*, Annu. Rev. Phys. Chem. **61**, 85 (2010), (cit. on p. 18).
- [61] O. A. von Lilienfeld, I. Tavernelli, U. Rothlisberger, and D. Sebastiani, *Optimization of Effective Atom Centered Potentials for London Dispersion Forces in Density Functional Theory*, Phys. Rev. Lett. **93**, 153004 (2004), (cit. on p. 18).
- [62] D. C. Langreth, M. Dion, H. Rydberg, E. Schröder, P. Hyldgaard, and B. I. Lundqvist, *Van der Waals density functional theory with applications*, Int. J. Quantum Chem. **101**, 599 (2005), (cit. on p. 18).
- [63] A. Tkatchenko and M. Scheffler, *Accurate Molecular Van Der Waals Interactions from Ground-State Electron Density and Free-Atom Reference Data*, Phys. Rev. Lett. **102**, 073005 (2009), (cit. on pp. 18, 105, 115).
- [64] Y. Zhao, J. Pu, B. J. Lynch, and D. G. Truhlar, *Tests of second-generation and third-generation density functionals for thermochemical kinetics*, Phys. Chem. Chem. Phys. **6**, 673 (2004), (cit. on p. 18).
- [65] S. Grimme, *Semiempirical hybrid density functional with perturbative second-order correlation*, J. Chem. Phys. **124**, – (2006), (cit. on p. 18).
- [66] T. Schwabe and S. Grimme, *Double-hybrid density functionals with long-range dispersion corrections: higher accuracy and extended applicability*, Phys. Chem. Chem. Phys. **9**, 3397 (2007), (cit. on p. 18).
- [67] C. Kittel and P. McEuen, *Introduction to solid state physics*, Wiley, New York, 1986, (cit. on p. 19).
- [68] N. W. Ashcroft and N. D. Mermin, *Solid state physics*, Holt, Rinehart and Winston, New York, 1976, (cit. on p. 19).
- [69] H. J. Monkhorst and J. D. Pack, *Special points for Brillouin-zone integrations*, Phys. Rev. B **13**, 5188 (1976), (cit. on pp. 20, 82, 88).
- [70] T. H. Dunning, *Gaussian basis sets for use in correlated molecular calculations. I. The atoms boron through neon and hydrogen*, J. Chem. Phys. **90**, 1007 (1989), (cit. on p. 20).
- [71] N. Godbout, D. R. Salahub, J. Andzelm, and E. Wimmer, *Optimization of Gaussian-type basis sets for local spin density functional calculations. Part I. Boron through neon, optimization technique and validation*, Can. J. Chem. **70**, 560 (1992), (cit. on p. 20).
- [72] R. Ditchfield, W. J. Hehre, and J. A. Pople, *Self-consistent molecular-orbital methods. IX. An extended Gaussian-type basis for molecular-orbital studies of organic molecules*, J. Chem. Phys. **54**, 724 (2003), (cit. on p. 20).
- [73] W. J. Hehre, R. Ditchfield, and J. A. Pople, *Self-consistent molecular orbital methods. XII. Further extensions of Gaussian-type basis sets for use in molecular orbital studies of organic molecules*, J. Chem. Phys. **56**, 2257 (1972), (cit. on p. 20).

-
- [74] S. Boys and F. Bernardi, *The calculation of small molecular interactions by the differences of separate total energies. Some procedures with reduced errors*, Mol. Phys. **19**, 553 (1970), (cit. on p. 21).
- [75] F. B. van Duijneveldt, J. G. C. M. van Duijneveldt-van de Rijdt, and J. H. van Lenthe, *State of the Art in Counterpoise Theory*, Chem. Rev. **94**, 1873 (1994), (cit. on p. 21).
- [76] B. Paizs and S. Suhai, *Comparative study of BSSE correction methods at DFT and MP2 levels of theory*, J. Comput. Chem. **19**, 575 (1998), (cit. on p. 21).
- [77] P. E. Blöchl, *Projector augmented-wave method*, Phys. Rev. B **50**, 17953 (1994), (cit. on p. 21).
- [78] A. H. Larsen, M. Vanin, J. J. Mortensen, K. S. Thygesen, and K. W. Jacobsen, *Localized atomic basis set in the projector augmented wave method*, Phys. Rev. B **80**, 195112 (2009), (cit. on p. 21).
- [79] D. R. Hamann, M. Schlüter, and C. Chiang, *Norm-Conserving Pseudopotentials*, Phys. Rev. Lett. **43**, 1494 (1979), (cit. on p. 22).
- [80] M. Fuchs and M. Scheffler, *Ab initio pseudopotentials for electronic structure calculations of poly-atomic systems using density-functional theory*, Comput. Phys. Commun. **119**, 67 (1999), (cit. on pp. 22, 39, 40, 44, 55, 88).
- [81] A. Messiah, *Quantum mechanics*, Courier Dover Publications, 2014, (cit. on p. 23).
- [82] G. P. Kerker, *Non-singular atomic pseudopotentials for solid state applications*, J. Phys. C: Solid State Phys. **13**, L189 (1980), (cit. on p. 23).
- [83] G. B. Bachelet, D. R. Hamann, and M. Schlüter, *Pseudopotentials that work: From H to Pu*, Phys. Rev. B **26**, 4199 (1982), (cit. on p. 23).
- [84] N. Troullier and J. L. Martins, *Efficient pseudopotentials for plane-wave calculations*, Phys. Rev. B **43**, 1993 (1991), (cit. on p. 23).
- [85] D. Vanderbilt, *Soft self-consistent pseudopotentials in a generalized eigenvalue formalism*, Phys. Rev. B **41**, 7892 (1990), (cit. on p. 23).
- [86] K. Toukan and A. Rahman, *Molecular-dynamics study of atomic motions in water*, Phys. Rev. B **31**, 2643 (1985), (cit. on p. 25).
- [87] G. Makov and M. C. Payne, *Periodic boundary conditions in ab initio calculations*, Phys. Rev. B **51**, 4014 (1995), (cit. on pp. 25, 31, 70).
- [88] S. Lany and A. Zunger, *Assessment of correction methods for the band-gap problem and for finite-size effects in supercell defect calculations: Case studies for ZnO and GaAs*, Phys. Rev. B **78**, 235104 (2008), (cit. on p. 25).
- [89] S. Lany and A. Zunger, *Accurate prediction of defect properties in density functional supercell calculations*, Modell. Simul. Mater. Sci. Eng. **17**, 084002 (2009), (cit. on pp. 25, 31).
- [90] C. Freysoldt, J. Neugebauer, and C. G. Van de Walle, *Fully Ab Initio Finite-Size Corrections for Charged-Defect Supercell Calculations*, Phys. Rev. Lett. **102**, 016402 (2009), (cit. on p. 25).
- [91] C. Freysoldt, J. Neugebauer, and C. G. Van de Walle, *Electrostatic interactions between charged defects in supercells*, physica status solidi (b) **248**, 1067 (2011), (cit. on p. 25).
- [92] C. Freysoldt, B. Grabowski, T. Hickel, J. Neugebauer, G. Kresse, A. Janotti, and C. G. Van de Walle, *First-principles calculations for point defects in solids*, Rev. Mod. Phys. **86**, 253 (2014), (cit. on p. 25).

- [93] H.-P. Komsa and A. Pasquarello, *Finite-Size Supercell Correction for Charged Defects at Surfaces and Interfaces*, Phys. Rev. Lett. **110**, 095505 (2013), (cit. on p. 25).
- [94] L. Vegard, *Die Konstitution der Mischkristalle und die Raumfüllung der Atome*, Z. Phys. **5**, 17 (1921), (cit. on p. 25).
- [95] J. Cheng, M. Sulpizi, J. VandeVondele, and M. Sprik, *Hole Localization and Thermochemistry of Oxidative Dehydrogenation of Aqueous Rutile TiO₂(110)*, ChemCatChem **4**, 636 (2012), (cit. on p. 25).
- [96] M. Born, *Volumen und Hydratationswärme der Ionen*, Z. Phys. **1**, 45 (1920), (cit. on p. 25).
- [97] L. Onsager, *Electric Moments of Molecules in Liquids*, J. Am. Chem. Soc. **58**, 1486 (1936), (cit. on p. 25).
- [98] J. Tomasi, B. Mennucci, and R. Cammi, *Quantum Mechanical Continuum Solvation Models*, Chem. Rev. **105**, 2999 (2005), (cit. on p. 25).
- [99] C. J. Cramer and D. G. Truhlar, *Continuum solvation models*, Springer, 2002, (cit. on p. 25).
- [100] T. A. Wesolowski and A. Warshel, *Frozen density functional approach for ab initio calculations of solvated molecules*, J.Phys.Chem. **97**, 8050 (1993), (cit. on p. 25).
- [101] N. Govind, Y. A. Wang, and E. A. Carter, *Electronic-structure calculations by first-principles density-based embedding of explicitly correlated systems*, J. Chem. Phys. **110**, 7677 (1999), (cit. on p. 25).
- [102] F. R. Manby, M. Stella, J. D. Goodpaster, and T. F. Miller, *A Simple, Exact Density-Functional-Theory Embedding Scheme*, J. Chem. Theory Comput. **8**, 2564 (2012), (cit. on p. 25).
- [103] P. P. Ewald, *Die Berechnung optischer und elektrostatischer Gitterpotentiale*, Ann. Phys. **369**, 253 (1921), (cit. on pp. 26, 30).
- [104] A. Toniolo, G. Granucci, and T. J. Martínez, *Conical Intersections in Solution: A QM/MM Study Using Floating Occupation Semiempirical Configuration Interaction Wave Functions*, J.Phys.Chem. A **107**, 3822 (2003), (cit. on p. 26).
- [105] P. K. Biswas and V. Gogonea, *A regularized and renormalized electrostatic coupling Hamiltonian for hybrid quantum-mechanical/molecular-mechanical calculations*, J. Chem. Phys. **123**, – (2005), (cit. on p. 26).
- [106] E. M. Sproviero, J. A. Gascón, J. P. McEvoy, G. W. Brudvig, and V. S. Batista, *QM/MM Models of the O₂-Evolving Complex of Photosystem II*, J. Chem. Theory Comput. **2**, 1119 (2006), (cit. on p. 26).
- [107] J. A. Gascón, S. S. F. Leung, E. R. Batista, and V. S. Batista, *A Self-Consistent Space-Domain Decomposition Method for QM/MM Computations of Protein Electrostatic Potentials*, J. Chem. Theory Comput. **2**, 175 (2006), (cit. on p. 26).
- [108] H. M. Senn and W. Thiel, *QM/MM Methods for Biomolecular Systems*, Angew. Chem. Int. Ed. **48**, 1198 (2009), (cit. on p. 26).
- [109] H. Hu, M. Elstner, and J. Hermans, *Comparison of a QM/MM force field and molecular mechanics force fields in simulations of alanine and glycine "dipeptides" (Ace-Ala-Nme and Ace-Gly-Nme) in water in relation to the problem of modeling the unfolded peptide backbone in solution*, Proteins Struct. Funct. Bioinf. **50**, 451 (2003), (cit. on p. 26).

-
- [110] R. Zhang, B. Lev, J. E. Cuervo, S. Y. Noskov, and D. R. Salahub, *Chapter 10 - A Guide to QM/MM Methodology and Applications*, Academic Press, 2010, (cit. on p. 26).
- [111] R. P. Feynman, *Forces in Molecules*, Phys. Rev. **56**, 340 (1939), (cit. on p. 28).
- [112] U. C. Singh and P. A. Kollman, *A combined ab initio quantum mechanical and molecular mechanical method for carrying out simulations on complex molecular systems: Applications to the CH₃Cl + Cl exchange reaction and gas phase protonation of polyethers*, J. Comput. Chem. **7**, 718 (1986), (cit. on p. 28).
- [113] H. M. Evjen, *On the Stability of Certain Heteropolar Crystals*, Phys. Rev. **39**, 675 (1932), (cit. on p. 29).
- [114] J. M. Vollmer, E. V. Stefanovich, and T. N. Truong, *Molecular Modeling of Interactions in Zeolites: An Ab Initio Embedded Cluster Study of NH₃ Adsorption in Chabazite*, J.Phys.Chem. B **103**, 9415 (1999), (cit. on p. 29).
- [115] A. A. Sokol, S. T. Bromley, S. A. French, C. R. A. Catlow, and P. Sherwood, *Hybrid QM/MM embedding approach for the treatment of localized surface states in ionic materials*, Int. J. Quantum Chem. **99**, 695 (2004), (cit. on pp. 29, 31, 32, 34, 60, 88, 92, 103).
- [116] B. Herschend, M. Baudin, and K. Hermansson, *A combined molecular dynamics+quantum mechanics method for investigation of dynamic effects on local surface structures*, J. Chem. Phys. **120**, 4939 (2004), (cit. on p. 29).
- [117] D. Parry, *The electrostatic potential in the surface region of an ionic crystal*, Surf. Sci. **49**, 433 (1975), (cit. on p. 30).
- [118] D. Parry, *Errata*, (cit. on p. 30).
- [119] "Appendix A: Mathematical Aspects of Equilibrium Thermodynamics", John Wiley & Sons, Inc., 2008, ISBN: 9780470164112, (cit. on pp. 30, 31).
- [120] P. Sherwood, A. H. de Vries, M. F. Guest, G. Schreckenbach, C. R. A. Catlow, S. A. French, A. A. Sokol, S. T. Bromley, W. Thiel, A. J. Turner, *et al.*, *QUASI: A general purpose implementation of the QM/MM approach and its application to problems in catalysis*, J. Mol. Struct. THEOCHEM **632**, 1 (2003), (cit. on pp. 32, 92, 110).
- [121] J. Kästner, J. M. Carr, T. W. Keal, W. Thiel, A. Wander, and P. Sherwood, *DL-FIND: An Open-Source Geometry Optimizer for Atomistic Simulations*, J.Phys.Chem. A **113**, 11856 (2009), (cit. on pp. 33, 92).
- [122] J. D. Gale, *GULP: A computer program for the symmetry-adapted simulation of solids*, J. Chem. Soc., Faraday Trans. **93**, 629 (1997), (cit. on pp. 33, 90, 92).
- [123] J. D. Gale and A. L. Rohl, *The General Utility Lattice Program (GULP)*, Mol. Simul. **29**, 291 (2003), (cit. on p. 33).
- [124] T. F. W. Smith and I.T.Todorov, *"The DL_POLY 2.0 User Manual"*, Daresbury Laboratory, STFC Daresbury Laboratory, Daresbury, Warrington WA4 4AD, Cheshire, UK, 2008, (cit. on p. 33).
- [125] A. B. Lidiard, *The Mott - Littleton method: an introductory survey*, J. Chem. Soc., Faraday Trans. 2 **85**, 341 (1989), (cit. on p. 33).
- [126] J. D. Jackson, *Classical electrodynamics*, Wiley New York etc., 1962, (cit. on pp. 34, 65).
- [127] V. Blum, R. Gehrke, F. Hanke, P. Havu, V. Havu, X. Ren, K. Reuter, and M. Scheffler, *Ab initio molecular simulations with numeric atom-centered orbitals*, Comput. Phys. Commun. **180**, 2175 (2009), (cit. on pp. 37, 39, 41, 42, 55, 88, 104).

- [128] D. Berger, A. J. Logsdail, H. Oberhofer, M. R. Farrow, C. R. A. Catlow, P. Sherwood, A. A. Sokol, V. Blum, and K. Reuter, *Embedded-cluster calculations in a numeric atomic orbital density-functional theory framework*, J. Chem. Phys. **141**, – (2014), (cit. on pp. 37, 79, 88, 92, 109).
- [129] N. A. Richter, S. Siculo, S. V. Levchenko, J. Sauer, and M. Scheffler, *Concentration of Vacancies at Metal-Oxide Surfaces: Case Study of MgO(100)*, Phys. Rev. Lett. **111**, 045502 (2013), (cit. on pp. 37, 101, 105).
- [130] X. Ren, P. Rinke, V. Blum, J. Wieferink, A. Tkatchenko, A. Sanfilippo, K. Reuter, and M. Scheffler, *Resolution-of-identity approach to Hartree-Fock, hybrid density functionals, RPA, MP2 and GW with numeric atom-centered orbital basis functions*, New J. Phys. **14**, 053020 (2012), (cit. on pp. 39, 41, 88, 104).
- [131] X. Ren, P. Rinke, G. E. Scuseria, and M. Scheffler, *Renormalized second-order perturbation theory for the electron correlation energy: Concept, implementation, and benchmarks*, Phys. Rev. B **88**, 035120 (2013), (cit. on p. 39).
- [132] I. Y. Zhang, X. Ren, P. Rinke, V. Blum, and M. Scheffler, *Numeric atom-centered-orbital basis sets with valence-correlation consistency from H to Ar*, New J. Phys. **15**, 123033 (2013), (cit. on pp. 39, 112).
- [133] A. D. Becke, *A multicenter numerical integration scheme for polyatomic molecules*, J. Chem. Phys. **88**, 2547 (1988), (cit. on p. 39).
- [134] B. Delley, *An all-electron numerical method for solving the local density functional for polyatomic molecules*, J. Chem. Phys. **92**, 508 (1990), (cit. on pp. 39, 41, 42).
- [135] V. Havu, V. Blum, P. Havu, and M. Scheffler, *Efficient $O(N)$ integration for all-electron electronic structure calculation using numeric basis functions*, J. Comput. Phys. **228**, 8367 (2009), (cit. on p. 39).
- [136] L. Kleinman and D. M. Bylander, *Efficacious Form for Model Pseudopotentials*, Phys. Rev. Lett. **48**, 1425 (1982), (cit. on pp. 39, 40, 88).
- [137] B. J. Austin, V. Heine, and L. J. Sham, *General Theory of Pseudopotentials*, Phys. Rev. **127**, 276 (1962), (cit. on p. 39).
- [138] *FHI98PP source*, <http://th.fhi-berlin.mpg.de/th/fhi98md/download/index.html#fhipp>, Accessed: 2013-09-30 (cit. on p. 40).
- [139] *Abinit web page*, <http://www.abinit.org/downloads/psp-links/pseudopotentials>, Accessed: 2013-09-29 (cit. on p. 40).
- [140] X. Gonze, R. Stumpf, and M. Scheffler, *Analysis of separable potentials*, Phys. Rev. B **44**, 8503 (1991), (cit. on p. 40).
- [141] J. Harris, *Simplified method for calculating the energy of weakly interacting fragments*, Phys. Rev. B **31**, 1770 (1985), (cit. on p. 40).
- [142] J. D. Talman, *Numerical methods for multicenter integrals for numerically defined basis functions applied in molecular calculations*, Int. J. Quantum Chem. **93**, 72 (2003), (cit. on p. 41).
- [143] J. D. Talman, *Optimization of numerical orbitals in molecular MO-LCAO calculations*, Int. J. Quantum Chem. **95**, 442 (2003), (cit. on p. 41).
- [144] J. D. Talman, *NumSBT: A subroutine for calculating spherical Bessel transforms numerically*, Comput. Phys. Commun. **180**, 332 (2009), (cit. on p. 41).

- [145] S. G. Louie, S. Froyen, and M. L. Cohen, *Nonlinear ionic pseudopotentials in spin-density-functional calculations*, Phys. Rev. B **26**, 1738 (1982), (cit. on p. 44).
- [146] D. Porezag, M. R. Pederson, and A. Y. Liu, *Importance of nonlinear core corrections for density-functional based pseudopotential calculations*, Phys. Rev. B **60**, 14132 (1999), (cit. on p. 44).
- [147] P. Pulay, *Convergence acceleration of iterative sequences. the case of scf iteration*, Chem. Phys. Lett. **73**, 393 (1980), (cit. on p. 44).
- [148] J. Gerratt and I. M. Mills, *Force Constants and Dipole-Moment Derivatives of Molecules from Perturbed Hartree-Fock Calculations. I*, J. Chem. Phys. **49**, 1719 (1968), (cit. on p. 44).
- [149] J. Gerratt and I. M. Mills, *Force Constants and Dipole-Moment Derivatives of Molecules from Perturbed Hartree-Fock Calculations. II. Applications to Limited Basis-Set SCF-MO Wavefunctions*, J. Chem. Phys. **49**, 1730 (1968), (cit. on p. 44).
- [150] R. Storn and K. Price, *Differential Evolution - A Simple and Efficient Heuristic for global Optimization over Continuous Spaces*, J. Global Optim. **11**, 341 (1997), (cit. on pp. 47, 90, 127).
- [151] *inspyred 1.0 documentation*, <http://inspyred.github.io/overview.html>, Accessed: 2014-05-06 (cit. on pp. 47, 90, 127).
- [152] *ChemShell User Manual: Hybrid Ab-Initio / Force-Field Calculations*, http://www.cse.scitech.ac.uk/ccg/software/chemshell/manual/hyb_new.html, Accessed: 2014-05-06 (cit. on p. 51).
- [153] *ChemShell Tutorial: Solid State Embedding with a Shell Model Potential*, http://www.cse.scitech.ac.uk/ccg/software/chemshell/tutorial/mgo_embed.html, Accessed: 2014-05-06 (cit. on pp. 51, 53, 56).
- [154] *ChemShell User Tutorial: Solid State Embedding with a Shell Model Potential*, http://www.cse.scitech.ac.uk/ccg/software/chemshell/tutorial/mgo_embed.html, Accessed: 2014-10-14 (cit. on p. 53).
- [155] T. Bredow, G. Geudtner, and K. Jug, *Embedding procedure for cluster calculations of ionic crystals*, J. Chem. Phys. **105**, 6395 (1996), (cit. on pp. 54, 58).
- [156] *"FHI-aims: A Users' Guide", Version 2013*, Fritz-Haber-Institut Berlin, 2013, (cit. on pp. 54–56).
- [157] *GULP:GULP help file*, http://projects.ivec.org/gulp/help/help_30_txt.html, Accessed: 2014-07-18 (cit. on p. 56).
- [158] D. O. Scanlon, C. W. Dunnill, J. Buckeridge, S. A. Shevlin, A. J. Logsdail, S. M. Woodley, C. R. A. Catlow, M. J. Powell, R. G. Palgrave, I. P. Parkin, *et al.*, *Band alignment of rutile and anatase TiO₂*, Nat. Mater. **12**, 798 (2013), (cit. on pp. 57, 58, 60, 89).
- [159] R. A. Parker, *Static Dielectric Constant of Rutile (TiO₂), 1.6-1060 K*, Phys. Rev. **124**, 1719 (1961), (cit. on pp. 58, 89).
- [160] R. Heise, R. Courths, and S. Witzel, *Valence band densities-of-states of TiO₂(110) from resonant photoemission and photoelectron diffraction*, Solid State Commun. **84**, 599 (1992), (cit. on p. 58).
- [161] R. S. Mulliken, *Electronic Population Analysis on LCAO-MO Molecular Wave Functions. I*, J. Chem. Phys. **23**, 1833 (1955), (cit. on pp. 58, 73).

- [162] F. Hirshfeld, *Bonded-atom fragments for describing molecular charge densities*, Theor. Chim. Acta **44**, 129 (1977), (cit. on p. 58).
- [163] J. F. Sanz, N. C. Hernández, and A. Márquez, *A first principles study of Pd deposition on the TiO₂(110) surface*, Theor. Chem. Acc. **104**, 317 (2000), (cit. on pp. 58, 89).
- [164] S. C. Ammal and A. Heyden, *Modeling the noble metal/TiO₂(110) interface with hybrid DFT functionals: A periodic electrostatic embedded cluster model study*, J. Chem. Phys. **133**, 164703 (2010), (cit. on pp. 58, 62, 91).
- [165] P. Reinhardt, M. Causà, C. M. Marian, and B. A. Heß, *Adsorption of CO on TiO₂(110) studied by means of a cluster model surrounded by multipoles obtained from slab calculations*, Phys. Rev. B **54**, 14812 (1996), (cit. on pp. 58, 89).
- [166] G. Pacchioni, A. M. Ferrari, and P. S. Bagus, *Cluster and band structure ab initio calculations on the adsorption of CO on acid sites of the TiO₂(110) surface*, Surf. Sci. **350**, 159 (1996), (cit. on p. 58).
- [167] T. Bredow and G. Pacchioni, *Electronic structure of an isolated oxygen vacancy at the TiO₂(110) surface*, Chem. Phys. Lett. **355**, 417 (2002), (cit. on pp. 58, 97).
- [168] A. S. Mazheika, V. E. Matulis, and O. A. Ivashkevich, *Quantum chemical study of adsorption of Ag₂, Ag₄ and Ag₈ on stoichiometric TiO₂(110) surface*, J. Mol. Struct. THEOCHEM **942**, 47 (2010), (cit. on p. 58).
- [169] B. G. Dick and A. W. Overhauser, *Theory of the Dielectric Constants of Alkali Halide Crystals*, Phys. Rev. **112**, 90 (1958), (cit. on pp. 58, 89, 90).
- [170] C. R. A. Catlow, C. M. Freeman, M. S. Islam, R. A. Jackson, M. Leslie, and S. M. Tomlinson, *Interatomic potentials for oxides*, Philos. Mag. A **58**, 123 (1988), (cit. on pp. 58, 59, 84, 89, 90).
- [171] F. A. Grant, *Properties of Rutile (Titanium Dioxide)*, Rev. Mod. Phys. **31**, 646 (1959), (cit. on p. 62).
- [172] S. Bates, G. Kresse, and M. Gillan, *A systematic study of the surface energetics and structure of TiO₂(110) by first-principles calculations*, Surf. Sci. **385**, 386 (1997), (cit. on p. 60).
- [173] P. Murugan, V. Kumar, and Y. Kawazoe, *Thickness dependence of the atomic and electronic structures of TiO₂ rutile (110) slabs and the effects on the electronic and magnetic properties of supported clusters of Pd and Rh*, Phys. Rev. B **73**, 075401 (2006), (cit. on p. 60).
- [174] A. Kiejna, T. Pabisiak, and S. W. Gao, *The energetics and structure of rutile TiO₂(110)*, J. Phys. Condens. Matter **18**, 4207 (2006), (cit. on p. 61).
- [175] A. Jentys and C. Catlow, *Structural properties of titanium sites in Ti-ZSM5*, Catal. Lett. **22**, 251 (1993), (cit. on pp. 65, 67, 74, 82).
- [176] H. Sato, K. Ono, T. Sasaki, and A. Yamagishi, *First-Principles Study of Two-Dimensional Titanium Dioxides*, J.Phys.Chem. B **107**, 9824 (2003), (cit. on p. 66).
- [177] B. Lee, C. Lee, C. S. Hwang, and S. Han, *Influence of exchange-correlation functionals on dielectric properties of rutile TiO₂*, Curr. Appl Phys. **11**, S293 (2011), (cit. on pp. 66, 84, 88–90).
- [178] A. Valdés, Z.-W. Qu, G.-J. Kroes, J. Rossmesl, and J. K. Nørskov, *Oxidation and Photo-Oxidation of Water on TiO₂ Surface*, J.Phys.Chem. C **112**, 9872 (2008), (cit. on pp. 70, 79, 81, 82, 87).

- [179] B. Hammer and J. Nørskov, *Theoretical surface science and catalysis — calculations and concepts*, **45**, 71 (2000), (cit. on p. 70).
- [180] K. Reuter, C. Stampf, and M. Scheffler, “AB Initio Atomistic Thermodynamics and Statistical Mechanics of Surface Properties and Functions”, Springer Netherlands, 2005, ISBN: 978-1-4020-3287-5, (cit. on pp. 70, 104).
- [181] C. Stampfl, *Surface processes and phase transitions from ab initio atomistic thermodynamics and statistical mechanics*, Catal. Today **105**, 17 (2005), (cit. on p. 70).
- [182] Z.-W. Qu and G.-J. Kroes, *Theoretical Study of Adsorption of O(3P) and H₂O on the Rutile TiO₂(110) Surface*, J. Phys. Chem. B **110**, 23306 (2006), (cit. on pp. 79, 81).
- [183] U. Diebold, *The surface science of titanium dioxide*, Surf. Sci. Rep. **48**, 53 (2003), (cit. on pp. 81, 87, 98).
- [184] A. Fujishima, X. Zhang, and D. A. Tryk, *TiO₂ photocatalysis and related surface phenomena*, Surf. Sci. Rep. **63**, 515 (2008), (cit. on pp. 81, 87).
- [185] M. A. Henderson, *A surface science perspective on photocatalysis*, Surf. Sci. Rep. **66**, 185 (2011), (cit. on pp. 81, 87, 98).
- [186] T. Thompson and J. T. J. Yates, *TiO₂-based Photocatalysis: Surface Defects, Oxygen and Charge Transfer*, Top. Catal. **35**, 197 (2005), (cit. on pp. 81, 87).
- [187] J. K. Nørskov, J. Rossmeisl, A. Logadottir, L. Lindqvist, J. R. Kitchin, T. Bligaard, and H. Jónsson, *Origin of the Overpotential for Oxygen Reduction at a Fuel-Cell Cathode*, J. Phys. Chem. B **108**, 17886 (2004), (cit. on pp. 81, 83).
- [188] P. J. D. Lindan and C. Zhang, *Exothermic water dissociation on the rutile TiO₂(110) surface*, Phys. Rev. B **72**, 075439 (2005), (cit. on p. 81).
- [189] M. Garcíá-Mota, A. Vojvodic, H. Metiu, I. C. Man, H.-Y. Su, J. Rossmeisl, and J. K. Nørskov, *Tailoring the Activity for Oxygen Evolution Electrocatalysis on Rutile TiO₂(110) by Transition-Metal Substitution*, ChemCatChem **3**, 1607 (2011), (cit. on p. 81).
- [190] M. Garcíá-Mota, A. Vojvodic, F. Abild-Pedersen, and J. K. Nørskov, *Electronic Origin of the Surface Reactivity of Transition-Metal-Doped TiO₂(110)*, J. Phys. Chem. C **117**, 460 (2013), (cit. on p. 81).
- [191] P. Zawadzki, J. Rossmeisl, and K. W. Jacobsen, *Electronic hole transfer in rutile and anatase TiO₂: Effect of a delocalization error in the density functional theory on the charge transfer barrier height*, Phys. Rev. B **84**, 121203 (2011), (cit. on p. 81).
- [192] H. Oberhofer and K. Reuter, *First-principles thermodynamic screening approach to photocatalytic water splitting with co-catalysts*, J. Chem. Phys. **139**, – (2013), (cit. on pp. 81, 82, 87).
- [193] S. Boys and F. Bernardi, *The calculation of small molecular interactions by the differences of separate total energies. Some procedures with reduced errors*, Mol. Phys. **19**, 553 (1970), (cit. on pp. 82, 112).
- [194] I. C. Man, H.-Y. Su, F. Calle-Vallejo, H. A. Hansen, J. I. Martínez, N. G. Inoglu, J. Kitchin, T. F. Jaramillo, J. K. Nørskov, and J. Rossmeisl, *Universality in Oxygen Evolution Electrocatalysis on Oxide Surfaces*, ChemCatChem **3**, 1159 (2011), (cit. on p. 83).
- [195] C. Di Valentin and D. Costa, *Anatase TiO₂ Surface Functionalization by Alkylphosphonic Acid: A DFT+D Study*, J. Phys. Chem. C **116**, 2819 (2012), (cit. on p. 82).

- [196] D. van der Vliet, D. S. Strmcnik, C. Wang, V. R. Stamenkovic, N. M. Markovic, and M. T. Koper, *On the importance of correcting for the uncompensated Ohmic resistance in model experiments of the Oxygen Reduction Reaction*, J. Electroanal. Chem. **647**, 29 (2010), (cit. on p. 83).
- [197] F. Furche and J. P. Perdew, *The performance of semilocal and hybrid density functionals in 3d transition-metal chemistry*, J. Chem. Phys. **124**, (2006), (cit. on p. 83).
- [198] J. K. Burdett, T. Hughbanks, G. J. Miller, J. W. Richardson, and J. V. Smith, *Structural-electronic relationships in inorganic solids: powder neutron diffraction studies of the rutile and anatase polymorphs of titanium dioxide at 15 and 295 K*, J. Am. Chem. Soc. **109**, 3639 (1987), (cit. on pp. 84, 88, 89).
- [199] J. G. Traylor, H. G. Smith, R. M. Nicklow, and M. K. Wilkinson, *Lattice Dynamics of Rutile*, Phys. Rev. B **3**, 3457 (1971), (cit. on pp. 84, 89).
- [200] R. Schaub, P. Thosttrup, N. Lopez, E. Lægsgaard, I. Stensgaard, J. K. Nørskov, and F. Besenbacher, *Oxygen vacancies as active sites for water dissociation on rutile TiO₂(110)*, Phys. Rev. Lett. **87**, 266104 (2001), (cit. on pp. 87, 98).
- [201] O. Bikondoa, C. L. Pang, R. Ithnin, C. A. Muryn, H. Onishi, and G. Thornton, *Direct visualization of defect-mediated dissociation of water on TiO₂(110)*, Nat. Mater. **5**, 189 (2006), (cit. on p. 87).
- [202] S. Wendt, P. T. Sprunger, E. Lira, G. K. Madsen, Z. Li, J. Ø. Hansen, J. Matthiesen, A. Blekinge-Rasmussen, E. Lægsgaard, B. Hammer, *et al.*, *The Role of Interstitial Sites in the Ti3d Defect State in the Band Gap of Titania*, Science **320**, 1755 (2008), (cit. on p. 87).
- [203] C. N. Rusu and J. T. Yates, *Defect Sites on TiO₂(110). Detection by O₂ Photodesorption*, Langmuir **13**, 4311 (1997), (cit. on p. 87).
- [204] Z. Zhang, K. Cao, and J. T. Yates, *Defect-Electron Spreading on the TiO₂(110) Semiconductor Surface by Water Adsorption*, J. Phys. Chem. Lett. **4**, 674 (2013), (cit. on p. 87).
- [205] S. Yang, A. T. Brant, and L. E. Halliburton, *Photoinduced self-trapped hole center in TiO₂ crystals*, Phys. Rev. B **82**, 035209 (2010), (cit. on p. 87).
- [206] P. Deák, B. Aradi, and T. Frauenheim, *Quantitative theory of the oxygen vacancy and carrier self-trapping in bulk TiO₂*, Phys. Rev. B **86**, 195206 (2012), (cit. on pp. 87, 98, 99).
- [207] M. Batzill, K. Katsiev, D. J. Gaspar, and U. Diebold, *Variations of the local electronic surface properties of TiO₂(110) induced by intrinsic and extrinsic defects*, Phys. Rev. B **66**, 235401 (2002), (cit. on p. 87).
- [208] A. Vijay, G. Mills, and H. Metiu, *Adsorption of gold on stoichiometric and reduced rutile TiO₂(110) surfaces*, J. Chem. Phys. **118**, 6536 (2003), (cit. on p. 87).
- [209] A. L. Shluger and A. M. Stoneham, *Small polarons in real crystals: concepts and problems*, J. Phys.: Condens. Matter **5**, 3049 (1993), (cit. on p. 87).
- [210] S. Yang, L. E. Halliburton, A. Manivannan, P. H. Bunton, D. B. Baker, M. Klemm, S. Horn, and A. Fujishima, *Photoinduced electron paramagnetic resonance study of electron traps in TiO₂ crystals: Oxygen vacancies and Ti³⁺ ions*, Appl. Phys. Lett. **94**, – (2009), (cit. on pp. 87, 99).

- [211] V. Saunders, C. Freyria-Fava, R. Dovesi, L. Salasco, and C. Roetti, *On the electrostatic potential in crystalline systems where the charge density is expanded in Gaussian functions*, Mol. Phys. **77**, 629 (1992), (cit. on p. 88).
- [212] D. R. Collins, W. Smith, N. M. Harrison, and T. R. Forester, *Molecular dynamics study of TiO₂ microclusters*, J. Mater. Chem. **6**, 1385 (1996), (cit. on p. 89).
- [213] C. G. Van de Walle and J. Neugebauer, *First-principles calculations for defects and impurities: Applications to III-nitrides*, J. Appl. Phys. **95**, 3851 (2004), (cit. on p. 92).
- [214] K. Reuter and M. Scheffler, *Composition, structure, and stability of RuO₂(110) as a function of oxygen pressure*, Phys. Rev. B **65**, 035406 (2001), (cit. on pp. 93, 101).
- [215] A. Janotti, J. Varley, P. Rinke, N. Umezawa, G. Kresse, and C. Van de Walle, *Hybrid functional studies of the oxygen vacancy in TiO₂*, Phys. Rev. B **81**, 085212 (2010), (cit. on pp. 93, 95–97).
- [216] T. Yamamoto and T. Ohno, *Screened hybrid density functional study on Nb- and Ta-doped TiO₂*, Phys. Rev. B **85**, 033104 (2012), (cit. on p. 93).
- [217] M. Landmann, E. Rauls, and W. G. Schmidt, *The electronic structure and optical response of rutile, anatase and brookite TiO₂*, J. Phys. Condens. Matter **24**, 195503 (2012), (cit. on p. 93).
- [218] C. Di Valentin, G. Pacchioni, and A. Selloni, *Electronic Structure of Defect States in Hydroxylated and Reduced Rutile TiO₂(110) Surfaces*, Phys. Rev. Lett. **97**, 166803 (2006), (cit. on pp. 95, 98, 99).
- [219] M. V. Ganduglia-Pirovano, A. Hofmann, and J. Sauer, *Oxygen vacancies in transition metal and rare earth oxides: Current state of understanding and remaining challenges*, Surf. Sci. Rep. **62**, 219 (2007), (cit. on p. 97).
- [220] T. Pabisiak and A. Kiejna, *Energetics of oxygen vacancies at rutile TiO₂(110) surface*, Solid State Commun. **144**, 324 (2007), (cit. on p. 97).
- [221] B. J. Morgan and G. W. Watson, *A DFT + U description of oxygen vacancies at the TiO₂ rutile (110) surface*, Surf. Sci. **601**, 5034 (2007), (cit. on p. 97).
- [222] J. Sauer, *Molecular models in ab initio studies of solids and surfaces: from ionic crystals and semiconductors to catalysts*, Chem. Rev. **89**, 199 (1989), (cit. on p. 97).
- [223] P. Krüger, S. Bourgeois, B. Domenichini, H. Magnan, D. Chandresris, P. Le Fèvre, A. M. Flank, J. Jupille, L. Floreano, A. Cossaro, A. Verdini, and A. Morgante, *Defect States at the TiO₂(110) Surface Probed by Resonant Photoelectron Diffraction*, Phys. Rev. Lett. **100**, 055501 (2008), (cit. on p. 98).
- [224] B. J. Morgan and G. W. Watson, *A Density Functional Theory + U Study of Oxygen Vacancy Formation at the (110), (100), (101), and (001) Surfaces of Rutile TiO₂*, J. Phys. Chem. C **113**, 7322 (2009), (cit. on p. 98).
- [225] M. A. Henderson, *Evidence for bicarbonate formation on vacuum annealed TiO₂(110) resulting from a precursor-mediated interaction between CO₂ and H₂O*, Surf. Sci. **400**, 203 (1998), (cit. on p. 98).
- [226] K. Onda, B. Li, and H. Petek, *Two-photon photoemission spectroscopy of TiO₂(110) surfaces modified by defects and O₂ or H₂O adsorbates*, Phys. Rev. B **70**, 045415 (2004), (cit. on p. 98).
- [227] S. Krischok, J. Günster, D. Goodman, O. Höfft, and V. Kempter, *MIES and UPS(HeI) studies on reduced TiO₂(110)*, Surf. Interface Anal. **37**, 77 (2005), (cit. on p. 98).

- [228] A. T. Brant, N. C. Giles, S. Yang, M. A. R. Sarker, S. Watauchi, M. Nagao, I. Tanaka, D. A. Tryk, A. Manivannan, and L. E. Halliburton, *Ground state of the singly ionized oxygen vacancy in rutile TiO₂*, J. Appl. Phys. **114**, – (2013), (cit. on p. 99).
- [229] F. D. Brandão, M. V. B. Pinheiro, G. M. Ribeiro, G. Medeiros-Ribeiro, and K. Krambrock, *Identification of two light-induced charge states of the oxygen vacancy in single-crystalline rutile TiO₂*, Phys. Rev. B **80**, 235204 (2009), (cit. on p. 99).
- [230] H.-Y. Lee, S. J. Clark, and J. Robertson, *Calculation of point defects in rutile TiO₂ by the screened-exchange hybrid functional*, Phys. Rev. B **86**, 075209 (2012), (cit. on p. 99).
- [231] B. Yoon, H. Häkkinen, U. Landman, A. S. Wörz, J.-M. Antonietti, S. Abbet, K. Judai, and U. Heiz, *Charging Effects on Bonding and Catalyzed Oxidation of CO on Au₈ Clusters on MgO*, Science **307**, 403 (2005), (cit. on p. 101).
- [232] A. S. Foster, F. Lopez Gejo, A. L. Shluger, and R. M. Nieminen, *Vacancy and interstitial defects in hafnia*, Phys. Rev. B **65**, 174117 (2002), (cit. on p. 101).
- [233] I. Balint and K. Aika, *Specific defect sites creation by doping MgO with lithium and titanium*, Appl. Surf. Sci. **173**, 296 (2001), (cit. on pp. 101, 105, 108).
- [234] F. Illas and G. Pacchioni, *Optical properties of surface and bulk F centers in MgO from ab initio cluster model calculations*, J. Chem. Phys. **108**, 7835 (1998), (cit. on p. 101).
- [235] D. Berger, P. Dinh, P. Reinhard, and E. Suraud, *A study of color centers in MgO using a hierarchical model*, EPJ D **66**, (2012), (cit. on p. 101).
- [236] Z. Yan, S. Chinta, A. A. Mohamed, J. P. Fackler, and D. W. Goodman, *The Role of F-Centers in Catalysis by Au Supported on MgO*, J. Am. Chem. Soc. **127**, 1604 (2005), (cit. on p. 101).
- [237] E. Wahlström, E. K. Vestergaard, R. Schaub, A. Rønnau, M. Vestergaard, E. Lægsgaard, I. Stensgaard, and F. Besenbacher, *Electron Transfer-Induced Dynamics of Oxygen Molecules on the TiO₂(110) Surface*, Science **303**, 511 (2004), (cit. on p. 101).
- [238] T. Brudevoll, E. A. Kotomin, and N. E. Christensen, *Interstitial-oxygen-atom diffusion in MgO*, Phys. Rev. B **53**, 7731 (1996), (cit. on p. 101).
- [239] R. A. Evarestov, P. W. M. Jacobs, and A. V. Leko, *Oxygen interstitials in magnesium oxide: A band-model study*, Phys. Rev. B **54**, 8969 (1996), (cit. on p. 101).
- [240] S. Sicolo and J. Sauer, *Interaction of CO with Electron-Rich Defects on MgO(100)*, J.Phys.Chem. C **117**, 8365 (2013), (cit. on p. 101).
- [241] S. Bhattacharya, S. V. Levchenko, L. M. Ghiringhelli, and M. Scheffler, *Stability and Metastability of Clusters in a Reactive Atmosphere: Theoretical Evidence for Unexpected Stoichiometries of Mg_MO_x*, Phys. Rev. Lett. **111**, 135501 (2013), (cit. on pp. 101, 104).
- [242] M. Scheffler and C. Weinert, “Chalcogen and vacancy pairs in silicon: electronic structure and stabilities”, Trans. Tech. Publ. Ltd, Switzerland, 1986, (cit. on pp. 101, 104).
- [243] S. Bhattacharya, S. V. Levchenko, L. M. Ghiringhelli, and M. Scheffler, *Efficient ab initio schemes for finding thermodynamically stable and metastable atomic structures: Benchmark of cascade genetic algorithms*, New. J. Phys. (Accepted), arXiv:1409.8522, (2014), (cit. on pp. 101, 105).
- [244] L. O. Paz-Borbón, G. Barcaro, A. Fortunelli, and S. V. Levchenko, *Au_N clusters (N = 1–6) supported on MgO(100) surfaces: Effect of exact exchange and dispersion interactions on adhesion energies*, Phys. Rev. B **85**, 155409 (2012), (cit. on p. 102).

- [245] S. Bhattacharya, S. V. Levchenko, and L. M. Ghiringhelli, *Private communication*, (cit. on pp. 102, 106).
- [246] D. R. Lide, *CRC Handbook of Chemistry and Physics, 79th ed.* CRC Press, Boca Raton, FL, 1998/1999, (cit. on p. 104).
- [247] R. A. Bartels and P. A. Smith, *Pressure and Temperature Dependence of the Static Dielectric Constants of KCl, NaCl, LiF, and MgO*, Phys. Rev. B **7**, 3885 (1973), (cit. on p. 104).
- [248] H. Grünewald, *CRC Handbook of Chemistry and Physics. 46th ed.* Angew. Chem. **78**, 912 (1966), (cit. on p. 104).
- [249] G.-X. Zhang, A. Tkatchenko, J. Paier, H. Appel, and M. Scheffler, *van der Waals Interactions in Ionic and Semiconductor Solids*, Phys. Rev. Lett. **107**, 245501 (2011), (cit. on p. 104).
- [250] J. A. Van Vechten, *Quantum Dielectric Theory of Electronegativity in Covalent Systems. I. Electronic Dielectric Constant*, Phys. Rev. **182**, 891 (1969), (cit. on p. 104).
- [251] D. Olson, W. Haag, and R. Lago, *Chemical and physical properties of the ZSM-5 substitutional series*, J. Catal. **61**, 390 (1980), (cit. on pp. 109, 113).
- [252] S. M. Csicsery, *Shape-selective catalysis in zeolites*, Zeolites **4**, 202 (1984), (cit. on p. 109).
- [253] P. B. Venuto, *Organic catalysis over zeolites: A perspective on reaction paths within micropores*, Microporous Mater. **2**, 297 (1994), (cit. on p. 109).
- [254] W. Haag, *Catalysis by Zeolites – Science and Technology*, **84**, 1375 (1994), (cit. on p. 109).
- [255] T. W. Keal, P. Sherwood, G. Dutta, A. A. Sokol, and C. R. A. Catlow, *Characterization of hydrogen dissociation over aluminium-doped zinc oxide using an efficient massively parallel framework for QM/MM calculations*, Proc. R. Soc. B. **467**, 1900 (2011), (cit. on p. 109).
- [256] G. J. Kramer, R. A. van Santen, C. A. Emeis, and A. K. Nowak, *Understanding the acid behaviour of zeolites from theory and experiment*, Nature **363**, 529 (1993), (cit. on pp. 109, 113).
- [257] M. Boronat, C. Martínez-Sánchez, D. Law, and A. Corma, *Enzyme-like Specificity in Zeolites: A Unique Site Position in Mordenite for Selective Carbonylation of Methanol and Dimethyl Ether with CO*, J. Am. Chem. Soc. **130**, 16316 (2008), (cit. on p. 109).
- [258] J. To, A. A. Sokol, S. A. French, N. Kaltsoyannis, and C. R. A. Catlow, *Hole localization in $[AlO_4]_0$ defects in silica materials*, J. Chem. Phys. **122**, – (2005), (cit. on p. 109).
- [259] G. Pacchioni, F. Frigoli, D. Ricci, and J. A. Weil, *Theoretical description of hole localization in a quartz Al center: The importance of exact electron exchange*, Phys. Rev. B **63**, 054102 (2000), (cit. on p. 109).
- [260] M. F. Guest, I. J. Bush, H. J. J. Van Dam, P. Sherwood, J. M. H. Thomas, J. H. Van Lenthe, R. W. A. Havenith, and J. Kendrick, *The GAMESS-UK electronic structure package: algorithms, developments and applications*, Mol. Phys. **103**, 719 (2005), (cit. on p. 109).
- [261] *Oil & Gas Journal*, <http://www.ogj.com/articles/print/vol-110/issue-07/special-report-ethylene-report/global-ethylene-capacity.html>, Accessed: 2014-08-04 (cit. on p. 109).
- [262] C. D. Chang and A. J. Silvestri, *The conversion of methanol and other O-compounds to hydrocarbons over zeolite catalysts*, J. Catal. **47**, 249 (1977), (cit. on p. 109).

- [263] L. Kubelková, J. Nováková, and K. Nedomová, *Reactivity of surface species on zeolites in methanol conversion*, J. Catal. **124**, 441 (1990), (cit. on pp. 109, 113).
- [264] F. Haase and J. Sauer, *Interaction of methanol with Brønsted acid sites of zeolite catalysts: an ab initio study*, J. Am. Chem. Soc. **117**, 3780 (1995), (cit. on pp. 109, 113).
- [265] S. R. Blaszowski and R. A. van Santen, *The Mechanism of Dimethyl Ether Formation from Methanol Catalyzed by Zeolitic Protons*, J. Am. Chem. Soc. **118**, 5152 (1996), (cit. on pp. 109, 113).
- [266] J. McMurry, *Organic Chemistry, Enhanced Edition*, Cengage Learning, 2009, (cit. on p. 110).
- [267] G. N. Vayssilov, H. A. Aleksandrov, G. P. Petrova, P. S. Petkov, V. Valtchev, S. Mintova, and M. Tsapatsis, *Computational Modeling of Nanoporous Materials*, Elsevier: Amsterdam, 2009, (cit. on p. 110).
- [268] J.-R. Hill and J. Sauer, *Molecular Mechanics Potential for Silica and Zeolite Catalysts Based on ab Initio Calculations. 2. Aluminosilicates*, J.Phys.Chem. **99**, 9536 (1995), (cit. on pp. 110, 114).
- [269] I. T. Todorov, W. Smith, K. Trachenko, and M. T. Dove, *DL-POLY_3: new dimensions in molecular dynamics simulations via massive parallelism*, J. Mater. Chem. **16**, 1911 (2006), (cit. on p. 110).
- [270] P. Sherwood, A. H. de Vries, S. J. Collins, S. P. Greatbanks, N. A. Burton, M. A. Vincent, and I. H. Hillier, *Computer simulation of zeolite structure and reactivity using embedded cluster methods*, Faraday Discuss. **106**, 79 (1997), (cit. on p. 110).
- [271] R. Ahlrichs and P. Taylor, *The choice of gaussian-basis sets for molecular electronic-structure calculations*, J. Chim. Phys. Phys.- Chim. Biol. **78**, 315 (1981), (cit. on p. 111).
- [272] A. D. Becke, *Density-functional thermochemistry. III, The role of exact exchange*, J. Chem. Phys. **98**, 5648 (1993), (cit. on pp. 111, 115).
- [273] C. Lee, W. Yang, and R. G. Parr, *Development of the Colle-Salvetti correlation-energy formula into a functional of the electron density*, Phys. Rev. B **37**, 785 (1988), (cit. on pp. 111, 115).
- [274] P. J. Stephens, F. J. Devlin, C. F. Chabalowski, and M. J. Frisch, *Ab Initio Calculation of Vibrational Absorption and Circular Dichroism Spectra Using Density Functional Force Fields*, J.Phys.Chem. **98**, 11623 (1994), (cit. on p. 111).
- [275] Y. Zhang, X. Xu, and W. A. Goddard, *Doubly hybrid density functional for accurate descriptions of nonbond interactions, thermochemistry, and thermochemical kinetics*, PNAS **106**, 4963 (2009), (cit. on p. 111).
- [276] J. Pérez-Ramírez, F. Kapteijn, G. Mul, and J. A. Moulijn, *NO-Assisted N₂O Decomposition over Fe-Based Catalysts: Effects of Gas-Phase Composition and Catalyst Constitution*, J. Catal. **208**, 211 (2002), (cit. on p. 112).
- [277] L. Guimaraes, H. A. de Abreu, and H. A. Duarte, *Fe(II) hydrolysis in aqueous solution: A DFT study*, Chem. Phys. **333**, 10 (2007), (cit. on p. 112).
- [278] R. A. van Santen and G. J. Kramer, *Reactivity Theory of Zeolitic Brønsted Acidic Sites*, Chem. Rev. **95**, 637 (1995), (cit. on p. 113).
- [279] T. Mole and J. Whiteside, *Conversion of methanol to ethylene over ZSM-5 zeolite in the presence of deuterated water*, J. Catal. **75**, 284 (1982), (cit. on p. 113).

-
- [280] J. Lercher, Y. Liu, and Y. Zhi, *Private communication*, (cit. on p. 113).
- [281] R. A. Jackson and C. R. A. Catlow, *Computer Simulation Studies of Zeolite Structure*, *Mol. Simul.* **1**, 207 (1988), (cit. on p. 114).
- [282] S. A. Zygmunt, L. A. Curtiss, P. Zapol, and L. E. Iton, *Ab Initio and Density Functional Study of the Activation Barrier for Ethane Cracking in Cluster Models of Zeolite H-ZSM-5*, *J.Phys.Chem. B* **104**, 1944 (2000), (cit. on pp. 114, 115).
- [283] M. J. Janik, J. Macht, E. Iglesia, and M. Neurock, *Correlating Acid Properties and Catalytic Function: A First-Principles Analysis of Alcohol Dehydration Pathways on Polyoxometalates*, *J.Phys.Chem. C* **113**, 1872 (2009), (cit. on p. 115).
- [284] J. Nocedal and S. J. Wright, *Numerical Optimization 2nd*, (2006), (cit. on p. 116).
- [285] R. van Santen, "Theory of Brønsted Acidity in Zeolites", Elsevier, 1994, (cit. on p. 116).
- [286] G. Henkelman and H. Jónsson, *Improved tangent estimate in the nudged elastic band method for finding minimum energy paths and saddle points*, *J. Chem. Phys.* **113**, 9978 (2000), (cit. on p. 118).

Acknowledgement

This work has only been made possible with the help of many people, who deserve a fair share of acknowledgement:

First of all I would like to thank Prof. Karsten Reuter for financial support, many advices and fruitful discussions, always friendly communication and most importantly for his patience. There have been longer periods during the developing and implementing phase of thesis where progress was hardly evident. During that time Prof. Reuter showed the perfect balance between not being pushy at all but still emphasizing importance of my work. That really kept me motivated during the whole time, and helped to overcome quite a few obstacles.

Many thanks go to every single member of the group, who made the last 4 years a really great time. Each one of them contributed their bit to establish a joyful working atmosphere, with lots of ping-ping and numerous group outings. *“It was great working with you guys.”* Special thanks go to Dr. Harald Oberhofer, who has been a most awesome supervisor. He was of great support in countless discussions, as a motivator, and not the least because of his way of keeping everything fun. Further, I highly appreciated collaborating with Prof. Volker Blum in the implementation work on the side of *FHI-aims*. He was of more than great support. On the *ChemShell* side I would like to thank Dr. Andrew Logsdail and Dr. Alexey Sokol for their hospitality in London. Further, I would like to thank Dr. Christoph Scheurer, Dr. Max Hoffmann and Christoph Schober for their technical support, and Ruth Mösch *to keep things ticking over*.

I would like to thank the *International Graduate School for Science and Engineering* for a scholarship, which made it possible to attend numerous conferences and workshops, including extended stays at the University of Cambridge and the University of California, Los Angeles. Thanks to their outstanding financial support and familiar atmosphere at graduate school events, I will keep my IGSSE time in good memory. Most of this work would not have been possible without the heavy use of supercomputer facilities. At this side, I thank Prof. Matthias Scheffler for unbureaucratically providing me with an access to the HYDRA-cluster, and again Harald Oberhofer letting me use most of the CPUs of his grant at SUPERMUC.

Special thanks go, once again, to Harald Oberhofer for his patient and self-sacrificing support during the last weeks in adding a significant level of structure to this thesis. On very short-notice Stephanie Heinath, Julian Seuring, Johannes Maidhof, Christoph Sieger and Patrick Brünner were of immense help in proof-reading.

I would like to thank my three parents for their unconditional support throughout, further all my friends, my brother, and not the least Steffi for *maintaining* my social life during my doctorate.

Finally, I would like to thank Steffi in many ways, for here patience, love and joy, too many to fit on this page ...

